Models and Simulations of the Electric Field in Deep Brain Stimulation
Comparison of Lead Designs, Operating Modes and Tissue Conductivity

Fabiola Alonso

LINKÖPING UNIVERSITY

Cover: Depiction of the electric field around DBS electrodes and the word brain 𓄑𓏏𓏤 .
The pictograph is contained in an ancient Egyptian Papyrus, transcribed in
the Seventeenth Century B.C. The papyrus is a medical treatise with the
earliest mention of the brain in human records.

MODELS AND SIMULATIONS OF THE ELECTRIC FIELD
IN DEEP BRAIN STIMULATION
COMPARISON OF LEAD DESIGNS, OPERATING MODES AND
TISSUE CONDUCTIVITY

Supervisor: Karin Wårdell
Co-supervisors: Simone Hemm
                Johannes Johansson

Department of Biomedical Engineering
Linköping University
SE-581 85 Linköping, Sweden

Todo es puerta,
basta la leve presión de un pensamiento…
Octavio Paz*, Noche en claro*

Everything is a door,
all one needs is the light push of a thought…
Translation by Eliot Weinberger

ABSTRACT

Deep brain stimulation (DBS) is an established surgical therapy for movement disorders such as Parkinson's disease (PD) and essential tremor (ET). A thin electrode is implanted in a predefined area of the brain with the use of stereotactic neurosurgery. In the last few years new DBS electrodes and systems have been developed with possibilities for using more parameters for control of the stimulation volume.

In this thesis, simulations using the finite element method (FEM) have been developed and used for investigation of the electric field (EF) extension around different types of DBS lead designs (symmetric, steering) and stimulation modes (voltage, current). The electrode surrounding was represented either with a homogeneous model or a patient-specific model based on individual preoperative magnetic resonance imaging (MRI). The EF was visualized and compared for different lead designs and operating modes.

In Paper I, the EF was quantitatively investigated around two lead designs (3389 and 6148) simulated to operate in voltage and current mode under acute and chronic time points following implantation.Simulations showed a major impact on the EF extension between postoperative time points which may explain the clinical decisions to change the stimulation amplitude weeks after implantation. In Paper II, the simulations were expanded to include two leads having steering function (6180, Surestim1) and patient-specific FEM simulations in the zona incerta. It was found that both the heterogeneity of the tissue and the operating mode, influence the EF distribution and that equivalent contact configurations of the leads result in similar EF. The steering mode presented larger volumes in current mode when using equivalent amplitudes. Simulations comparing DBS and intraoperative stimulation test using a microelectrode recording (MER) system (Paper III), showed that several parallel MER leads and the presence of the non-active DBS contacts influence the EF distribution and that the DBS EF volume can cover, but also extend to, other anatomical areas.

Paper IV introduces a method for an objective exploitation of intraoperative stimulation test data in order to identify the optimal implant position in the thalamus of the chronic DBS lead. Patient-specific EF simulations were related to the anatomy with the help of brain atlases and the clinical effects which were quantified by accelerometers. The first results indicate that the good clinical effect in ET is due to several structures around the ventral intermediate nucleus of the thalamus.

SVENSK SAMMANFATTNING

Djup hjärnstimulering (deep brain stimulation, DBS) är en metod för att ta bort symtom från olika rörelsesjukdomar, t.ex. Parkinsons sjukdom och essentiell tremor. En liten elektrod opereras in i ett väl bestämt område i hjärnan med stereotaktisk teknik. Elektroden påverkar nervceller och fungerar då som en "pacemaker".

Under de senare åren har flera nya typer av DBS-elektroder och system introducerats. I denna avhandling, studeras olika DBS-elektrodkonfigurationer och deras inverkan på det stimulerade området i hjärnan. Finita element metoden (FEM) används för att skapa datormodeller av elektroderna och av den omgivande hjärnvävnadens elektriska egenskaper (konduktivitet). Hjärnmodellerna kan vara homogena och representera grå vävnad eller vara heterogena dvs. patient-specifika. De senare byggs utifrån en persons magnetresonans (MR) bilder genom att ersätta vävnadtypen med dess respektive konduktivitet. Därefter utför simuleringar av det elektriska fältet (EF) runt elektroden. Resultaten visualiseras för en förbestämd isonivå genom att överlagra elektrod och simulerat EF på MR-bilden. Utbredning av EF och dess volym används som mått vid jämförelse.

Elektriska fältet kring DBS elektroderna har jämförts med varandra för olika kontaktinställningar, simulationsmoder (ström, spänning) och stimulationsamplituder. Vidare har simuleringar vid olika tidpunkter, akut och kronisk, undersökts. Detta är baserat på att en förändring av vävnadens konduktivitet runt elektroden sker över tid. Jämförelse har också systematisk utförts för en rad olika situationer relaterat till mikroelektrodstimulering, en metod som används vid själva operationen för att söka upp det bästa målområdet där DBS elektroden ska placeras. Vidare har patientspecifika simuleringar kopplats samman med mätning av rörelse och intraoperativ stimulering för att påbörja arbetet med att skapa kartor av vilka områden som ger bäst effekt av stimuleringen.

Simuleringarna visar att det är viktigt att ta hänsyn till den individuella hjärnans konduktiva egenskaper, dvs. patientspecifika simuleringar, och att man bör vänta med den slutliga amplitudinställningen ungefär en månad efter det kirurgiska ingreppet, dvs. när vävnadsegenskaperna stabiliserats runt elektroden. DBS-elektroder som kan styra EF visar på större volymer i strömstyrd inställning jämfört med spänningsstyrd. Stora kontaktytor i elektroden spets bör undvikas. Vid användning av intraoperativ teststimulering bör det beaktas att de kroniska DBS EF-volymerna inte alltid är spridda i samma anatomiska områden. Avhandlingen presenterar metoder och resultat i fyra artiklar som har publicerats i internationella vetenskaplig tidskrifter.

LIST OF PUBLICATIONS

This thesis is based on the following papers which were published with an open access (CC BY) license. The papers are appended at the end of the thesis.

I. **Alonso, F**., Hemm-Ode, S., & Wårdell, K. (2015). Influence on Deep Brain Stimulation from Lead Design, Operating Mode and Tissue Impedance Changes–A Simulation Study. *Brain Disorders and Therapy*, *4,* pp. 1-8.

II. **Alonso, F**., Latorre, M. A., Göransson, N., Zsigmond, P., & Wårdell, K. (2016). Investigation into deep brain stimulation lead designs: a patient-specific simulation study. *Brain sciences*, *6*(3), 39, pp.1-16.

III. **Alonso, F.**, Vogel, D., Johansson, J., Wårdell, K., & Hemm, S. (2018). Electric Field Comparison between Microelectrode Recording and Deep Brain Stimulation Systems—a Simulation Study. *Brain sciences*, *8*(2), 28, pp. 1-15.

IV. Hemm, S., Pison, D., **Alonso, F**., Shah, A., Coste, J., Lemaire, J. J., & Wårdell, K. (2016). Patient-Specific Electric Field Simulations and Acceleration Measurements for Objective Analysis of Intraoperative Stimulation Tests in the Thalamus. *Frontiers in human neuroscience*, (10), 577, pp. 1-14

RELATED PUBLICATIONS

1. **Alonso F**, Latorre M, Wårdell K, Comparison of Three Deep Brain Stimulation Lead Designs under Voltage and Current Modes. In: Jaffray D (eds) IFMBE Proceedings Springer, vol 51, pp 1196-1199, 2015

2. Johansson JD, **Alonso F**, Wårdell K, Modelling Details for Electric Field Simulations of Deep Brain Stimulation. In: Lhotska L, Sukupova L, Lacković I, Ibbott G (eds). IFMBE Proceedings, Springer, pp 645-648, vol 68/1, 2018

3. Shah AA, **Alonso F**, Vogel D, Wårdell K, Coste J, Lemaire JJ, Pison D and Hemm S, Analysis of Adverse Effects of Stimulation During DBS Surgery by Patient-Specific FEM Simulations, Proceedings of IEEE EMBC USA, pp 1-5, 2018, Accepted

4. Johansson D, **Alonso F**, Wårdell K, Patient-Specific Simulations of Deep Brain Stimulation Electric Field with Aid of In-house Software ELMA, In Manuscript 2018

ABBREVIATIONS

CC	Coverage coefficient
CNS	Central Nervous System
CSF	Cerebrospinal fluid
CT	Computer tomography
cZi	Caudal part of the zona incerta
DBS	Deep brain stimulation
DC	Sørensen-Dice coefficient
EF	Electric field
ET	Essential tremor
FEM	Finite element method
FF	Fields of Forel
FP	Floating potential
GND	Ground
GPi	Globus pallidus internus
IPG	Implantable pulse generator
MER	Microelectrode recording
MRI	Magnetic resonance imaging
OCD	Obsessive compulsive disorder
PES	Perielectrode space
PD	Parkinson's disease
PDE	Partial differential equation
PSA	Posterior subthalamic area
ROI	Region of interest
SNc	Substantia nigra pars compacta
SNr	Substantia nigra pars reticulata
STN	Subthalamic nucleus
VIM	Ventro intermediate nucleous
VTA	Volume of tissue activated
Zi	Zona incerta

Contents

1 INTRODUCTION

Deep brain stimulation (DBS) is an established surgical therapy to reduce the symptoms of movement disorders and its indications are rapidly expanding towards other neurological and psychiatric diseases [1]. The surgery is minimally invasive and consists of the implantation of thin electrodes into the deep part of the brain (Fig. 1). The electrodes, connected to a battery-operated implantable pulse generator (IPG) typically placed below the clavicle, generate an electric field stimulating a very specific and carefully selected subcortical region causing symptom relief in patients who do not respond to drug treatment.

DBS therapy was first approved in Europe in 1995 for essential tremor (ET) and in 1997 by the United States Food and Drug Administration (FDA) [2]. It is also approved for Parkinson's disease (PD), the main indication for DBS nowadays, and dystonia (under a Humanitarian Device Exemption (HDE) in the US). In Europe, Australia and other countries outside the US, the therapy is also approved to treat epilepsy, obsessive compulsive disorder (OCD) and treatment-resistant depression[3, 4].

For several years, the only approved DBS systems were produced by Medtronic (Minneapolis, MN, USA). They consisted of four cylindrical electrodes connected to a voltage-driven IPG also known as neurostimulators. A few years ago, Abbot (St. Paul, MN, USA) formerly St. Jude Medical, and Boston Scientific (Natick, MA, USA) expanded the DBS technology introducing new electrode and neurostimulators designs [5, 6]. Segmented electrodes capable of steering the electric field, current-controlled neurostimulators, rechargeable IPG capable of delivering specific parameters to each contact independently and new patterns of stimulation are examples of new DBS technology currently available and under clinical trials [4, 7].
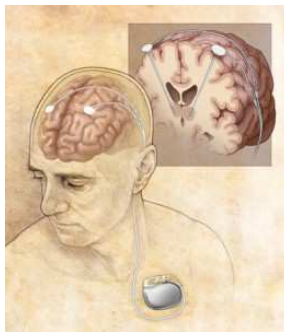
Figure 1 Deep brain stimulation system. Neurostimulator implanted below the clavicle sends electrical pulses through the extensions to the electrodes implanted in subcortical regions. (*Used with permission of Mayo Foundation for Medical Education and Research. All rights reserved.*)

Since 1997 more than 150 000 patients around the world have been implanted with a DBS system [8]. The rapid development of the DBS therapy has been possible due to its reproducible therapeutic efficacy in numerous clinical trials, its safety, and programming flexibility, but also to the readily available DBS devices and the supporting technology, including magnetic resonance imaging (MRI) and devices for electrophysiological measurements [3]. Despite the successful and promising results of the DBS therapy, fundamental questions remain unclear, hindering the optimization of the current applications. The neurophysiological mechanisms through which electrical stimulation results in clinical benefits, the best target region to reduce side effects, or the appropriate time to receive the therapy are issues yet to be settled [1]. Intensive research from different fields aims for a better understanding of the mechanisms of action, observing for instance, changes in neurotransmitter levels before and after DBS using microdialysis in rats [9, 10]; changes in cortical activity through functional imaging in patients [11]; and computer models to investigate the neural response to the electrical stimulation [12-15].

The intrinsic purpose of DBS is to modulate neural activity with extracellular electric fields [16], which in turn depends on the stimulation parameters (amplitude, pulse width, frequency) and the physiological properties of the brain tissue [17]. The introduction of new technology has increased the number of stimulation parameters making the evaluation of the effects of DBS through clinical and animal experiments, both impractical and ethically questionable.

Up to date and since 2004 [18] computer models have been used to address the neural response to DBS in highly controlled conditions. Models and simulations have also been used to visualize the stimulation field around the DBS electrodes which is currently not possible by means of any imaging modality, contributing to further investigation of the DBS mechanisms of action.

The focus of this thesis is to evaluate the influence of different characteristics of the new DBS systems in terms of the electric field (EF) distribution. Comparisons of the EF distribution obtained from different electrode designs, operating modes, and set up were performed by means of computer models and simulations based on the finite element method (FEM).

2 NEUROPHYSIOLOGY AND NEUROLOGICAL DISEASES

The brain, as part of the central nervous system (CNS), is responsible for a wide variety of tasks. From motor behaviours such as walking or eating, to more sophisticated cognitive behaviours, considered typically human, such as thinking or speaking [19].

The brain (Fig. 2) is composed of the cerebrum, the cerebellum and the brainstem. The brainstem conveys information between the spinal cord and the cerebrum. It receives and processes sensory information from the skin and muscles of the head, and also provides motor control for the head's muscles. The cerebellum, connected to the brain stem through major fibre tracts, regulates the force and range of movement and is involved in the learning of motor skills.

The cerebrum comprises the large, heavily wrinkled outer layer, the cerebral cortex. It is separated by the corpus callosum into two hemispheres, and three deep-lying structures: the basal ganglia, the hippocampus and the amygdaloid nuclei. The basal ganglia are involved in the regulation of motor performance, the hippocampus is related to memory storage and the amygdaloid nuclei participates in the coordination of the autonomic and endocrine of emotional states [19]. These and other complex tasks achieved by the brain are accomplished by interconnected nerve cells, the neurons.
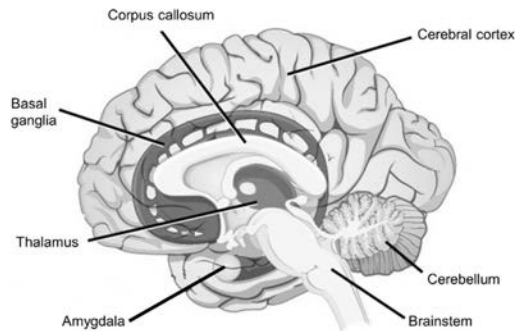
Figure 2 Schematic representation of the human brain anatomy, sagittal view.
(Modified from https://upload.wikimedia.org/wikipedia/commons/5/5e/Figure_35_03_02b.jpg)

2.1 SIGNALLING UNIT OF THE NERVOUS SYSTEM

Information within and from neurons, is carried by electrical and chemical signals. Transient electrical signals are important to transmit time-sensitive information rapidly and over long distances. The morphology of a typical neuron consists of four regions (Fig. 3), each with a distinct role in the generation and transmission of signals and the communication with other neurons. The cell body or soma, is the metabolic site of the cell from which two kinds of processes (neurites) emerge: a highly branched and short outgrowth, the dendrites; and a single long, tubular extension, the axon. Dendrites receive signals from other nerve cells and the axon conveys signals to other neurons.
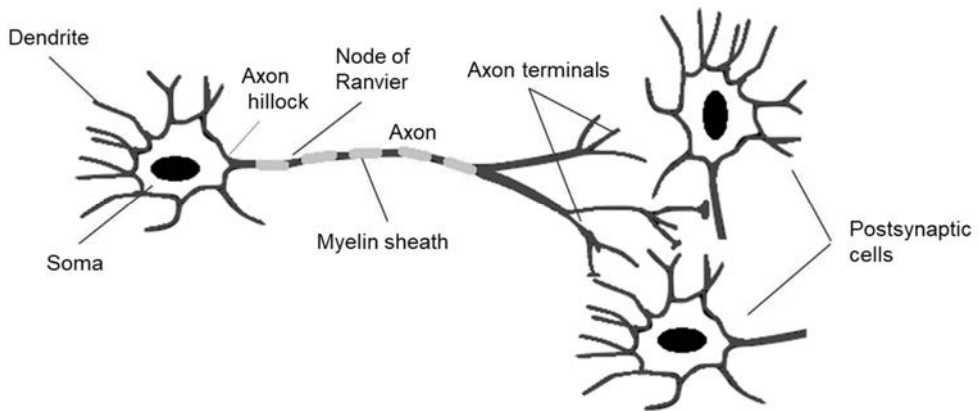
Figure 3 Basic representation of the structure of a typical neuron; most axons in the central nervous system are between 0.2 µm and 20 µm thick. The branches of a single axon can form synapses up to 1000 postsynaptic cells [19]. The CNS is visibly divided into grey matter (areas with preponderance of cell bodies) and white matter (areas with preponderance of axons, white appearance given by the fatty myelin sheaths)

The electrical signals conveyed by the axons are called action potentials and occur due to a temporary change in the flow of positive and negative ions into and out of the cells. At rest, the extracellular space contains a higher concentration of positive charge while the cytoplasm has an excess of negative charge. The transmembrane potential V_m exists by virtue of the difference in concentration of ions inside and outside the cell, $V_m = V_{in} - V_{out}$. By convention the potential outside the cell is zero, thus the resting membrane potential V_r is equal to V_{in} whose value is typically within -60 to -70 mV.

The rapid changes of the membrane potential underlying the communication within the nervous system are possible due to ion channels (proteins integrated in

the membrane) which are optimally tuned to respond to chemical and physical signals. In addition to ion channels, nerve cells contain another kind of proteins capable of moving or pumping ions across the cell membrane and are important to establish and maintain the concentration gradients inside and outside the cell.

The action potential is all or non-phenomena, and to be triggered the stimuli need to surpass a threshold value of potential for a minimum time. Thus, signalling in the brain depends on the ability of the neurons to respond to small stimuli with fast and large changes in the electric potential across the cell membrane [19].

The propagation speed of action potentials is increased by virtue of myelin sheaths wrapping the axon, significantly reducing its membrane capacitance. The sheath is interrupted at regular intervals by the nodes of Ranvier where action potentials are regenerated. The axon can transmit an electrical signal over distances ranging from 0.1 mm to 2 m.

The communication with other neurons is chemically driven by the neurotransmitter transmission at specialized zones known as synapses. Under physiological conditions, action potentials are initiated at the axon hillok and travel without attenuation along the axon (orthodromic direction) to reach the axon terminals, causing the release of neurotransmitters stored in the synaptic vesicles. The major transmitter in inhibitory neurons is GABA (gamma-Aminobutyric acid), the glutamate in turn is the main excitatory neurotransmitter. The neurotransmitter may have an excitatory or inhibitory effect depending on the type of receptor in the postsynaptic cell. [19]. Most axon terminals end near the dendrites of postsynaptic cells, but it can happen that they end on the cell body or less often at the beginning or end of the receiving neuron. Artificially generated action potentials can also travel antidromically, i.e. from the stimulus site towards the cell soma [20]. Dopamine (DA) is another neurotransmitter that has an important function in motor control, motivation, emotion, attention and reward.

2.2 MOTOR CONTROL AND RELEVANT STRUCTURES

The control of the motor system is organized hierarchically, from the highest levels at the cerebral cortex to the lowest level constituted by motor neurons of the spinal cord. In general, voluntary movement in humans is initiated by activity at the motor cortical areas which in turn send and receive signals from the thalamus and the more primitive regions within the brain, the basal ganglia.

2.2.1 BASAL GANGLIA

The basal ganglia consist of several interconnected grey matter nuclei and were first described by Thomas Willis in the 17th century [21]. Through observations of brains of patients who had died from long paralysis, Willis implicated the motor function to the corpus striatum and this concept predominated during 200 years forming the basis for localizing several movement disorders to the striatum in the middle of the 19th century. Along the substantia nigra (SN), the subthalamic nucleus (STN) and the globus pallidus (GP), the corpus striatum (composed of the caudate nucleus, putamen and the nucleus accumbus) denotes a substructure of the basal ganglia (Fig. 4).

 The basal ganglia were originally believed to only control motor functions, however it is known now that they are critically implicated in cognition and motivation. Thus, diseases of the basal ganglia are often a combination of movement, emotion and cognitive disorders [22].

  Insights into the complex organization and function of the basal ganglia have been possible through examination of the motor circuit by experimental studies activating or inactivating portions of the basal ganglia; by electrophysiological recordings of single neurons and by imaging and behavioural studies [19]. Contrary to cortical motor areas, which are relatively easy to access and study through non-invasive techniques, the role of the basal ganglia and the cerebellum in the motor control has been explained mainly theoretically. Indeed, the advent of deep brain stimulation has contributed with new possibilities to assess some of the functions and connections of this part of the brain.

  Since the late 1980s conceptual models of the basal ganglia function have been proposed providing the knowledge to develop pharmacological and surgical therapies to treat movement disorders, especially Parkinson's disease [21]. There is no consensus of the connectivity between the different basal ganglia nuclei. However, the most accepted view considers the striatum as the major input receiving glutamatergic excitatory signals from the cerebral cortex, brainstem and thalamus; while the internal part of the globus pallidus (GPi) and the substantia nigra pars reticulata (SNr) are regarded as the output regions signalling back to the original cortical area and the brain stem through the thalamus [23].

   The modern understanding of the connectivity of the basal ganglia is based on a model proposed by Albin and De Long [24, 25] , which considers the initiation and execution of motor programmes through the interplay of two pathways (Fig. 4), both originating in the striatum (putamen in the motor circuit): the *direct* (permissive) pathway where GABAergic inhibitory monosynaptic signals project directly to both output nuclei (GPi and SNpr) and the *indirect* (inhibitory) pathway where the signals from the striatum first reach the external part of the globus pallidus (GPe) which in

turn projects its inhibitory output, both directly and through the STN (the only excitatory nucleus of the basal ganglia) to the output nuclei [19, 22, 23].
 The STN then excites the GPi causing an increasing inhibition of the thalamocortical motor neurons. According to this model, the inhibition of the GPi through the striatum is slower but more powerful than the excitatory input from the STN. Thus, during a voluntary movement, the resulting decreased activity in the GPi selectively disinhibits the desired motor actions in the cerebral cortex [22].
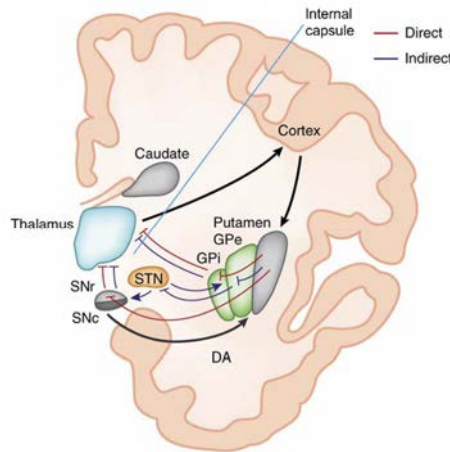
Figure 4 Schematic representation of the coronal view of the basal ganglia and surrounding structures. The classical model of the physiological condition where the dopamine (DA) from the SNc activates striatal neurons expressing D1 receptor (direct pathway, shown in red) and inhibits striatal neurons expressing D2 receptor (indirect pathway, shown in blue). The output nuclei, GPi and SNr, project to the thalamus, which in turns sends efferents to the cortex, completing the cortico-basal ganglia-thalamo-cortical loop. [Modified from [26] with permission from Springer Nature, License number: 4350830820163]

The key to the normal basal ganglia functions are the tonically active neurons of the GPi/SNpr continuously inhibiting the motor portions of the thalamus, braking the motor pattern generators in the cerebral cortex and brain stem [22, 27]. Thus, cortical activation of striatal neurons that are part of the direct pathway, will transiently remove inhibition of thalamocortical neurons allowing cortical regions to be active, thus facilitating movement. On the contrary, phasic activation of striatal projections belonging to the indirect pathway will remove inhibition of the STN allowing activation of the GPi/SNpr transiently increasing inhibition of the thalamocortical neurons and therefore inhibiting movement. The projections between the pallidum and the thalamus follow two routes, one from the lateral region of the GPi, passing around the internal capsule, finally accessing the Field of Forel (prerubral field). The other route starts more medially in the GPi projecting through

the internal capsule to form the lenticulat fasciculus, situated between the STN and the zona incerta (Zi) [28].

New insights into the functional organization of the basal ganglia have modified the classical model of a single motor loop proposing instead a complex network of several loops where cortical and subcortical projections interact with internal re-entry loops [28].

2.2.2 THALAMUS

The thalamus is responsible for processing most of the information reaching the cerebral cortex from the rest of the central nervous system. In the motor circuit, the ventral thalamic nuclei receive input from the basal ganglia and the cerebellum, and transmit the information to the motor regions of the frontal lobe [19]. The anatomy of the thalamus is very complex due to the large amount of nuclei it comprises and their complicated and confusing labelling [29]. Around fifty nuclei have been identified so far and are commonly classified in four groups in relation to the internal medullary lamina: anterior, medial, ventrolateral, and posterior (Fig. 5) [19].
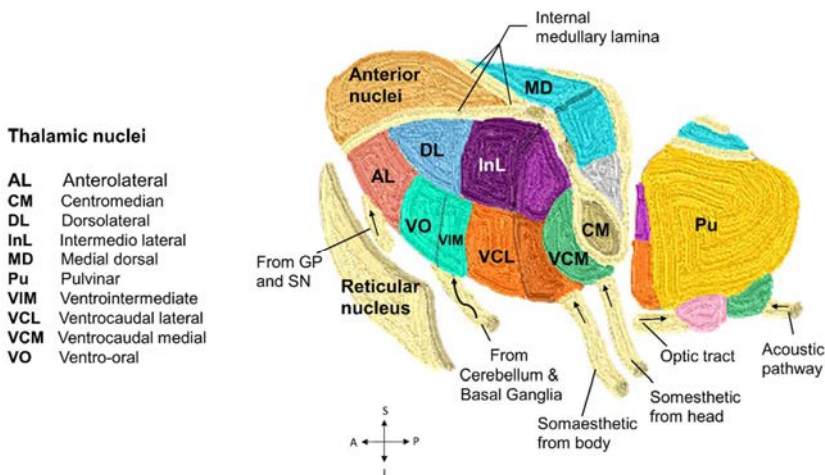
Figure 5 Schematic representation of the thalamus (sagittal view. A: anterior, P: posterior; S: superior and I: inferior) and some of its nuclei, labelled in accordance with [29]. The total volume of the thalamic nuclei is around 6.1 cm^3.

The ventral intermediate nucleus (VIM) of the thalamus is an established neurosurgical target for either ablation or deep brain stimulation to treat tremor in ET and PD [30]. VIM is centrally located within the cerebello-thalamo-cortical

network which connects the dentate nucleus of the cerebellum to the primary motor cortex through the dentate-rubro-thalamic tract (DRT) [31].

In clinical practice, the inner anatomy of the thalamus for specific individuals is indirectly approached according to a stereotactic atlas or directly seeking the nuclei boundaries on MRI scans [29]. The VIM however, is not readily visible with conventional stereotactic magnetic resonance sequences and several imaging techniques have been proposed to better identify this nucleus [29, 32, 33].

2.2.3 SUBTHALAMIC NUCLEUS AND ZONA INCERTA

The subthalamic region, ventral to the thalamus, comprises the STN and the zona incerta (Fig. 6). The STN, is a lens-shaped structure of about 240 mm^3 [34], surrounded by several fibre tracts from the zona incerta and the Fields of Forel. It provides a powerful excitatory input to the GPi and SNpr neurons, thus it has an important role in the inhibition pattern of the basal ganglia output. In addition to the GABAergic input from the GPe, there is a hyperdirect connection between the cortex and the STN which is activated when a voluntary movement is initiated by cortical mechanisms [22]. The STN also receives dopaminergic projection from the SNc. Regarding the efferents, the STN not only projects to the basal ganglia output nuclei but also to the ventral thalamic motor nuclei [28]. The subthalamic nucleus is the target of choice in deep brain stimulation for Parkinson's disease, however it is not known if the clinical outcome responds to excitation of neurons in the STN and/or in the surrounding fibre tracts.

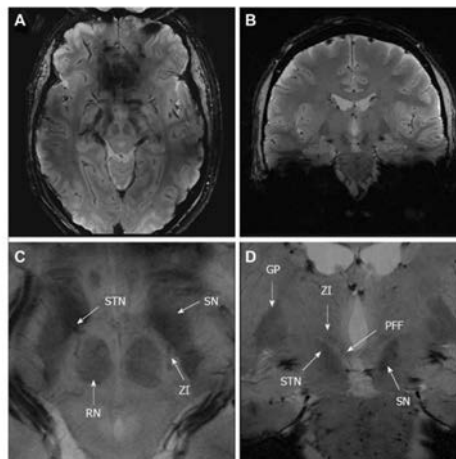*Figure 6* 7 tesla MRI (FLASH2D-T2Star) of the subthalamic area, **A.** axial view and **B.** coronal view. C and D corresponding magnification displaying the labels of the structures of interest: STN: subthalamic nucleus; RN, red nucleus, SN, substantia nigra; ZI, zona incerta; GP, globus pallidus, and PPF, pallidofugal fibres. Modified from [35]

The zona incerta, is located between the STN and the thalamus with extensive connections to the cerebral cortex, basal ganglia, brain stem and spinal cord. It is formed by various types of neurons with different sizes and shapes. The cytoarchitectonic diversity derives in multiple functions including the control of visceral activity, arousal, attention and maintaining posture and locomotion [36]. At the location of the zona incerta, prominent tracts such as cerebellar peduncle (between the cerebellum and the brain stem), nigrostriatal tract, the thalamic fasciculus and the lenticular fasciculus, converge before reaching their final destination [37]. The caudal part of the zona incerta (cZi) has been shown to be an effective DBS target in the treatment of tremor in Parkinson's disease [38, 39]. Another term related to the region of the Zi is the posterior subthalamic area (PSA) which comprises adjacent structures that can explain the therapeutic effects of DBS [38].

2.3 MOVEMENT DISORDERS

The connection between the cortex and the basal ganglia, encompasses several segregated and parallel loops which have been classified into motor, associative (cognitive) and limbic (emotional) domains. A dysfunction of any of these circuits, in consequence, results in movement and/or behavioural and cognitive disorders [40]. The prevalence of movement disorders is often difficult to estimate due to lack of pathologic substrate, reliance on a clinical diagnosis, and a high rate of under diagnosis [22].

2.3.1 ESSENTIAL TREMOR

Essential tremor is considered one of the most common movement disorders, occurring in 1 % of the total population and around 5 % of the people over 60 years old [41]. The prevalence rate, however, may vary widely due to the lack of a biologic marker or a clearly defined phenotype, making it difficult to differentiate ET from other conditions which present a phenotypic overlap, especially tremor in dystonia or Parkinson's disease [22]. The term essential indicates that the cause of the tremor is not identified, but it is clinically well characterized [42]. A classical characteristic of ET is the action tremor affecting the upper limbs, this is, the tremor that occurs with a voluntary movement of a muscle. The diagnosis criteria have a wide variation among clinicians; thus, according to the Consensus Statement on the Classification of Tremors [43], the definition of ET considers: *1)* isolated tremor syndrome of bilateral upper limb action tremor, *2)* at least 3 years' duration, *3)* with or without tremor in other locations (e.g., head, voice, or lower limbs); and *4)* absence of other

neurological signs, such as dystonia, ataxia (uncoordinated muscle movement) or parkinsonism. In addition, the exclusion criteria for ET diagnosis, include isolated focal tremors (voice, head), orthostatic tremor (involuntary rhythmic muscle movement) with a frequency greater than 12 Hz; task and position-specific tremor, and sudden onset and step-wise deterioration.

The ET syndrome presents multiple etiologies, some hypothesis of the pathophysiology comprise neurodegeneration, abnormal function of the inhibitory neurotransmitter GABA and oscillating network [44].
The tremor severity and handicap vary widely in patients with essential tremor, impairment to achieve daily activities has been assessed by using the Fahn-Tolosa-Marín (FTM) tremor rating scale, validated for ET in 2007 [45]. The assessment and quantification of the tremor is a major clinical and research problem and so is the efficacy of the treatment.

The treatment for ET patients includes several types of medication [46], however the medical treatment in up to 50% of the patients does not provide sufficient tremor control. The neurosurgical approach for these patients could represent an appropriate alternative; VIM thalamic DBS is the most commonly used neurosurgical procedure to treat tremor in patients who do not respond to medication. With an optimal positioning of the DBS electrode and the appropriate stimulation parameters, it is possible to completely or nearly completely reduce the contralateral limb tremor [47].

2.3.2 PARKINSON'S DISEASE

Parkinson's disease was clinically described for the first time by James Parkinson in his treatise on the shaking palsy in 1817 [22]. Parkinson's disease is a complex neurological disorder with a wide variety of symptoms. The cardinal characteristics are akinesia (impairment of movement initiation), bradykinesia (reduction in the amplitude and velocity of voluntary movements), muscular rigidity and tremor. Patients may also present other motor disturbances such as shuffling gait, flexed posture, reduced facial expression, decreased blinking and small handwriting [19]. Non-motor symptoms may include depression, anxiety, cognitive impairment, sleep disturbances and autonomic dysfunction.

The salient pathological feature of idiopathic Parkinson's disease is the degeneration of dopaminergic cells in the substantia nigra pars compacta that project to the striatum (represented with the black dashed line in Fig. 7). Dopamine loss in this region is thought to be the cause of the movement abnormalities, since patients respond to dopamine replacement therapies.

The classical model of the direct/indirect pathway has been successful to interpret the experimental and clinical findings in animal models and patients suffering PD

after a pallidotomy, subthalamotomy and DBS of the STN. Effects of lesions or DBS of the STN for instance, confirm its key role in the indirect pathway.
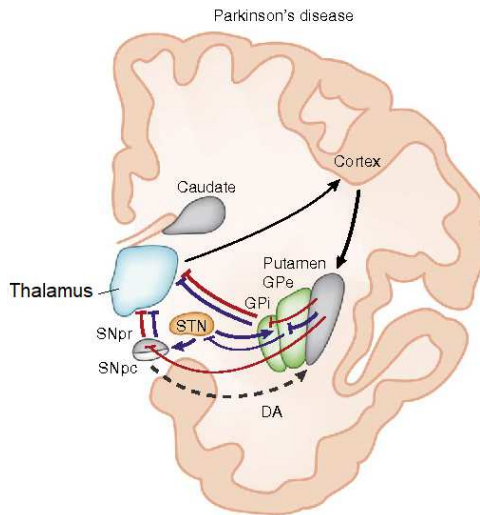
Figure 7 Schematic representation of classical model in Parkinson's disease. The degeneration of the dopaminergic pathways (shown with the dashed line) from the SNc to the striatum causes an imbalance between the direct and indirect pathway resulting in abnormal activation of the GPi and SNr finally over inhibiting the thalamic neurons projecting to the motor cortex. [With permission from Springer Nature, License number: 4350830820163]

Not all patients with PD are candidates to be treated with DBS. The patient's age at onset, the rate of progression of the disease, the specific symptoms and the presence of non-motor disturbances, are some factors used to determine if a patient will be benefited or not by DBS. Patients with idiopathic PD are normally considered good candidates for DBS. Thus, a thorough examination of a patient's disease history, symptoms and dopamine responsiveness is performed in order to refer a patient for surgery. The preferred moment to intervene is when the patient starts to be disturbed in the achievement of their daily activities.

For PD, DBS has been applied to the VIM, the STN, the caudate Zi, the GPi, [47]. Patients responsive to levodopa (precursor of dopamine), have shown high improvement to STN and GPi DBS. Patients who do not respond to levodopa usually do not respond to DBS either.

The assessment of PD is achieved by the Unified Parkinson's Disease Rating Scale (UPDRS). The UPDRS goal is to provide a comprehensive and practical scale

that can be used independently of the severity of the disease, the treatment or the age of the patient [48]. It is based on a questionnaire to evaluate the patient according to specific items, the score ranges from 0 to 108 with higher scores corresponding to higher disability. The UPDRS is widely used to assess patient response to new treatments. For DBS for instance, the efficacy of the surgery is evaluated by comparing the UPDRS before and after the DBS implantation [47].

2.3.3 DYSTONIA

Dystonia is characterized by involuntary, prolonged, patterned and repetitive muscle contraction of opposite muscles, frequently causing twisting movements and abnormal postures of the affected body parts [22, 49]. Dystonia may be classified according to: a) severity, varying from a task or position-specific dystonia to a life-threatening myoglobinuria due to the breakdown of the contracting muscles involved; b) clinical characteristics, c) distribution, depending on the body part that is affected, it may vary from focal to generalized dystonia; d) age at onset and e) etiology, further subdivided into primary and secondary dystonia.

The pathophysiology of dystonia is not well understood, most of the patients with dystonia do not present abnormalities in the basal ganglia identifiable with imaging techniques or autopsy studies. However, there is convincing evidence that dystonia is a disease of the central nervous system, specifically of the basal ganglia and brain stem or both. Dystonia has been associated with lesions in the putamen, the GPi, striatopallidal complex and thalamus, particularly the ventral intermediate and the ventral caudate nuclei [22].

The treatment of dystonia includes oral medication, chemical denervation, limb immobilization, physical therapy and surgical approaches. The surgical approach is required when medical therapies are inadequate. Surgeries may be performed in the peripheral nervous system (rhizotomy, ramisectomy, myotomy) or in the central nervous system (pallidotomy or thalamotomy). Deep brain stimulation is another surgical procedure which is a recognized treatment option due to its safety and reversibility, in contrast to ablative procedures that may induce unstable responses and unacceptable side effects.

The prevalence of dystonia is difficult to establish with certainty due to the frequent underdiagnosed and underreported cases; the different types of dystonia also limit the comparability of studies. A study of dystonia epidemiology from 2004 estimated a prevalence rate of 24-50 per million for primary early-onset dystonia and 101-430 per million for late-onset dystonia [50].

Due to the multiple etiologies and varying clinical presentations in dystonia, determining which patients are candidates to receive DBS is more difficult than it is for ET or PD. It is known, however, that some forms of dystonia will respond better

than others, thus the characterization of the type of dystonia is very useful to determine if the patient will benefit or not from the DBS surgery.

DBS of the GPi has been proved to be an effective treatment for disabling primary dystonia and some types of secondary dystonia [51, 52]. Limited reports of thalamic DBS do exist but with disappointing results, however it is still uncertain if other targets can be helpful to treat dystonia [47]. The established indications for movement disorders are summarized in Table 1.

Table 1 Established indications for DBS and the target choice

Disorder	Target
Essential tremor	VIM, Zi
Parkinson's disease	STN
Dystonia	GPi

2.3.4 RELATED NEUROLOGICAL DISEASES

Severe forms of Gilles de la Tourette syndrome, obsessive compulsive disorders, depression, epilepsy and pain are other clinical applications where DBS may represent an effective therapy. DBS for epilepsy, for instance, has shown effective reduction of seizures in patients with drug-resistant epilepsy where resecting surgery is not suitable. The optimal target is still not known [53] but suppressive seizure effects have been achieved by stimulation of the anterior hippocampus [54].

Reports of DBS of the nucleus accumbens have shown satisfactory results in cases of alcohol and nicotine addiction. DBS in the subgenual cingulum has shown some promise for treating eating disorders, such as anorexia nervosa [1]. Several neurological conditions including Alzheimer's disease [55], autism [56], cognitive decline or dementia [57] have been reported to show improvement after DBS in the hypothalamus, basolateral amygdala and the nucleus basalis of Meynert respectively. Potential future applications for DBS include post-traumatic minimally conscious state and tinnitus. In many cases, the main target and the inclusion criteria are still to be determined [1].

3 DEEP BRAIN STIMULATION

3.1 HISTORICAL PERSPECTIVE

The use of electricity aiming therapeutic effects dates back to ancient times when the electric torpedo fish and the eel were used to treat ailments such as headache and arthritis[58] and even for depression and epilepsy. However its use was rather sporadic and unscientific [59]. It was not until 1800 with the development of the voltaic pile [60] and the realization of the effects of electric currents on the nervous system that electricity became a valuable tool for exploration and therapy. Concomitant advances in neurophysiology and physics allowed the use of electricity for medical purposes and by the 19th century, many large hospitals had electrical departments with Leyden jars, batteries and electromagnetic induction machines [61].

The first electrical stimulation of the human brain is credited to Roberts Bartholow [62] who in 1874 availed himself of the ulcerated scalp of a patient to have easy access in order to electrically stimulate the cerebral cortex through inserted wires. The patient experienced muscle contractions in the right limbs and a generalized seizure after Bartholow increased the electrical current.

In the late-nineteenth century, Victor Horsley described athetosis (slow, involuntary writhing movement of the limbs) as a result of abnormal cortical discharges and performed a cortical ablation to treat dyskinesia. It was the first attempt to surgically treat movement disorders.

Explorations of the brain continued during the early years of the 20th century increasing the knowledge of the relation between cortical regions and complex neurological functions such as movement, memory and sensation [58]. Brain surgeries such as prefrontal lobotomy and topectomy, were performed to treat psychiatric disorders and abandoned later on. Attempts to alleviate the symptoms associated with movement disorders lesioning the cerebral cortex or the spinal cord (rhizotomies) were not successful enough, patients were left with significant paresis or paralysis [63] . Observations from those procedures and experiments in animals allowed the scientific community to infer the relation between movement patterns and deeper structures in the brain [64]. In 1939, Russell Meyers pioneered a surgical approach to treat Parkinson's disease (PD) by extirpating the head of the caudate nucleus (located near the centre of the brain). The relative success of this operation encouraged him and other surgeons to perform more surgeries in other deep regions. Around the 1950s, Irving Cooper, during a surgery on a patient with tremor and rigidity by accident cut the anterior choroidal artery. The procedure was aborted but the patient unexpectedly experienced relief of the symptoms without presenting

motor weakness. Cooper, by studying the cerebral blood vessels in cadavers, deduced that the damaged artery supplied the basal ganglia [63, 65]. This accidental discovery and the findings made by Meyer made it possible to conclude that selective destruction of specific parts of the basal ganglia could lead to the mitigation of symptoms in movement disorders without causing paralysis, as cortical lesions did. Open surgeries of subcortical regions were accepted, however they were not safe enough leading to a considerable risk of mortality [64].

Deeper regions in the human brain were not safely reached until the introduction of the stereotactic frame by Spiegel et al., [66] in 1947. The stereotactic apparatus frame delineates the brain as a three-dimensional system of Cartesian coordinates, initially proposed by Horley and Clarke [67]. It was originally used along pneumoencephalograms (ventricle visualization using X-rays) to determine intracerebral landmarks, from which the location of a specific structure within the brain could be measured. Afterwards, Spiegel and Wycis developed the first stereotactic atlas of the human brain based on photographs of coronal brain slices, using the posterior commissure and the midline as a reference to guide surgery. The frame and the atlas allowed the accurate insertion of a probe, needle or electrode to the desired anatomical region reducing the high risks of open procedures [68]. Because the stereotactic frame was not commercially available, neurosurgeons were required to design and produce their own apparatus. During the 1950s a variety of stereotactic frames were introduced, including the Cosman-Roberts-Well [69] frame and the one developed by Lars Leksell in 1949 [70] (Fig. 8) which depicts the target in Cartesian coordinates.

Figure 8 Leksell Stereotactic System®. The Multipurpose Stereotactic Arc is attached to the frame (G frame) and adjusted so its centre coincides with the surgical target. A probe carrier is attached to the arc so the electrodes always point to the target. The arc can be rotated around the X axis (anterior-posterior) and the carrier can be moved along the arc for lateral adjustment. This permits reaching the target regardless of the entry point. (Images courtesy of Elekta AB Sweden).

In 1957, Tailarach introduced another intracerebral landmark based on the anterior and posterior commissure (AC-PC) to locate brain structures independent of individual differences [71]. Later on, Schaltenbrand and Bailey introduced a comprehensive brain atlas, based on 111 brains sectioned in the coronal, sagittal and axial planes [72]. More recent atlases used for neurosurgical planning include Morel's atlas [73] and the atlas of the human brain [74].

Reaching deeper regions using stereotactic instruments became an alternative for other surgeons around the world, lowering the incidence of complications. The targeting however, was not entirely accurate due to incorrect relationships between the structures of interest and the ventricles between patients or due to brain shift. A common procedure to assess the correct position prior the ablation and also to detect any side effect, was to electrically stimulate the region of interest. By performing electrical stimulation in awake patients, it was possible to worsen or alleviate symptoms such as tremor, incidentally providing information about stimulation parameters, particularly the frequency used. Different stimulation thresholds of frequency were studied before performing thalamotomies or subthalamatomies finding, for instance, that symptoms were aggravated with low frequency (6-60 Hz) stimulation but when using high frequency (60-100 Hz) stimulation, the symptoms were improved [75].

In the 1960s parallel research in pharmacology came up with the discovery of the relation between the depletion of dopamine and parkinsonian symptoms. Arvid Carlsson was one of the pioneers to show that levodopa could be used to alleviate parkinsonism and restore the dopamine depletion [76]. In 1968, the introduction of levodopa for the treatment of Parkinson's disease and the irreversible side effects and complications of resecting brain tissue, provoked a drastic decline of surgical interventions to treat movement disorders. Over time, however, it was observed that patients could become refractory or develop dyskinesias due to prolonged levodopa administration.

Electrical stimulation was of great diagnostic value to localize the focus of pathology however its therapeutic use was mainly to treat pain. Indeed, the application of electrical stimulation to thalamic and upper brain regions to produce analgesic effects was what gave birth to the trademark *DBS* for the first commercially marketed devices by Medtronic in 1970 [3]. The therapeutic use of chronic stimulation via implanted electrodes in subcortical regions is credited to Bechtereva who defined the method as therapeutic electrical stimulation (TES) in 1973 [77].

The modern era of DBS to treat movement disorders began in 1987 when Alim Benabid published his landmark paper reporting the interruption of tremor using

high frequency (100 Hz) stimulation of the thalamic ventral intermediate nucleus [30].

3.2 DBS SYSTEMS

Deep brain stimulation therapy, consists of a continuous delivery of electrical pulses through chronically implanted electrodes within deep regions in the brain. The electrodes are connected through extensions to the neurostimulator which is programmed by the clinician. Initially, the cardiac pacemaker technology was used in therapy for chronic pain, however, the devices were unable to deliver the electric pulses with the required frequency to interfere with the conduction of pain [78].

The power source of the neurostimulator was large and not implantable, thus the electrodes had to be externalised in order to be connected.

Improvements of the battery and circuitry of cardiac pacemakers were adapted to neurostimulation devices and by the end of the 1980s, with the advent of the lithium battery, fully implantable neurostimulators were available [3] [4].

During the first decades DBS systems remained the same, however, the increasing scientific understanding of the effects of the electrical stimulation of regions deep within the brain made it possible to reconsider the design goals of the DBS systems. Nowadays, three companies develop DBS systems, Medtronic, Abbot, and Boston Scientific, all competing to improve the patient outcome and the cost-benefit ratio of the therapy. Some of the ongoing challenges for the DBS systems development from the engineering perspective include: a) electric field steering, b) stimulation pattern according to the disorder to be treated, c) MRI compatible systems, d) rechargeable batteries, e) variable temporal pattern and f) closed-loop systems to provide intelligent DBS therapies. Fig.9 presents a modern DBS system driven by current, using directional leads[1].

---

[1] The terminology found in DBS literature frequently refers *electrode* and *lead* indistinctly to the whole shaft that is implanted in the brain, including the insulation and the metallic contacts. Strictly, an electrode is the conductive part of the shaft and in this thesis, it is used as a synonym for contact. The lead design includes the distribution and the shape of the contacts.

Figure 9 DBS system produced by Boston Scientific, consisting of a non-rechargeable IPG (Vercise PC), the clinician and patient programmers, extensions and directional leads. (Picture courtesy of Boston Scientific [79].

3.2.1 DBS LEADS

The initial design of the leads for permanent implantation were custom-made, multi-contact, Teflon-coated, made of stainless steel, with a loop at the distal end used to engage the insertion tool [3].The first generation of the leads marketed by Medtronic in the 1980s was based in this original design, and consisted of four 1-mm cylindrical platinum-iridium (Pt-Ir) contacts separated by 2 mm. The non-conductive surfaces of the leads were insulated with epoxy. The leads also included a loop at the distal end to attach the insertion tool. A cannula with a retractable stylet tip engaged to the distal loop, was used to insert the leads. The leads were easy to insert but the presence of the loop increased the risk of haemorrhage or neurological damage due to the tissue adhesion and ingrowth [3].

The design and the materials used for the DBS leads evolved in terms of safety, removability, and prevention of tissue growth (with a twist-lock connector instead of the loop at the proximal end), based on the technology of pacemakers and spinal cord stimulators [3].

The increasing awareness of the particularities of the brain tissue surrounding the electrode, has motivated new lead designs capable for instance, of increasing the precision of the stimulation field in order to increase therapeutic effect while avoiding side effects.

Today's leads consist of Pt-Ir wires, isolated by fluoropolymer. The non-conductive surfaces are made of 80A urethane. The conductive surfaces which are in contact with brain tissue are made of Pt-Ir. Silicone, nylon and urethane are used for the connectors and anchor accessories, which are in contact with the extracranial

tissue, neck and chest. The lead body, due to the flexible urethane, has a hollow core to contain a removable tungsten stylet. The stylet provides the rigidity to the leads to be accurately inserted [3]. Fig. 10 presents the models of standard and new designs of DBS leads.

Figure 10 A. DBS directional lead, St. Jude 6180 (pictured over a 5mm squared sheet of paper). **B.** Schematic representation of designs from different manufacturers. Annular (3387, 3389 and 6148) and split ring electrodes (6180 and Cartesia) cross section displayed in the lower panel. Surestim1 model, proposed by Sapiens (now Medtronic) is not commercially available. The numbering of the contacts is determined by each company, starting from the distal contact named C0 for Medtronic models and C1 for the others.

Medtronic 3387 model is quadripolar, with 1.5 long and 1.27 mm in diameter contacts. The contacts are spaced 1.5 mm apart and are typically used for VIM or GPi DBS. Medtronic 3389 model is also quadripolar with the same dimensions. The contacts are spaced 0.5 mm apart and it is frequently used for STN DBS.

The lead model 6148 by St. Jude (now Abbot) has the distal tip completely covered by the electrode. Model 6180 by St. Jude and Cartesia by Boston Scientific, are directional leads due to the partitioned contacts. Cartesia electrodes are powered by independent current sources. Surestim1 consists of 40 small electrodes arranged in 10 rows.

The studies in this thesis included the leads shown in Fig. 10 except for Medtronic 3387 and Boston Scientific Cartesia.

3.2.2 NEUROSTIMULATORS

The implantable neurostimulator is hermetically sealed with a titanium sheet case which is insulated with a thin biocompatible film, except for the portion of the surface in contact with the subcutaneous tissue flap of the neurostimulator pocket [3].

The DBS system and the patient's body form a closed electrical circuit where the neurostimulator is the electrical source that causes an electrical current to flow through the extension and lead wires, the electrodes, across the electrode-tissue interface, and finally flowing back through the tissue to the neurostimulator case, which is the return electrode of the circuit. Direct currents produce lesions to the tissue, therefore long term stimulation is delivered in the form of pulsing. Constant current flows for a certain period of time in one direction, then the current is reversed, and then the circuit is open until the next pulse [80, 81]. Neurostimulators can operate in current or voltage controlled mode. During voltage-controlled DBS, the current injected into the tissue depends on the impedance of the whole circuit, including the wires and tissue impedance; thus, a change in impedance has an impact in the current delivered to the tissue (Fig. 11 A, lower panel). In current mode (Fig. 11 B), in contrast, the potential is internally adjusted to maintain the same current injection, therefore a change in impedance in the circuit does not affect the amount of current injected into the tissue [82] [83].

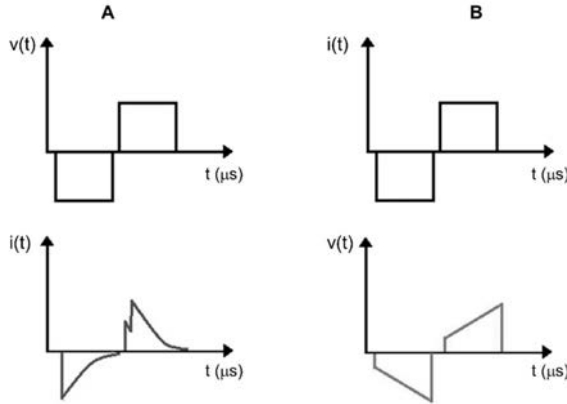*Figure 11* Operating modes of the neurostimulator, A. Voltage-controlled stimulation; B. Current-controlled stimulation. The upper panel represents the output signal of the stimulator, the bottom panel shows the current and the potential applied for each case. For the voltage-controlled stimulation, the current applied to the tissue drops exponentially due to the impedance of the electrode-tissue interface [82].

The stimulation is delivered using biphasic charge-balanced pulses (Fig. 12) in order to avoid damage in the electrode and the surrounding tissue. The polarity of the stimulation is commonly cathodic, that is, the working electrode (the electrode closer to the tissue to be stimulated) is driven negatively, acting as the cathode generating negative potentials in the extracellular medium; followed by an anodic phase where the working electrode is driven positively, as shown in Fig. 12.

The first phase of biphasic pulsing is the stimulation phase used to excite the surrounding neural tissue, i.e., the triggering of action potentials; the second phase is used to reverse the electrochemical process occurring during the stimulation phase. In the absence of a reversal phase, the electrode is unable to discharge completely between pulses leading to accumulation of charge, resulting in a drift of the electrode potential [81]. According to experimental and computational modelling, cathodic stimulation (Fig. 12) is more effective at stimulating axons than anodic stimulation [84, 85].
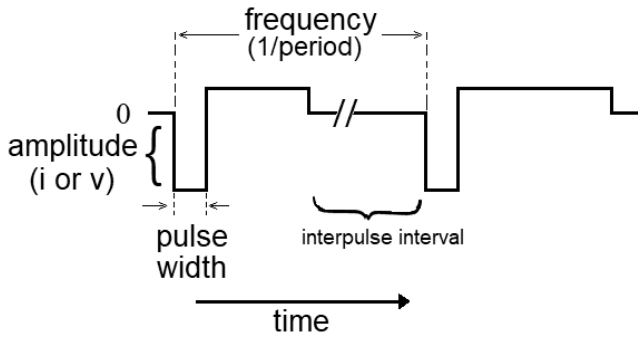

Figure 12 Cathodic stimulation with asymmetrical biphasic charge-balanced pulses [81].

The system may be programmed to monopolar, selecting any of the contacts as the cathode and the neurostimulator case as the anode, or bipolar configuration selecting one contact as the anode and another as the cathode. According to the specific therapy, the stimulation amplitude, frequency and pulse rate may be adjusted within a certain range which is specified by the manufacturing company (Table 2).

Another strategy to program the DBS system is to use interleaved pulses, where two stimulation programmes (specifying the active electrode, amplitude and pulse width) can be automatically alternated. Interleaving programming has been shown to be useful when different contacts reduce the symptoms but at different amplitudes [86]. Table 2 presents a comparison of representative neurostimulators commercially available today [87].

Table 2 Adjustable stimulation parameters of commercially available DBS systems.

Manufacturer	Model	Amplitude	Frequency (Hz)	Pulse Width (µs)	Waveform
Medtronic	Activa PC (Not rechargeable)	0-10.5 V/ 0-25.5 mA	2-250 (Voltage mode) 30-250 (Current mode)	60-450 (30 µs steps)	Square biphasic pulse
Abbot*	Infinity	0-12.75 mA	2-240	20-500	Square biphasic pulse
Boston Scientific	Vercise	0.1-20 mA	2-255	10-450	Stim ramp ON (1-10 seg)

*Formerly St. Jude Medical's system.

3.3 DBS SURGERY

DBS implantation relies to a great extent on the technical resources available in each clinical centre. Despite the differences in the procedure, the ultimate goal is to implant the leads as safely and accurately as possible in the planned target and avoid being close to vessels, fibre tracts (such as the internal capsule) or other neighbouring nuclei that can cause side effects [47].

The surgical protocol has three fundamental phases, a) a preoperative stage, where the target and the trajectory to reach it are planned; b) the operative phase that corresponds to the DBS lead implantation; and c) the postoperative stage when the IPG is placed [88]. The reason to have two implantation stages is because the site for the IPG placement is not accessible within the same sterile field as the cranial burr hole to insert the DBS leads [3].

3.3.1 ANATOMICAL TARGET AND TRAJECTORY PLANNING

Prior to the implantation, medical images of the patient are acquired to determine the location of the target where the electrode is intended to be implanted.

In order to introduce a reference system to the images, fiducials are affixed to the skull of the patient, commonly using stereotactic systems. Many centres prefer the Leksell Stereotactic System ® (LSS) (Fig. 8) which depicts the target in the Cartesian coordinate system and the planned trajectory is set by the ring (posterior-anterior) and arc (left-right) angles [89]. Alternatives such as the Cosman-Robert-Wells, CRW or Riechert-Mundinger frame exist, where the target is described by polar coordinates [90]. Thus any point within the patient's brain can be designated

as a set of three numbers [91]. The preoperative images to determine the target point, may be obtained by using computed tomography (CT) or MRI which allows direct visualization of the anatomical target [92]. Some centres obtain the preoperative MRI with an MRI indicator box attached to the stereotactic frame. The preferred procedure in many centres is to obtain CT scans with the indicator box, which are then fused or co-registered to the preoperative MRI [93]. The image fusion may cause an error of 1.3 mm [92].

After imaging, the coordinates are calculated for an initial microelectrode, or DBS electrode track. Targeting is often a combination of indirect and direct methods [88, 94].

The target can be indirectly defined based on its relation to visible landmarks, typically the anterior commissure (AC) and posterior commissure (PC), intercommissural line or midcommissural point. Indirect targeting may also include the use of a standard atlas (such as Schaltenbrand and Wahren) co-registered to the patient's intercommisural line. The direct method relies on the visualization of the target itself and the calculation of its coordinates. The target and trajectory calculation is usually performed with commercially available stereotactic software [91]. Targets such as the STN or the globus pallidus can be visualized on an MRI scan; different MRI sequences may be used to enhance the visualization of these targets, however the ventral intermediate nucleus has not been reliably visualized with any sequence [93]. The success of DBS substantially relies on this stage, thus extensive research is being conducted to improve the targeting procedure focused on alternative frames or imaging protocols. Once the imaging is performed, and the target and trajectory accurately calculated, the patient is prepared for the implant. The stereotactic arc is fixed to the patient's head in a way that the centre of the arc coincides with the anatomical target. The site of the incision is located and a burr hole is drilled in the skull [88].

Regardless of the imaging modality used, the imaged anatomical target can be confirmed through intraoperative neurophysiological exploration. Methods for this purpose include impedance measurements, macroelectrode stimulation, semi microelectrode recording or single cell microelectrode recording (MER) which is a commonly used method [88, 92]. An example of the MER lead is shown in Fig. 13.

The proposed target areas such as the VIM, the STN, or the GPi can be distinguished by their characteristic discharge patterns. Irregular and high-frequency patterns in the GPi and the STN, for instance, can be found in patients with advanced PD. Thus, analysis of the spontaneous neuronal activity along the trajectory is useful to differentiate the proposed target from neighbouring subcortical structures [95].
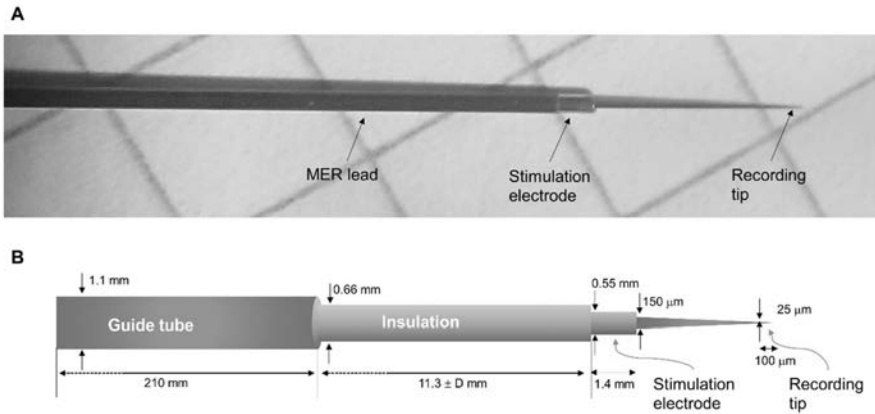
Figure 13 **A**. Example of a Microelectrode recording (MER) lead used for intraoperative recordings and test stimulations (pictured over a 5mm squared sheet of paper). **B.** Schematic representation of the MER lead including the guide tube that is used to insert the MER. The lead is displaced within the guide tube to place the electrode at the desired position.

Once the target is physiologically confirmed, some centres perform intraoperative clinical testing via macro stimulation (using the macro electrode of the MER system) prior to placing the DBS lead. MER was introduced by AlbeFessard in 1961 and later adopted as a routine surgical tool in many centres [96].

In general, the stimulation is performed at the same positions as for MER in order to evaluate the therapeutic benefit or the presence of adverse effects from increasing stimulation current. The procedure requires the patient to be awake to determine the symptom reduction or worsening [91]. Once the target is corroborated, the MER lead is retracted and replaced by the permanent DBS lead.

3.3.2 DBS LEAD IMPLANTATION

The implantation of DBS leads has traditionally been performed under local anaesthesia deducing the optimal site from neurophysiological recordings and clinical feedback obtained with intraoperative stimulation tests. However, the availability of modern imaging technologies has made it possible to visualize the relevant anatomy directly in vivo and as a consequence the possibility to perform the entire surgery under general anaesthesia. The selection of the protocol depends on the clinical centre, nevertheless the trend worldwide is to perform MRI-guided and MRI-verified DBS due to its safety and efficacy [7]. Some centres confirm intraoperatively the position of the permanent lead using 2D-X-Ray or more commonly fluoroscopy [88, 91].

After the DBS lead is implanted, the majority of the centres confirm the lead placement and the absence of haemorrhage via CT scans or MRI which can be done with or without the frame [91]. The neurostimulator is then placed, commonly in the subclavicular region. The correct placement of the lead is the first step to achieve a successful therapy. The optimization of the therapy relies on the postoperative management when an optimal selection of stimulation parameters can result in a maximal symptom suppression with minimal stimulation induced side effects.

3.3.3 DBS PROGRAMMING

The programming of the IPG is a complicated and time-consuming task due to the amount of possible setting combinations. The adjustment of the stimulation parameters for DBS are in principle based on trial and error [97, 98]. It can be performed soon after the procedure or several weeks after, depending on the condition of the patient and the common practice at the clinic. The selection of the stimulation parameters can be effective for the cases where the effect of stimulation is immediate, however, the application of DBS to disorders that take weeks or months to show effects, like dystonia, are more challenging to program. The clinical personnel normally follow guidelines for general parameter selection and make adjustments according to observable behavioural responses to the stimulation. Clinicians can modify the electrode configuration, designating which electrode(s) is active and its polarity. The electrical parameters that can be adjusted include the amplitude, pulse width and frequency. A basic programming sequence for PD for instance, consists in setting the pulse width and frequency to fixed values, e.g. 60 µs, 130 Hz, and increasing the stimulation amplitude stepwise (0.2- 0.5 V) with a monopolar configuration [99].

The frequency or rate of the stimulation refers to the number of stimulation pulses given per second, measured in pulse per second (pps) or hertz (Hz). In terms of DBS, high frequency is considered above 100 Hz. Cathodic pulses above the threshold applied at low frequency can initiate action potentials, however frequencies below 50 Hz do no improve parkinsonian signs [98]. On the other hand, high frequency (>100 Hz) DBS has been shown to be effective to reduce tremor and other symptoms in patients with movement disorders [97, 98]. Changes in frequency are generally less effective than changes in amplitude or pulse width in terms of clinically measurable effects.

3.3.4 RISKS AND COMPLICATIONS

Like any surgery, DBS implies risks of complications which can be derived at any stage of the surgical procedure and even before it. An inappropriate patient selection

may result in irreversible mental health deterioration [100]; it has been shown that more than 30 % of DBS failures were attributable to an inappropriate referral to surgery [101]. Surgical complications include haemorrhage, stroke, infection, lead erosion with infection, lead migration, lead fraction and death. It has been shown that lead fraction and migration, have declined in occurrence due to improved technology [102]. Haemorrhage complications are rare, nevertheless when occurting, there is a high risk of causing permanent neurological disability or death [103]. Investigational tools such as optical probes, when used as the guide for the creation of the trajectory, might prevent the risk of haemorrhage by detecting blood flow peaks in advance [104].

Intraoperative complications may occur from the physiological exploration of the target. Every extra penetration of brain tissue implies an increased risk of bleeding [93]. The insertion of multiple MER leads, may increase the risk of infection since it prolongs the operating time. Regardless of the method used, complications arise due to lack of expertise of the specific method rather than the method itself [100].

Postoperative complications may result from negative environmental influence such as magnetic devices that can interfere with the implanted DBS by inadvertently turning it off, or the use of diathermy treatments [105].

Complications related to the stimulation depend on the target stimulated, adverse effects for thalamic DBS may include paraesthesia, muscular cramps, dystonia, dizziness, and gait and balance disturbances, and decreased fine movement. As an example, stimulation-induced side effects for STN DBS may include personality and cognitive changes, dysarthria, weight gain, or mood changes [100]. Many stimulation-induced side effects are tractable or even reversible by adjusting the stimulation parameters or by shutting the DBS down.

3.4 Mechanisms of action

There is no consensus yet on the mechanisms of action for the therapeutic effect of deep brain stimulation in movement disorders or any other neurological disease. In principle, when the DBS system is turned on, a neural response is elicited resulting in thousands of synaptic events through the dense axonal branching [34]. The synaptic events induced by the artificial electric stimulation may derive in excitation or inhibition depending on the specific pathway being stimulated. Subsequent network-level changes have been hypothesized and still explored in the endeavour to address whether afferent or efferent axons are stimulated and whether DBS has local or more systemic effects.

Some of the methods to investigate the effects of electrical stimulation in the brain are based on extracellular recordings, field potential recordings [106], functional

imaging [107], or microdialysis studies to address changes in neurotransmitter levels during DBS [10]. Studies have been conducted specially for PD across different pathological models, including animal (mouse and primate) in vivo and in vitro models, and also in human patients. Investigation in humans is largely restricted due to ethical issues. A drawback of electrophysiological studies in animal models is that Parkinson's disease is induced using neurotoxins to provoke dopamine loss which may result in an incomplete spectrum of the characteristic symptoms present in the real disease. Another problem in animal models, is the discrepancy between animal and human neuronal behaviour, e.g. the beta band oscillation presents different frequencies for each species [108]. Observations that DBS modifies different symptoms from the same disease, such as tremor and rigidity in Parkinson, at different time points have suggested hypotheses regarding different oscillatory patterns within the basal ganglia-thalamo-cortical network depending on the symptom. For example, tremor has been linked to thalamic bursting activity at ~4 Hz [109] while rigidity to ~20 Hz oscillations in the basal ganglia [110].

One of the main challenges to elucidate the mechanisms of DBS is the diverse time frames where the symptom removal occurs. This means the DBS effect can be observed within seconds (tremor arrest in PD), within minutes (rigidity in PD or anxiety in OCD), or it may take days, weeks or even months for the effects to be observable, such as motor tics in Tourette's syndrome, or seizure frequency in epilepsy [108].

The initial hypothesis to explain the therapeutic effect of DBS proposed that overactive neurons in the STN or the GPi were blocked. This idea originated from observations of the clinical effects of DBS which resembled those provoked by lesioning the target regions, in agreement with the classic rate model (where a dopamine depletion leads to an increased STN/ GPi activity inhibiting in turn the thalamus, causing akinesia). The proposed neuronal inhibition in the stimulated site is controversial considering the basic physiological principle of the neural response to electrical stimulation [111]. Furthermore, several studies have shown that therapeutic high frequency (~>100 Hz) DBS of GPi and STN, indeed increased the GPi output [112-114]. These findings disagree with theories arguing that PD is caused by an overactivity of the GPi, suggesting a reappraisal of the basal ganglia model itself. Alternative hypotheses consider an indirect inhibition of the pathologic activity in the GPi, resonance amplification or regularization of GPi activity, induced by the DBS [115]. Since different targets have been shown to be effective for at least some symptoms of PD, recent hypotheses tend to consider the effects of DBS from a *systemic* perspective rather than focus on its local effects [115]. The understanding of the mechanisms of action is fundamental to maximize the benefits and avoid the side effects of DBS.

4 ELECTRICAL STIMULATION MODELLING

Neurons as electrochemical systems are susceptible to be stimulated for therapeutic purposes, either chemically using drugs or electrically by applying electric or magnetic stimuli and more recently mechanically by means of ultrasound [116]. The pharmacological approach is the first choice for patients suffering from neurological disorders, however it presents several disadvantages such as the delayed onset of the drug effect and the inability to provide a constant and sustained delivery of the active drug for long periods of time.

The electrical stimulation of the nervous system, in principle, is achieved in a more localized and controllable manner by adjusting the stimulation parameters and the position of the stimulation electrode. In clinical applications, such as in DBS, the electrical stimulation is applied using relatively large electrodes capable of injecting current into the extracellular space surrounding the neuronal elements. The injected current redistributes the electric potentials in the tissue generating an electric field capable of generating action potentials by the excitation mechanism first described by Hodgkin and Huxley in 1952 [117].

The basis for the effect of the electrical stimulation then, is the fact that action potentials can be triggered by applying a changing electric field close to excitable tissue. Despite this fact having been experimentally demonstrated, the fundamental principles of the interaction between the electric field and the neurons are still not completely understood [118].

In the endeavour to understand how applied currents can result in excitation, the electrical stimulation can be considered and modelled at three levels: at the electrode level, where the tissue and the electrode are modelled with an equivalent electrical circuit; at the tissue level, where the tissue is modelled as the volume conductor where an electric field is generated by the electrical stimulation; and at the neuronal level, modelling how the electric field influences the membrane potential of a neuron, ultimately triggering or suppressing an action potential [119].

4.1 ELECTRODE LEVEL

At the electrode level, the model represents the electrode, the tissue and the mechanisms of charge transfer between them. Electrodes and connecting wires currently used in stimulation devices are metallic, where electrons conduct the charge; in the biological tissue on the other hand, the charge is carried by ions such as sodium, potassium, and chloride. When the metal electrodes are placed inside a physiological medium such as the extracellular fluid (ECF) in the brain, an interface develops between the electrode and the tissue. The primary process at the electrode-

tissue interface (ETI) is the transduction of charge carriers from electrons in the metallic electrode to ions in the physiological medium.

In general, the charge transfer at an electrode-electrolyte interface can occur via two primary mechanisms: capacitive (non-Faradaic), where no charges are transferred between the electrode and the electrolyte; or Faradaic (direct), implying electrochemical oxidation and reduction reaction between the electrode and the electrolyte. If only non-Faradaic redistribution of charges takes place, equal and opposite charges in the electrode and the electrolyte are redistributed by Coulombic forces generating the so called double-layer capacitance which can be modelled with an electrical capacitor (C_{dl}, Fig. 14). If there is a transfer of electrons due to an electrochemical reaction, then a Faradaic resistance is included in the circuit (R_F, Fig. 14).

In stimulation therapies such as DBS, the charge transfer must be avoided to prevent permanent tissue damage. For Platinum/Iridium (Pt/Ir) alloy electrodes, such as those used in DBS, the charge transfer mechanism is both, capacitive and Faradaic [120], however the surfaces of these electrodes are oxide coated to decrease the Faradaic resistance (R_F) and increase the double-layer capacitance making the charge transfer neglectable [121] [122].
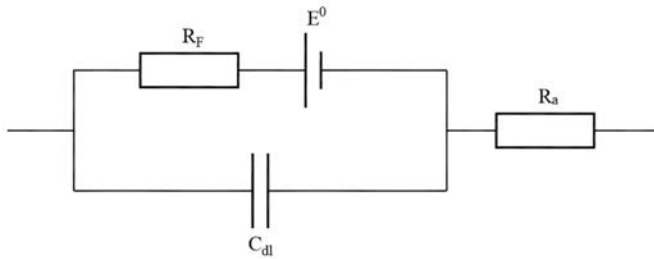

Figure 14 Equivalent circuit representation of an electrode in biological tissue. R_F represents the Faradaic resistance, E^0 the standard electrode potential (when no current is applied), R_a the access resistance, and C_{dl} the double layer capacitance

In addition to the aforementioned strategies to reduce the charge transfer, the capacitance can be increased by roughening the electrode surface so the microscopic area of overlap between the electrode and tissue is larger. The tissue at this level is modelled with a single conductor with an ohmic resistance, known as the access resistance (R_a, Fig. 14), representing the free flow of ions. The total impedance driven by the neurostimulator includes the impedance of the electrode, the connecting wires, the ETI and the tissue. For typical stimulation therapies, the impedance is dominated by the ETI (C_{dl} and R_F) and the tissue (R_a). The access resistance for a spherical electrode with a radius of r_a, in an infinite conducting

medium with a homogeneous and isotropic resistivity ρ is given by $R_a = \rho/4\pi r_a$. This indicates that one way to reduce the access resistance is by increasing the geometric surface area of the electrode [122]. Electric circuit representations are useful to understand the contribution of the different impedances and potentials during stimulation. In electronic circuits, however, the electric current is confined to a one-dimensional flow within insulated wires, implying that the electric current does not vary with location and it is only a function of time, therefore these kinds of models are not sufficient to represent the current and electric field spatial distribution in biological tissue.

4.2 BRAIN TISSUE LEVEL

In biological tissue the electric current is distributed in a three-dimensional medium, the "volume conductor", where the current density **J** (the amount of current flowing through a cross-section of unit area) depends on both, time and space [123]. At the tissue level, the volume conductor is usually assumed to be homogeneous, resistive and isotropic. For typical physiological electrical conductivities (σ), and frequencies below 1 kHz, quasistatic conditions can be assumed to calculate the electric field in regions smaller than 1 m. Under these conditions, currents and fields behave at any instant as if they were stationary [124]. Mathematically it can be expressed with the continuity equation for steady currents (where there is no variation of charge density with respect to time, $\frac{\partial \rho}{\partial t} = 0$) [125]:

$$\nabla \cdot \mathbf{J} = 0 \tag{1}$$

where ∇ is the del or nabla operator (denoting the derivative). In addition, at the macroscopic tissue level, the volume conductor is considered linear, implying that it satisfies Ohm's law:

$$\mathbf{J} = \sigma\mathbf{E} \tag{2}$$

This means that the current density, **J** (A/m), is directly proportional to the electric field, **E** (V/m) with the electrical conductivity, σ (S/m) as a constant of proportionality. The electric field can be defined as the force acting on a unit charge at a given point in space. It is measured in volts/meter and as a field variable, it takes different values at different points in space.

The electric conductivity is a macroscopic constitutive parameter of the medium, an intrinsic property of each material that describes its ability to conduct electric currents. For biological materials, the local conductivity is different depending on whether the cell membrane, extracellular fluid or other tissue is considered. The

conductivity in inhomogeneous media is a function of location and frequency i.e. $\sigma = \sigma(r, f)$, however, in practice the media are usually divided into multiple regions with different conductivities. Hence, $\sigma(r)$ can be replaced by separate conductivities σ_1, σ_2, σ_3, etc. which are constant within each region [123].

Measuring the conductivity of biological tissue in vivo presents difficulties, and at frequencies below 1 MHz values are scarce and uncertain [126]. Several techniques exist to assess conductivity distribution, however direct and non-invasive methods to measure the current density J and E inside the body are not yet available [127]. Examples of novel methods are Electrical Impedance Tomography (EIT) [128], Electric Properties Tomography (EPT) [129], magnetic resonance electrical impedance tomography (MRETI) [127]. Most recent attempts to reconstruct the full anisotropic conductivity are based in the combination of MREIT and diffusion tensor imaging [130]. Anisotropy is the property of being directional dependent; the white matter in the brain tissue exhibits anisotropy due to the parallel arrangement of axons. Thus, the longitudinal conductivity of white matter is higher than the transverse conductivity [131].

The conductivity values of different brain tissue types relevant for DBS presented in Table 3 were extracted from a database published in 1996 [132, 133] and adjusted according to specific frequency (130 Hz) and pulse width (60 μs) of the neurostimulator settings, according to:

$$\sigma = \frac{\int \sigma(\omega) H(\omega)}{\int H(\omega)} d\omega \qquad (3)$$

where $H(\omega)$ is the normalization of the spectrum of the neurostimulator signal $h(t)$ for frequencies between 10 to 10^6 Hz [134].

Table 3 Electric conductivity of the relevant tissue types for DBS at 130 Hz and 60 μs.

Brain tissue	Electric conductivity (S/m)
White matter	0.0754
Grey matter	0.1230
Cerebrospinal fluid	2.0000
Blood	0.7000

The weight of the conductivity is relevant for the grey and white matter which are sensitive to the spectral content of the stimulation pulse width.

If the electric potential, V, can be determined, then the electric field can be calculated by a gradient calculation [125] :

$$\mathbf{E} = -\nabla V \tag{4}$$

As specified by the two postulates of electrostatics in free space, the divergence and curl of $\mathbf{E}$ are [125]:

$$\nabla \cdot \mathbf{E} = \frac{\rho}{\varepsilon_0} \tag{5}$$

and

$$\nabla \times \mathbf{E} = 0 \tag{6}$$

where ρ is the charge density of free charges and ε_0 is the vacuum permittivity. Eq. 5 indicates that a static electric field is divergence-free only in the absence of charge; while Eq. 6 implies that the curl of static electric fields is zero. The curl free vector can be expressed as the gradient of a scalar field (in relation to a common identity involving the nabla operator $\nabla \times (\nabla V) \equiv 0$).

Substituting Eq. 4 into Eq. 5

$$-\nabla^2 V = \frac{\rho}{\varepsilon_0} \tag{7}$$

For tissue, in general it holds that $\rho = 0$, thus Eq. 7 can be reduced to Laplace's equation:

$$-\nabla^2 V = 0 \tag{8}$$

The electrical potential distribution obtained at the tissue level represents the extracellular potential and can be solved by means of finite element analysis. An example is shown in Fig. 15 for a DBS lead in monopolar configuration, setting the active contact to 1 V.
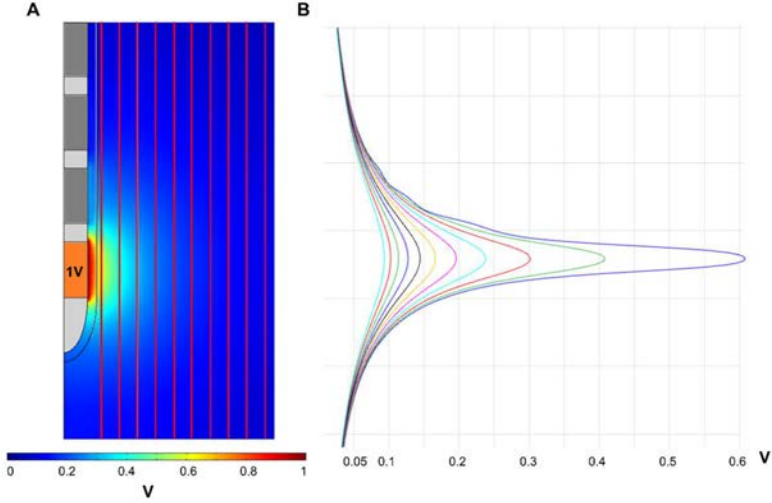
Figure 15 2D axisymmetric FEM model for simulation of the electric potential generated by a DBS electrode set to 1 V. **A**. Electrical potential spatial distribution obtained with a homogeneous medium. Red lines parallel to the lead axis used to evaluate the electric potential at different distances from the active contact. **B.** Electrical potential along each evaluation line where the closest evaluation line to the lead, presents the maximum electric potential.

Eq. 8, however, does not include any information about the nerve fibre, thus in order to calculate the induced transmembrane polarization, the extracellular potential is typically combined with an axon representation based on electrical networks [135].

4.3 NEURONAL LEVEL

The electric potential distribution obtained at the tissue level can be used to investigate the membrane potential in the neurons. Activation or inhibition of the neuron can occur anywhere in the cell, however axonal activation is commonly assumed [111].

Myelinated nerves can be modelled with an equivalent electrical network (Fig. 16 B) which considers the nodal capacitance C_m and a variable conductance G_m to reflect the variation of ionic channels (Na$^+$ and K$^+$) during the generation of an action potential, and the internodal axoplasmic conductance G_a.
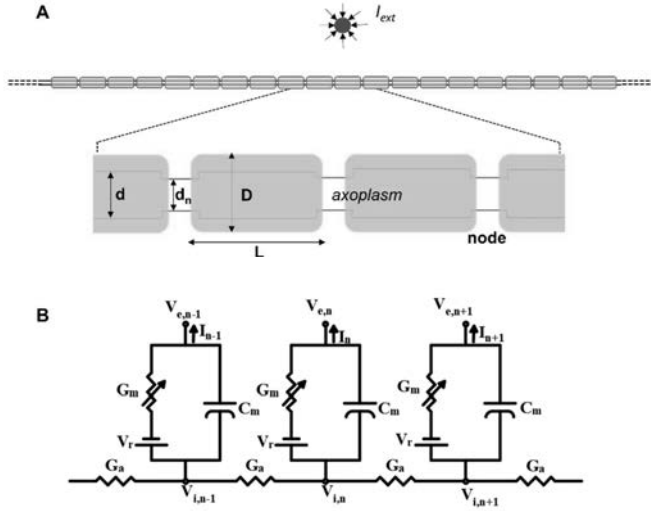
Figure 16 Schematic representation of an axon submitted to extracellular stimulation (represented with the red dot at the top). **A**. Myelinated axon with its geometric parameters, d: inner axon diameter, d_n: nodal axon diameter, D: diameter including the myelin sheath, and L: internodal length. **B.** Electrical model representing the myelinated axon, where $V_{e,n}$ is the external potential at node *n*, $V_{i,n}$ is the internal potential at node n, G_m is the nodal membrane conductance, G_a is the axial internodal conductance, C_m is the nodal capacitance, and V_r is the resting potential (-70 mV) [136].

The currents through the electrical network lead to a set of partial differential equations discrete in space and continuous in time:

$$C_n \frac{dV_{m,n}}{dt} + G_m V_n - G_a[V_{m,n-1} - 2V_{m,n} + V_{m,n+1}] = G_a[V_{e,n-1} - 2V_{e,n} + V_{e,n+1}] \qquad (9)$$

where the first term describes the capacitive membrane current at each node n, along the fibre and $V_{m,n}$ indicates the membrane potential at the node. The second term represents the ion channel kinetics (fast and slow potassium and sodium conductance) at each node and the third term describes the current running in the axon due to inside potentials at the locations $n-1, n,$ and $n+1$ driven through the conductance G_a.

The right-hand part of Equation 12 describes the sources that are driving the fibre; the axonal excitation is determined by the extracellular potentials $V_e(n)$, outside each node n [137] and it is assumed that these potentials are not influenced by the fibre response, therefore are determined only by the choice of electrode and the conductivity of the extracellular space [135]. This term is called the activating

function, AF, and it is proportional to the second order spatial derivative of the extracellular potential:

$$AF \approx \Delta^2 V_e(n) = V_{e,n-1} - 2V_{e,n} + V_{e,n+1} \tag{10}$$

The activating function has been used to determine the most likely site to trigger or block an action potential.

Single [138] and double [139] cable models have been used to determine the axonal activation. In this thesis (Paper II), the single cable model was used. For this model, the geometry of the axon (Fig. 16 A) is defined by the length (in mm) between the nodes, L, the outer diameter (in μm) D, the internodal axon diameter (in μm) d, and the inner diameter of the axon (in μm) d_n (Fig. 16). The relation between the internodal length and the axon inner diameter is derived from morphometric data obtained from mammalian nerves (from the central nervous system). This relationship is valid for outer diameters ranging from 1.5 to 10 μm.

Fig. 17 shows an example of the activation distance obtained when solving Eq. 9 for different stimulation amplitudes and specific axon parameters and pulse width.
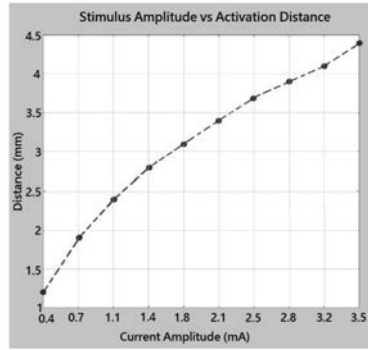

Figure 17 Activation distance calculated for an axon with a diameter D = 3.5 μm, and a pulse width of 60 μs. External stimulation applied with a conventional DBS lead.

The foundational principles of modelling extracellular stimulation belong to McNeal in 1976 [136] and were used extensively to study the response of peripheral nerves [140, 141]. More recent investigations have considered characteristics of the central nervous system using more complex representations of the neuron, including the dendrites, soma and axon terminals [18]. By coupling multiple neuron models to finite element simulations, the volume of tissue activated (VTA) can be derived.

4.4 INFLUENCE OF STIMULATION PARAMETERS

In addition to the theoretical approach described above, empirical results have been used to develop a basic understanding of the impact of each adjustable stimulation parameter on the nervous system response, namely the amplitude, the frequency and the pulse-width.

The amplitude of the pulse is the main parameter used to control the intensity of the stimulation. It is related to the radius of stimulation, i.e., the threshold amplitude required to activate a neuron increases as the distance of the neuron to the electrode increases. This relationship was first described by Stoney et al., [142] by examining the stimulating current thresholds to excite single pyramidal tract cells using a microelectrode; the threshold amplitude is described by:

$$I_{th} = I_0 + kr^2 \qquad (11)$$

where r is the distance between the axon and the electrode, I_0 the minimum threshold at the closest distance to the electrode (this is, $r = 0$) and k is the amplitude-distance constant. The parameter k controls how rapidly the threshold current increases as the distance between the electrode and axon increases and its value depends on the diameter of the axon that is excited [142, 143].

In addition to a threshold amplitude, a minimum stimuli duration is also required to excite an axon at a given distance. An empirical relationship between the pulse width and the threshold charge was first derived by Weiss in 1901 [144]. The strength-duration relation was linear and described in terms of charge, Equation 12 below shows an expression equivalent to Weiss's formulation using current instead according to $Q_{th} = I_{th}t$, where Q_{th} is the threshold charge and t the duration of the pulse (pulse width):

$$I_{th} = I_0 \cdot t + I_0 \cdot \tau_e \qquad (12)$$

where I_{th} is the threshold current, I_0 the minimum threshold current for long pulses ($t \to \infty$) and τ_e is the experimental parameter specific to the tissue under stimulation. Later on, Lapicque [145] reprised Weiss's equation and introduced the term *rheobase* to describe the minimum threshold current achieved for long pulses; he also defined *chronaxie* as the duration of a threshold current with an amplitude two times the rheobase. Thus, the strength-duration relationship in terms of these terms is:

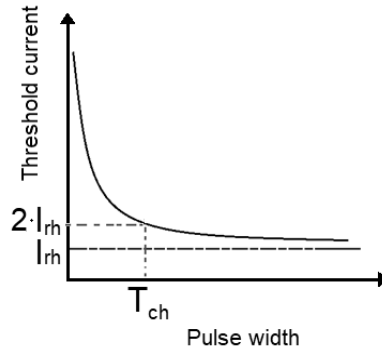$$I_{th}(PW) = I_{rh}\left(1 + \frac{T_{ch}}{PW}\right) \qquad (13)$$

Figure 18 Strength-duration relationship, the threshold current (I_{th}) decreases as the pulse width increases in a nonlinear manner. The minimum current to trigger an action potential for long pulses is called the rheobase current (I_{rh}) and the chronaxie represents the minimum duration time of the pulse to elicit an action potential having twice the rheobase current

This nonlinear relationship has been well fit to data obtained experimentally [146, 147] or with mathematical models [148, 149], however, neither current-distance nor current-duration data have been reported for central finely myelinated fibres [111]. The relationship described above (Fig. 18) has been obtained using intracellular stimulation and can differ from extracellular stimulation [150], nonetheless, it has been a useful resource to program the DBS parameters since it describes how the pulse width affects the energy delivered by the neurostimulator. The stimulation has been found to be more efficient when the pulse width is equal to the chronaxie [83]. The chronaxie value depends on certain characteristics of the fibres to be excited. For large myelinated axons, chronaxies are generally within a range of 30-200 µs while for small myelinated axons, chronaxies are within an interval of 200-700 µs [111].

Theoretical and experimental results suggest that DBS generates action potentials in the axons surrounding the electrode [111, 112]. The extent of the activation of axons during extracellular stimulation, however, is complex to determine due to the large number of contributing factors and the uncertainty of the characteristics of the axons surrounding the electrode.

The activation threshold, for instance, largely varies depending on the type and size of the axons. The orientation of the axon in relation to the electric field also contributes to its activation, the electric properties of the tissue, the geometry of the electrode and the stimulation parameters.

5   THE FINITE ELEMENT METHOD

The finite element method (FEM) is a numerical technique used to approximate the solution of physical problems whose solution requires the determination of the spatial distribution of one or more variables over a domain with a geometry often too complex to be solved analytically [151]. The first publications on the use of FEM models were for aircraft structural analysis in the beginning of the 1940s and its use was mainly to study failures, or to verify a design already completed due to the laborious manual calculations. Due to its sound mathematical basis and the introduction of general-purpose computer programs for finite element analysis in the early 1970s, the method has been increasingly extended to a wide variety of engineering applications, from heat transfer to electromagnetic fields analysis [152]. Currently, around fifty companies offer finite element formulations in ready-to-use form for commercial and academic usage [153]. Regardless of the software used, solving a problem by means of finite element analysis involves three main stages, problem identification, modelling, and discretization [151].

5.1   PROBLEM IDENTIFICATION

The first step is to identify and classify the problem based on the physical phenomena involved; for instance if the problem is time-dependent or not (stationary), if it is linear, or what results are being searched for [151]. Physical problems that involve field quantities, i.e. quantities that vary in time and space, are typically described in terms of partial differential equations (PDEs) which are solved numerically.

The studies included in this thesis were focused on the electric field distribution in a volume conductor and a quasistatic condition was assumed, as described in section 4.2. The models and simulations were performed using COMSOL Multiphysics (Comsol AB, Stockholm, Sweden) which contains several built-in physics interfaces along with the corresponding material properties. This makes it possible to build models by selecting the appropriate physical quantity to be approximated without defining the underlying equations. The physics interface consists of predefined PDEs and a number of associated boundary conditions. The problem can be defined in 1D, 3D, 2D in-plane and 2D axisymmetric dimensions and solved for stationary, time or frequency dependent conditions.

5.2 MODELLING

The next step is to model the problem. The model should include the essential features of the problem and it may exclude superfluous details as long as the actual problem is described with sufficient accuracy.

5.2.1 GEOMETRY

In contrast to ordinary differential equations where functions are defined in 0D dimension with only one dependent variable (usually function of time), PDEs require at least 1D to represent the spatial dependency. In Comsol, it is possible to model objects in 3D directly, however using an appropriate symmetry of the object, the size of the model can effectively be reduced, decreasing the computation time allowing for modelling more complex physics and geometries.

If a 2D axisymmetric is used for example, the interface assumes the situation where the geometry and fields are axially symmetric. The geometry and the physical conditions remain constant in the rotational direction and vary along the rz-plane.

For symmetric leads such as Medtronic 3389 or St. Jude 6148 (Fig. 10), the model can be defined with a 2D axisymmetric geometry as shown in Fig. 19 C.
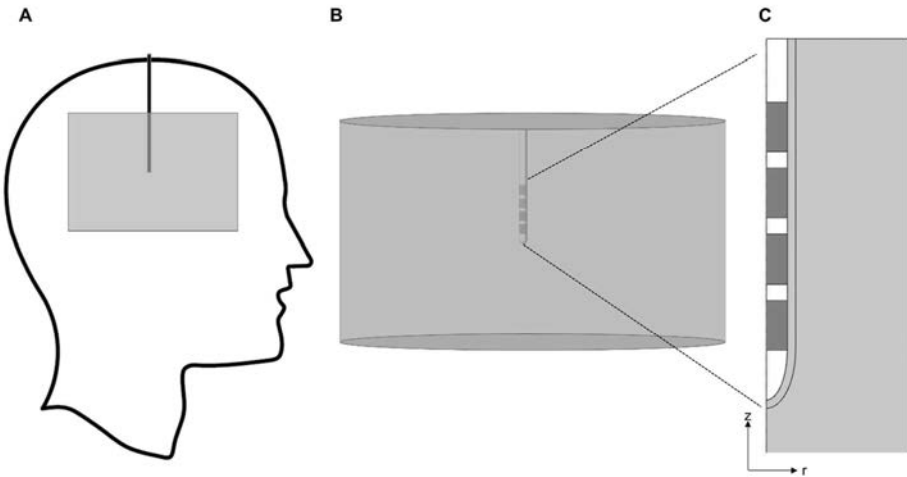
Figure 19 Schematic representation of the head and the DBS lead. **A.** Sagittal view of the head showing the region of interest (grey square) surrounding the lead. **B.** Volume derived from the revolution around the z axis of the 2D axisymmetric model shown in **C.**

The models used for this thesis simplified the human head to a region of interest (ROI) surrounding the DBS lead, as described in Section 8.3.

The geometric model becomes a mathematical model when the behaviour is described by the selected differential equations and boundary conditions. The mathematical model is an idealization where the geometry, boundary conditions and material properties are simplified based on the understanding of the problem.

5.2.2 GOVERNING EQUATION

The electric field generated by an electrode placed in a volume conductor obeys a simplified version of Maxwell's macroscopic equations together with the constitutive relations (experimentally obtained). The equations included in Comsol (within the interface *electric currents*) consider a general form of Ohm's law:

$$\mathbf{J} = \sigma\mathbf{E} + \mathbf{J}_e \qquad (14)$$

where $\mathbf{J}_e$ is an externally current density. The equation of continuity for steady currents:

$$\nabla \cdot \mathbf{J} = -\nabla \cdot (\sigma\nabla V - \mathbf{J}_e) = 0 \qquad (15)$$

is used to determine the spatial distribution of the scalar electric potential, V and Equation (4) to obtain the electric field.

5.2.3 BOUNDARY CONDITIONS

Problems described by PDEs, require boundary conditions to be prescribed. In general, thee boundary conditions can be classified in three types, *Dirichlet*, *Neumann*, and *Robin* (which is a combination of Dirichlet and Neumann) [125]. For the electric current interface, a Dirichlet type condition defines the value of the electric potential everywhere on the boundary (equivalent to the displacement in mechanical terms). A Neumann condition in turn, is used to prescribe the normal derivative of the potential (when specified on a closed surface indicates the charge distribution); for the electric currents interface in Comsol, the Neumann condition corresponds to the normal current density. The Robin condition is used to prescribe the relation of the variable and its gradient on the boundary; for electric currents, the physical interpretation of a mixed boundary is the impedance.

For the electric currents interface, Comsol includes around thirteen boundary conditions. The boundary conditions relevant to the studies included in this thesis are:

- *Electric Potential*, provides a potential as the boundary condition $V = V_0$
- *Ground*, used to implement a zero potential as the boundary condition $V = 0$
- *Electric Insulation*, default boundary condition to state that there is no electric current flowing into the boundaries. The electric insulation boundary states that the normal current density is zero locally but the tangential electric field and current density can still be large. The boundary condition is defined as $\boldsymbol{n} \cdot \boldsymbol{J} = 0$
- *Floating Potential*, FP, is used for interior or exterior boundaries to model a metallic electrode with a conductivity much higher than its surrounding medium. With this condition, the potential is not known; floating potential adds equations to the system to set the voltage on the metal to be constant, and computed at runtime. It can be used to model an electrode which extracts no current from the system (setting the floating potential current to zero). The resulting potential depends on the integral of the current into the surface *S*. The default value in Comsol is zero corresponding to a non-connected electrode but the electrode may inject a current I_0 in the model specified by the user or obtained from a circuit connection, according to Eq. 16.

$$\int_{d\Omega} -\boldsymbol{n} \cdot \boldsymbol{J} dS = I_0 \tag{16}$$

The floating potential boundary condition in Comsol includes the option "Floating potential group" which controls how potentials are assigned to the boundaries selected. It either sets the same potential to all boundaries or each boundary with a unique potential.

This boundary condition also has the effect of not obtaining any tangential electric field or current density, this is:

$$\boldsymbol{n} \times \boldsymbol{E} = 0 \tag{17}$$

- *Terminal*, is used to connect external circuits, transmission lines or boundaries with specified voltage or current. It can be set to current in order to specify a total current I_0 flowing from the terminal or to voltage to specify a fixed electric potential V_0.

5.2.4 MATERIAL PROPERTIES

The constitutive relationships support Maxwell equations by describing the behaviour of specific materials under the influence of current and electric fields. The material can be inhomogeneous, anisotropic, nonlinear, dispersive, etc. In an inhomogeneous medium, the constitutive parameters change in space, thus different field properties will apply at different parts of the material structure. In anisotropic media, the field relationship at any point varies according to the direction of propagation, implying the need to define the constitutive relationship with a 3-by-3 tensor; anisotropic parameters are required for examining permittivity or conductivity. Nonlinear materials refer to those whose permeability or permittivity are affected by the intensity of the electromagnetic field. And lastly, dispersive media refer to material properties that are frequency dependent.

The material for the studies of this thesis, refers to the electrical conductivity, σ, and depending on the study, homogeneous or heterogeneous material was assigned.

5.3 DISCRETIZATION

The finite element method approximates the solution of a continuous function of an unknown field variable, by dividing the problem domain into several finite elements with a simple geometry, connecting one to another according to specific principles at points called nodes. The particular arrangement of the elements is the mesh, which is numerically represented by a system of algebraic equations to be solved for unknowns at nodes. One of the advantages of the FEM is that the approximation is easily improved by increasing the amount of elements where high gradients are expected [151, 152].

The studies included in this thesis used a mesh controlled by the physics where the smallest elements are used for regions with high gradients which occur close to the stimulation source as shown in Fig. 20.
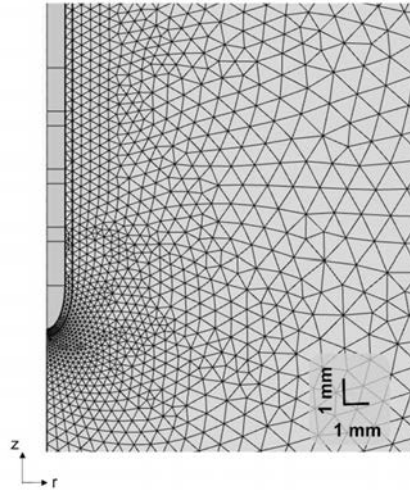
Figure 20 2D axisymmetric model mesh, with an increased density of elements close to the tip of the lead. Mesh consisting of ca. 30 000 domain elements.

The size of the elements is a built-on parameter in Comsol and it ranges from *extremely coarse* to *extremely fine*. As the element size decreases, the solution approaches to the exact solution, however limitations on computer and time resources limit the simulations to an approximation of the exact solution. The aim when setting the mesh is to minimize the difference between the approximated and the exact solution and guarantee that the error is within certain limits of tolerance, depending on the model. A common way to set an appropriate mesh size is to monitor an output parameter, for different mesh sizes. The mesh is set to a coarse size and then it is decreased until the output parameter converges to the same value. Another way to assess the mesh is the *element quality* which indicates the length to width ratio of the element. The quality of the element can go from 0 to 1 where 1 represents the optimal element and 0 indicates a degenerated element. The mesh quality depends on the physics and solvers but usually a value above 0.1 is considered a good mesh.

5.4 SOLVERS AND RESULTS EVALUATION

Once the geometry, the material properties and the boundary conditions have been defined and the model has been discretized, the software automatically generates matrices that describe the behaviour of each element and combines them into a set of equations with the form $[K]\{u\} = \{f\}$. $[K]$ is referred as the *stiffness* matrix, $\{f\}$ as the force vector and $\{u\}$ as the unknown vector. Thus, for the electric currents case,

$[K]$ refers to the electrical conductivity, $\{u\}$ the electric potential and $\{f\}$ the electric current applied. Once $\{f\}$ and $[K]$ are determined, the method to obtain the unknown $\{u\}$ can be either direct or iterative. The direct method approximates the solution $\{u\} = [K]^{-1}\{f\}$ by matrix factorization where the number of operations depend on the number of unknowns. It can be costly in terms of memory for large 3D geometries. Iterative solvers in turn, begin with an initial guess and then calculate successive updates to ultimately converge to the solution. Models defined in 2D can generally be solved by direct methods and the iterative solvers are preferred for 3D models including nonlinear, parametric or time-dependent problems.

The results of the simulations can be influenced by different kind of errors, from incorrect usage of the software and model errors, to discretization errors [151] [154]. Modelling errors due to oversimplification and assumptions made to represent the actual physical problem, can be amended by increasing the complexity of the model at the expense of more computational resources.

Discretization errors refer to the difference between the exact solution and the numerical approximation, and for stable models it should approach zero, as the elements size is minimized. Frequently, the discretization error is the main source of error in the simulations thus it is recommended to use a derived value to compare different mesh sizes. A small difference of the derived value obtained using different meshes will indicate a small error and also that the numerical model is stable [155].

5.5 POST-PROCESSING AND RESULTS VISUALIZATION

Once the computation is finished, there are multiple ways to analyse and evaluate the results. Depending on the interface used, Comsol proposes default, suitable plots to visualize the variables under inspection. For the electric currents interface, for instance, the default plot is the colour coded surface of the electric potential (Fig. 21 B), but it is possible to visualize any variable that can be calculated from the original computed variable. In Fig. 21 A, the electric field and the activating function were plotted by specifying the first and second derivative of the electric potential, respectively.
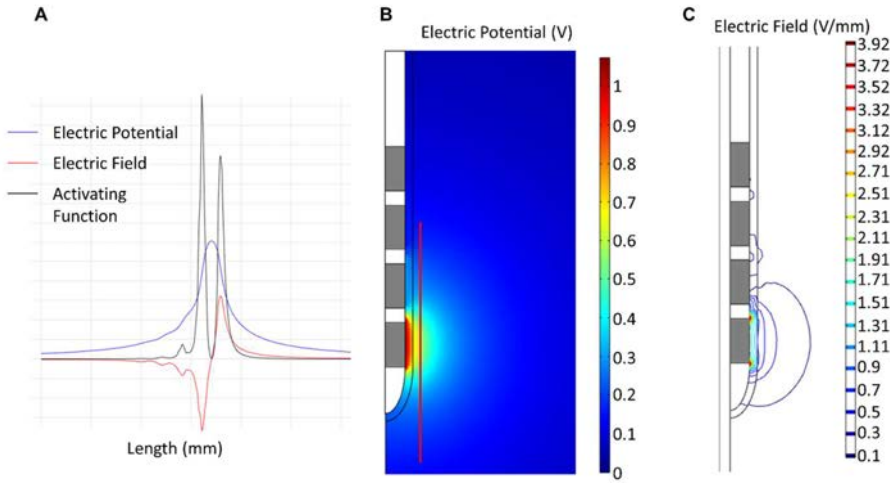
Figure 21 Three ways to present and evaluate the results. **A.** Line graph showing the magnitude of three variables obtained at an evaluation line placed in front of the lead (red line in B), parallel to the lead axis. **B**. Colour coded surface showing the magnitude of the electric potential. **C**. Isocontours (isolevels) of the electric field magnitude.

At the post-processing stage, field variables can be visualized and analysed in various ways. The results presented in this thesis were mainly based on electric field isocontours (Fig. 21 C) and isosurfaces for the 3D models. The maximal extension of the specific EF isolevel was evaluated externally by exporting the isontour. The volume within the EF isosurface was calculated with the volume integration tool available in Comsol.

6 DBS MODELS

The need of scientific understanding of the mechanisms of action has been the main motivation for the development of DBS models. In the endeavour to predict the effects of DBS, insights of the spatial extent of activation and the required model complexity have been gained.

The theoretical foundation of modern computer models of DBS relies on mathematical descriptions and findings from experimental investigations that started in the beginning of the 20th century.

The first models analysed the propagation of an action potential along a myelinated nerve assuming the nodes of the membrane behaved according to the equations provided by Hodgkin and Huxley, who were the first to quantitatively describe axonal membrane currents for the giant axon of the squid [117]. In those models, however, the excitation was assumed to be initiated at one of the axon nodes, which is valid only for stimuli applied through microelectrodes. For the case of macroelectrodes, the stimulation occurs in a broader fashion inducing currents at many nodes simultaneously. Years before Hodgkin and Huxley's publication, Rushton [156] theoretically described excitation thresholds in relation to specific electrode geometry. He used bipolar electrodes in direct contact with nonmyelinated and myelinated fibres and derived a curve of the relationship between excitation threshold and the distance between the electrodes. Monopolar electrode configuration models were used by BeMent and Ranck [157] to study the relation between the excitation threshold of a myelinated nerve and the distance between the electrode and the nerve node. The models assumed steady-state stimulation, considering that excitation thresholds were only determined for a pulse of infinite duration.

McNeal [136] introduced theoretical models using a two-steps approach to study extracellular stimulation for finite duration pulses. The first step is the calculation of the extracellular potential distribution induced by an electrode, and the second step is the determination of the neural response to the extracellular potentials.

The extracellular potentials for simple geometries can be obtained analytically, or numerically using different methods such as finite difference, discretized integral equation [158], or more recently by the finite element method.

The neural response in turn, is calculated by numerical integration of the nonlinear differential equations describing the transmembrane potential along the axon.

Models for deep brain stimulation have included this two-steps approach aiming to investigate the fundamental question regarding the DBS mechanisms of action.

However, several models related to DBS have focused on the first step to investigate the influence of particular uncertainties on the extracellular potential distribution.

In 2004 for instance, McIntyre et al., [13] developed 3D FEM models in combination with a double cable model to study activation thresholds of large diameter myelinated axons. Two FEM models were used to compare the electric field, one with a homogeneous isotropic conductivity of 0.3 S/m and the other considered anisotropic conductivity, based on diffusion tensor imaging (DTI). The models considered the Medtronic 3387 DBS lead and a theoretical point source, for comparative analysis. Correlations between axonal excitation thresholds and the activating function were provided for a 5.7 µm diameter myelinated axon.

One year later, Hemm et al., [159] present the results of a theoretical model for a patient-specific case. The theoretical model consisted of homogeneous and isotropic resistivity and the Medtronic 3389 lead. The results present isofieldlines of 0.1 V/mm and 0.2 V/mm overlapped with the preoperative MRI of a patient with dystonia.

Åström et al., [160] investigated the influence on the electric field from cysts by means of 2D axisymmetric and 3D FEM models. The model was developed for the Medtronic 3387 DBS lead in a monopolar configuration. The surrounding medium was considered as a nucleus of grey matter with a conductivity of 0.09 S/m, surrounded by white matter with an isotropic conductivity of 0.06 S/m. The cysts were modelled with different shapes and sizes, filled with cerebrospinal fluid with a conductivity of 2 S/m and placed at different positions. The magnitude of the electric field was visualized with a surface plot (from 0 to 2 V) and a marked isocontour of 0.5 V/mm. A line graph of the relation between the electric field strength (measured on a perpendicular line to the electrode) and the distance is also presented showing the effects for the different cases explored.

In 2007, Yousif et al., [161] investigated the influence of the electrode brain interface, in the potential distribution induced by DBS. A 3D FEM model of the Medtronic 3389 lead was developed including a layer of peri-electrode space (PES) surrounding the implanted electrode. The surrounding brain tissue was modelled as a homogeneous cylinder of grey matter with a conductivity of 0.2 S/m. The PES thickness was arbitrarily set to 250 µm and used to simulate an acute stage by assigning a conductivity of 1.7 S/m representing a leakage of cerebrospinal fluid. A chronic stage was also simulated representing the growth of giant cells at the electrode surface, with a lower conductivity in the PES (0.125 S/m). The results presented are a comparison of the potential distribution with and without the PES. The potential distribution is displayed with a colour coded surface plot from 0 to -2 V and a line graph showing the relation of the electric field measured radially outwards from the surface of the active contact.

In 2007, Butson et al., [162] published a methodology to predict the volume of tissue activated (VTA) by DBS. A 3D FEM model was developed for the Medtronic 3387 lead and the surrounding medium was based on patient-specific MRI datasets. Pre and post-operative MRI volumes were co-registered with diffusion tensor MRI to take into account the anisotropy of the electrical properties surrounding the DBS electrode. The localization of the lead was performed by isosurfacing the halo around the electrode shaft in the post-operative MRI. The active electrode was set as a voltage boundary condition in a monopolar cathodic configuration. The FEM model also included a 500 µm thick encapsulation layer with a conductivity of 0.07 S/m. The potential distribution obtained with the FEM model was used to calculate the VTA according to the methodology previously published by the same group [13, 163]. The results present a comparison of the VTA for isotropic and anisotropic models. The VTAs were displayed along the surrounding anatomical structures. A linear graph relating the VTA and the stimulation voltage is also presented to compare isotropic versus anisotropic models for different stimulus pulse widths. The authors also performed clinical measurements based on electromyogram recordings at different regions in the limbs of a patient with primary symptoms of freezing and rigidity.

A methodology (developed at the Department of Biomedical Engineering at Linköping University) to build a patient-specific DBS modelling and visualization was presented by Åström et al., in 2009 [14]. The proposal presented is for the creation of anisotropic FEM models based on pre- and postoperative magnetic resonance images of the patient acquired during the DBS surgery. The method consists of the image-based segmentation of several different MR-images to identify anatomical areas with grey matter, white matter, cerebrospinal fluid and blood. The classified voxels are used to allot electrical conductivity values. The method includes the co-registration of the pre and postoperative images in order to visualize the electrode artefacts for the placement of the electrodes. The Medtronic 3389 leads were used and the electric field was simulated. The authors present patient-specific simulations of bilateral DBS visualizing the electric field with isosurfaces at 0.2 V/mm and isocontours at different planes. Elliptic glyphs are also shown to illustrate the impact of the electric field on straight axons in one point. Line graphs of the electric potential, electric field and activation function are presented along an axon representation to visualize areas of depolarization and hyperpolarization. The method was used on patients with speech problems [164].

In 2012, Schmidt et al. [12] presented a comparison of isotropic and anisotropic models in terms of electric potential distribution. A 3-D finite element head model was developed based on T1-weighted MRI and co-registered with diffusion tensor imaging (DT-MRI). The brain tissue was segmented into white matter, grey matter, and cerebrospinal fluid. The Medtronic 3387 leads were used in bipolar and unipolar

configuration. The authors present isolines of the potential distribution at different planes which show the anisotropy ratio graded in grey intensities. The discrepancy between isotropic and anisotropic models is assessed based on the average deviation between the corresponding potential field distributions computed using the normalized root-mean square error. The deviations between isotropic and anisotropic field distributions found by the authors for bipolar and unipolar configurations, remained between 0.5 % and 1 % within the region of interest.

In 2015 [138] Åström et al., published an investigation of the relationship between different electrical entities to visualize the stimulation field. In the methodology, the authors used a combination of the potential distribution obtained with a homogeneous 3D FEM model and a single cable model for the neural response. The fibre geometry used was based on mammalian central nerve fibres with a 1.5 to 10 µm diameter interval. The Medtronic 3389 lead was modelled with a homogeneous surrounding tissue with a conductivity of 0.1 S/m. Cathodic monopolar simulations were performed using contact 1 as the active electrode and setting non-active contacts to floating potential. The results present the relation between the activation threshold and the distance to the electrode for three entities: electric potential (V), electric field and the activation function. The line graphs include the comparisons of different axon diameters and stimulus pulse widths. The authors also provide a comparison between the isosurfaces of the three entities and a look up table for relating the EF to an axon diameter and pulse width.

The underlying problem of the electrical stimulation, especially in deep regions of the brain is that neither the electrical signals nor their immediate effect can be observed directly. DBS models with different degrees of complexity have been extremely useful to visualize the potential extension of the stimulation field, however most of the models are based on the standard DBS lead operated in voltage mode.

Surgeons and clinical staff in general, are acquainted with some empirical rules such as higher amplitude corresponds to further stimulation. The stimulation field however, depends on several factors and their influence is not intuitive.

Computer models represent a valuable tool to evaluate different features introduced by new DBS technology. In this thesis, studies based on FEM models have been developed to investigate how new lead designs and operating modes affect the distribution of the electric field and potentially the stimulation field, around DBS electrodes.

7 AIM

The overall aim of the studies included in this thesis was to quantitatively investigate the electric field (EF) for different lead designs, operated in different modes and the influence from the surrounding medium. The evaluation was based on the volume and maximal extension of a fixed electric field isolevel. In particular, the aims were to:

- Investigate the influence of the operating mode, voltage and current controlled stimulation, through models with different electrode-tissue interfaces (mimicking different time points after the DBS implantation). (Paper I)
- Evaluate the effect of different DBS lead designs using homogeneous and heterogeneous (patient-specific) models of the brain (Papers I & II).
- Compare the electric field between intraoperative microelectrode test stimulation and chronic DBS (Paper III).
- Use electric field simulations of intraoperative microelectrode test stimulation in combination with quantitative tremor evaluation to identify the optimal implant position of the chronic DBS lead (Paper IV).

8 METHODS

The studies included in this thesis used FEM models to investigate the spatial distribution of the electric field around DBS and MER electrodes. The FEM software used was Comsol Multiphysics versions 4.3a, 4.4 and 5.2 (Comsol AB, Sweden). All the models and simulations were performed using a standard personal computer (Intel 3.40 GHz processor and 16 GB internal memory).

2D axisymmetric and 3D FEM models with specific characteristics were developed to compare different lead designs and operating modes. The studies (except for Paper I) used clinical data to develop 3D patient-specific models to investigate the influence of the medium heterogeneity on the electric field distribution. The studies were approved by the respective local ethics committee and informed written consent from the patient was received. Table 4 summarizes the models used in each study, including the operating mode and if clinical data were used or not.

Table 4 Main comparisons and characteristics of the models corresponding to the published articles.

Lead	3389 – 6148 (Paper I)	3389-6148-6180-Surestim1 (Paper II)	MER-3389 (Paper III)	MER (Paper IV)
Model	2D Axisymmetric Homogeneous	3D Homogeneous-Patient-specific	2D Axisymmetric-3D Homogeneous-Patient-specific	3D Patient-specific
Operating mode	Current-voltage	Current-voltage	Current-voltage	Current
Clinical data	No	Yes	Yes	Yes

8.1 GEOMETRY AND BOUNDARY CONDITIONS

The selection of the dimension was determined by the symmetry of the lead under study and the brain model used. For symmetric electrodes such as Medtronic model 3389, or St. Jude 6148, a 2D axisymmetric geometry (Fig. 22 B, C) was sufficient to investigate the influence of the lead design and the operating mode.

Studies that involved non-symmetric electrodes such as the Medtronic Surestim1 lead or St. Jude 6180 (Fig. 10) or a heterogeneous surrounding, required a 3D model.

The MER stimulation electrode was modelled using both 2D axisymmetric (Fig. 22 D) and 3D representations determined in accordance with the aim of the study.

The models of the leads were built according to the DBS and MER systems manufacturer's specifications (Fig. 10 and 13). The thickness and surface texture of the contacts, were disregarded assuming them to be perfectly polarizable electrodes, when active. A cathodic monopolar configuration was used for all investigations setting the active electrode to constant current or voltage using the *terminal* boundary condition and the outer boundaries as the returning electrode set to ground (Fig. 22 C).

The non-active contacts were set to floating potential; the shaft and the spaces between the contacts were set to electric insulation. The corresponding equations for the imposed boundaries are specified in section 5.2.3.
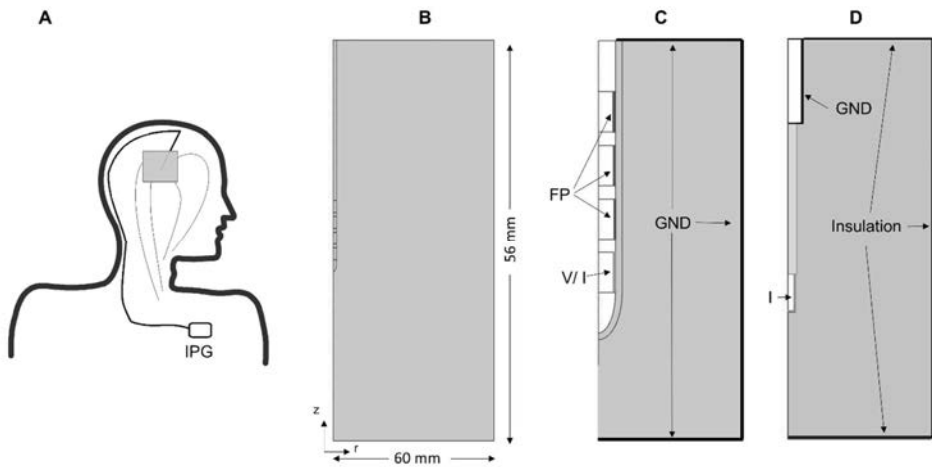

Figure 22 **A.** Schematic representation of the head and the electric current pathway between the active contact and the case of the IPG (depicted with the thin lines) B. 2D axisymmetric model of the DBS lead and the brain tissue. **C**. Amplification of the DBS lead showing the boundary conditions applied to the electrodes. The outer boundaries were set as the returning or reference electrode set to ground. **D.** Boundary conditions for the intraoperative stimulation setup where the guide tube is used as the reference electrode.

For the intraoperative test stimulation setup, the boundary condition for the returning electrode (GND) was set to the guide tube instead and the outer boundaries were set to electrical insulation (Fig. 22 D).

8.2 BRAIN TISSUE MODEL

The brain model represents the volume conductor which is described by the electrical conductivity. For the 2D axisymmetric and the homogeneous 3D models, the conductivity corresponded to a single value of grey matter assuming homogeneity in the tissue. The conductivity for the heterogeneous model in turn, corresponds to different values obtained from the patient's MRI.

The model of the volume conductor consisted in a reduced region of the brain, whose size was dictated by the configuration used. In a cathodic monopolar configuration, the current (depicted with the thin lines in Fig. 23 A) flows through all the tissue from the stimulation electrode to the neurostimulator case. Thus, the amount of tissue included between the ground and the active contact affects the potential and electric field distribution. To determine an appropriate size of the region of interest around the lead, the electric field was evaluated while reducing the distance to ground. The area of the ROI was decreased until the EF presented no change.

8.2.1 PATIENT-SPECIFIC 3D MODEL

The patient-specific 3D model was based on either T1 or T2 weighted MRI of the patient. An in-house Matlab GUI (ELMA) [165] was used to convert the medical images into data files in a format readable by Comsol. Pre and post-operative image batches were co-registered and reduced to a region of interest to perform the simulations only around the DBS leads. The whole MRI batch (Fig. 23 A) is first reduced to a number of slices at the level of interest (usually around 40 slices, 2 mm thick) then, the reduced batch is cropped to a smaller region of interest (Fig. 23 B) around the basal ganglia.
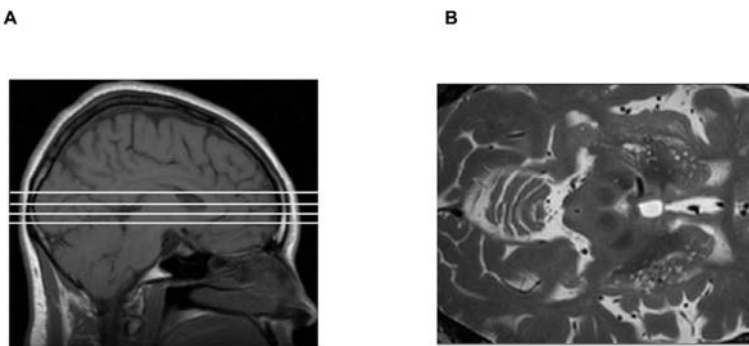
Figure 23 **A**. Sagittal view of a magnetic resonance image showing the slices (white lines) at the zone of interest, **B.** Axial view of one slice cropped to the region of interest.

The resulting ROI is a cuboid with the dimensions of the cropped image set. The electric field was evaluated with this and larger sizes. For the cases where the image set was too small, the model was enlarged to ensure no effect from the ground set to the outer boundaries, as already described.

The preoperative MR images were intensity-based segmented into grey matter, white matter, cerebrospinal fluid and blood. The classified MRI voxels were assigned with the corresponding conductivity values obtained from tabulated data and weighted with the spectral distribution of the Fourier transform of the pulse shape, presented in Table 3. The values were mapped to their original location in the MRI set. The resulting conductivity matrix was then imported into the FEM model as an interpolation function. Fig. 24 A presents an axial slice of the preoperative T2-weighted MRI used to obtain the patient-specific conductivity model shown in Fig. 24 B.
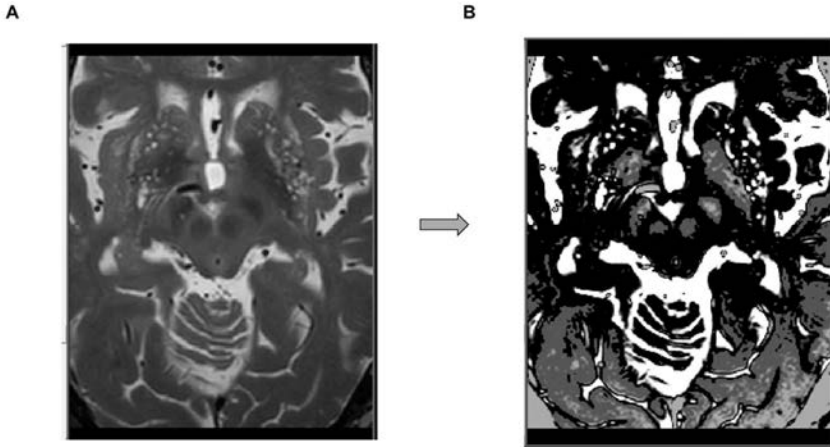

Figure 24 **A.** Preoperative T2 weighted MRI used to segment the relevant tissue types. **B.** Same slice after segmentation and designation of the corresponding conductivity values. CSF represented with high intensity values (white); grey matter with lower intensity values (light grey regions); and white matter with the lowest values in this image (black).

For the cases where the ROI was too small, the conductivity values of the border were automatically repeated to fill the enlarged region.

8.2.2 PERI-ELECTRODE SPACE

The models included a 250 µm thick layer around the lead called peri-electrode space to mimic an acute or chronic stage after implantation. The acute stage corresponds to the moment immediately after the leads insertion while the chronic considers the surrounding tissue conditions several weeks after the DBS

implantation. The PES is part of the brain model however it was only used around DBS leads. Investigations including the MER lead did not consider the PES. In Paper I, the acute stage was represented with a high electrical conductivity (2 S/m) and the chronic stage, represented fibrous tissue with a low conductivity (0. 0754 S/m). Papers II and IV only used the PES to model the chronic time point. In Paper I, the influence of the PES on the electric field was investigated for 125 µm, 250 µm, and 500 µm.

The conductivity value of the tissue around the electrode is debatable, especially for the acute stage. The values used were based on previous studies that also considered a peri-electrode space [166].

8.3 LEADS PLACEMENT

The DBS leads for the 3D models, were placed according to coordinates of two points taken from the leads' artefacts visible on the postoperative image and noted by the surgeon or clinical staff in Leksell coordinates. The coordinates for the MER lead in turn, correspond to the target and entry point extracted from the navigation system and were already provided in Cartesian coordinates.

The leads were initially aligned along the z direction, and then rotated according to the coordinates obtained from the clinical staff.

The procedure followed to place the DBS and the MER leads in the 3D models was the same. As an example, the MER leads are used to describe this procedure. The middle part of the contact at the tip is placed at the target coordinates as shown in Fig. 25 A. An axis of rotation (perpendicular to the projection of the trajectory in the xy plane) is calculated as [Yt-Ye, Xe-Xt, 0]. The lead is then rotated around this axis with an angle ϕ calculated as:

$$\Phi = cos^{-1}\left(\frac{Ze-Zt}{\sqrt{(X_e-X_t)^2+(Y_e-Y_t)^2+(Z_e-Z_t)^2}}\right) \qquad (18)$$
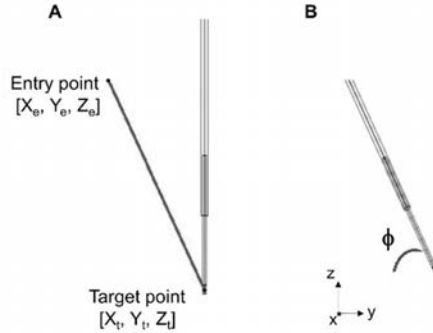
Figure 25 Localization of the MER lead in the FEM model. **A**. Initial position of the lead pointing down parallel to the z axis, with the tip at the target position. Planning coordinates shown with the red line. **B.** MER lead tilted

8.4 SIMULATIONS

The simulations were computed for typical, clinically relevant stimulation amplitudes, i.e., 1, 2, 3, and 4 V. In order to obtain equivalent amplitude values between modes, simulations were run with a parametric sweep of current amplitudes of 0.8 to 10 mA in steps of 0.1 mA (corresponding also to the actual step size of the neurostimulator). The EF isocontours (0.2 V/mm) obtained for each type of stimulation were displayed simultaneously to determine which amplitudes generated exactly the same EF distribution. For this purpose, a homogeneous grey matter model without including the peri-electrode space was used.

8.4.1 OPERATING MODE

The operating mode was explicitly investigated in Papers I and II. In Paper I, the model with no peri-electrode space included, was used to compare the EF at different time points mimicked by using different PES conductivities. To isolate the influence of the operating mode, the electric field was evaluated setting the active electrode to voltage and compared to the EF obtained setting the electrode to the equivalent current. The difference between operating modes was also investigated in Paper II through different brain models, i.e. homogeneous vs. heterogeneous. In this case, the standard DBS lead 3389 and the homogeneous brain tissue model were used to obtain the equivalent current amplitude. Paper III compared implicitly the operating mode by setting the DBS electrode to voltage and the MER stimulation electrode to current.

8.4.2 LEAD DESIGN AND TISSUE HETEROGENEITY

Different lead designs were compared against the standard lead 3389 (Fig. 10), in Paper I the lead 6148 was evaluated to observe the influence of the larger electrode at the tip of the lead. In Paper II, the comparison was extended to include leads capable to steer the field with split electrodes. In this investigation, each lead was set to both operating modes using the equivalent stimulation amplitude obtained with the lead 3389. The number of active contacts for the directional leads (6180 and Surestim1) was determined by an equivalence of contact surface area. This resulted in the activation of three contacts for St. Jude 6180 and eight consecutive contacts around the Surestim1 lead.

The simulations were run using both homogeneous and patient-specific models to assess the influence of the heterogeneity of the surrounding tissue. For the patient-specific models, the simulations were performed at two positions corresponding to the Zi and the VIM which is a virtual target along the trajectory of the lead. For the Zi a specific investigation was performed using the actual stimulation amplitude programmed to the active contact of the lead 3389. Additional simulations were run on order to find the equivalent current that generated the same EF as the clinically programmed.

The EF was compared between the standard lead 3389 and the directional leads by activating one single electrode of the split ring of lead 6180 and four contacts (in a diamond configuration (two consecutive contacts of row 6 and one contact of row 7 and 5). The active contacts were also set to both voltage and current to assess the influence of the dimension of the electrodes.

8.4.3 INTRAOPERATIVE MER STIMULATION TEST VS. CHRONIC DBS

The difference of the setup between the DBS and intraoperative test stimulation was investigated in Paper III. The boundary conditions for the returning electrode for the MER model were switched to assess the influence of the ground closer to the stimulation contact.

Simulations were run placing the DBS lead at different positions along the same trajectory of the MER lead in order to evaluate the influence of the non-active contacts in the DBS. The EF distribution was compared to the EF generated by the MER stimulation electrode.

The influence of the position of the active DBS contact in relation to the target was evaluated by placing the middle point, the lower, and the upper edge of the active contact at the target.

The EF was also evaluated for different intraoperative scenarios considering a single MER lead at a central trajectory and up to two more trajectories placed 2 mm apart parallel (posterior and medial).

A clinical case was investigated using the patient-specific model and the actual stimulation amplitudes used. The MER stimulation lead was placed at the position and set to the stimulation amplitude, which resulted in the optimal clinical outcome; the DBS lead in turn, was placed at the planned position (using the entry and target coordinates), setting the electrode to the programmed stimulation amplitude defined six months after surgery.

8.4.4 INTRAOPERATIVE MER STIMULATION FOR TARGET OPTIMIZATION

The simulations for the clinical cases presented in Paper IV were performed only with the MER lead. During the surgery, two parallel leads (central and posterior) were inserted in both hemispheres for the stimulation tests. The probes were slid within the guide tubes in order to place the stimulation electrode at different positions. The active contact was set to 0.2- 3.0 mA in steps of 0.2 mA. The therapeutic effects at each position and amplitude were quantitatively measured by wrist accelerometer recordings. The methodology was applied to five patients, summarized in Fig. 26.
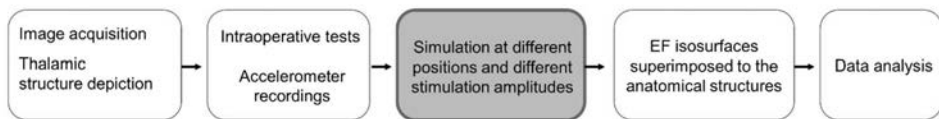
Figure 26 Summary of the methodology followed to perform the patient-specific simulations of the intraoperative stimulation tests. The simulations (section highlighted to indicate the part of the process performed at Linköping University) were performed in order to relate the anatomical structures included within the EF isosurfaces and the patient therapeutic outcome. The pre-simulations stage was performed at Clermont-Ferrand clinic and the data processing and analysis at the University of Applied Sciences and Arts Northwestern Switzerland.

A patient-specific model was built from each patient's MRI. The model considered two parallel MER leads in accordance with the surgical procedure, one along the central trajectory and another placed 2 mm posterior. The ground was set to the guide tube and the outer boundaries to electrical insulation. The non- active contact of the parallel lead was set to floating potential. The amplitude set to the active contact corresponded to the values used during the intraoperative stimulation tests. The EF was simulated for each lead at 143 positions in total, for the five patients.

8.4.5 NEURON MODEL SIMULATIONS

The relation between the EF and the neural tissue was accomplished by combining FEM and neuron models. The electric potential obtained around different lead designs (Paper II) was extracted from parallel evaluation lines placed at four positions (anterior, posterior, lateral and medial). The FEM simulations were computed for each lead using both the homogeneous and the patient-specific brain model. The neuron simulations were run for different axon diameters and pulse widths. Fig. 27 shows an example of the methodology, using the directional lead Surestim1 surrounded by the evaluation lines. The electric potential along these lines, is then applied to a 4 µm thick axon with a pulse width of 60 µs, using the neuron model.

The activation distance is measured from the surface of the lead to the point where activation no longer occurs. This distance is then related to the extension of the selected EF isocontour in the FEM model, at different stimulation amplitudes.
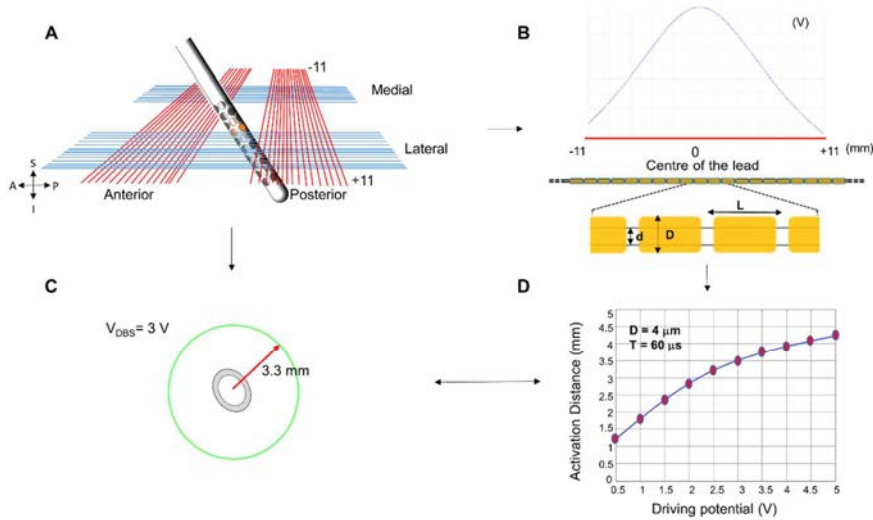

Figure 27 FEM model combined with the neuron model **A**. Surestim1 lead surrounded by evaluation lines (red and blue lines) to extract the electric potential distribution. **B**. Potential distribution along one evaluation line (posterior second closest red line) to be applied to the neuron model depicted in yellow. **C**. EF 0.2 V/mm isocontour obtained for 3 V set to all the electrodes of row 6 and 7 showing the distance between the isocontour and the centre of the lead **D.** Activation distance obtained for a neuron diameter of 4 µm and a pulse width of 60 µs.

8.5 DATA ANALYSIS

The visualization and quantification of the electric field was based on a fixed value of 0.2 V/mm. This value has been proposed as a predictor of the stimulation field for axons with a diameter around 4 µm and DBS with a pulse of 60 µs [138]. All the studies included in this thesis have used this isolevel to evaluate the influence of the operating modes, lead designs, the surrounding heterogeneity and non-active contacts.

8.5.1 VISUALIZATION

The results of the simulations were visualized using the tools available in Comsol. For the 2D axisymmetric models, the EF isocontours under comparison were displayed together to visually asses the differences, as presented in Fig. 28 A. The electric field for the 3D models in general, was visualized with isosurfaces (Fig. 28 B) and also with isocontours at planes of interest (Fig. 28 C). For the patient-specific cases, the preoperative MRI was imported into the software and used to display the electric field superimposed to the axial plane (Fig. 29 B and C).
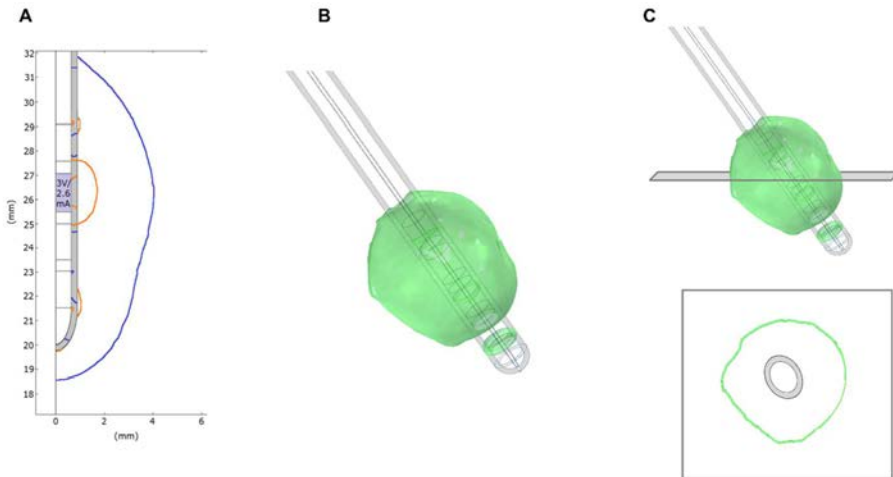
Figure 28 Visualization of the 0.2 V/mm electric field isolevel **A.** isocontours for 2D axisymmetric models, **B.** Isosurface for 3D models, and **C.** Isocontour visualized at an axial cut plane placed at the middle of the active contact shown in the upper panel.
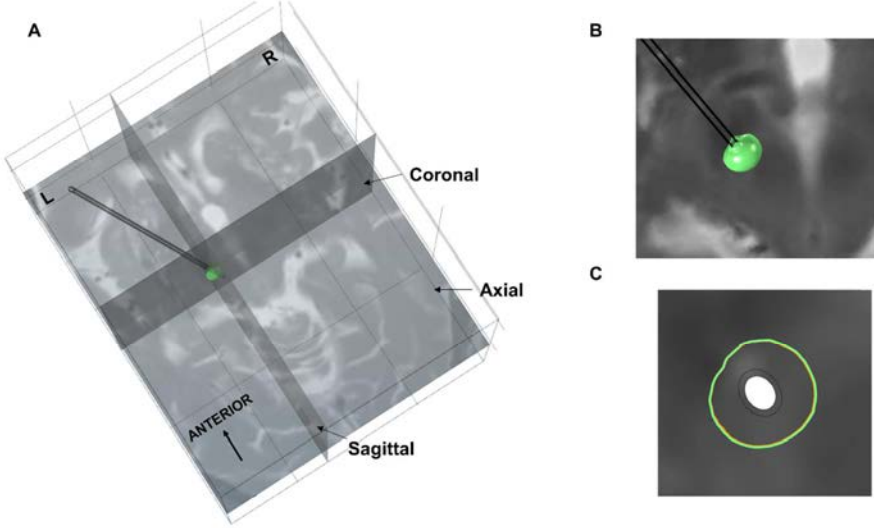
Figure 29 **A**. Orthogonal planes used to visualize the electric field isocontours, axial plane corresponds to an axial slice of a preoperative MRI. **B**. Closer view showing the 0.2 V/mm EF isosurface and the MRI axial plane. **C**. 0.2 V/mm isocontour at the axial plane.

8.5.2 QUANTIFICATION

For the 2D models, the coordinates of EF isocontour were extracted from Comsol in order to calculate the maximum distance between the lead axis and the isocontour. The same procedure was followed for the isocontours at different cut planes in the 3D models. In Paper I, evaluation points parallel to the lead axis were placed at 1, 3, and 5 mm from the lead surface to measure the EF intensity.

The volume enclosed by the 0.2 V/mm isosurface was directly obtained from Comsol using the volume integration feature. In Paper III, similarity coefficients between the EF volumes of the DBS (V_{DBS}) and the MER (V_{MER}) stimulation electrodes were calculated according to:

$$DC = 2\frac{|V_{DBS} \cap V_{MER}|}{|V_{DBS}| + |V_{MER}|} \quad (19)$$

$$CC = \frac{|V_{DBS} \cap V_{MER}|}{|V_{MER}|} \quad (20)$$

the vertical lines in Equations 19 and 20 indicate a summation of the included voxels. A Sørensen-Dice (DC) coefficient equal to 1 indicates a perfect overlap between the volumes; the coverage coefficient (CC) was calculated based on the EF obtained with the MER electrode.

9 RESULTS

The simulations have shown that the extension and volume of the electric field is influenced by the operating mode, the lead design, the peri-electrode space and the heterogeneity of the surrounding medium. In general, the EF extension was larger for current-controlled stimulation compared to voltage mode. The use of a peri-electrode space showed that for high conductivities around the lead, the EF extension is enlarged under voltage control. Models considering the surrounding heterogeneity resulted in non-uniform EF distributions. Representative results from each investigation are presented here.

9.1 OPERATING MODE

   The results from the first investigation showed a different effect on the electric field applying voltage or current to the active contact. Compared to an initial condition where both operating modes generate exactly the same EF distribution, a larger EF extension was obtained at the acute stage (PES with a higher electrical conductivity) in voltage mode. The EF extent obtained for current-control in turn was shorter, as shown in Fig. 30 B. For the chronic condition (lower conductivity PES) using voltage-control resulted in a shorter EF extension (Fig. 30 C) while for current mode, the EF extension was slightly shorter than the initial condition. Hence, the EF simulated with both operating modes, differed from that obtained at the initial condition where the PES is not included in the model.
Differences in the operating mode were also visible when the tissue heterogeneity was considered in the model. Fig. 31 shows a comparison of the electric field using the homogeneous (with a single value of conductivity corresponding to grey matter) and the patient-specific model. The EF for this particular model, presented 12 % larger extension in current mode, compared to voltage control.
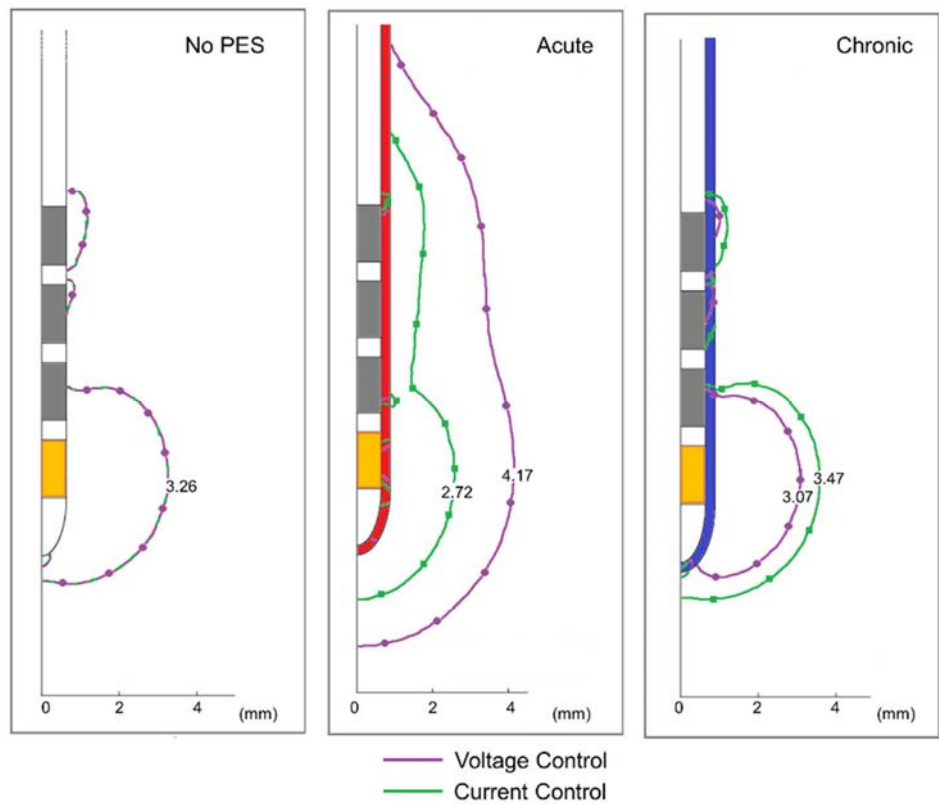
Figure 30 Electric field distribution using current and voltage-controlled stimulation, for lead 3389. **A.** Perfect overlap of the EF isocontour using equivalent values (3V or 3.4 mA set to the contact depicted in yellow) for a homogeneous conductivity of 0.123 S/m with no PES. **B.** EF distribution including a PES with a higher conductivity (2 S/m) than the surrounding (acute stage) showing a larger EF for voltage controlled and a shorter EF extension for current-control. **C.** EF generated by current is slightly larger than with its equivalent voltage amplitude.
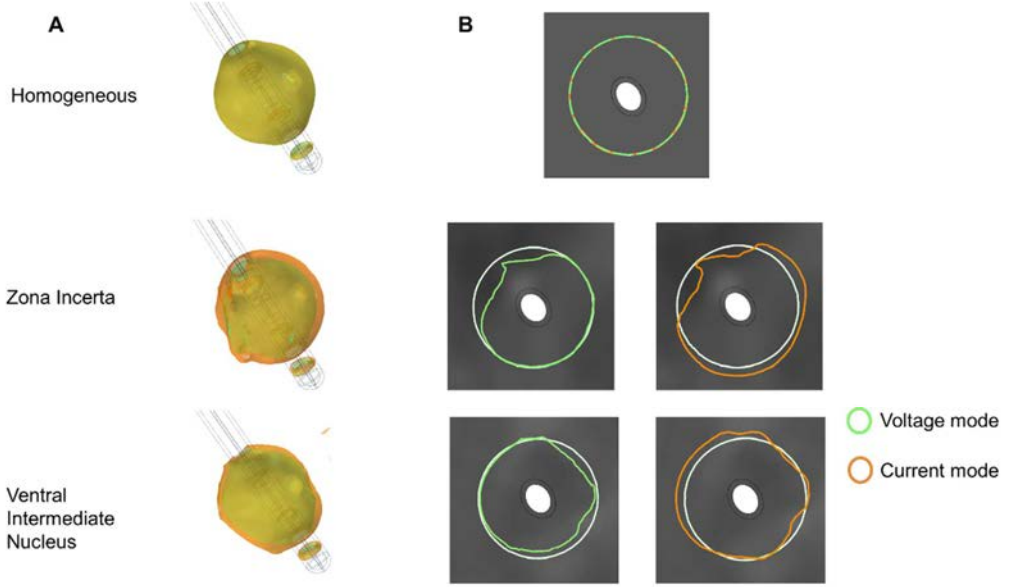
Figure 31 EF distribution obtained for voltage and current controlled stimulation. **A.** EF isosurfaces using a homogeneous model and patient-specific brain models at the level of the Zi and the VIM overlapping the EF for both modes. **B.** Corresponding isocontours at an axial cut plane localized at the middle of the active contact. Isocontours for each mode overlapped to the homogeneous isocontour depicted in white (lower panel)

9.2 LEAD DESIGN AND TISSUE HETEROGENEITY

The results obtained from the evaluation of the EF using different lead designs (Paper II) showed that when an equivalent contact surface is activated, it is possible to obtain a very similar EF distribution using directional leads. Fig. 32 shows the EF isocontours generated by each lead. For St. Jude 6180 for instance, the equivalent surface corresponded to the three electrodes of the split ring while for Medtronic Surestim1 lead, all the contacts from rows 6 and 7 (Fig. 10) were active. Simulations were run with the patient-specific brain model applying equivalent stimulation amplitudes, 3 and 3.4 mA. Fig. 32 presents the EF simulated at the level of the VIM.
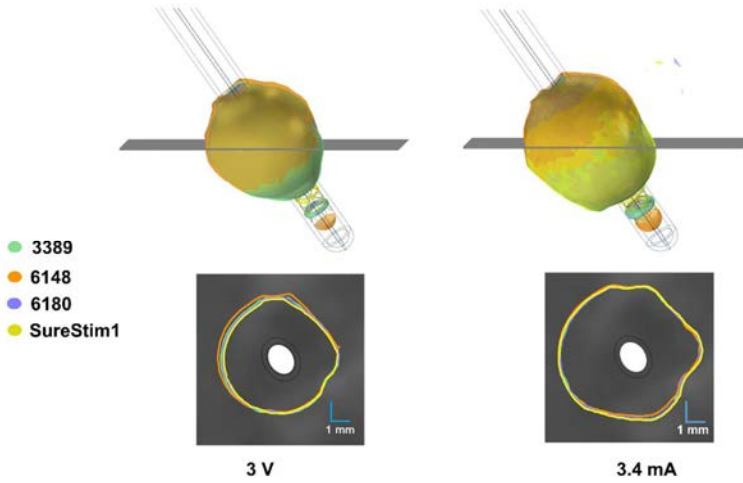
67

Figure 32 Electric field obtained using each DBS lead setting equivalent number of contacts to voltage (3 V) and current (3.4 mA). EF isosurfaces and isocontours overlapped, upper and lower panel respectively. Simulations   were obtained at the (left upper and bottom panel) and current (right).

By using different planes to visualize the electric field, it was possible to assess the directionality of the leads as presented in Fig. 33 C. From these results, it is also possible to observe that small contacts operated in current-controlled stimulation, result in a larger EF extension which can lose directionality despite the fewer electrodes activated.

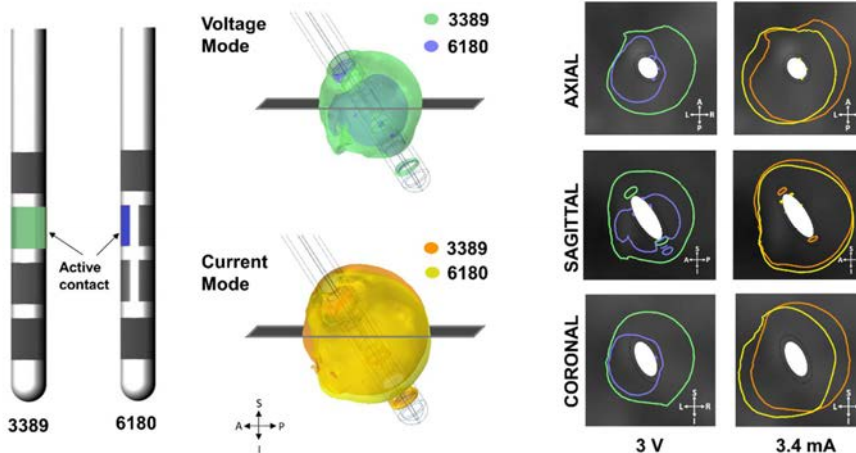*Figure 33* Electric field for a symmetric lead (Medtronic 3389) and for a steering field lead (St. Jude 6180). C2 and only one contact from the split ring (C6) were set to either 3 V or 3.4 mA. The middle panel presents the EF isosurfaces obtained with each lead overlapped for each operating mode. The EF isocontours at each plane (right panel) show no steered field for current control stimulation.

9.3 INTRAOPERATIVE MER STIMULATION VS. DBS

The simulations based on the setup for the intraoperative stimulation tests showed that grounding the guide tube does not influence the EF distribution around the stimulation contact, as shown in Fig. 34. However, simulations showed the presence of EF around the guide tube (Fig. 34 A) for intraoperative settings. The extension of the EF around the guide tube corresponds to the stimulation amplitude. For the case where the guide tube is considered as floating potential (Fig. 34 B) no electric field was obtained for stimulation lower than 3 mA.
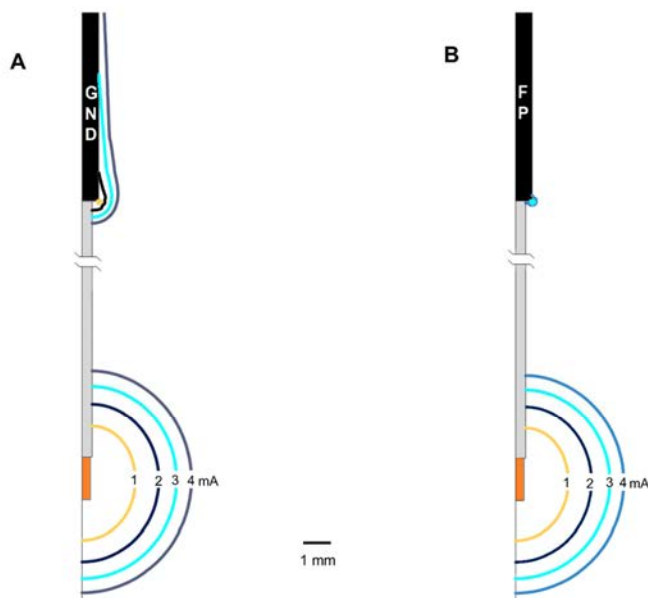
Figure 34 Influence on the electric field distribution from the intraoperative stimulation test set up. **A.** Isocontours obtained applying 1 to 4 mA to the stimulation contact (shown in orange colour) setting the guide tube to ground. **B.** EF isocontours for the same stimulation amplitude, guide tube set to floating potential, and the external boundaries to ground.

Similar results (presented in Paper III) were obtained at different distances between the stimulation contact and the guide tube. Simulations also showed that non-active contacts of the parallel MER trajectories and the DBS influence the EF distribution.

The EF obtained with the MER macro stimulation electrode was compared to the EF simulated with the standard 3389 DBS lead. Fig. 35 shows the superposition of the EF for both electrodes for different stimulation parameters. Fig. 35 A presents the EF obtained with the settings used clinically, where the intraoperative electrode was set to 0.4 mA, corresponding to the stimulation amplitude that resulted in the best clinical outcome. For the DBS, contact C2 was set to 2 V which was the stimulation amplitude programmed six months after implantation.

In accordance with the coordinates obtained clinically, the middle part of the MER and DBS active contacts differed by 2.34 mm in the anterior posterior direction, by 0.59 mm in the medial-lateral direction and by 1.80 mm in the inferior-superior direction. The difference between the stimulation contacts localization reduced the similarity coefficients, thus a higher stimulation amplitude set to the first DBS electrode, C0, was proposed resulting in a considerably higher coverage coefficient (as shown in Fig. 35 B and D).
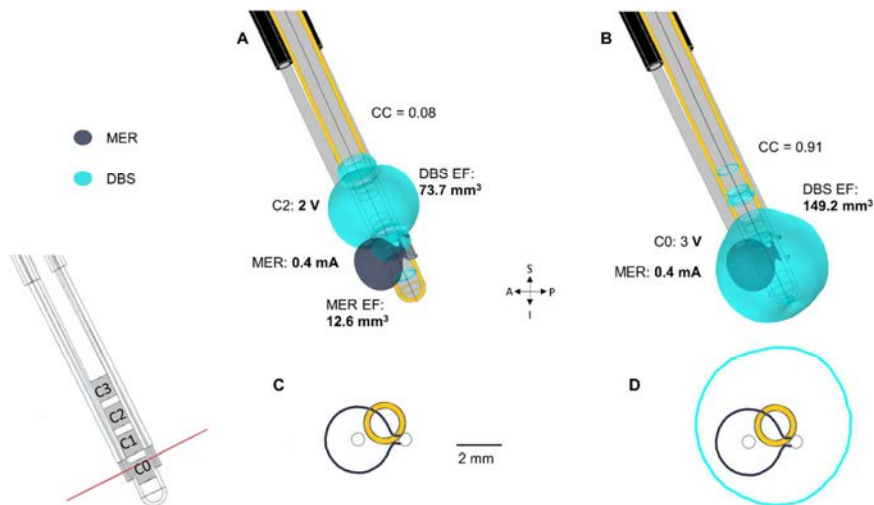
Figure 35 Electric field overlap between MER and DBS. **A.** Electric field simulated for the real values used at the clinic, showing a low CC coefficient. **B**. Hypothetical case showing the EF using a larger amplitude for the DBS contact. **C.** EF isocontour (dark blue) obtained with the intraoperative stimulation electrode at the perpendicular plane placed at the target (shown with the red line to the left); and D) EF isocontour (cyan) obtained with the DBS setting the first contact to a higher stimulation amplitude.

9.4 INTRAOPERATIVE MER STIMULATION FOR TARGET OPTIMIZATION

The electric field around the MER stimulation contact was simulated at 143 test positions with different stimulation amplitudes. Around 300 simulations were performed deriving in a comparison of the clinical improvement and the volume of the thalamic structure within the EF isosurface. Fig. 36 shows an example of the EF isosurfaces (0.2 V/mm) obtained for two trajectories at different positions. The EF was superimposed to the extracted thalamic structures and visualized at different axial cut planes corresponding to the stimulation position. The colour of the isosurfaces corresponds to the improvement measured with the wrist accelerometer. For the right hemisphere for instance, a stimulation of 0.4 mA showed an improvement of the symptoms larger than 50% (Fig. 36 A and B). Simulations for the left trajectory at 3 mm beyond the target, with a stimulation amplitude of 3 mA showed an improvement lower than 25 % (Fig. 36 C shown in red)

The axial cut planes displayed in Fig. 36 B and D show the structures within the EF 0.2 V/mm isocontour.
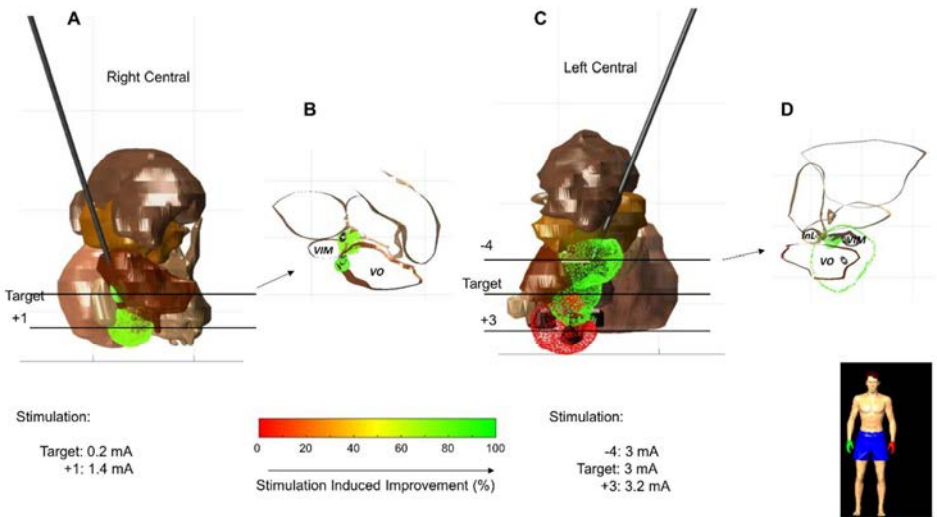
Figure 36 Electric field simulated for two MER trajectories superimposed to the extracted thalamic structures of each hemisphere (frontal view). **A**. EF isosurfaces obtained with the right electrode at the target and 1 mm beyond. **B.** Axial cut plane showing the EF 0.2 V/mm isocontour superimposed to the thalamic structures at the target. **C.** EF isosurfaces obtained with the left electrode 4 mm before the target, at the target and 3 mm beyond. **D.** Axial cut plane showing the EF 0.2 V/mm isocontour superimposed to the thalamic structures 4 mm before the target.

10 OVERVIEW OF PAPERS

Paper I
The first publication was based in 2D axisymmetric models and the brain was considered as a homogeneous medium. Two lead designs, Medtronic 3389 and St. Jude 6148 were investigated. It was shown how the larger electrode at the tip of the lead 6148 influences the electric field extending it below the tip of the lead. The influence of the operating mode was observed by using different conductivities at the peri-electrode space mimicking postoperative time points. This paper presents the procedure followed to obtain equivalent stimulation amplitudes between operating modes.

Paper II
The second investigation extended the comparison between lead designs adding two directional leads, St. Jude 6180 and Medtronic SureStim1. 3D models considering both homogeneous and patient-specific surrounding were used to compare the lead designs and the operating modes. A clinical case for stimulation of the zona incerta was also presented along with a hypothetical case showing the possible benefit of using directional leads. The results of the simulations showed that the steering function of the leads depends on the amplitude used. It was also shown that smaller electrodes operated in current mode can achieve a large EF extension.

Paper III
The third study presents another comparison between leads and operating modes. The standard Medtronic 3389 lead and the stimulation contact of the MER lead were investigated to observe differences between intraoperative and chronic conditions. Simulations of clinically used stimulation values showed discrepancy of the electric field between intraoperative and chronic scenarios.

Paper IV
The last investigation presents a methodology to use patient-specific simulations of the electric field in combination with an objective assessment of symptoms based on movement acceleration measurements. The study was applied to five patients, and it showed that the specific isovalue of 0.2 V/mm can represent a good predictor of the actual stimulation field.

11 DISCUSSION AND CONCLUSION

The studies included in this thesis have used the finite element method to investigate how the electric field spatial distribution is modified by differences in the lead design, the operating mode and the surrounding medium. The methods and results obtained are discussed from different perspectives to assess the usefulness and limitations of the models and simulations.

11.1 ELECTRIC FIELD

The selection of the electric field as the electrical entity to be visualized and evaluated, responds to the primary aim of the studies. The lead design including the electrode geometry and the distribution of the contacts; the operating mode, the stimulation parameters and the electrical properties of the tissue, all these contribute to changes in the electric field and can be explored by means of FEM models. Previous studies [160, 167-169] have also used the electric field to evaluate the influence of the stimulation parameters and electrical characteristics of the tissue.

Other research groups have investigated different aspects of DBS through the visualization of VTAs [162, 170, 171]. The estimation of the VTA normally requires coupling the electric potential distribution -obtained with the FEM model- to the neuron model which considers some characteristics of the neuron relevant to the axonal activation. The extent of activation during extracellular stimulation, however, is complex to determine due to the uncertainty of the neuron characteristics surrounding the electrode, such as axons' diameter and their orientation with respect to the stimulating electrode. Therefore, activation distances are calculated for a certain range of axon diameters positioned perpendicular to the electrode axis (assuming a higher probability of activation with this orientation). In addition, estimating the VTA is computationally intensive as it requires a large number of neuron simulations to determine a 3D surface.

The electric field estimation with a volume conductor model does not include the neuron characteristics, nevertheless it is possible to relate a certain magnitude of the EF to the activation of neurons sharing specific characteristics. A study by Åström et al., [138] investigated this relationship by coupling FEM models to neuron models. The results showed, for instance, that the activation threshold for neurons around 3μm, requires an electric field magnitude between 0.167 to 0.322 S/m for stimulation pulse widths between 30 to 120 μs where a shorter pulse implies a higher activation threshold. Specific results obtained by Åström correlated well to activation distances empirically estimated by Kuncel et al., [172].

The studies included in this thesis have used a fixed EF value of 0.2 V/mm, corresponding to a pulse width of 60 μs. The use of a single value to display the EF, and not colour-coded field maps, allowed relative comparisons between leads. In addition, having a fixed isolevel made it possible to visualize the simulated EF superimposed to the anatomical structures displayed in the patient MRI.

At the tissue level, uncertainty exists regarding the electrical characteristics of the surrounding tissue in normal conditions and it is known that there exists a change in the conductivity in the brains of patients who suffer PD or other neurological disorders [130]. Furthermore, it is not known the size or type of neurons responsible for the therapeutic outcome or adverse effects of DBS. Therefore, caution has to be taken when considering the 0.2 V/mm EF isosurface as the stimulation field.

In Paper IV, a first step in relating this isolevel to clinical outcome was performed and despite all the possible inaccuracies derived from the co-registration of the images, the image segmentation errors, the uncertainty of the conductivity values and the disregard of the anisotropy, it was possible to observe that the targeted region was consistently present within the limits of the 0.2 V/mm isocontour.

More studies are naturally required to increase the likelihood of this isolevel as a good estimator of the real stimulation field, or to hypothesize that the neurons responsible of the clinical outcome are possibly 3 to 4 μm thick.

An important consideration when the electric field is used to represent the stimulation field is that the EF does not show differences in the type of stimulation. That is, simulations using 1 V or -1 V (anodic or cathodic) will generate exactly the same EF distribution. That difference however, is crucial in terms of neuronal stimulation where anodic stimulation is significantly less likely to occur in comparison to cathodic stimulation [111].

11.2 FEM MODELS

Computer models have been extensively used to investigate different aspects related to the DBS therapy [13, 16, 160, 173-175], in the first place due to the need of a numerical method to calculate the solution of partial differential equations but also because of the possibility to visualize the variable under inspection. The finite element method has been the common choice by most of the research groups including ours, because of its flexibility to handle complex geometries and heterogeneous material properties, in comparison to the finite difference method or boundary element method. In particular, our group began using FEM models in 1999 [176] to study the heat generated by RF electrodes and as a natural step, its use continued for investigation of the electric field. The 2D axisymmetric model of the brain and the lead 3389 used in Paper I was inherited from a model previously developed by Åström et al., [160] and it was updated in terms of boundary

conditions and geometry for the investigation of new lead designs, current-controlled stimulation and surrounding media.

11.2.1 BOUNDARY CONDITIONS

The active contact was set either to ideal voltage or current source, assuming that the electrodes are perfectly polarizable implying a neglectable charge transfer as is the case for the Pt-Ir electrodes used for DBS [121, 122]. Other groups have assumed this condition [177] however, Wei et al., [178] observed that under clinical stimulating conditions the voltage response of a real electrode was different from that of the ideally polarizable electrode, suggesting that part of the charge transfer occurs due to Faradaic reactions. Moreover, recent studies [179] have found discrepancies in activation thresholds between models considering ideal voltage or current sources versus models including the capacitance of the electrode-tissue interface. For comparative studies, such as those included in this thesis, the temporal-dependent voltage distribution can be disregarded since it would equally influence the electric field distribution. However, when the FEM models are used in combination with neuron models the potential distribution becomes crucial to accurately determine the threshold of activation.

Due to the relatively recent introduction of current-controlled electrodes, few studies have modelled DBS for this condition [171, 177] nonetheless with an unsatisfactory description of the boundary condition, specifying only the amplitude used. In a recent paper, Pelot et al., [180] proposed to use *boundary current source* to model current source electrodes, however, this boundary condition requires including the contact as a subdomain. The current is determined in terms of current density, thus it depends on the dimensions of the stimulating electrode. In addition, the boundary requires the conductivity of the electrode (Pt in the case of that study) making it possible to obtain numerical instabilities when used with adjacent boundaries of low conductivities such as those representing the insulating parts of the lead contacting the surrounding tissue (silicone for that study). The models developed for all the investigations presented in this thesis have used the boundary condition *terminal* to apply a total current through the surface of the electrode. Using this boundary, the current set is distributed throughout the boundary independently of its dimensions, making it possible to perform direct comparisons of different electrode sizes. Additionally, this boundary does not require the conductivity of the contact to be defined, reducing the possibility of numerical instabilities and computation time, since the electrode subdomain does not require to be discretized.

11.2.2 PERI-ELECTRODE SPACE AND BRAIN MODEL

The models built for Papers I, II and III considered an interface between the DBS lead and the surrounding tissue. The interface (PES) was included to represent changes in the conductivity due to the presence of a foreign object in biological tissue [181]. The thickness and conductivity value of the PES are uncertain, especially for the acute case, due to the difficulties to obtain in-vivo measurements. The value used in Paper I (2 S/m) was based on a previous study by Yousif et al. [166] where the authors relate the conductivity at the acute stage to the leakage of cerebrospinal fluid immediately after the insertion of the leads. Other studies [182] however, have reported impedance values at several time points after DBS implantation which correspond to lower conductivities than those used in Paper I. For the chronic stage, there is no certainty either of the accurate conductivity values. Several post mortem studies have shown the growth of fibrous tissue on explanted leads [183, 184]. Papers I, II and III assigned a conductivity value corresponding to white matter (0.0754 S/m) to mimic fibrous tissue. This value is within the range of the conductivity used in other studies [166, 185].

Despite the exact values of the conductivity at the acute stage, it is known that the conductivity is larger immediately after the surgery than several weeks after implantation [181, 182, 186]. The contrasting values assigned to the PES to mimic different stages were useful to assess the difference between operating modes in Paper I.

In Paper II, the PES corresponded only to the chronic stage and the comparison between homogeneous and patient-specific models was what made visible the influence of the operating mode. In this study, a larger extension of the EF in current mode was observed, indicating that the surrounding tissue had a lower conductivity. The inclusion of the PES in conjunction with patient-specific brain models showed that an electric field isolevel of 0.2 S/m can be a good approximation to the stimulation field for neurons around 4μm diameter.

Homogeneous models have been useful to assess differences in the lead designs, however, it is known that neglecting the heterogeneity and anisotropy of the surrounding tissue underestimates the extent of the electric field [187-189]. The electrical characteristics of the cerebrospinal fluid, the grey matter and the white matter are very different, thus it is expected that their inclusion causes a considerable impact on the EF distribution. The models for Papers II, III and IV were built including the heterogeneity obtained from the patients' MRI.

A limitation of the patient-specific brain models built for the studies presented in this thesis, is that the anisotropy of the tissue was not considered. In a study by Åström et al., [188] the electric field was compared with a homogeneous and anisotropic models. The results showed a slightly larger extension of the EF when

the anisotropy was included in the model. This deviation is especially relevant for Paper IV where the simulated electric field was superimposed to the anatomical regions.

Regarding the dimensions, the size of the brain model respond to a region of interest where the probability to activate neurons is higher. The dimensions of the model are also determined by the minimum distance between the active electrode and the return electrode (ground), required to not affect the electric field distribution. A short distance to ground would increase the gradient of the potential and a more realistic model, e.g., 30 cm, between the stimulation contact and the ground representing the IPG in the chest would increase the computation time of the model with no effect close to the stimulated region. Other studies [190] have shown that variations in the dimensions of the volume conductor are unlikely to contribute to the impedance measurements obtained clinically, resulting in no relevant impact in the VTA.

11.3 OPERATING MODE

The general method to determine the current amplitude value that allowed fair comparisons in Papers I, II and III were based on the extension of the electric field itself. By setting the leads under comparison to the current amplitude that resulted in the same EF distribution using the homogeneous model, it was possible to evaluate the influence of the electrode design, and the conductivity of the surrounding media. The essential distinction between current and voltage control is that in current mode, the internal circuitry of the neurostimulator is designed to maintain constant the output current at the expense of modifications in the output voltage. In turn, the traditional mode maintains the output voltage constant, implying a variable current injection (Fig. 11). The influence of the operating mode can be observed, according to Equations 2 and 4, by varying the electrical conductivity of the surrounding medium. The results obtained in Paper I showed that for a high conductivity around the lead (acute stage), the electric field extension is reduced for current-controlled stimulation. In this case, the drop of potential in the region surrounding the electrode is low, therefore in order to maintain the same current the voltage applied decreases. In addition, in Paper I simulations showed that at the acute stage, high values of current were required to generate the same EF extension as for voltage mode. For voltage control in turn, the voltage applied is maintained constant, therefore the drop of voltage increases in the tissue beyond the interface, enlarging the EF. Similar results were obtained by Butson et al., [190] for different impedance models, considering different conductivities in the electrode-tissue interface.

Comparisons of operating modes in DBS have not been addressed explicitly by means of computer models. In an experimental study, Lempka et al., [191] determined the stimulation current to be applied by measuring the current generated by an electrode operated in voltage mode. The current measured varied, depending on the impedance of the electrode, between 100 and 300 µA applying a 90 µs pulse with an amplitude of -1 V. Theoretical studies have investigated both operating modes either using values relevant to clinical applications [179] or assuming an electrode impedance of 1 kΩ, comparing 1 V to 1 mA [171].

The trend of the technology to use current- controlled stimulation responds to the capacity of a current source to inject the same current regardless of the impedance of the medium, assuming that the volume of tissue activated is determined by the current injection [192]. Thus, tissue changes either in time or due to the pathology do not affect the stimulation volume. While the rationale is theoretically sound, the few clinical studies comparing both modes have not revealed a large disparity in the clinical outcome [192, 193].

11.4 LEAD DESIGN

The introduction of new DBS lead designs has been one of the main motivations to perform the studies of this thesis. FEM models and simulations have successfully shown differences and similarities between different lead designs. In Paper I, it was shown the influence of a larger contact at the tip of the lead; the simulations showed an EF generated below the tip of lead 6148. Scarce published data exist regarding this specific lead but it is presumably not in production anymore. In Paper II, steering lead designs were evaluated in both operating modes. The main result of that study is the EF simulated for smaller electrodes under current-controlled stimulation. Simulations showed that in order to steer the field, lower stimulation has to be applied. This result is in agreement with an experimental study by Grill et al., [194] where an inverse relation was shown between the surface area and the impedance of the electrode. A clinical trial by Contarino et al., [195] compared a 32 contacts directional lead similar to lead Surestim1, to the conventional lead Medtronic 3389. Their results showed that the steering lead is capable of generating the same effects as the standard lead when programmed in spherical mode, which is in accordance with the theoretical results obtained in Paper II. The group tested four directional modes and concluded that steering the field can increase the therapeutic window. The stimulation amplitude was applied at fixed steps of 0.5 mA until side effects were induced, up to 8 mA. Their report includes a schematic representation of the stimulation field however, it is not clear what stimulation amplitude induced side effects. Results from other computer-based studies [196, 197] coincide in showing that steering leads are capable of reproducing equivalent fields as the

standard ring design. The authors also conclude that steering function may be beneficial. This specific lead design, however, is not yet commercially available. Plausible reasons include the high current density of smaller contacts and the increase of programming combinations.

11.5 CLINICAL RELEVANCE

All the studies presented in this thesis aimed to contribute toward a better understanding of the implications of new lead designs and operating modes. Even though electric field models are limited in the representation of the actual stimulation field, and inaccuracies exist due to the assumptions made, the simulations have successfully highlighted differences that clinicians can avail from, when selecting the lead and at the programming stage. The rapid development of imaging technology has allowed increasing the accuracy when targeting anatomical structures, however the stimulation programming still relies on the clinical outcome.

The clinical cases explored in Papers II and III are examples of how computer models can aid the clinicians to visualize hypothetical cases, otherwise difficult to explore clinically. The methodology introduced in Paper IV explored the possibility of relating the clinical outcome, objectively assessed by accelerometer measurements, with EF simulations.

11.6 FUTURE WORK AND CONCLUSION

In a review from 1975, J. Ranck pointed out that "More is known about stimulation of mammalian CNS than most workers are aware of. Much of what is unknown seems solvable with current modes" [111]. There is indeed an increasing understanding of the neural response to electrical stimulation at the local level, however, its effect at the network level remains unknown. Moreover, there is still, no consensus about the optimal target to stimulate, in order to achieve symptom removal without adverse effects [198]. This has lead current investigations to dig into the study of pathway activation. Recently, patient-specific DBS models have introduced explicit representation of the axons derived from tractography [199-201], to determine a potential relation between pathway activation and symptom improvement or side effects. The foreseen challenge is to successfully manage the huge amount of data derived from the relation between simulations and clinical outcome. The intention is to provide a clinical tool capable of encompassing the derived data, and assist the clinicians in the identification of the optimal position of the DBS lead.

In conclusion, the use of FEM models in the studies presented in this thesis have allowed to noninvasively quantify the influence of different factors over a wide variation of stimulation settings.

ACKNOWLEDGMENTS

Finally, it is here, the elation of closing a cycle, with a mix of sadness and happiness. I am deeply thankful to all the persons who have contributed to make this journey smooth and significant.

Linköping, July 25 2018.

12 APPENDIX A: MODEL CORRECTIONS

Through the development of the models there were two main corrections between consecutive publications. In Paper II one of the boundary conditions required a correction due to a misleading definition in Comsol. In Paper III, the geometry was corrected due to misunderstanding of the real set up of the intraoperative leads.

12.1 FLOATING POTENTIAL

The boundary conditions settings for the floating potential include a checkbox to group or not, all the boundaries. For the first investigation included in this thesis, the non-active contacts were mistakenly grouped, thus a single potential was shared by all the contacts. This was observed when comparing other lead designs in the second investigation, thus the model boundary conditions were corrected accordingly. Fig 37 shows both scenarios for two different lead designs.
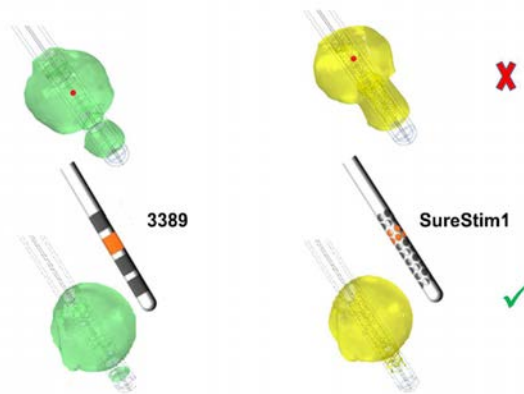
Figure 37 Electric field distribution obtained for different settings in the floating potential boundary condition. Upper panel, wrong setting by grouping the non-active contacts forcing a unique potential for all. Lower panel, correct selection without grouping the non-active contacts.

12.2 PARALLEL MER LEAD PLACEMENT

Between the publication of Paper IV and Paper III there was a correction of the position of the MER leads. The correction consisted in the movement of the parallel lead so the middle contacts were positioned at the same plane perpendicular to the leads' trajectory as shown in fig. 38.
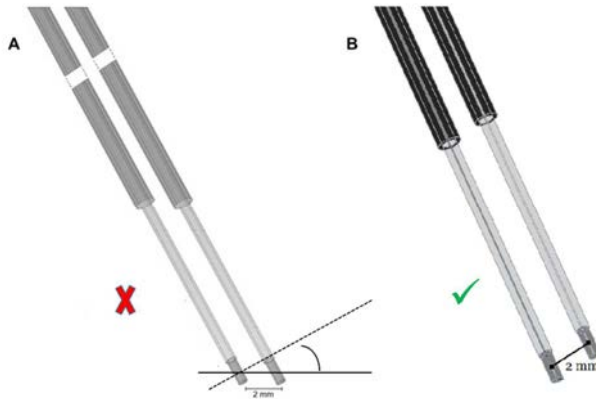
Figure 38 Correction of the placement of the posterior parallel lead. **A**. Wrong placement of the leads, with the tip of the leads aligned to the axial plane **B.** Correction aligning the middle points of the stimulation contacts at a perpendicular plane with respect to the leads' trajectory.
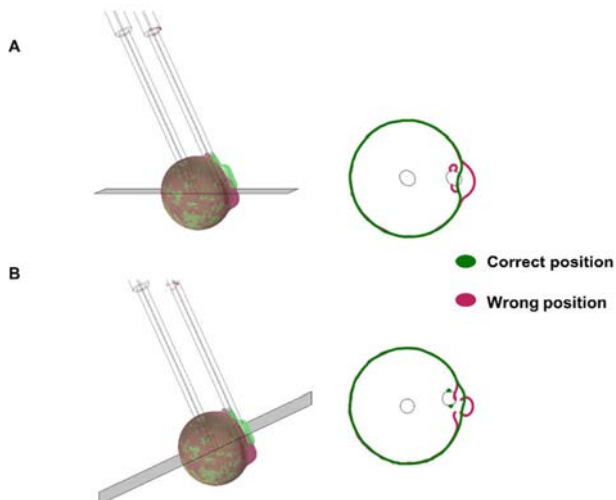
Figure 39 EF isosurface and isocontours obtained for each case applying 1 mA to the active contact of the central lead. **A.** Isocontours obtained at the axial plane shown to the left, **B.** Isocontours obtained at the perpendicular plane shown to the left. The EF volume for the wrong placed lead was ~0.2 mm³ larger.

REFERENCES

[1]   M. Hariz, P. Blomstedt, and L. Zrinzo, "Future of brain stimulation: new targets, new indications, new technology," *Mov Disord,* vol. 28, pp. 1784-92, Nov 2013.

[2]   U.S. Food & Drug. (2015, November 2017). *FDA News Release - FDA approves brain implant to help reduce Parkinson's disease and essential tremor symptoms*. Available: https://www.fda.gov/NewsEvents/Newsroom/PressAnnouncements/ucm451152.htm

[3]   R. J. Coffey, "Deep brain stimulation devices: a brief technical history and review," *Artificial organs,* vol. 33, pp. 208-220, 2009.

[4]   A. Sarem-Aslani and K. Mullett, "Industrial perspective on deep brain stimulation: history, current state, and future developments," *Frontiers in integrative neuroscience,* vol. 5, 2011.

[5]   (2009). *News Release- St. Jude Medical Receives CE Mark Approval for World's Smallest, Longest-Lasting Rechargeable Deep Brain Stimulator for Parkinson's Disease*. Available: http://media.sjm.com/newsroom/news-releases/news-releases-details/2009/News-Release---St-Jude-Medical-Receives-CE-Mark-Approval-for-Worlds-Smallest-Longest-Lasting-Rechargeable-Deep-Brain-Stimulator-for-Parkinsons-Disease/default.aspx

[6]   (2012, Nov. 23). *CE Mark approval of the Vercise™ Deep Brain Stimulation (DBS) System for the treatment of Parkinson's disease, entering a new therapeutic category*. Available: http://news.bostonscientific.com/2012-10-18-Boston-Scientific-Announces-Third-Quarter-2012-Results

[7]   M. Hariz, "Deep brain stimulation: new techniques," *Parkinsonism Relat Disord,* vol. 20 Suppl 1, pp. S192-6, Jan 2014.

[8]   Medtronic. (2017, November 2017). *Medtronic SureTune(TM)3 Earns CE Mark for Deep Brain Stimulation Therapy*. Available: http://newsroom.medtronic.com/phoenix.zhtml?c=251324&p=RssLanding&cat=news&id=2279215

[9]   N. Bruet, F. Windels, A. Bertrand, C. Feuerstein, A. Poupard, and M. Savasta, "High frequency stimulation of the subthalamic nucleus increases the extracellular contents of striatal dopamine in normal and partially dopaminergic denervated rats," *J Neuropathol Exp Neurol,* vol. 60, pp. 15-24, Jan 2001.

[10]   P. Zsigmond, M. Nord, A. Kullman, E. Diczfalusy, K. Wårdell, and N. Dizdar, "Neurotransmitter levels in basal ganglia during levodopa and deep brain stimulation treatment in Parkinson's disease," *Neurology and Clinical Neuroscience,* vol. 2, pp. 149-155, 2014.

[11]   M. Zonenshayn, A. Y. Mogilner, and A. R. Rezai, "Neurostimulation and functional brain imaging," *Neurol Res,* vol. 22, pp. 318-25, Apr 2000.

[12]   C. Schmidt and U. van Rienen, "Modeling the field distribution in deep brain stimulation: the influence of anisotropy of brain tissue," *IEEE Trans Biomed Eng,* vol. 59, pp. 1583-92, Jun 2012.

[13]   C. C. McIntyre, S. Mori, D. L. Sherman, N. V. Thakor, and J. L. Vitek, "Electric field and stimulating influence generated by deep brain stimulation of the subthalamic nucleus," *Clin Neurophysiol,* vol. 115, pp. 589-95, Mar 2004.

[14]   M. Åström, L. U. Zrinzo, S. Tisch, E. Tripoliti, M. I. Hariz, and K. Wårdell, "Method for patient-specific finite element modeling and simulation of deep brain stimulation," *Med Biol Eng Comput,* vol. 47, pp. 21-8, Jan 2009.

[15]   W. M. Grill and C. C. McIntyre, "Extracellular excitation of central neurons: implications for the mechanisms of deep brain stimulation," *Thalamus & Related Systems,* vol. 1, pp. 269-277, 2001.

[16]   C. R. Butson, S. E. Cooper, J. M. Henderson, and C. C. McIntyre, "Predicting the effects of deep brain stimulation with diffusion tensor based electric field models," *Med Image Comput Comput Assist Interv,* vol. 9, pp. 429-37, 2006.

[17]   M. L. Kringelbach, A. L. Green, and T. Z. Aziz, "Balancing the brain: resting state networks and deep brain stimulation," *Front Integr Neurosci,* vol. 5, p. 8, 2011.

[18]   C. C. McIntyre, W. M. Grill, D. L. Sherman, and N. V. Thakor, "Cellular effects of deep brain stimulation: model-based analysis of activation and inhibition," *J Neurophysiol,* vol. 91, pp. 1457-69, Apr 2004.

[19]   E. R. Kandel, J. H. Schwartz, T. M. Jessell, S. A. Siegelbaum, and A. J. Hudspeth, *Principles of neural science*, 5 ed.: McGraw-hill New York, 2000.

[20]   H. Swadlow and S. Waxman, "Observations on impulse conduction along central axons," *Proceedings of the National Academy of Sciences,* vol. 72, pp. 5156-5159, 1975.

[21]   D. J. Lanska, "The history of movement disorders," *Handbook of clinical neurology,* vol. 95, pp. 501-546, 2009.

[22]   J. Jankovic and E. Tolosa, *Parkinson's disease and movement disorders*: Lippincott Williams & Wilkins, 2007.

[23]   M. DeLong and T. Wichmann, "Changing views of basal ganglia circuits and circuit disorders," *Clin EEG Neurosci,* vol. 41, pp. 61-7, Apr 2010.

[24]   R. L. Albin, A. B. Young, and J. B. Penney, "The functional anatomy of basal ganglia disorders," *Trends in neurosciences,* vol. 12, pp. 366-375, 1989.

[25]   M. R. DeLong, "Primate models of movement disorders of basal ganglia origin," *Trends in neurosciences,* vol. 13, pp. 281-285, 1990.

[26]   P. Calabresi, B. Picconi, A. Tozzi, V. Ghiglieri, and M. Di Filippo, "Direct and indirect pathways of basal ganglia: a critical reappraisal," *Nature neuroscience,* vol. 17, p. 1022, 2014.

[27]   J. Nolte, "The human brain: an introduction to its functional anatomy," 2002.

[28]   J. L. Lanciego, N. Luquin, and J. A. Obeso, "Functional neuroanatomy of the basal ganglia," *Cold Spring Harbor perspectives in medicine,* p. a009621, 2012.

[29]   J. J. Lemaire, L. Sakka, L. Ouchchane, F. Caire, J. Gabrillargues, and J. M. Bonny, "Anatomy of the human thalamus based on spontaneous contrast and microscopic voxels in high-field magnetic resonance imaging," *Neurosurgery,* vol. 66, pp. 161-72, Mar 2010.

[30]   A.-L. Benabid, P. Pollak, A. Louveau, S. Henry, and J. De Rougemont, "Combined (thalamotomy and stimulation) stereotactic surgery of the VIM thalamic nucleus for bilateral Parkinson disease," *Stereotactic and functional neurosurgery,* vol. 50, pp. 344-346, 1987.

[31]   H. Akram, V. Dayal, P. Mahlknecht, D. Georgiev, J. Hyam, T. Foltynie, *et al.*, "Connectivity derived thalamic segmentation in deep brain stimulation for tremor," *NeuroImage: Clinical,* vol. 18, pp. 130-142, 2018.

[32]   T. Behrens, H. Johansen-Berg, M. Woolrich, S. Smith, C. Wheeler-Kingshott, P. Boulby*, et al.*, "Non-invasive mapping of connections between human thalamus and cortex using diffusion imaging," *Nature neuroscience,* vol. 6, p. 750, 2003.

[33]   S. C. Deoni, B. K. Rutt, A. G. Parrent, and T. M. Peters, "Segmentation of thalamic nuclei using a modified k-means clustering algorithm and high-resolution quantitative magnetic resonance imaging at 1.5 T," *Neuroimage,* vol. 34, pp. 117-126, 2007.

[34]   C. D. Hardman, J. M. Henderson, D. I. Finkelstein, M. K. Horne, G. Paxinos, and G. M. Halliday, "Comparison of the basal ganglia in rats, marmosets, macaques, baboons, and humans: volume and neuronal number for the output, internal relay, and striatal modulating nuclei," *Journal of Comparative Neurology,* vol. 445, pp. 238-255, 2002.

[35]   H. U. Kerl, L. Gerigk, M. A. Brockmann, S. Huck, M. Al-Zghloul, C. Groden*, et al.*, "Imaging for deep brain stimulation: The zona incerta at 7 Tesla," *World J Radiol,* vol. 5, pp. 5-16, Jan 28 2013.

[36]   J. Mitrofanis, "Some certainty for the "zone of uncertainty"? Exploring the function of the zona incerta," *Neuroscience,* vol. 130, pp. 1-15, 2005.

[37]   C. Watson, C. R. Lind, and M. G. Thomas, "The anatomy of the caudal zona incerta in rodents and primates," *Journal of anatomy,* vol. 224, pp. 95-107, 2014.

[38]   P. Blomstedt, A. Fytagoridis, M. Åström, J. Linder, L. Forsgren, and M. I. Hariz, "Unilateral caudal zona incerta deep brain stimulation for Parkinsonian tremor," *Parkinsonism & related disorders,* vol. 18, pp. 1062-1066, 2012.

[39]   P. Plaha, Y. Ben-Shlomo, N. K. Patel, and S. S. Gill, "Stimulation of the caudal zona incerta is superior to stimulation of the subthalamic nucleus in improving contralateral parkinsonism," *Brain,* vol. 129, pp. 1732-1747, 2006.

[40]   J. A. Obeso, M. C. Rodriguez-Oroz, M. Stamelou, K. P. Bhatia, and D. J. Burn, "The expanding universe of disorders of the basal ganglia," *Lancet,* vol. 384, pp. 523-31, Aug 9 2014.

[41]   E. D. Louis and J. J. Ferreira, "How common is the most common adult movement disorder? Update on the worldwide prevalence of essential tremor," *Mov Disord,* vol. 25, pp. 534-41, Apr 15 2010.

[42]   G. Deuschl and D. Berg, "Essential tremor: state of the art," *Nervenarzt,* pp. 394-399, Feb 5 2018.

[43]   K. P. Bhatia, P. Bain, N. Bajaj, R. J. Elble, M. Hallett, E. D. Louis*, et al.*, "Consensus Statement on the classification of tremors. from the task force on tremor of the International Parkinson and Movement Disorder Society," *Mov Disord,* vol. 33, pp. 75-87, Jan 2018.

[44]   R. C. Helmich, I. Toni, G. Deuschl, and B. R. Bloem, "The pathophysiology of essential tremor and Parkinson's tremor," *Curr Neurol Neurosci Rep,* vol. 13, p. 378, Sep 2013.

[45]   G. Deuschl, J. Raethjen, H. Hellriegel, and R. Elble, "Treatment of patients with essential tremor," *Lancet Neurol,* vol. 10, pp. 148-61, Feb 2011.

[46]   T. Zesiewicz, R. Elble, E. Louis, R. Hauser, K. Sullivan, R. Dewey*, et al.*, "Practice parameter: therapies for essential tremor report of the quality standards subcommittee of the American Academy of Neurology," *Neurology,* vol. 64, pp. 2008-2020, 2005.

[47]   W. J. Marks Jr, *Deep brain stimulation management*: Cambridge University Press, 2015.

[48]   C. G. Goetz, B. C. Tilley, S. R. Shaftman, G. T. Stebbins, S. Fahn, P. Martinez-Martin*, et al.*, "Movement Disorder Society-sponsored revision of the Unified Parkinson's Disease Rating Scale (MDS-UPDRS): scale presentation and clinimetric testing results," *Movement disorders: official journal of the Movement Disorder Society,* vol. 23, pp. 2129-2170, 2008.

[49]   A. Berardelli, J. C. Rothwell, M. Hallett, P. D. Thompson, M. Manfredi, and C. D. Marsden, "The pathophysiology of primary dystonia," *Brain,* vol. 121 (Pt 7), pp. 1195-212, Jul 1998.

[50]   G. Defazio, G. Abbruzzese, P. Livrea, and A. Berardelli, "Epidemiology of primary dystonia," *Lancet Neurol,* vol. 3, pp. 673-8, Nov 2004.

[51]   T. Trottenberg, J. Volkmann, G. Deuschl, A. Kühn, G.-H. Schneider, J. Müller*, et al.*, "Treatment of severe tardive dystonia with pallidal deep brain stimulation," *Neurology,* vol. 64, pp. 344-346, 2005.

[52]   W. Sako, S. Goto, H. Shimazu, N. Murase, K. Matsuzaki, T. Tamura*, et al.*, "Bilateral deep brain stimulation of the globus pallidus internus in tardive dystonia," *Movement Disorders,* vol. 23, pp. 1929-1931, 2008.

[53]   C. Pollo and K. Schindler, "Deep Brain Stimulation for Epilepsy: an Update."

[54]   M. Velasco, F. Velasco, A. L. Velasco, B. Boleaga, F. Jimenez, F. Brito*, et al.*, "Subacute electrical stimulation of the hippocampus blocks intractable temporal lobe seizures and paroxysmal EEG activities," *Epilepsia,* vol. 41, pp. 158-169, 2000.

[55]   C. Hamani, M. P. McAndrews, M. Cohn, M. Oh, D. Zumsteg, C. M. Shapiro*, et al.*, "Memory enhancement induced by hypothalamic/fornix deep brain stimulation," *Ann Neurol,* vol. 63, pp. 119-23, Jan 2008.

[56]   V. Sturm, O. Fricke, C. P. Bührle, D. Lenartz, M. Maarouf, H. Treuer*, et al.*, "DBS in the basolateral amygdala improves symptoms of autism and related self-injurious behavior: a case report and hypothesis on the pathogenesis of the disorder," *Frontiers in human neuroscience,* vol. 6, p. 341, 2013.

[57]   H.-J. Freund, J. Kuhn, D. Lenartz, J. K. Mai, T. Schnell, J. Klosterkoetter*, et al.*, "Cognitive functions in a patient with Parkinson-dementia syndrome undergoing deep brain stimulation," *Archives of neurology,* vol. 66, pp. 781-785, 2009.

[58]   M. A. Butler, J. M. Rosenow, and M. S. Okun, "History of the therapeutic use of electricity on the brain and the development of deep brain stimulation," in *Deep Brain Stimulation in Neurological and Psychiatric Disorders*, ed: Springer, 2008, pp. 63-82.

[59]   T. Keller and E. S. Krames, ""On the shoulders of giants": A history of the understandings of pain, leading to the understandings of neuromodulation," *Neuromodulation: Technology at the Neural Interface,* vol. 12, pp. 77-84, 2009.

[60]   G. Pancaldi, *Volta: Science and culture in the age of enlightenment*: Princeton University Press, 2005.

[61]   L. McWhirter, A. Carson, and J. Stone, "The body electric: a long view of electrical therapy for functional neurological disorders," *Brain,* vol. 138, pp. 1113-1120, 2015.

[62]   J. P. Morgan, "The first reported case of electrical stimulation of the human brain," *Journal of the history of medicine and allied sciences,* vol. 37, p. 51, 1982.

[63]   G. H. Baltuch and M. B. Stern, *Deep brain stimulation for Parkinson's disease*: CRC Press, 2007.

[64]   P. L. Gildenberg, "Evolution of basal ganglia surgery for movement disorders," *Stereotactic and functional neurosurgery,* vol. 84, pp. 131-135, 2006.

[65]   C. G. Goetz, "The history of Parkinson's disease: early clinical descriptions and neurological therapies," *Cold Spring Harb Perspect Med,* vol. 1, p. a008862, Sep 2011.

[66]   E. A. Spiegel, H. T. Wycis, M. Marks, and A. J. Lee, "Stereotaxic Apparatus for Operations on the Human Brain," *Science,* vol. 106, pp. 349-50, Oct 10 1947.

[67]   R. Clarke and V. Horsley, "On a method of investigating the deep ganglia and tracts of the central nervous system (Cerebellum)(Reprinted from Br Med J, pg 1799, 1906)," *CLINICAL ORTHOPAEDICS AND RELATED RESEARCH,* pp. 3-6, 2007.

[68]   J. M. Schwalb and C. Hamani, "The history and future of deep brain stimulation," *Neurotherapeutics,* vol. 5, pp. 3-13, 2008.

[69]   J. Arle, "Development of a classic: The Todd-Wells apparatus, the BRW, and the CRW stereotactic frames," in *Textbook of Stereotactic and Functional Neurosurgery*, ed: Springer, 2009, pp. 453-467.

[70]   L. Leksell, D. Leksell, and J. Schwebel, "Stereotaxis and nuclear magnetic resonance," *Journal of Neurology, Neurosurgery & Psychiatry,* vol. 48, pp. 14-18, 1985.

[71]   J. Talairach, *Atlas d'anatomie stéréotaxique: repérage radiologique indirect des noyaux gris centraux des régions mésencéphalo-sous-optique et hypothalamique de l'homme*: Masson, 1957.

[72]   G. Shaltenbrand, "Introduction to Stereotaxis with an Atlas of the Human Brain," *Stuttgart,* 1959.

[73]   A. Morel, M. Magnin, and D. Jeanmonod, "Multiarchitectonic and stereotactic atlas of the human thalamus," *Journal of Comparative Neurology,* vol. 387, pp. 588-630, 1997.

[74]   J. K. Mai, M. Majtanik, and G. Paxinos, *Atlas of the human brain*: Academic Press, 2015.

[75]   M. I. Hariz, P. Blomstedt, and L. Zrinzo, "Deep brain stimulation between 1947 and 1987: the untold story," *Neurosurgical focus,* vol. 29, p. E1, 2010.

[76]   A. Carlsson, M. Lindqvist, and T. Magnusson, "3, 4-Dihydroxyphenylalanine and 5-hydroxytryptophan as reserpine antagonists," *Nature,* vol. 180, p. 1200, 1957.

[77]   N. Bechtereva, A. Bondartchuk, V. Smirnov, L. Meliutcheva, and A. Shandurina, "Method of electrostimulation of the deep brain structures in treatment of some chronic diseases," *Stereotactic and Functional Neurosurgery,* vol. 37, pp. 136-140, 1975.

[78]   J. Gardner, "A history of deep brain stimulation: Technological innovation and the role of clinical assessment tools," *Social studies of science,* vol. 43, pp. 707-728, 2013.

[79]   (June 4). Available: http://www.bostonscientific.com/content/dam/bostonscientific/neuro/portfolio-group/Vercise%20Deep%20Brain%20Stimulation/vercise_pc_systemfunction_d_960x720px_eu_trans.png

[80]   J. C. Lilly, J. R. Hughes, E. C. Alvord Jr, and T. W. Galkin, "Brief, noninjurious electric waveform for stimulation of the brain," *Science,* 1955.

[81]   D. R. Merrill, M. Bikson, and J. G. Jefferys, "Electrical stimulation of excitable tissue: design of efficacious and safe protocols," *J Neurosci Methods,* vol. 141, pp. 171-98, Feb 15 2005.

[82]   G. Zouridakis, *Biomedical technology and devices handbook*: CRC press, 2003.

[83]   D. T. Brocker and W. M. Grill, "Principles of electrical stimulation of neural tissue," *Handb Clin Neurol,* vol. 116, pp. 3-18, 2013.

[84]   F. Rattay, "Analysis of the electrical excitation of CNS neurons," *IEEE Transactions on Biomedical Engineering,* vol. 45, pp. 766-772, 1998.

[85]   C. C. McIntyre and W. M. Grill, "Excitation of central nervous system neurons by nonuniform electric fields," *Biophys J,* vol. 76, pp. 878-88, Feb 1999.

[86]   S. Miocinovic, P. Khemani, R. Whiddon, P. Zeilman, D. Martinez-Ramirez, M. S. Okun*, et al.*, "Outcomes, management, and potential mechanisms of interleaving deep brain stimulation settings," *Parkinsonism & related disorders,* vol. 20, pp. 1434-1437, 2014.

[87]   A. Amon and F. Alesch, "Systems for deep brain stimulation: review of technical features," *Journal of Neural Transmission,* vol. 124, pp. 1083-1091, 2017.

[88]   A. Abosch, L. Timmermann, S. Bartley, H. G. Rietkerk, D. Whiting, P. J. Connolly*, et al.*, "An international survey of deep brain stimulation procedural steps," *Stereotact Funct Neurosurg,* vol. 91, pp. 1-11, 2013.

[89]   L. Lunsford, D. Kondziolka, and D. Leksell, "Leksell stereotactic apparatus," in *Textbook of stereotactic and functional neurosurgery*, ed: Springer, 2009, pp. 469-485.

[90]   J. Krauss, "The Riechert/Mundinger Stereotactic Apparatus," in *Textbook of stereotactic and functional neurosurgery*, ed: Springer, 2009, pp. 487-494.

[91]   S. Hemm and K. Wårdell, "Stereotactic implantation of deep brain stimulation electrodes: a review of technical systems, methods and emerging tools," *Med Biol Eng Comput,* vol. 48, pp. 611-24, Jul 2010.

[92]   F. Duffner, H. Schiffbauer, S. Breit, S. Friese, and D. Freudenstein, "Relevance of image fusion for target point determination in functional neurosurgery," *Acta neurochirurgica,* vol. 144, pp. 445-451, 2002.

[93]   A. R. Rezai, B. H. Kopell, R. E. Gross, J. L. Vitek, A. D. Sharan, P. Limousin*, et al.*, "Deep brain stimulation for Parkinson's disease: surgical issues," *Mov Disord,* vol. 21 Suppl 14, pp. S197-218, Jun 2006.

[94]   R. M. Richardson, "Chapter 13 - Functional Neurosurgery: Deep Brain Stimulation and Gene Therapy A2 - Golby, Alexandra J," in *Image-Guided Neurosurgery*, ed Boston: Academic Press, 2015, pp. 297-323.

[95]   G. Nikkhah and M. Pinsker, *Stereotactic and functional neurosurgery*: Springer, 2013.

[96]   P. L. Gildenberg, "The history of stereotactic neurosurgery," *Neurosurg Clin N Am,* vol. 1, pp. 765-80, Oct 1990.

[97]   E. Moro, R. Esselink, J. Xie, M. Hommel, A. Benabid, and P. Pollak, "The impact on Parkinson's disease of electrical parameter settings in STN stimulation," *Neurology,* vol. 59, pp. 706-713, 2002.

[98]   M. Rizzone, M. Lanotte, B. Bergamasco, A. Tavella, E. Torre, G. Faccani*, et al.*, "Deep brain stimulation of the subthalamic nucleus in Parkinson's disease: effects of variation in stimulation parameters," *Journal of Neurology, Neurosurgery & Psychiatry,* vol. 71, pp. 215-219, 2001.

[99]   J. Volkmann, E. Moro, and R. Pahwa, "Basic algorithms for the programming of deep brain stimulation in Parkinson's disease," *Movement Disorders,* vol. 21, 2006.

[100]   M. I. Hariz, "Complications of deep brain stimulation surgery," *Movement disorders,* vol. 17, 2002.

[101]   M. S. Okun, M. Tagliati, M. Pourfar, H. H. Fernandez, R. L. Rodriguez, R. L. Alterman*, et al.*, "Management of referred deep brain stimulation failures: a retrospective analysis from 2 movement disorders centers," *Archives of neurology,* vol. 62, pp. 1250-1255, 2005.

[102]   J. M. Bronstein, M. Tagliati, R. L. Alterman, A. M. Lozano, J. Volkmann, A. Stefani*, et al.*, "Deep brain stimulation for Parkinson disease: an expert consensus and review of key issues," *Arch Neurol,* vol. 68, p. 165, Feb 2011.

[103]   L. Zrinzo, T. Foltynie, P. Limousin, and M. I. Hariz, "Reducing hemorrhagic complications in functional neurosurgery: a large case series and systematic literature review," *Journal of neurosurgery,* vol. 116, pp. 84-94, 2012.

[104]   P. Zsigmond, S. Hemm-Ode, and K. Wårdell, "Optical Measurements during Deep Brain Stimulation Lead Implantation: Safety Aspects," *Stereotactic and functional neurosurgery,* vol. 95, pp. 392-399, 2017.

[105]   J. G. Nutt, V. Anderson, J. Peacock, J. Hammerstad, and K. Burchiel, "DBS and diathermy interaction induces severe CNS damage," *Neurology,* vol. 56, pp. 1384-1386, 2001.

[106]   A. Galvan, A. Devergnas, and T. Wichmann, "Alterations in neuronal activity in basal ganglia-thalamocortical circuits in the parkinsonian state," *Frontiers in neuroanatomy,* vol. 9, p. 5, 2015.

[107]   H.-K. Min, S.-C. Hwang, M. P. Marsh, I. Kim, E. Knight, B. Striemer*, et al.*, "Deep brain stimulation induces BOLD activation in motor and non-motor networks: an fMRI comparison study of STN and EN/GPi DBS in large animals," *Neuroimage,* vol. 63, pp. 1408-1420, 2012.

[108]   K. Ashkan, P. Rogers, H. Bergman, and I. Ughratdar, "Insights into the mechanisms of deep brain stimulation," *Nature Reviews Neurology,* vol. 13, p. 548, 2017.

[109]   T. Zirh, F. Lenz, S. Reich, and P. Dougherty, "Patterns of bursting occurring in thalamic cells during parkinsonian tremor," *Neuroscience,* vol. 83, pp. 107-121, 1998.

[110]   A. A. Kühn, A. Tsui, T. Aziz, N. Ray, C. Brücke, A. Kupsch*, et al.*, "Pathological synchronisation in the subthalamic nucleus of patients with Parkinson's disease relates to both bradykinesia and rigidity," *Experimental neurology,* vol. 215, pp. 380-387, 2009.

[111]   J. B. Ranck Jr, "Which elements are excited in electrical stimulation of mammalian central nervous system: a review," *Brain research,* vol. 98, pp. 417-440, 1975.

[112]   T. Hashimoto, C. M. Elder, M. S. Okun, S. K. Patrick, and J. L. Vitek, "Stimulation of the subthalamic nucleus changes the firing pattern of pallidal neurons," *Journal of neuroscience,* vol. 23, pp. 1916-1923, 2003.

[113]   E. B. Montgomery, "Effects of GPi stimulation on human thalamic neuronal activity," *Clinical Neurophysiology,* vol. 117, pp. 2691-2702, 2006.

[114]   M. E. Anderson, N. Postupna, and M. Ruffo, "Effects of high-frequency stimulation in the internal globus pallidus on the activity of thalamic neurons in the awake monkey," *Journal of neurophysiology,* vol. 89, pp. 1150-1160, 2003.

[115] E. B. Montgomery Jr and J. T. Gale, "Mechanisms of action of deep brain stimulation (DBS)," *Neuroscience & Biobehavioral Reviews,* vol. 32, pp. 388-407, 2008.

[116] S. Hameroff, M. Trakas, C. Duffield, E. Annabi, M. B. Gerace, P. Boyle*, et al.*, "Transcranial ultrasound (TUS) effects on mental states: a pilot study," *Brain Stimulation: Basic, Translational, and Clinical Research in Neuromodulation,* vol. 6, pp. 409-415, 2013.

[117] A. L. Hodgkin and A. F. Huxley, "A quantitative description of membrane current and its application to conduction and excitation in nerve," *The Journal of physiology,* vol. 117, pp. 500-544, 1952.

[118] D. Durand and J. Bronzino, "Electric stimulation of excitable tissue," *The biomedical engineering handbook,* vol. 2, 2000.

[119] M. van Dongen and W. Serdijn, "Design of Efficient and Safe Neural Stimulators," 2015.

[120] S. F. Cogan, "Neural stimulation and recording electrodes," *Annu Rev Biomed Eng,* vol. 10, pp. 275-309, 2008.

[121] R. Venugopalan and R. Ideker, "Bioelectrodes," in *Biomaterials Science (Third Edition)*, ed: Elsevier, 2013, pp. 957-966.

[122] B. Howell and W. Grill, "Design of electrodes for stimulation and recording," in *Implantable Neuroprostheses for Restoring Function*, ed: Elsevier, 2015, pp. 59-93.

[123] P. L. Nunez and R. Srinivasan, *Electric fields of the brain: the neurophysics of EEG*: Oxford University Press, USA, 2006.

[124] R. Plonsey, "Volume conductor theory," *The biomedical engineering handbook,* pp. 119-125, 1995.

[125] D. K. Cheng, *Field and wave electromagnetics*: Pearson Education India, 1989.

[126] C. Gabriel, A. Peyman, and E. Grant, "Electrical conductivity of tissue at frequencies below 1 MHz," *Physics in medicine & biology,* vol. 54, p. 4863, 2009.

[127] J. K. Seo and E. J. Woo, "Electrical tissue property imaging at low frequency using MREIT," *IEEE Transactions on Biomedical Engineering,* vol. 61, pp. 1390-1399, 2014.

[128] D. S. Holder, *Electrical impedance tomography: methods, history and applications*: CRC Press, 2004.

[129] T. Voigt, U. Katscher, and O. Doessel, "Quantitative conductivity and permittivity imaging of the human brain using electric properties tomography," *Magnetic Resonance in Medicine,* vol. 66, pp. 456-466, 2011.

[130] M. Chauhan, A. Indahlastari, A. K. Kasinadhuni, M. Schär, T. H. Mareci, and R. J. Sadleir, "Low-Frequency Conductivity Tensor Imaging of the Human Head in vivo using DT-MREIT: First Study," *IEEE Transactions on Medical Imaging,* 2017.

[131] P. W. Nicholson, "Specific impedance of cerebral white matter," *Experimental neurology,* vol. 13, pp. 386-401, 1965.

[132] S. Gabriel, R. W. Lau, and C. Gabriel, "The dielectric properties of biological tissues: III. Parametric models for the dielectric spectrum of tissues," *Phys Med Biol,* vol. 41, pp. 2271-93, Nov 1996.

[133] D. Andreuccetti, R. Fossi, and C. Petrucci, "Dielectric properties of body tissue. Italian National Research Council," *Institute for Applied Physics, Florence, Italy http://niremf. ifac. cnr. it/tissprop,* 2005.

[134] K. Wardell, L. Zrinzo, M. Hariz, and M. Andersson, "Patient-specific brain modelling for deep brain stimulation simulations," in *Neural Engineering (NER), 2013 6th International IEEE/EMBS Conference on*, 2013, pp. 148-151.

[135] E. N. Warman, W. M. Grill, and D. Durand, "Modeling the effects of electric fields on nerve fibers: determination of excitation thresholds," *IEEE Transactions on Biomedical Engineering,* vol. 39, pp. 1244-1254, 1992.

[136] D. R. McNeal, "Analysis of a model for excitation of myelinated nerve," *IEEE Trans Biomed Eng,* vol. 23, pp. 329-37, Jul 1976.

[137] F. Rattay, "Analysis of models for external stimulation of axons," *IEEE transactions on biomedical engineering,* pp. 974-977, 1986.

[138] M. Åström, E. Diczfalusy, H. Martens, and K. Wårdell, "Relationship between neural activation and electric field distribution during deep brain stimulation," *IEEE Trans Biomed Eng,* vol. 62, pp. 664-72, Feb 2015.

[139] C. C. McIntyre, A. G. Richardson, and W. M. Grill, "Modeling the excitability of mammalian nerve fibers: influence of afterpotentials on the recovery cycle," *Journal of neurophysiology,* vol. 87, pp. 995-1006, 2002.

[140] F. Rattay and M. Aberham, "Modeling axon membranes for functional electrical stimulation," *IEEE Transactions on Biomedical Engineering,* vol. 40, pp. 1201-1209, 1993.

[141] W. Wesselink, J. Holsheimer, and H. Boom, "A model of the electrical behaviour of myelinated sensory nerve fibres based on human data," *Medical & biological engineering & computing,* vol. 37, pp. 228-235, 1999.

[142] S. Stoney Jr, W. Thompson, and H. Asanuma, "Excitation of pyramidal tract cells by intracortical microstimulation: effective extent of stimulating current," *Journal of neurophysiology,* vol. 31, pp. 659-669, 1968.

[143] S. L. BeMent and J. B. Ranck Jr, "A quantitative study of electrical stimulation of central myelinated fibers," *Experimental neurology,* vol. 24, pp. 147-170, 1969.

[144] G. Weiss, "Sur la possibilite de rendre comparables entre eux les appareils servant a l'excitation electrique," *Archives Italiennes de Biologie,* vol. 35, pp. 413-445, 1901.

[145] L. Lapicque, "Definition experimentale de l'excitabilite. Soc. Biologic 77 (1909)," ed: Französisch, 1909.

[146] J. Yeomans, N. Maidment, and B. Bunney, "Excitability properties of medial forebrain bundle axons of A9 and A10 dopamine cells," *Brain research,* vol. 450, pp. 86-93, 1988.

[147] R. J. Jensen, O. R. Ziv, and J. F. Rizzo, "Thresholds for activation of rabbit retinal ganglion cells with relatively large, extracellular microelectrodes," *Investigative ophthalmology & visual science,* vol. 46, pp. 1486-1496, 2005.

[148] H. Bostock, "The strength-duration relationship for excitation of myelinated nerve: computed dependence on membrane parameters," *The Journal of Physiology,* vol. 341, pp. 59-74, 1983.

[149] C. C. McIntyre and W. M. Grill, "Sensitivity analysis of a model of mammalian neural membrane," *Biological cybernetics,* vol. 79, pp. 29-37, 1998.

[150] D. Boinagrov, J. Loudin, and D. Palanker, "Strength–duration relationship for extracellular neural stimulation: numerical and analytical models," *Journal of neurophysiology,* vol. 104, pp. 2236-2248, 2010.

[151] R. D. Cook, *Concepts and applications of finite element analysis*: John Wiley & Sons, 2007.

[152] H. G. Rao, *Finite Element Method Vs. Classical Methods*: New Age International (P) Limited, Publishers, 2007.

[153] (May 23 2018). *List of finite element software packages*. Available: https://en.wikipedia.org/wiki/List_of_finite_element_software_packages

[154] C. Shah, "Mesh discretization error and criteria for accuracy of finite element solutions," in *Ansys Users Conference*, 2002, p. 12.

[155] (2015, May 31). *multiphysicsCYCLOPEDIA*. Available: https://www.comsol.com/multiphysics/fea-software

[156] W. Rushton, "The effect upon the threshold for nervous excitation of the length of nerve exposed, and the angle between current and nerve," *The Journal of physiology,* vol. 63, pp. 357-377, 1927.

[157] S. L. BeMent and J. B. Ranck Jr, "A model for electrcal stimulation of central myelinated fibers with monopolar electrodes," *Experimental neurology,* vol. 24, pp. 171-186, 1969.

[158] A. Heringa, D. F. Stegeman, G. J. Uijen, and J. De Weerd, "Solution methods of electrical field problems in physiology," *IEEE Transactions on Biomedical Engineering,* pp. 34-42, 1982.

[159] S. Hemm, G. Mennessier, N. Vayssiere, L. Cif, and P. Coubes, "Co-registration of stereotactic MRI and isofieldlines during deep brain stimulation," *Brain Res Bull,* vol. 68, pp. 59-61, Dec 15 2005.

[160] M. Åström, J. D. Johansson, M. I. Hariz, O. Eriksson, and K. Wårdell, "The effect of cystic cavities on deep brain stimulation in the basal ganglia: a simulation-based study," *J Neural Eng,* vol. 3, pp. 132-8, Jun 2006.

[161] N. Yousif, R. Bayford, P. G. Bain, and X. Liu, "The peri-electrode space is a significant element of the electrode–brain interface in deep brain stimulation: a computational study," *Brain research bulletin,* vol. 74, pp. 361-368, 2007.

[162] C. R. Butson, S. E. Cooper, J. M. Henderson, and C. C. McIntyre, "Patient-specific analysis of the volume of tissue activated during deep brain stimulation," *Neuroimage,* vol. 34, pp. 661-70, Jan 15 2007.

[163] C. Butson, J. Hall, J. Henderson, and C. McIntyre, "Patient-specific models of deep brain stimulation: 3D visualization of anatomy, electrode and volume of activation as a function of the stimulation parameters," in *Soc Neurosci Abstr*, 2004.

[164] M. Åström, E. Tripoliti, M. I. Hariz, L. U. Zrinzo, I. Martinez-Torres, P. Limousin*, et al.*, "Patient-specific model-based investigation of speech intelligibility and movement during deep brain stimulation," *Stereotact Funct Neurosurg,* vol. 88, pp. 224-33, 2010.

[165] K. Wårdell, E. Diczfalusy, and M. Åström, "Patient-specific modeling and simulation of deep brain stimulation," in *Patient-Specific Modeling in Tomorrow's Medicine*, ed: Springer, 2011, pp. 357-375.

[166] N. Yousif, R. Bayford, and X. Liu, "The influence of reactivity of the electrode-brain interface on the crossing electric current in therapeutic deep brain stimulation," *Neuroscience,* vol. 156, pp. 597-606, Oct 15 2008.

[167] C. C. McIntyre and N. V. Thakor, "Uncovering the mechanisms of deep brain stimulation for Parkinson's disease through functional imaging, neural recording, and neural modeling," *Critical Reviews™ in Biomedical Engineering,* vol. 30, 2002.

[168] S. Hemm, G. Mennessier, N. Vayssiere, L. Cif, H. El Fertit, and P. Coubes, "Deep brain stimulation in movement disorders: stereotactic coregistration of two-dimensional electrical field modeling and magnetic resonance imaging," *J Neurosurg,* vol. 103, pp. 949-55, Dec 2005.

[169] A. M. Kuncel and W. M. Grill, "Selection of stimulus parameters for deep brain stimulation," *Clin Neurophysiol,* vol. 115, pp. 2431-41, Nov 2004.

[170] C. Schmidt, P. Grant, M. Lowery, and U. van Rienen, "Influence of uncertainties in the material properties of brain tissue on the probabilistic volume of tissue activated," *IEEE Trans Biomed Eng,* vol. 60, pp. 1378-87, May 2013.

[171] C. R. Butson and C. C. McIntyre, "Current steering to control the volume of tissue activated during deep brain stimulation," *Brain Stimul,* vol. 1, pp. 7-15, Jan 2008.

[172] A. M. Kuncel, S. E. Cooper, and W. M. Grill, "A method to estimate the spatial extent of activation in thalamic deep brain stimulation," *Clin Neurophysiol,* vol. 119, pp. 2148-58, Sep 2008.

[173] S. Hemm, G. Mennessier, N. Vayssiere, L. Cif, and P. Coubes, "Co-registration of stereotactic MRI and isofieldlines during deep brain stimulation," *Brain research bulletin,* vol. 68, pp. 59-61, 2005.

[174] B. Howell, S. Naik, and W. M. Grill, "Influences of interpolation error, electrode geometry, and the electrode–tissue interface on models of electric fields produced by deep brain stimulation," *IEEE transactions on Biomedical Engineering,* vol. 61, pp. 297-307, 2014.

[175] C. C. McIntyre, S. Miocinovic, and C. R. Butson, "Computational analysis of deep brain stimulation," *Expert Rev Med Devices,* vol. 4, pp. 615-22, Sep 2007.

[176] O. Eriksson, J. Wren, D. Loyd, and K. Wårdell, "A comparison betweenin vitro studies of protein lesions generated by brain electrodes and finite element model simulations," *Medical & biological engineering & computing,* vol. 37, pp. 737-741, 1999.

[177] C. R. Butson and C. C. McIntyre, "Tissue and electrode capacitance reduce neural activation volumes during deep brain stimulation," *Clinical neurophysiology,* vol. 116, pp. 2490-2500, 2005.

[178] X. F. Wei and W. M. Grill, "Impedance characteristics of deep brain stimulation electrodes in vitro and in vivo," *Journal of neural engineering,* vol. 6, p. 046008, 2009.

[179] S. F. Lempka, B. Howell, K. Gunalan, A. G. Machado, and C. C. McIntyre, "Characterization of the stimulus waveforms generated by implantable pulse generators for deep brain stimulation," *Clinical Neurophysiology,* vol. 129, pp. 731-742, 2018.

[180] N. A. Pelot, B. J. Thio, and W. M. Grill, "Modeling Current Sources for Neural Stimulation in COMSOL," *Frontiers in Computational Neuroscience,* vol. 12, p. 40, 2018.

[181] T. D. Kozai, A. S. Jaquins-Gerstl, A. L. Vazquez, A. C. Michael, and X. T. Cui, "Brain tissue responses to neural implants impact signal sensitivity and intervention strategies," *ACS chemical neuroscience,* vol. 6, pp. 48-67, 2015.

[182] C. Lungu, P. Malone, T. Wu, P. Ghosh, B. McElroy, K. Zaghloul, *et al.,* "Temporal macrodynamics and microdynamics of the postoperative impedance at the tissue–

electrode interface in deep brain stimulation patients," *J Neurol Neurosurg Psychiatry,* vol. 85, pp. 816-819, 2014.

[183] C. Haberler, F. Alesch, P. R. Mazal, P. Pilz, K. Jellinger, M. M. Pinter*, et al.*, "No tissue damage by chronic deep brain stimulation in Parkinson's disease," *Annals of neurology,* vol. 48, pp. 372-376, 2000.

[184] M. S. Nielsen, C. Bjarkam, J. Sørensen, M. Bojsen-Møller, N. A. Sunde, and K. Østergaard, "Chronic subthalamic high-frequency deep brain stimulation in Parkinson's disease–a histopathological study," *European journal of neurology,* vol. 14, pp. 132-138, 2007.

[185] C. R. Butson and C. C. McIntyre, "Role of electrode design on the volume of tissue activated during deep brain stimulation," *J Neural Eng,* vol. 3, pp. 1-8, Mar 2006.

[186] S. Hemm, N. Vayssiere, G. Mennessier, L. Cif, M. Zanca, P. Ravel*, et al.*, "Evolution of brain impedance in dystonic patients treated by GPI electrical stimulation," *Neuromodulation,* vol. 7, pp. 67-75, Apr 2004.

[187] A. Chaturvedi, C. R. Butson, S. F. Lempka, S. E. Cooper, and C. C. McIntyre, "Patient-specific models of deep brain stimulation: influence of field model complexity on neural activation predictions," *Brain Stimul,* vol. 3, pp. 65-7, Apr 2010.

[188] M. Åström, J. J. Lemaire, and K. Wårdell, "Influence of heterogeneous and anisotropic tissue conductivity on electric field distribution in deep brain stimulation," *Med Biol Eng Comput,* vol. 50, pp. 23-32, Jan 2012.

[189] B. Howell and C. C. McIntyre, "Role of soft-tissue heterogeneity in computational models of deep brain stimulation," *Brain stimulation,* vol. 10, pp. 46-50, 2017.

[190] C. R. Butson, C. B. Maks, and C. C. McIntyre, "Sources and effects of electrode impedance during deep brain stimulation," *Clinical Neurophysiology,* vol. 117, pp. 447-454, 2006.

[191] S. F. Lempka, M. D. Johnson, S. Miocinovic, J. L. Vitek, and C. C. McIntyre, "Current-controlled deep brain stimulation reduces in vivo voltage fluctuations observed during voltage-controlled stimulation," *Clin Neurophysiol,* vol. 121, pp. 2128-33, Dec 2010.

[192] J. M. Bronstein, M. Tagliati, C. McIntyre, R. Chen, T. Cheung, E. L. Hargreaves*, et al.*, "The rationale driving the evolution of deep brain stimulation to constant-current devices," *Neuromodulation,* vol. 18, pp. 85-9, Feb 2015.

[193] C. Lettieri, S. Rinaldo, G. Devigili, F. Pisa, M. Mucchiut, E. Belgrado*, et al.*, "Clinical outcome of deep brain stimulation for dystonia: constant-current or constant-voltage stimulation? A non-randomized study," *Eur J Neurol,* Jul 10 2014.

[194] X. F. Wei and W. M. Grill, "Current density distributions, field distributions and impedance analysis of segmented deep brain stimulation electrodes," *J Neural Eng,* vol. 2, pp. 139-47, Dec 2005.

[195] M. F. Contarino, L. J. Bour, R. Verhagen, M. A. Lourens, R. M. de Bie, P. van den Munckhof*, et al.*, "Directional steering: a novel approach to deep brain stimulation," *Neurology,* vol. 83, pp. 1163-1169, 2014.

[196] H. C. Martens, E. Toader, M. M. Decre, D. J. Anderson, R. Vetter, D. R. Kipke*, et al.*, "Spatial steering of deep brain stimulation volumes using a novel lead design," *Clin Neurophysiol,* vol. 122, pp. 558-66, Mar 2011.

[197]   K. J. Van Dijk, R. Verhagen, A. Chaturvedi, C. C. McIntyre, L. J. Bour, C. Heida*, et al.*, "A novel lead design enables selective deep brain stimulation of neural populations in the subthalamic region," *Journal of neural engineering,* vol. 12, p. 046003, 2015.

[198]   W. Hamel, J. A. Koppen, F. Alesch, A. Antonini, J. A. Barcia, H. Bergman*, et al.*, "Targeting of the Subthalamic Nucleus for Deep Brain Stimulation: A Survey Among Parkinson Disease Specialists," *World Neurosurg,* vol. 99, pp. 41-46, Mar 2017.

[199]   V. A. Coenen, B. Mädler, H. Schiffbauer, H. Urbach, and N. Allert, "Individual fiber anatomy of the subthalamic region revealed with diffusion tensor imaging: a concept to identify the deep brain stimulation target for tremor suppression," *Neurosurgery,* vol. 68, pp. 1069-1076, 2011.

[200]   A. Horn, M. Reich, J. Vorwerk, N. Li, G. Wenzel, Q. Fang*, et al.*, "Connectivity predicts deep brain stimulation outcome in Parkinson's disease," *Annals of Neurology,* 2017.

[201]   H. Akram, S. N. Sotiropoulos, S. Jbabdi, D. Georgiev, P. Mahlknecht, J. Hyam*, et al.*, "Subthalamic deep brain stimulation sweet spots and hyperdirect cortical connectivity in Parkinson's disease," *Neuroimage,* vol. 158, pp. 332-345, Sep 2017.

PAPER I

Research Article   **Open Access**

Influence on Deep Brain Stimulation from Lead Design, Operating Mode and Tissue Impedance Changes – A Simulation Study

Fabiola Alonso[1], Simone Hemm-Ode[1,2] and Karin Wårdell[1]*

[1]Department of Biomedical Engineering, Linköping University, Sweden
[2]University of Applied Sciences and Arts Northwestern Switzerland, School of Life Sciences, Institute for Medical and Analytical Technologies, Switzerland

Abstract

Background: Deep brain stimulation (DBS) systems in current mode and new lead designs are recently available. To switch between DBS-systems remains complicated as clinicians may lose their reference for programming. Simulations can help increase the understanding.

Objective: To quantitatively investigate the electric field (EF) around two lead designs simulated to operate in voltage and current mode under two time points following implantation.

Methods: The finite element method was used to model Lead 3389 (Medtronic) and 6148 (St Jude) with homogenous surrounding grey matter and a peri-electrode space (PES) of 250 μm. The PES-impedance mimicked the acute (extracellular fluid) and chronic (fibrous tissue) time-point. Simulations at different amplitudes of voltage and current (n=236) were performed using two different contacts. Equivalent current amplitudes were extracted by matching the shape and maximum EF of the 0.2 V/mm isolevel.

Results: The maximum EF extension at 0.2 V/mm varied between 2-5 mm with a small difference between the leads. In voltage mode EF increased about 1 mm at acute compared to the chronic PES. Current mode presented the opposite relationship. Equivalent EFs for lead 3389 at 3 V were found for 7 mA (acute) and 2.2 mA (chronic).

Conclusions: Simulations showed a major impact on the electric field extension between postoperative time points. This may explain the clinical decisions to reprogram the amplitude weeks after implantation. Neither the EF extension nor intensity is considerably influenced by the lead design. However, the EF distribution is affected by the larger contact of Lead 6148 generating an electric field below the tip.

Introduction

Deep brain stimulation (DBS) is an established therapy for movement disorders such as Parkinson's disease (PD), essential tremor and dystonia [1]. To date more than 120,000 patients have received DBS implants. During the first two decades of the modern DBS era all implantations were performed using the same type of stimulation control and lead configuration; a four contact lead connected to a voltage controlled neurostimulator. In 2009 the first current controlled DBS device was introduced in Europe on PD patients. Today several DBS lead designs and stimulation modes are available but still not fully established as clinical alternatives. Furthermore intensive research is being performed to develop new DBS systems, e.g. for steering of the simulation field [2-5].

Present literature seems to show that current controlled stimulation induces at least as good clinical effects as voltage controlled stimulation [6,7], and that it should be preferred towards voltage controlled devices due to the automatic voltage adjustment as impedance changes [8,9]. Nevertheless, to switch from one mode to the other remains complicated as clinicians risk to lose their reference for programming. The same is valid for switching from one commercially available lead design to another as the differences or the influence of the design on voltage, current or electric field distribution has not been discussed so far to our knowledge. In addition to questions concerning the design, neurologists often have to deal with changes in impedance during postoperative patient management, not only due to hardware complications [10], but due to tissue changes around the electrode [11-13].

A way to try to provide answers to the above formulated questions concerning different DBS lead designs, stimulation modes and influence of impedance changes is to use computer models to simulate the electrical behaviour around active DBS-contacts. Current controlled stimulation systems have not been studied as much as voltage-controlled systems. The few studies published rely on in vivo experimental recordings performed in animals [9] or experiments where the brain tissue is not included in the study [14]. Computational model studies have been designed to analyse the influence of different pulse waveforms or electrode-tissue interface considering both voltage and current controlled stimulation [15-17].

Our group has previously used the finite element method (FEM) to investigate the influence on the DBS fields from tissue types such as cystic cavities [18] and white matter heterogeneity and anisotropy [19]. Also, patient-specific models and simulations of DBS have been used to increase the understanding of the response to stimulation for a number of targets including the subthalamic nucleus [20-23] the globus

pallidus internus [24-27], and the ventral intermedius nucleus of the thalamus for essential tremor [28]. Such patient-specific simulations should preferable take into account both, the tissue's heterogeneity (e.g. differences between grey and white matter) and the anisotropy of the white matter [19]. When studying the differences between lead designs and stimulation modes however, it is an advantage to reduce the number of parameters that can influence the outcome. Especially when comparing different stimulation modes and lead designs, the relative difference is most important and not the actual extent of the stimulation. Therefore a homogenous tissue model with impedance often mimicking grey tissue, is preferred [18] and also used for the present study.

Stimulation results may be represented and visualized by different electrical quantities such as the electric field (EF) [21,24,25], the second difference of the electric potential [3,4], and the volume of tissue activated derived from neuron models coupled to finite element simulations [17,20,29]. By using a fixed isolevel the EF can be used for relative comparisons between simulations, and also allow for visualization directly in the mm-scale. The electric field is also the entity which shows the least influence on the activation threshold caused by change in axon diameter, pulse width and amplitude [29]. Therefore EF is a suitable entity for the present study, where the aim is to investigate the influence on the electric field from two DBS-lead designs, two operating modes i.e. current or voltage stimulation, and the impedance in the peri-electrode space (PES). The PES was set to mimic two post-operative time points: the acute stage corresponding to leakage of extracellular fluid and a chronic condition related to fibrous tissue [30].
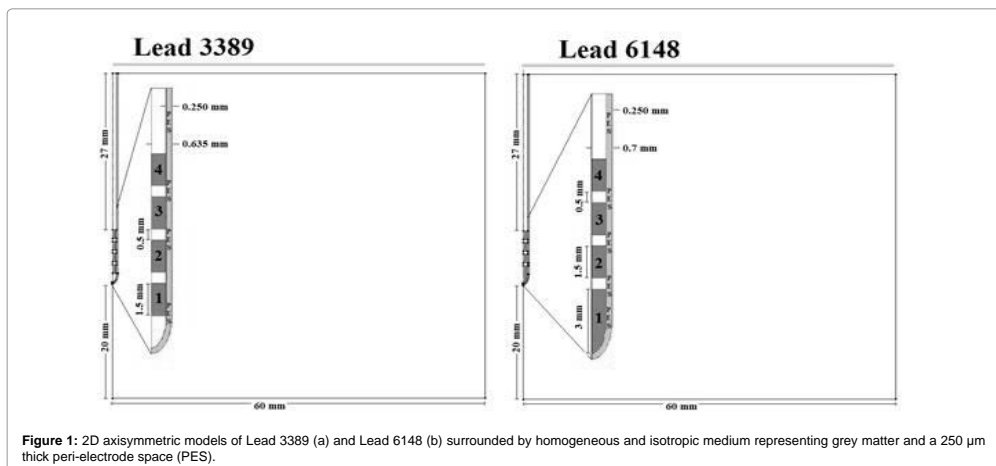
Materials and Methods

DBS leads and brain models

The investigation was based on two different DBS lead designs: Lead 3389 (Medtronic Inc., USA) (Figure 1a) and Lead 6148 (St Jude Medical Inc., USA) (Figure 1b). 2D axisymmetric FEM models were developed using COMSOL Multiphysics Version 4.3a (Comsol Multiphysics AB, Sweden). The geometry of the leads is based on the manufacturers' respective technical specifications and consists in four platinum iridium alloy (Pt/Ir) contacts separated by 0.5 mm of insulation. The contacts are 1.5 mm long except for Lead 6148's distal contact which is 3 mm long and covers the tip of the lead. The diameter of Lead 3389 is 1.27 mm while it is 1.4 mm for Lead 6148 (Figure 1). The brain tissue surrounding the lead was modelled as a homogeneous and isotropic medium in a rectangular shape (60 mm × 56 mm), with electrical conductivity and relative permittivity corresponding to grey matter (σ=0.09 S/m and ∈=3.9 × 106 [31]). A PES of 250 μm was added to the models in order to mimic the interface between the electrode and the brain tissue at two different time points post DBS-implantation. For the acute stage, which simulates the leakage of extracellular fluid provoked immediately after leads insertion, the electrical conductivity and relative permittivity were set to values corresponding to cerebral spinal fluid (CSF) σ=2 S/m and ∈=109 respectively [31]. The chronic stage, where fibrous tissue covers the electrode surface a few weeks after surgery, was mimicked by using σ=0.06 S/m and ∈=1.7 × 106 instead for the PES [32].

Governing equation and boundary conditions

The boundary conditions for the leads were set in accordance with a monopolar configuration which considers the active contact as the cathode, and the outer boundaries of the tissue as the anode representing the ground from the impulse generator. The boundary for the active contact was set as either a voltage or current ideal source. The non-active contacts were assigned to floating potential [26,33] and the spaces between the contacts were set as electric insulation. The electric field was measured at different points in front of the lead using different mesh densities and stimulated region sizes in order to assure that neither the chosen boundaries of the stimulation region nor the mesh density affected the electric field value. The mesh applied was set to the finest resolution available with a denser distribution of elements around the leads. This corresponded to 28297 elements with a minimum element size of 0.0012 mm and an average element quality of 0.9824. The simulations were performed using electric currents physics interface which is able to model electric currents in conductive media; the electric field distribution around the DBS electrode was obtained

Figure 1: 2D axisymmetric models of Lead 3389 (a) and Lead 6148 (b) surrounded by homogeneous and isotropic medium representing grey matter and a 250 μm thick peri-electrode space (PES).

using the COMSOL MUltifrontal Massively Parallel sparse direct Solver (MUMPS). The electric field generated is calculated using the equation of continuity for steady currents:

$$\nabla \bullet J = -\nabla \bullet (\sigma \nabla V) = 0 \ [A/m^3] \quad (1)$$

Where $\nabla \bullet$ is the divergence, J the current density, ∇ the gradient, V the electric potential and σ the electrical conductivity. More details regarding the modelling and simulation principle can be found in [18,21,34].

Simulations

Two investigations were performed. The first included both leads under voltage controlled stimulation (leads comparison). In this setting simulations (n=32) were performed for acute and chronic scenarios for both leads using the first (lower) and the third (second upper) contacts. The stimulation amplitudes applied were 1 - 4 V in steps of 1 V. For the second examination only one of the leads (3389) was considered using both voltage and current controlled stimulation (operating modes comparison). Equivalent current values capable to generate exactly the same EF distribution as the voltage stimulation i.e. 1, 2, 3, 4 V were found by performing a parametric sweep from 0.8 to 10 mA in steps of 0.1 mA (n=204).

Data analysis

The EF was visualized and analysed using an isolevel of 0.2 V/mm [22,24,27]. The maximum EF extension of this isolevel was measured for all voltage simulations and plotted against the respective lead and contact. A fixed amplitude of 3 V was used to present the results and for further investigation of the electric field's shape, extension and intensity between leads. The EF intensity was measured by placing 16 evaluation points parallel to the leads with a separation of 0.5 mm between each other. This measurement was performed at 1, 3 and 5 mm from the leads' surface. Equivalent current amplitudes for Lead 3389, resulting in the same EF distribution and shape as obtained with 1, 2, 3 and 4 V under chronic conditions, were extracted. This was achieved displaying both types of stimulation isolevels simultaneously, and comparing them visually at each stimulation amplitude. The current value which isolevel overlapped the isolevel for voltage stimulus was considered the equivalent current amplitude.

Results

Leads comparison

In Figure 2 the distribution of the EF around the active contacts is presented for Lead 3389 (Figure 2a and 2b) and Lead 6148 (Figure 2c and 2d) as simulated for 3V, a PES of 250 μm under acute and chronic conditions. The shape and maximal extension of the EF considerably differed between the two simulated time points for all currents. At the acute stage, the EF was broadened below the tip in both leads regardless of the active contact. At the chronic stage, the EF was also distributed below the tip for Lead 6148 (Figure 2c and 2d). The maximum EF extension was about 1 mm greater at the acute time point compared to chronic conditions. Plots of the maximum EF extension as related to the four voltage stimulation amplitudes are presented in Figure 3 for each lead and contact.

Figure 4 presents the electric field intensity measured for 3 V at 1 mm from the contact surface. The evaluation was performed for both leads under the two tissue scenarios. The intensity at the acute stage was approximately 0.1 V/mm larger. Both leads presented the highest EF
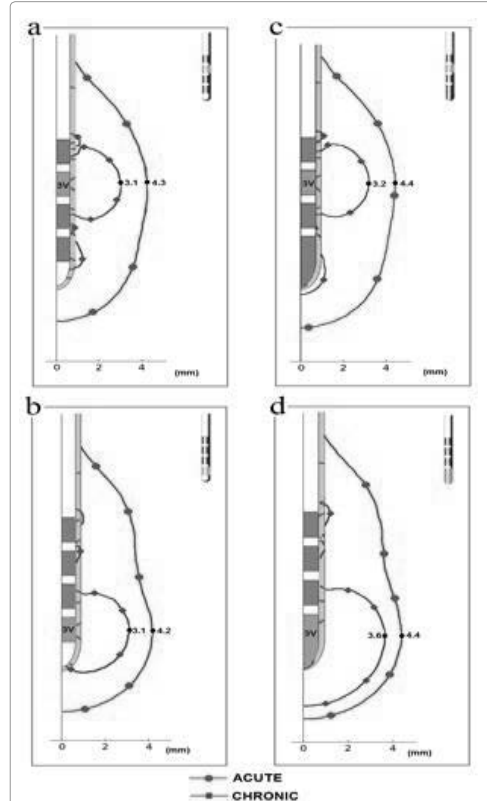
Figure 2: Electric field isolevels (0.2 V/mm) obtained for voltage controlled stimulation (3 V) under acute and chronic conditions (red and blue lines respectively). Maximum EF extension shown in mm for each isolevel. Simulations performed with Lead 3389 (a and b) and Lead 6148 (c and d), using the third (a and c) and the first (b and d) contact as the active electrode.

intensity in front of the middle of the active contact. Similar behavior was found at the 3 and 5 mm distant evaluation points.

Operating modes comparison

Table 1 presents the equivalent current amplitude values to the commonly used voltage values for both contacts, leads and the two different PES. The PES corresponding to the acute stage, required higher current stimulation settings in order to obtain the same electric field distribution as when using voltage controlled stimulation. As an example, equivalent EFs for 3 V were found with 7 mA (acute) and 2.2 mA (chronic) stimulation. Figure 5 presents a comparison of the EF isolevels using 3 V and 2.2 mA for both postoperative time points for Lead 3389. The electric field isolevels perfectly overlap in the chronic scenario (Figure 5c and 5d). In the acute stage, however, which has an impedance in the PES radically different from the surrounding grey

Figure 3: Relation between the maximum electric field extension and the voltage amplitudes for the third and first contacts of Lead 3389 (a and b) and Lead 6148 (c and d). Measurements obtained from simulations under acute and chronic conditions (red and blue lines respectively).
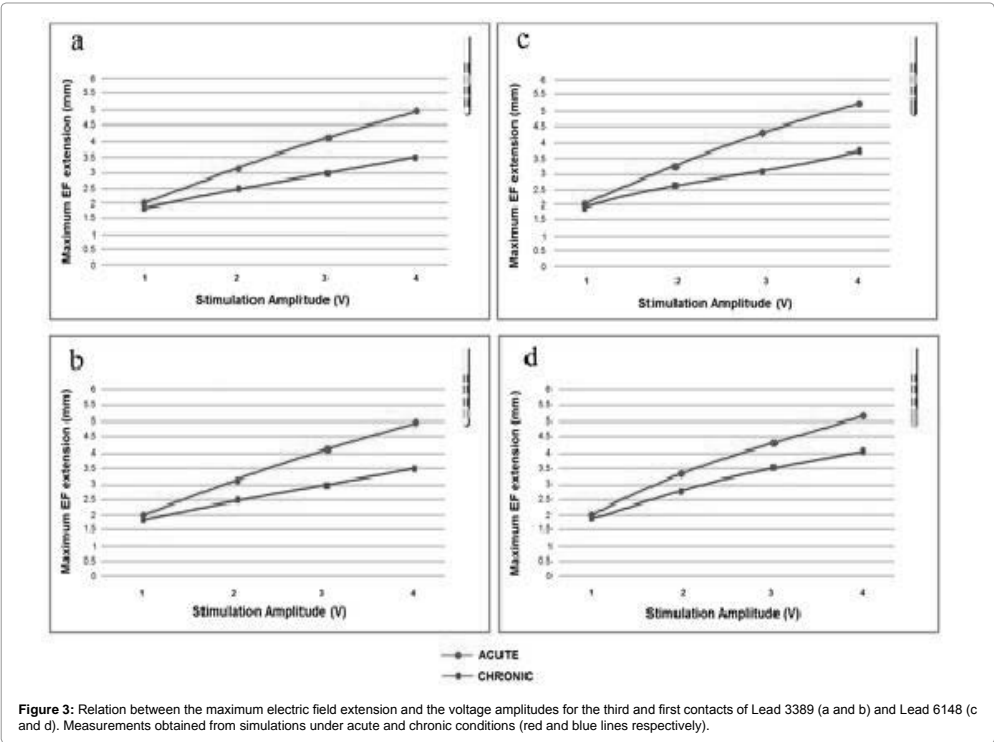
Voltage Stimulation Amplitude (V)	Equivalent Current Stimulation Amplitude (mA)			
	Acute		Chronic	
	LEAD 3389	LEAD 6148	LEAD 3389	LEAD 6148
	Third/First Contact	Third/First Contact	Third/First Contact	Third/First Contact
1	2.3/2.3	2.3/2.4	0.7/0.7	0.7/1.1
2	4.5/4.5	4.5/4.7	1.5/1.5	1.5/2.2
3	7.0/7.0	7.0/7.1	2.2/2.2	2.3/3.2
4	9.0/9.0	9.0/9.5	2.9/2.9	3.0/4.3

Table 1: Current amplitude values for the third and first contacts with the best match to the commonly clinically used voltage amplitudes for Lead 3389 and Lead 6148 at two post-implantation stages.

matter a significant change in EF in both voltage and current modes is seen for both active contacts. The electric field is spread along the lead (Figure 5a and 5b). Compared to the chronic stimulation the electric field is also extending about 1 mm further away in voltage mode and about 1mm shorter in current mode (Figure 5a and 5b). Figure 6 shows the relation between the maximum EF extension and the stimulation amplitudes for both current and voltage stimulations. For current controlled stimulation the EF extension increases in steps of about 0.5 mm for both time points. In voltage mode the EF extension had a higher increase with amplitude at the acute stage (Figure 6a and 6b). The EF intensities measured for voltage and current controlled stimulation are presented in Figure 7. The intensity obtained at the acute stage for current control (Figure 7c and 7d) is lower (0.6 V/mm) than for voltage stimulation regardless of the contact used.

Discussion

In this computer simulations study the influence on the electric field from two different DBS-lead designs both operating in voltage and current modes have been compared. In order to mimic realistic time points, crucial in the postoperative DBS management, the impedance in the space around the electrodes was varied at the same time as grey matter was assumed as target tissue. For typical amplitudes used in the clinic, the simulations showed electric field extensions ranging from 2 to 5 mm which is in agreement with other studies [35].

Leads comparison

New DBS-lead designs are presently introduced in health care, and it is therefore imperative to increase the clinical knowledge about similarities and differences between different lead configurations. In general, the shape and maximum extension of the electric field were very similar for both leads in voltage mode, especially with a PES mimicking the leakage of extracellular fluid, i.e. the acute stage post implantation. When simulating the chronic time point, however, Lead

Figure 4: Electric field intensity evaluated at 1 mm from the electrode surface under voltage controlled stimulation (3 V). a) Third and b) first contact of Lead 3389 and third and first of Lead 6148 (c and d). Measurements performed for acute and chronic conditions.
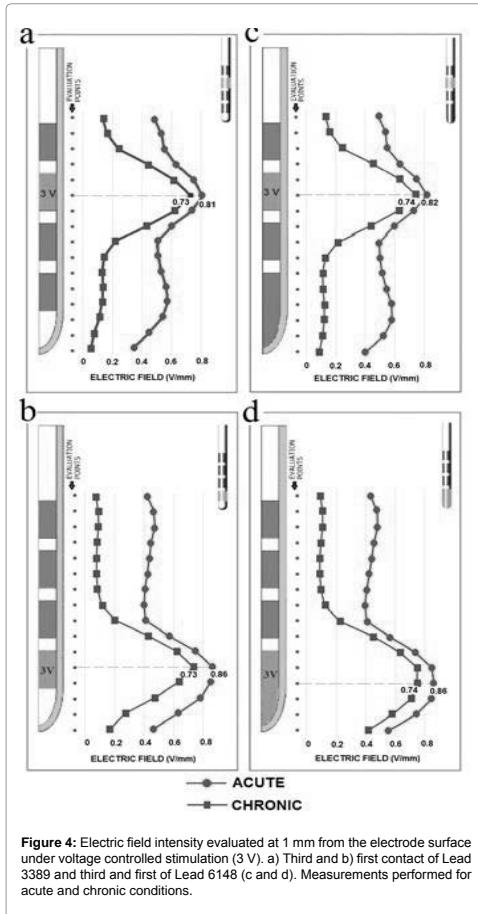
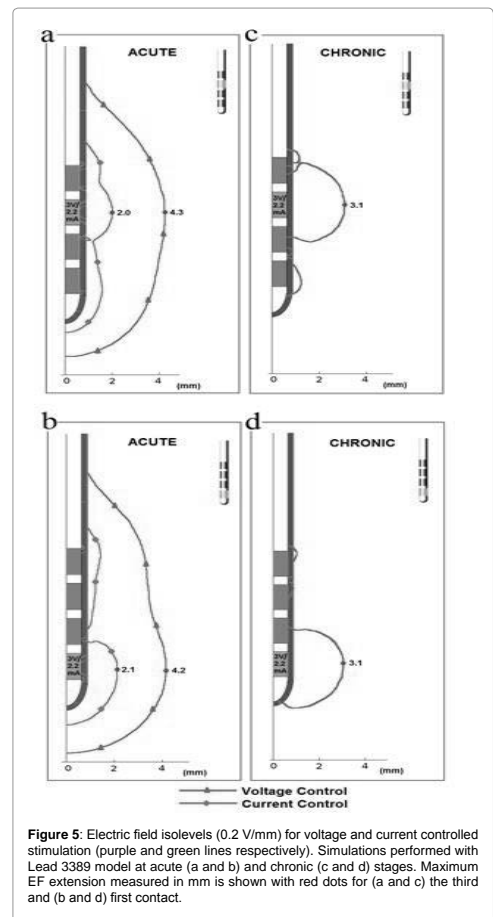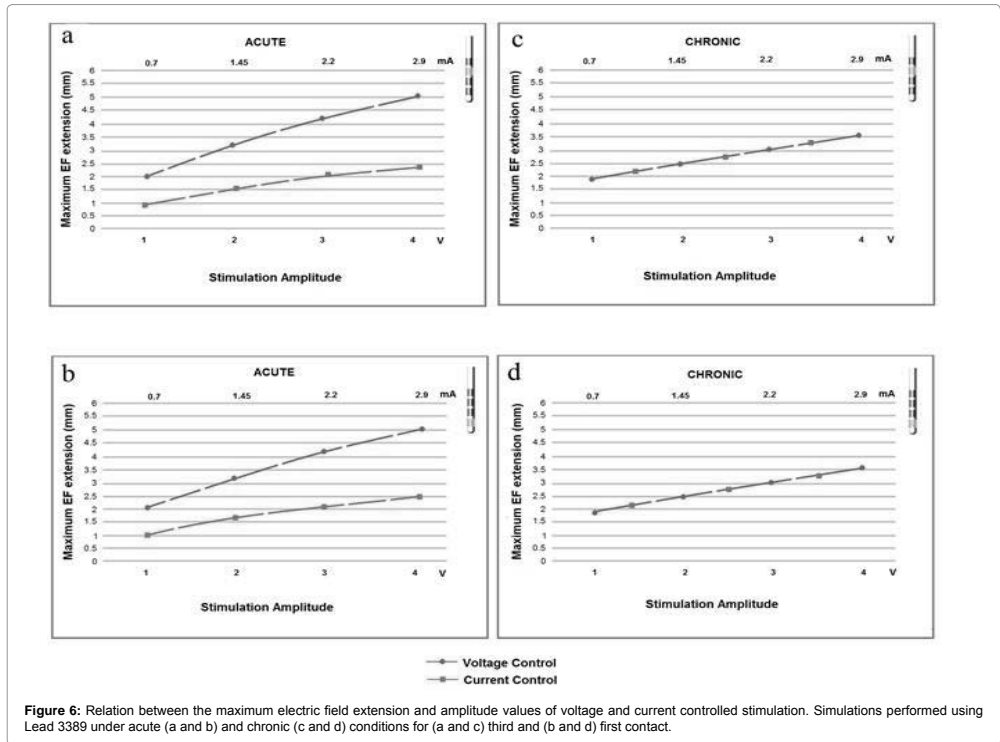6148 exhibited an EF below the tip regardless of the active electrode. This behaviour indicates that additional tissue regions millimetres away from an active contact may be stimulated (Figure 2c and 2d). Lead 6148 is 0.13 mm thicker and its contact at the tip is twice the length hence it has a considerable larger area. While Lead 3389 required the same current amplitude regardless of the active contact, Lead 6148 needed a higher current to achieve the same EF when using the tip contact. For instance, the equivalent current amplitude for 3 V was 2.3 mA using the third contact but 3.2 mA for the first (Table 1). A larger contact reduces the current density and consequently the current applied has to be increased to achieve the same electric field.

Operating mode

Simulations showed that in voltage mode the EF extension is

significantly enlarged when the PES has a lower impedance (higher conductivity) that the surrounding tissue as in the acute time point (Figure 5a and 5b). An explanation could be that due to the lower impedance the energy is not maintained in the PES but delivered further away i.e. similarly to a voltage divider between the PES and surrounding tissue compartments. A similar behaviour of the electric field was shown for FEM-simulated CSF-filled cystic cavities i.e. perivascular Virchow-Robin spaces, sometimes appearing in the pallidum [18]. On the contrary, in current mode a lower impedance in the PES reduces the voltage in that region in order to maintain the same current therefore shortening the EF based on Ohm's law. This behaviour is consistent with the results of the EF intensity (Figure 7) and with the corresponding adjustment of the current amplitude values shown in Table 1. These results can be compared with the postoperative adjustment of the stimulation amplitude commonly done within a

Figure 5: Electric field isolevels (0.2 V/mm) for voltage and current controlled stimulation (purple and green lines respectively). Simulations performed with Lead 3389 model at acute (a and b) and chronic (c and d) stages. Maximum EF extension measured in mm is shown with red dots for (a and c) the third and (b and d) first contact.

Figure 6: Relation between the maximum electric field extension and amplitude values of voltage and current controlled stimulation. Simulations performed using Lead 3389 under acute (a and b) and chronic (c and d) conditions for (a and c) third and (b and d) first contact.

few weeks following DBS implantation in Parkinson's disease [36]. Furthermore, the EF extension at 0.2 V/mm obtained at different stimulation amplitudes (Figure 6) at chronic stage is comparable with the clinical neurophysiological stimuli-response studies which suggest a linear correlation between a stimulation threshold and distance, i.e. 3 mA corresponds to 3 mm [35,37,38]. In vivo studies [9] and a recent review by Bronstein et al. [8] suggest the use of current controlled DBS systems based on their low susceptibility to the conductivity of the brain.

Peri-electrode space thickness

The thickness and change over time of the PES is debatable. Clinical [11] and animal [12] studies have reported, based on in-vivo measurements, that impedance increases following implantation, but that it rapidly decreases again to some extent during clinically relevant stimulation. Post-mortem studies [39,40] have shown that there might be differences in the thickness of this region. Nielsen et al. found a 150 μm thick fibrillary gliosis layer around the electrode tract and Haberler and colleagues a layer less than 500 μm. In addition, these studies showed that the PES differed depending on the brain target investigated. In the present study a PES thickness between the values suggested by Nielsen and Haberler was selected and kept constant for comparative simulations. The selected PES thickness, 250 μm, has also been used in

previous simulation studies by Yousif et al. [30]. In order to investigate the influence from the PES thickness additional simulations (n=12) were performed for PES of 125 μm, 250 μm and 500 μm at 3 V with the acute and chronic tissue settings using the third contact active for Lead 3389. By changing the PES thickness in the simulations it was found that there is a small (≤ 0.3 mm) influence on the electric field (Table 2) when the thickness was doubled. The difference was more pronounced at the acute stage when the electric conductivity was set to CSF. By keeping as many parameters as possible constant, we could compare the leads and stimulation modes for a range of amplitudes and different post-operative mimicked tissue conditions [17,41,42]. Relative comparisons were possible by using a fixed EF isolevel, here set to 0.2 V/mm. This isolevel has been used in several previous investigations [22,24,27] and it has also been pointed out as a possible predictor of neural activation [29].

To gain more detailed knowledge about DBS and tissue interaction, future models and simulations could be made more complex, both regarding simulation of the PES, and by using patient-specific information e.g. from MRI and diffusion tensor imaging as input [21,22]. Simulations can also be combined with axon cable models for increased knowledge of the influence from various axon diameter, as well as pulse width of the DBS-systems [29,43]. It should, however, be stressed that model based studies always contain simplifications of

PES thickness (µm)	Distance from electrode surface (mm)			
	Voltage control		Current control	
	Acute	Chronic	Acute	Chronic
125	4.0	3.1	2.4	3.3
250	4.3	3.1	2.3	3.3
500	4.6	3.0	2.0	3.3

Table 2: Distance (mm) reached from electrode surface by the electric field isolevel of 0.2 V/m for different thicknesses peri-electrode space (PES) and Lead 3389 using the third contact. Simulations were done with 3V and 2.5 mA for equivalent electric fields.
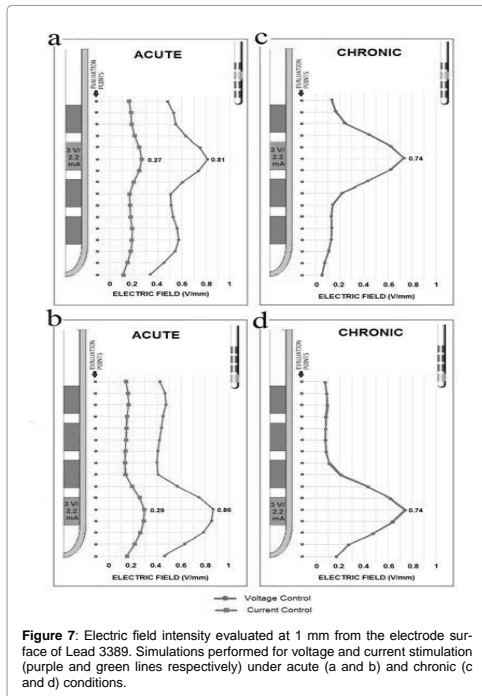
Figure 7: Electric field intensity evaluated at 1 mm from the electrode surface of Lead 3389. Simulations performed for voltage and current stimulation (purple and green lines respectively) under acute (a and b) and chronic (c and d) conditions.

real clinical situations [42], but nevertheless can serve as a guide for increased understanding of electric field spread in different clinical situations and comparisons between different leads, tissue conditions and stimulation modes.

Conclusions

FEM-simulations of the electric field in voltage and current modes for two DBS lead-designs have been performed at different time-points following implantation. The results show a significant influence from the peri-electrode space at the acute time point when impedance was lower (higher conductivity) than surrounding grey matter. In voltage mode, the electric field was broadened while in current mode shortened. These results can help to clarify the postoperative adjustments of the DBS-amplitudes often necessary a few weeks after implantation. The lead designs showed no relevant difference in the maximal electric

field extension, nevertheless due to a larger contact at its tip, Lead 6148 spread the electric field below the lead at all stages independent of the active contact. This behaviour suggests a careful planning and parameter selection in order to achieve a predefined electric field magnitude and shape.

References

1. Hemm S, Wårdell K (2010) Stereotactic implantation of deep brain stimulation electrodes: a review of technical systems, methods and emerging tools. Med Biol Eng Comput 48: 611-624.

2. Åström M, Tripoliti E, Zrinzo L, Martinez-Torres I, Limousin P, et al. (2008) Voltage steering to control deep brain stimulation-induced speech deficits. Acta Neurochirurgica Springer 953-954.

3. Butson CR, McIntyre CC (2008) Current steering to control the volume of tissue activated during deep brain stimulation. Brain Stimul 1: 7-15.

4. Martens HC, Toader E, Decré MM, Anderson DJ, Vetter R, et al. (2011) Spatial steering of deep brain stimulation volumes using a novel lead design. Clin Neurophysiol 122: 558-566.

5. Liu HG, Ma Y, Zhang K, Ge M, Meng FG, et al. (2013) Subthalamic deep brain stimulation with a new device in Parkinson's disease: an open-label trial. Neuromodulation 16: 212-218.

6. Ramirez de Noriega F, Eitan R, Marmor O, Lavi A, Linetzky E, et al. (2015) Constant Current versus Constant Voltage Subthalamic Nucleus Deep Brain Stimulation in Parkinson's Disease. Stereotact Funct Neurosurg 93: 114-121.

7. Lettieri C, Rinaldo S, Devigili G, Pisa F, Mucchiut M, et al. (2015) Clinical outcome of deep brain stimulation for dystonia: constant-current or constant-voltage stimulation? A non-randomized study. Eur J Neurol 22: 919-926.

8. Bronstein JM, Tagliati M, McIntyre C, Chen R, Cheung T, et al. (2015) The rationale driving the evolution of deep brain stimulation to constant-current devices. Neuromodulation 18: 85-88.

9. Lempka SF, Johnson MD, Miocinovic S, Vitek JL, McIntyre CC (2010) Current-controlled deep brain stimulation reduces in vivo voltage fluctuations observed during voltage-controlled stimulation. Clin Neurophysiol 121: 2128-2133.

10. Farris S, Vitek J, Giroux ML (2008) Deep brain stimulation hardware complications: the role of electrode impedance and current measurements. Mov Disord 23: 755-760.

11. Hemm S, Vayssiere N, Mennessier G, Cif L, Zanca M, et al. (2004) Evolution of Brain Impedance in Dystonic Patients Treated by GPi Electrical Stimulation. Neuromodulation 7: 67-75.

12. Lempka SF, Miocinovic S, Johnson MD, Vitek JL, McIntyre CC (2009) In vivo impedance spectroscopy of deep brain stimulation electrodes. J Neural Eng 6: 046001.

13. Satzer D, Lanctin D, Eberly LE, Abosch A (2014) Variation in deep brain stimulation electrode impedance over years following electrode implantation. Stereotact Funct Neurosurg 92: 94-102.

14. Simpson J, Ghovanloo M (2007) An Experimental Study of Voltage, Current, and Charge Controlled Stimulation Front-End Circuitry in IEEE International Symposium on Circuits and Systems. ISCAS, New Orleans.

15. Butson CR, McIntyre CC (2005) Tissue and electrode capacitance reduce neural activation volumes during deep brain stimulation. Clin Neurophysiol 116: 2490-2500.

16. Grant PF, Lowery MM (2010) Effect of dispersive conductivity and permittivity in volume conductor models of deep brain stimulation. IEEE Trans Biomed Eng 57: 2386-2393.

17. Schmidt C, Grant P, Lowery M, van Rienen U (2013) Influence of uncertainties in the material properties of brain tissue on the probabilistic volume of tissue activated. IEEE Trans Biomed Eng 60: 1378-1387.

18. Astrom M, Johansson JD, Hariz MI, Eriksson O, Wårdell K (2006) The effect

of cystic cavities on deep brain stimulation in the basal ganglia: a simulation-based study. J Neural Eng 3: 132-138.

19. Aström M, Lemaire JJ, Wårdell K (2012) Influence of heterogeneous and anisotropic tissue conductivity on electric field distribution in deep brain stimulation. Med Biol Eng Comput 50: 23-32.

20. Butson CR, Cooper SE, Henderson JM, McIntyre CC (2007) Patient-specific analysis of the volume of tissue activated during deep brain stimulation. Neuroimage 34: 661-670.

21. Aström M, Zrinzo LU, Tisch S, Tripoliti E, Hariz MI, et al. (2009) Method for patient-specific finite element modeling and simulation of deep brain stimulation. Med Biol Eng Comput 47: 21-28.

22. Åström M, Tripoliti E, Hariz MI, Zrinzo LU, Martinez-Torres I, et al. (2010) Patient-specific model-based investigation of speech intelligibility and movement during deep brain stimulation. Stereotact Funct Neurosurg 88: 224-233.

23. Chaturvedi A, Butson CR, Lempka SF, Cooper SE, McIntyre CC (2010) Patient-specific models of deep brain stimulation: influence of field model complexity on neural activation predictions. Brain Stimul 3: 65-67.

24. Hemm S, Mennessier G, Vayssiere N, Cif L, Fertit HE, et al. (2005) Deep brain stimulation in movement disorders: stereotactic coregistration of two-dimensional electrical field modeling and magnetic resonance imaging. J Neurosurg 103: 949-955.

25. Vasques X, Cif L, Hess O, Gavarini S, Mennessier G, et al. (2009) Stereotactic model of the electrical distribution within the internal globus pallidus during deep brain stimulation. J Comput Neurosci 26: 109-118.

26. Wårdell K, Zrinzo L, Hariz M, Andersson M (2013) Patient-Specific Brain Modelling for Deep Brain Stimulation Simulation in 6th International IEEE EMBS Conference on Neural Engineering proceedings 148-151.

27. Wårdell K, Kefalopoulou Z, Diczfalusy E, Andersson M, Åström M, et al. (2015) Deep brain stimulation of the pallidum internum for gilles de la tourette syndrome: a patient-specific model-based simulation study of the electric field. Neuromodulation 18: 90-96.

28. Kuncel AM, Cooper SE, Grill WM (2008) A method to estimate the spatial extent of activation in thalamic deep brain stimulation. Clin Neurophysiol 119: 2148-2158.

29. Åström M, Diczfalusy E, Martens H, Wårdell K (2015) Relationship between Neural Activation and Electric Field Distribution during Deep Brain Stimulation. IEEE Trans Biomed Eng 62: 664-672.

30. Yousif N, Bayford R, Bain PG, Liu X (2007) The peri-electrode space is a significant element of the electrode-brain interface in deep brain stimulation: a computational study. Brain Res Bull 74: 361-368.

31. Andreuccetti D, Fossi R, Petrucci C (2005) Dielectric properties of the tissue. Italian National Research Council, Institute for Applied Physics, Florence, Italy.

32. Yousif N, Bayford R, Liu X (2008) The influence of reactivity of the electrode-brain interface on the crossing electric current in therapeutic deep brain stimulation. Neuroscience 156: 597-606.

33. Schmidt C, van Rienen U (2012) Modeling the field distribution in deep brain stimulation: the influence of anisotropy of brain tissue. IEEE Trans Biomed Eng 59: 1583-1592.

34. Wårdell K, Diczfalusy E, Åström M (2011) Patient-Specific Modeling and Simulation of Deep Brain Stimulation. Studies in Mechanobiology, Tissue Engineering and Biomaterials 9: 357-375.

35. Nossek E, Korn A, Shahar T, Kanner AA, Yaffe H, et al. (2011) Intraoperative mapping and monitoring of the corticospinal tracts with neurophysiological assessment and 3-dimensional ultrasonography-based navigation. Clinical article. J Neurosurg 114: 738-746.

36. Limousin P, Tisch S (2009) DBS stimulator programming. In: Bain P (ed) Deep brain stimulation, Oxford university press. 65-71.

37. Ohue S, Kohno S, Inoue A, Yamashita D, Harada H, et al. (2012) Accuracy of diffusion tensor magnetic resonance imaging-based tractography for surgery of gliomas near the pyramidal tract: a significant correlation between subcortical electrical stimulation and postoperative tractography. Neurosurgery 70: 283-293.

38. Seidel K, Beck J, Stieglitz L, Schucht P, Raabe A (2013) The warning-sign hierarchy between quantitative subcortical motor mapping and continuous motor evoked potential monitoring during resection of supratentorial brain tumors. J Neurosurg 118: 287-296.

39. Haberler C, Alesch F, Mazal PR, Pilz P, Jellinger K, et al. (2000) No tissue damage by chronic deep brain stimulation in Parkinson's disease. Ann Neurol 48: 372-376.

40. Nielsen MS, Bjarkam CR, Sørensen JC, Bojsen-Møller M, Sunde NA, et al. (2007) Chronic subthalamic high-frequency deep brain stimulation in Parkinson's disease--a histopathological study. Eur J Neurol 14: 132-138.

41. Schmidt C, van Rienen U (2012) Quantification of uncertainties in brain tissue conductivity in a heterogeneous model of deep brain stimulation using a non-intrusive projection approach. Conf Proc IEEE Eng Med Biol Soc 2012: 4136-4139.

42. Howell B, Naik S, Grill WM (2014) Influences of interpolation error, electrode geometry, and the electrode-tissue interface on models of electric fields produced by deep brain stimulation. IEEE Trans Biomed Eng 61: 297-307.

43. McIntyre CC, Mori S, Sherman DL, Thakor NV, Vitek JL (2004) Electric field and stimulating influence generated by deep brain stimulation of the subthalamic nucleus. Clin Neurophysiol 115: 589-595.

PAPER II

Investigation into Deep Brain Stimulation Lead Designs: A Patient-Specific Simulation Study

Fabiola Alonso [1,*], Malcolm A. Latorre [1], Nathanael Göransson [1,2], Peter Zsigmond [2,3] and Karin Wårdell [1]

[1]   Department of Biomedical Engineering, Linköping University, Linköping 58185, Sweden;
       malcolm.latorre@liu.se (M.A.L.); Nathanael.Goransson@regionostergotland.se (N.G.);
       karin.wardell@liu.se (K.W.)
[2]   Department of Neurosurgery, Linköping University Hospital, Region Östergötland, Linköping 58185,
       Sweden; Peter.Zsigmond@regionostergotland.se
[3]   Department of Clinical and Experimental Medicine, Linköping University, Linköping 58185, Sweden
[*]   Correspondence: fabiola.alonso@liu.se; Tel.: +46-101-030-000

Abstract: New deep brain stimulation (DBS) electrode designs offer operation in voltage and current mode and capability to steer the electric field (EF). The aim of the study was to compare the EF distributions of four DBS leads at equivalent amplitudes (3 V and 3.4 mA). Finite element method (FEM) simulations (n = 38) around cylindrical contacts (leads 3389, 6148) or equivalent contact configurations (leads 6180, SureStim1) were performed using homogeneous and patient-specific (heterogeneous) brain tissue models. Steering effects of 6180 and SureStim1 were compared with symmetric stimulation fields. To make relative comparisons between simulations, an EF isolevel of 0.2 V/mm was chosen based on neuron model simulations (n = 832) applied before EF visualization and comparisons. The simulations show that the EF distribution is largely influenced by the heterogeneity of the tissue, and the operating mode. Equivalent contact configurations result in similar EF distributions. In steering configurations, larger EF volumes were achieved in current mode using equivalent amplitudes. The methodology was demonstrated in a patient-specific simulation around the zona incerta and a "virtual" ventral intermediate nucleus target. In conclusion, lead design differences are enhanced when using patient-specific tissue models and current stimulation mode.

Keywords: deep brain stimulation (DBS); steering; patient-specific; electric field; finite element method; neuron model; brain model; zona incerta (ZI); electrode design

1. Introduction

Deep brain stimulation (DBS) is an established technique to alleviate the symptoms caused by several movement disorders such as Parkinson's disease and essential tremor. DBS is now also expanding towards other symptoms such as psychiatric illness [1]. The technique has been proven to be successful even though the mechanisms of action are still uncertain, which makes it difficult to have complete control on the desired effect and avoid side effects.

Traditionally, DBS systems have operated in voltage mode using conventional ring-shaped electrodes generating a symmetrical stimulation field around the lead. Recently, new electrode designs offer the capability to steer the stimulation field allowing some compensation for a possible lead misplacement [2,3]. The operating mode has also been modified delivering current instead of voltage stimulation. Current controlled systems, in comparison to voltage, automatically adjust the voltage to changes in the surrounding tissue impedance, in order to deliver a constant current [4]. Brain tissue is an electrically conductive medium in which the distribution of the electric field (EF) can be calculated

and visualized with computer models that solve the corresponding differential equation. In this study, the finite element method (FEM) has been used to evaluate and compare the EF from four different leads used in DBS systems.

Numerous computational models have been used to predict and visualize the first derivative of the electric potential, i.e., the EF [5–8] or the second derivative of the electric potential generated by DBS systems [9,10]. However, these are usually employed using traditional leads with voltage control operating mode. We have previously compared the conventional leads *Medtronic 3389* and *St. Jude Medical 6148* in different operating modes and time points [11]. Other simulations studied the influence from heterogeneity and anisotropy for the 3389 lead [12,13]. This study extends the comparisons to include two steering field leads, *St. Jude Medical 6180* and *Medtronic SureStim1*. When comparing FEM simulations, a fixed isolevel EF has been useful in making relative simulation comparisons for the 3389 lead [5,6,8]. In a previous study [14], neuron model simulations were run for a range of stimulation amplitudes, pulse lengths and axon diameters. These settings and physiological parameters should be taken into account in the choice of isolevel.

The aim of the study was to compare four DBS lead EF distributions in both voltage and current modes as presented in homogenous and heterogeneous, i.e., patient-specific, tissue models for the zona incerta (ZI) and the ventral intermediate nucleus (VIM) brain targets. Furthermore, steering effect simulations were investigated and compared with conventional 3389 lead EF. Visualization of the 3389 EF for the implanted ZI target with the patient-specific stimulation settings was demonstrated.

2. Materials and Methods

2.1. Patient Data, Surgery and Imaging

DBS data and images from one patient with tremor dominant Parkinson's disease implanted in the ZI at the Department of Neurosurgery, Linköping University Hospital were included in the study. An additional "virtual target", VIM, along the planned trajectory was used for the simulations. Informed written consent was received from the patient and the study was approved by the local ethics committee in Linköping (2012/434-31).

Prior to surgery and under general anaesthesia, the Leksell Stereotactic System (G frame, Elekta Instrument AB, Linköping, Sweden) was attached. Thereafter, a 3 Tesla, T2-weigthed magnetic resonance imaging (MRI) Philips Intera, Eindhoven, The Netherlands) with 2 mm contiguous axial slices ($2 \times 0.5 \times 0.5$) mm^3 was performed. Direct anatomical targeting was planned using Surgiplan$^®$ (Elekta Instrument AB). Surgery followed the routine protocol [15] for DBS implantation and was completed in a single procedure. The probe's position was verified by intraoperative fluoroscopy (Philips BV Pulsera, Philips Medical Systems, Eindhoven, The Netherlands). A postoperative computer tomography (CT) was performed to confirm the lead's positioning the day after surgery, and a second CT was taken after 4.5 weeks (chronic time point). These CT images were separately co-registered with the preoperative MRI using Surgiplan$^®$. From the postoperative image artefacts, the surgeon noted the Leksell$^®$ coordinates (x, y, z) of a point at the lowest contact and another reference point 10 mm above the AC-PC line along the lead axis. These coordinates were used to place the lead within the brain model. The electrode position at the chronic time point was considered for the simulations in this study. The Leksell$^®$ coordinates for ZI and VIM targets were also identified for simulations.

2.2. FEM Modelling and Simulation

The leads and brain tissue were modelled in the FEM software COMSOL Multiphysics 5.2 (Comsol AB, Stockholm, Sweden).

2.2.1. DBS Leads

The lead geometry was based on the specifications from the corresponding manufacturing companies (Figure 1). Lead 3389 (Medtronic Inc., Minneapolis, MN, USA) and lead 6148 (St. Jude

Medical Inc., Saint Paul, MN, USA) consist of four cylindrical platinum iridium alloy electrodes or contacts separated by 0.5 mm of insulating material. The contacts are 1.5 mm long except for lead 6148's distal contact which is 3 mm long and covers the tip of the lead. The lead 3389 has a diameter of 1.27 mm and a contact surface of 6 mm^2 while lead 6148 is 1.4 mm, with a contact surface area of 6.6 mm^2. The steering lead 6180 (St. Jude Medical Inc., Saint Paul, MN, USA) has the same dimensions as lead 3389 and similar disposition of the contacts except for the two middle contacts which are partitioned axially into three sections; a single segment of the split-ring contact has a surface area of 1.8 mm^2. SureStim1 lead (Medtronic Eindhoven Design Centre BV, Eindhoven, The Netherlands) also has a diameter of 1.27 mm and consists of 40 elliptical contacts of 0.66×0.74 mm^2 arranged on 10 rows of four contacts each, along the lead; each contact surface area is 0.39 mm^2 [2]. The stereotactic coordinates obtained from Surgiplan$^®$ from the co-registered postoperative CT along with the fiducial points of the preoperative MRI were used to calculate the Cartesian coordinates and the angle of the lead for the FEM mode. The first contact of the lead 3389 was placed at the lower point noted by the surgeon; lead 6148 and the steering leads' locations were adjusted to match the middle point of the active contacts.
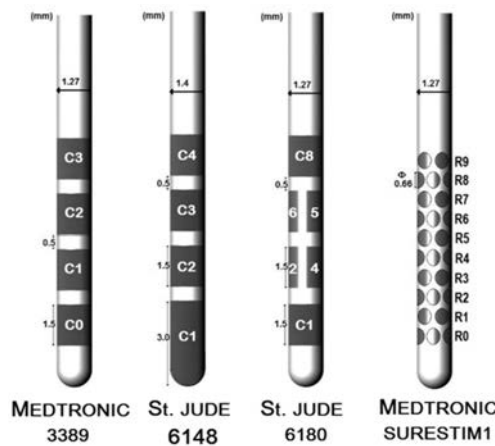
Figure 1. Representation of the conventional and the steering field leads.

2.2.2. Brain Tissue Model

Patient-specific brain tissue models were based on preoperative MRI. An in-house developed program (ELMA) [16,17] was used to convert the medical images into COMSOL FEM software readable files. With the ELMA tool, the preoperative image was cropped to a region of interest (Figure 2a), including the VIM and the ZI. Within that region, the tissue was classified into grey matter, white matter, blood or cerebrospinal fluid based on the image intensity values. Average intensity values were calculated from three slices of the preoperative image set. Finally, the electrical conductivity, σ, was assigned according to grey matter (σ = 0.123 S/m), white matter (σ = 0.075 S/m), blood (σ = 0.7 S/m) and cerebrospinal fluid (σ = 2.0 S/m). The corresponding electric conductivities for each tissue type were obtained from tabulated values [18,19] weighted with the spectral distribution of the pulse shape [20]. The conductivity for each voxel was calculated by an interpolation function which takes into account the effects of partial volumes, thus voxels with intensity levels between grey and white matter receive an electrical conductivity between grey and white matter. The result was a cuboid of about 100 mm per side (Figure 2b) containing the electrical conductivity values for each classified voxel of the preoperative MR image. The model included a peri-electrode space (PES) of 0.25 mm to mimic the electrode–tissue interface at the chronic stage [21]. The electrical conductivity assigned to

the PES corresponded to the white matter assuming its similarity to fibrous tissue (σ = 0.075 S/m) which is believed to wrap around the lead at the chronic stage [22].
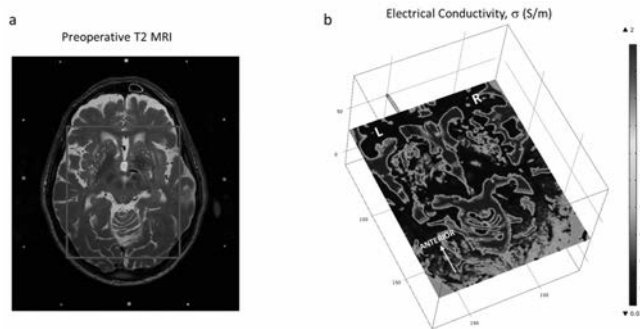
Figure 2. (**a**) Demarcation of the region of interest on the patient T2 MRI dataset (cauda-cranial point of view) and (**b**) Brain model displaying one slice of the interpolated conductivity matrix (cranio-caudal point of view) and the trajectory of the lead. Axial images displayed at the level of the ZI.

The electric field was calculated by the equation for steady currents:

$$\nabla \cdot \boldsymbol{J} = -\nabla \cdot (\sigma \nabla V) = 0 \ (\text{A/m}^3) \tag{1}$$
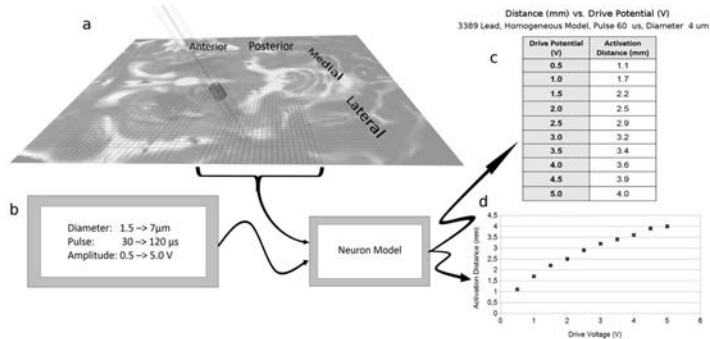
where $\boldsymbol{J}$ is the current density (A/m^2), V is the electric potential (V). For patient-specific models, σ corresponds to the interpolation matrix extracted by ELMA. For the homogeneous model, a single σ value corresponding to grey matter conductivity was considered for the whole brain tissue. The electrodes were set in a monopolar configuration where the active contact is considered as a voltage or current source and the outer boundaries are grounded ($V = 0$ V). For the conventional leads, the third contact (C2 and C3, for Medtronic 3389 and St. Jude 6148 respectively) was active. For SureStim1 eight consecutive electrodes corresponding to ring 6 and 7 were selected, and for the St. Jude 6180 lead the contacts 5, 6, 7 constituting the third ring were active. The active contacts of each lead were driven with either 3 V or 3.4 mA which is the equivalent current amplitude for Medtronic 3389 lead in a homogeneous model (σ = 0.123 S/m). The equivalent stimulation current value was considered as that required to achieve the same electric field to the one obtained with voltage control [11]. The inactive contacts were set to floating potential ($\int -\boldsymbol{n} \cdot \sigma \nabla V dS = 0 \ (A)$; $\boldsymbol{n} \times (-\nabla V) = 0 \ (V/m)$) and the non-conductive surfaces of the lead were set to electric insulation ($\boldsymbol{n} \cdot \nabla V = 0 \ (V/m)$) where $\boldsymbol{n}$ is the surface normal vector. The mesh applied was physics-controlled with a denser distribution around the leads. The mesh was set to the finest resolution available resulting in more than 2,000,000 tetrahedral elements (minimum element size of 0.026 mm). For the steering configuration, a single contact (C5) was selected for lead 6180 while for lead SureStim1, four contacts in a diamond configuration (two adjacent contacts from ring 6 and one contact from ring 5 and 7 anteriorly oriented) were active. The 3D models with ~3 million degrees of freedom were solved using the iterative COMSOL built-in conjugate gradients solver.

2.3. Neuron Model Simulations

An axon cable model was used in combination with the FEM model. A complete description of the neuron model is found in Åström et al. 2015 [14]. FEM modelling was completed for each lead design (*n* = 16) with a stimulation amplitude of 1 V or 1 mA for both homogenous and patient-specific brain tissue models for the VIM target. The electric potential was evaluated at the axial plane around the lead's third contact (Figure 3a). The potential lines were extracted from the medial, lateral, posterior and anterior locations from the axial plane. The potential along the 62 parallel lines separated by

0.1 mm was exported and used as input data to the cable model to calculate the neuron activation distances. Simulations (*n* = 832) were performed for a fixed pulse width (60 µs) with variation in amplitudes (0.5–5 V in steps of 0.5 V; and 0.5–5 mA in steps of 0.5 mA) and variation in axon diameters (1.5–7.5 µm in steps of 0.5 µm) (Figure 3b).

Distance (mm) vs. Drive Potential (V)
3389 Lead, Homogeneous Model, Pulse 60 us, Diameter 4 µm

Drive Potential (V)	Activation Distance (mm)
0.5	1.1
1.0	1.7
1.5	2.2
2.0	2.5
2.5	2.9
3.0	3.2
3.5	3.4
4.0	3.6
4.5	3.9
5.0	4.0

Diameter: 1.5 -> 7µm
Pulse: 30 -> 120 µs
Amplitude: 0.5 -> 5.0 V

Neuron Model

Figure 3. Neuron model application and single calculation run. (**a**) The voltage gradient extraction lines generated from FEM (COMSOL) simulation. The posterior lines have been replaced by the real potential values along the lines, as can be seen by the deviation of the line close to the electrode; (**b**) Input to the neuron model and the model block [14]; (**c**) Data points output from the Neuron model for the 3389 lead, with the specific input parameters of FEM output (homogeneous model and 3389 lead), pulse length of 60 µs, and neuronal diameter of 4 µm. The output is the distance from the surface of the lead to the distance where activation no longer happens; (**d**) The graphical implementation of the one data set.

2.4. Electric Field Simulations

FEM simulations of the electric field (*n* = 38) were performed in different stages setting to 3 V or 3.4 mA the third contact or equivalent as previously described. First, homogenous and patient-specific tissue models were investigated solely with lead 3389 (*n* = 6). Patient-specific simulations included two targets, the ZI and the VIM. Secondly, patient-specific models (one for each target, moving the leads accordingly, approximately 4 mm along the trajectory) were used to compare the electric field achieved by the four leads (*n* = 16) for the two operating modes. The patient-specific model of the actual implantation site in ZI was also used to investigate the EF achieved by lead 3389 with the actual stimulation 1.6 V, set four and a half weeks after implantation, which relieved the patient's symptoms. Simulations were also performed for the corresponding equivalent value in current mode (*n* = 4). At last, simulations with steering configurations for lead 6180 and SureStim1 were performed (*n* = 8). For investigation of the steering function, additional simulations (*n* = 4) were performed for St. Jude 6180 and SureStim1 and compared with the Medtronic 3389 lead.

2.5. Data Analysis

The neuron model simulation output is a table of activation distances (mm) which can be presented as plots against the stimulation amplitudes (Figure 3c,d). The average deviation in activation distances between the leads was calculated as mean ± standard deviation (S.D.) for 3 V and 3.4 mA stimulation amplitudes for all axon diameters simulated. An EF isolevel of 0.2 V/mm corresponding to an axon diameter of approximately 4 µm was selected to compare the activation distances between the leads.

The EF isolevel 0.2 V/mm was superimposed on the preoperative 3T MRI, and visualized at the axial, sagittal and coronal planes. The isocontours for each simulation were extracted in order to measure the maximal distance (mm) from the isocontour to the centre of the active electrode. A program in MatLab was developed for this purpose. COMSOL's integration function was used to

calculate the volumes (mm^3) inside the 0.2 V/mm EF isosurfaces for all leads. Relative differences in percentages were calculated for voltage and current control in order to compare the results for (I) homogeneous vs. patient-specific models; (II) 3389 lead vs. leads 6148, 6180 and SureStim1.

3. Results

3.1. Neuron Model Simulations

The selection of an EF isolevel of 0.2 V/mm was supported by the neuron model simulations (Figure 3) for an axonal diameter of 4.0 μm in both homogenous and heterogeneous tissue models (Figure 4a,b).
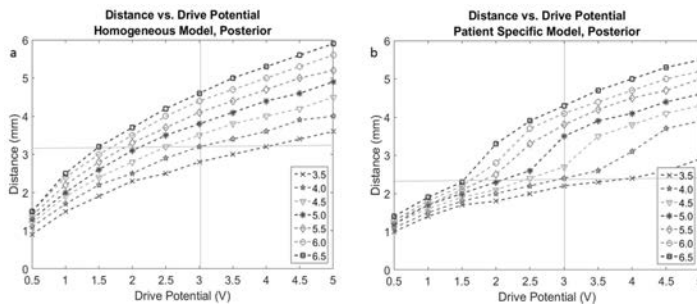
Figure 4. Activation distance plots based on FEM analysis for voltage driven lead 3389 with fixed parameters of 60 μs pulse width, drive potentials range of 0.5 to 5 V, and neuron diameters ranging from 3.5 μm to 6.5 μm. (**a**) Homogeneous tissue model and (**b**) patient-specific tissue model.

Figure 5 presents the activation distances at the posterior direction for all four leads in voltage (Figure 5a,c) and current modes (Figure 5b,d), as well as homogeneous (Figure 5a,b) and patient-specific (Figure 5c,d) brain models. Plots of the other three directions (anterior, lateral, medial) are part of the Appendix A (Figures A1–A3).
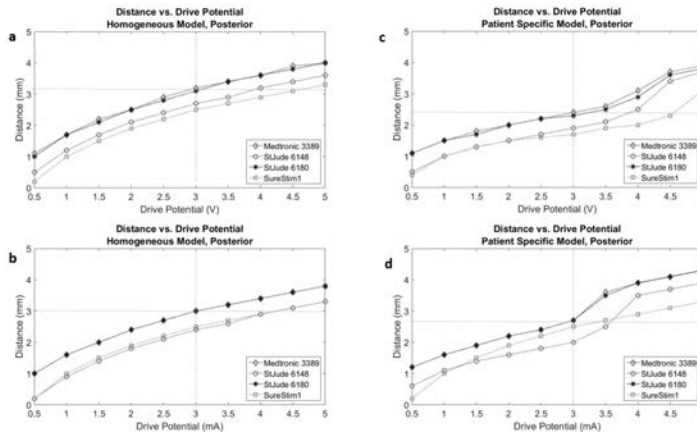
Figure 5. Activation distances for four leads mapped onto a single plot under the same test conditions of 60 μs pulse width, neuron diameter of 4 μm, configuration of all leads in 3389 lead single ring equivalent. (**a**) Homogeneous tissue model with voltage driven electrode; (**b**) Homogeneous tissue model with current driven electrode; (**c**) Patient-specific tissue model with voltage driven electrode; (**d**) Patient-specific tissue model with current driven electrode.

3.2. Homogenous vs. Patient-Specific Models

The electric field around the 3389 lead was compared for homogeneous and patient-specific models at the ZI and the VIM. Figure 6 shows the influence of the heterogeneity of the tissue. The EF extension for homogeneous tissue model was 3.3, 3.6 and 3.4 mm at the axial, sagittal and coronal planes, respectively, while for the patient-specific model the extension varied from 3.3 to 3.9 mm. The average EF distribution was 12% larger in current mode. This was valid for the three directions explored, in both anatomical regions investigated. The EF volumes achieved at the ZI were larger than those at VIM. The volumetric difference between targets (Table 1) was higher in current mode (12%) than in voltage mode (5%).
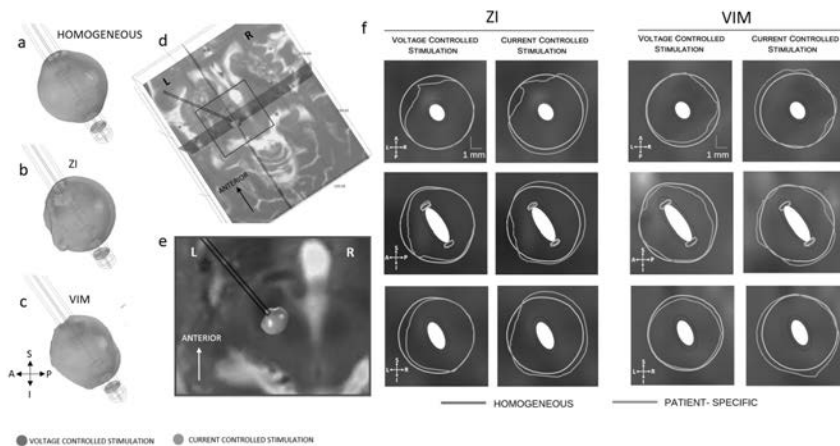
Figure 6. Electric field (EF) distribution (0.2 V/mm) in voltage and current control stimulation mode. (**a**) Homogeneous model (**b**) patient-specific model, ZI and (**c**) VIM; (**d**) Axial, sagittal and coronal cut planes, crossing at the middle point of the active contact (**e**) closer view of the axial plane of the preoperative MRI at the ZI and (**f**) electric field isocontours (0.2 V/mm) of lead 3389 for homogeneous and patient-specific brain models. EF obtained at 3 V (first and third column) and 3.4 mA (second and fourth column). A: anterior, P: posterior, S: superior, I: inferior, L: left, R: right.

Table 1. Homogeneous and patient-specific electric field (EF) volumes (<0.2 V/mm isosurface) achieved with different operating modes and the relative difference between each target and the homogeneous volumes.

Model	Voltage Volumes (mm^3)	Current Volumes (mm^3)	Voltage Difference (%)	Current Difference (%)
HOMOGENEOUS	144	144	0	0
ZI	118.0	177.4	−18.0	22.9
VIM	111.0	160.5	−23.2	11.4

3.3. Lead Comparison

The EF volumes (Figures 7 and 8) within the 0.2 V/mm isosurface were approximately 49% larger for current controlled stimulation than for voltage mode. The relative difference of the EF volumes between the ZI and the VIM are shown in Table 2, for voltage and current controlled stimulation, respectively.

The electric field simulated for the four different lead designs was visualized at axial, sagittal and coronal planes crossing at the centre of each lead in the middle of the active contacts (Figure 9). The maximum extension of the 0.2 V/mm isocontour in voltage mode was achieved with lead 6148

while for current lead SureStim1 presented the largest EF extension. An example of the maximum EF spatial extension at the ZI, measured from the lead axis, is shown in Table 3.
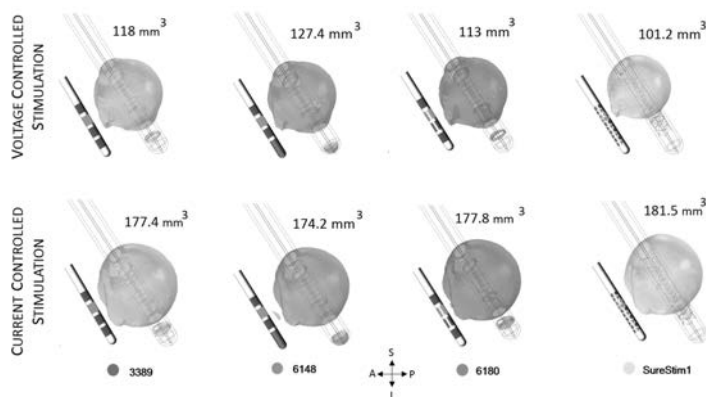
Figure 7. Electric field (EF) simulated at ZI for each lead depicted with an isosurface of 0.2 V/mm. Active contacts (shown in orange in each lead schematic) set to 3 V (first row) and 3.4 mA (bottom row). EF volume within the selected isosurface shown to the right of the lead. A: anterior, P: posterior, S: superior, I: inferior, L: left, R: right.
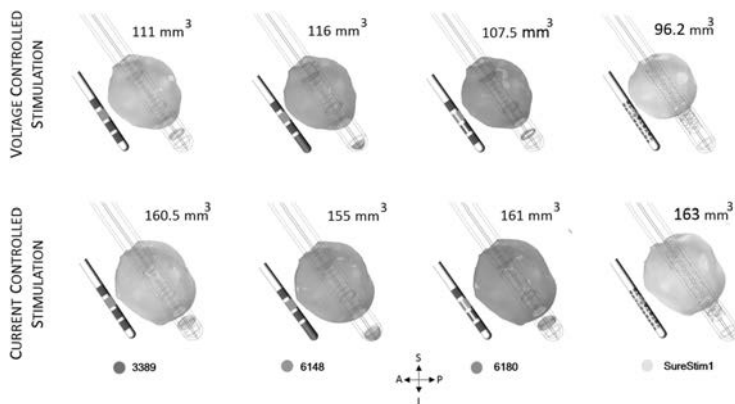
Figure 8. Electric field (EF) simulated at VIM for each lead depicted with an isosurface of 0.2 V/mm. Active contacts (shown in orange in each lead schematic) set to 3 V (first row) and 3.4 mA (bottom row). EF volume within the selected isosurface shown to the right of the lead. A: anterior, P: posterior, S: superior, I: inferior, L: left, R: right.

Table 2. Electric field (EF) volume determined by the 0.2 V/mm isosurface achieved by 3 V and 3.4 mA. Relative difference between the targets calculated for each operating mode.

Lead	ZI (mm^3)		VIM (mm^3)		Relative Difference (%)	
	Voltage	**Current**	**Voltage**	**Current**	**Voltage**	**Current**
3389	118.0	177.4	111.0	160.5	5.9	9.5
6148	127.4	174.2	116.0	155.0	8.9	11.0
6180	113.0	177.8	107.5	161.0	4.9	9.4
SureStim1	101.2	181.5	96.2	163.0	4.9	10.2
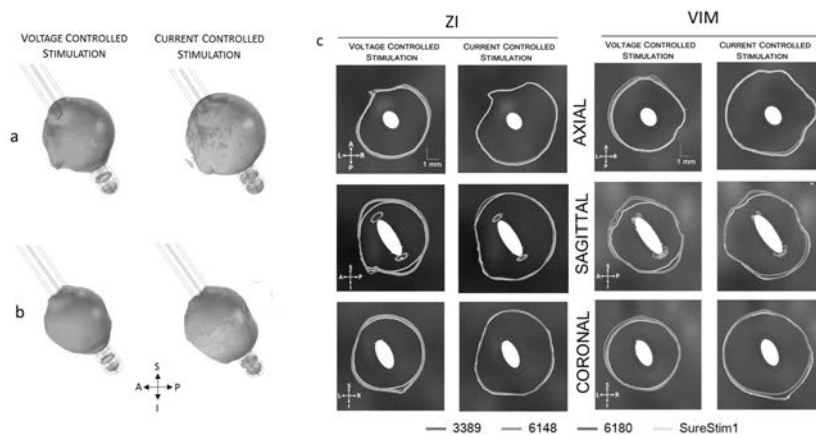
Figure 9. Electric field (EF) 0.2 V/mm isosurfaces achieved by each lead superimposed for each EF distribution of each lead operated in voltage (3 V) and current (3.4 mA). (**a**) EF isosurfaces at ZI in voltage (left) and current (right); (**b**) isosurfaces at VIM for voltage (left) and current (right); (**c**) Isocontours (0.2 V/mm) at the axial, sagittal and coronal planes. The cut planes for visualization were placed at the coordinates of the middle point of the active contacts. A: anterior, P: posterior, S: superior, I: inferior, L: left, R: right.

Table 3. Maximum spatial extension (mm) of the 0.2 V/mm electric field isolevel achieved at each plane for voltage (3 V) and current (3.4 mA) controlled stimulation for all leads. Measurements performed at the ZI.

Plane	3389		6148		6180		SureStim1	
	Voltage	Current	Voltage	Current	Voltage	Current	Voltage	Current
AXIAL	3.34	3.85	3.46	3.84	3.29	3.86	3.23	3.94
SAGITTAL	3.40	3.87	3.50	3.85	3.35	3.90	3.17	3.90
CORONAL	3.50	3.83	3.55	3.80	3.32	3.84	3.23	3.88

3.4. Patient-Specific Stimulation Amplitude Setting

The patient-specific simulation for the ZI using lead 3389, is presented in Figure 10. The equivalent amplitude for the patient-specific voltage of 1.6 V was 1.3 mA in current mode. This value achieved the most similar EF extension (~2.5 mm) and volume (46 mm^3) (Figure 10).
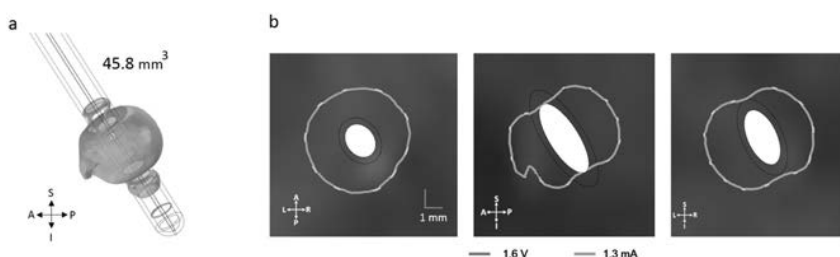
Figure 10. (**a**) Electric field (EF) distribution when the contact is set to 1.6 V and the equivalent current 1.3 mA (superimposed); (**b**) Isocontours for voltage and current superimposed. The maximal EF extent using an isolevel of 0.2 V/mm measured from the middle point of the active contact was 2.5 mm in all planes for both operating modes. A: anterior, P: posterior, S: superior, I: inferior, L: left, R: right.

3.5. Steering Function

The EF volumes within the 0.2 V/mm isosurface and the corresponding isocontours (Figure 11, Table 4) show that the EF distribution was notably different between operating modes for both leads. The spatial extension of the electric field was around 50% smaller in voltage mode. The smaller EF volumes are shown in Figure 11a,b. The axial and coronal views (first and third columns of Figure 11e) show the steering effect on the EF. The large EF distribution achieved by 3.4 mA did not show the steering effect (second and fourth columns of Figure 11e). The diamond configuration used for SureStim1 (1.6 mm^2 surface area) achieved larger EF volume (Figure 11b) than that using one contact of the 6180 lead (1.8 mm^2) for voltage mode. The opposite relation was observed in current mode, where 6180 lead achieved a larger EF volume (Figure 11d).
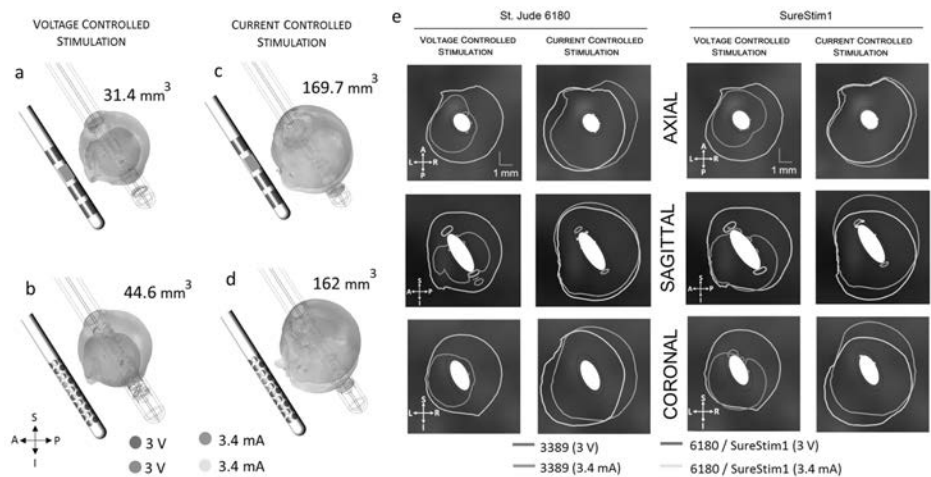
Figure 11. Comparison of the electric field (EF) isosurfaces (0.2 V/mm) at the zona incerta between the standard lead 3389 and the steering leads (active contacts shown in orange in the lead schematic). EF superimposed for lead 3389 (green/orange volumes) and (**a**) lead 6180 contact 5 active; (**b**) SureStim1 lead using the diamond configuration, operated in voltage mode (smaller volumes in blue); (**c**) Lead 6180 and (**d**) SureStim1 setting the contacts to current mode (EF volumes in yellow); (**e**) EF isocontours (0.2 V/mm) at the axial, sagittal and coronal planes for both leads operated in voltage and current mode. A: anterior, P: posterior, S: superior, I: inferior, L: left, R: right.

Table 4. Maximum spatial extension of the 0.2 V/mm electric field isolevel (mm) achieved by steering configurations. Relative difference between operating modes calculated for each lead.

Plane	6180		SureStim1		Relative Difference (%)	
	Voltage	Current	Voltage	Current	6180	SureStim1
AXIAL	2.80	4.18	2.51	3.65	49	45
SAGITTAL	2.92	3.95	3.18	4.46	36	40
CORONAL	2.68	4.54	3.15	4.69	69	49

4. Discussion

In this study, the influence on the electric field around DBS leads, from surrounding tissue and lead design, has been investigated by means of computer simulations. Both symmetrical and steering functions were considered and compared in current and voltage modes.

4.1. FEM and Neuron Modelling

The FEM models in this study have considered constant voltage and current amplitudes instead of the actual biphasic pulse used for the stimulation. This implies a quasi-static solution for the electric potential decoupled from the capacitive, inductive and wave propagation effects. Nevertheless, the conductivity values, for this FEM simulation method, took into consideration the frequency and pulse length components of the stimulation pulse [20]. The comparison of the leads relied on setting as many variables (e.g., isolevel, neuron diameter, pulse width, frequency, tissue variability, time points) to constant values. This results in an evaluation in a fixed environment where the differences in the achieved EF is sufficient to assess the leads. The selection of the 0.2 V/mm isolevel was initially based on previous studies by Hemm et al. [5] and Åström et al. [14]. However, the FEM model used by Åström did not consider the PES and used a homogenous model with a slightly different conductivity value for the grey matter. Therefore, the electric potential lines imported to the neuron model showed minor deviations compared to the previous study. The neuron simulations in the present study indicated that for neurons of 4 μm diameter, a 3 V drive potential reaches an activation distance of 3.2 mm. These results were tested against the FEM simulated EF extensions for one direction and plane, which support the EF isolevel of 0.2 V/mm in the patient-specific model.

Neuron diameter results were in the range of those found in [14,23–25], with consideration for driving parameter variations i.e., pulse width. FEM simulated EF extensions ranged from 3.3 to 3.5 mm in voltage mode. The FEM simulation values would imply a neuronal diameter between 4 and 5 μm. These diameters are at present a best guess at the true neuronal diameters in the vicinity of the electrode and should encompass a range of small diameters. As expected, the activation distance for the patient-specific model is distinct from that of the homogeneous model for all leads (Figures 5 and A1–A3).

A variation of 1 mm in activation distance with the working assumption of a 4 μm diameter neuron would result in an increase in neuron recruitment of approximately 250 extra neurons along a radius. For example, if the activation distance increases by 1 mm from 3 mm, the recruitment volume would change to the power of three, i.e., neuron activation expands significantly. An equivalent decrease in activation distance would result in a possible reduction of activated neurons along any radius from the centre of the volume. Calculating the activation distance in different directions (medial, posterior, anterior, lateral) allowed us to assess the influence of the lead's angle (trajectory) and thus the sensitivity to the direction (Figures 5 and A1–A3).

4.2. Homogeneous vs. Patient-Specific Tissue Models

The initial part of the study encompasses a comparison between homogeneous and patient-specific models for the standard 3389 lead in voltage and current modes. Several studies have shown the impact of the anisotropy and heterogeneity of the brain model. The McIntyre group [17] compared the axonal activation during monopolar DBS for different types of models, and concluded that simplistic models, such as the homogeneous model, overestimate the extent of neural activation. Åström et al. [12] observed an alteration of the electric field when the brain was modelled as heterogeneous isotropic tissue as opposed to homogeneous grey matter. These studies, however, were limited to voltage control stimulation. The novelty of the present study relies on the inclusion of current controlled stimulation. Our results show distinct behavior for each operating mode. The 3389 lead EF volume is smaller for the patient-specific model than for the homogeneous model in voltage mode. In current mode, on the contrary, the volume is larger. Furthermore, when comparing the EF volume between targets, the EF difference is larger in current stimulation (12% vs. 5% for voltage). The interest in using current controlled stimulation [26] partly relies on the consideration that it is the capacitive current that determines the neuronal effect; maintaining a constant current presumably would avoid the reprogramming of the DBS which normally occur for voltage controlled systems due to changes in the tissue impedance around the lead [4]. In agreement, the review by Bronstein et al. [24] considers the stimulation field as the electrical delivery which is a function of the voltage divided by the impedance, i.e., current.

The fundamental difference of this study is that the leads are evaluated in terms of the achieved EF and not in the current delivery. The results are numerically obtained considering Equation (1), where the EF is directly proportional to the current density and inversely proportional to the electrical conductivity obeying Ohm's law. The anisotropy of the tissue has not been included in the model, nevertheless with the introduction of tractography and white matter tracing [7,27], this feature will be important to consider in future simulations. Given that white matter is anisotropic, then the white matter tracing can help make the tissue conductivity classification even better.

4.3. DBS Leads Comparison

In the second part of the study, only patient-specific models were used to investigate the EF achieved by four different lead designs operated in voltage and current modes. The results of the simulations showed a very similar EF distribution around each lead, however SureStim1 showed a more spherically shaped EF distribution. In general, the EF extension and volume were higher using current mode and lower for voltage mode. The total current delivered by the electrode is determined by the electrode surface area and the average of the current density. Thus, applying a fixed total current of 3.4 mA to a smaller active area, as SureStim1 lead (3.12 mm^2) increases the current density, leading to an increase of the EF (Equation (1)). An experimental evaluation of segmented electrodes by Wei and Grill [28] showed that the electrode impedance was inversely proportional to its surface area. This implies that larger contacts would require higher current intensities to achieve the same EF than smaller electrodes. Another example of this behavior is lead 6148, which electrodes have the largest surface area (6.6 mm^2) achieving the smallest EF in current mode.

Several studies have compared the conventional steering leads either experimentally [29] or based on computer models [2,30,31]. In the experimental study, Contarino et al. [29] temporally inserted a 32 contact lead (similar to SureStim1) which was set with different configurations and current stimulation amplitudes ranging from 0.5 to 8 mA. The steering lead was then replaced by the permanent conventional 3389 lead. The performance of the steering lead was assessed by the current thresholds required to either induce side effects or clinical benefits in comparison to the conventional lead outcome in patients undergoing DBS surgery. By setting 12 consecutive contacts, the Contarino group observed equivalent current thresholds between the steering and the conventional leads. In the present study, eight consecutive electrodes achieved a larger EF volume than the 3389 lead when set to 3.4 mA, implying that choosing 12 contacts instead of eight would increase the difference with the conventional lead even more. This result reflects the influence of the smaller electrodes of SureStim1 lead.

Other computer based studies compared the steering and the conventional leads operated in either voltage or current mode. Martens et al. [2], for instance, investigated a lead of 64 contacts using eight consecutive contacts set to 2.6 mA and observed that a potential field distribution very similar to the generated by the standard ring electrode; our results showed a larger EF for SureStim1 in current mode. The difference between Martens' model and ours, is the brain model. While they consider homogeneous tissue with a single value of conductivity (0.1 S/m), we include a heterogeneous matrix of electrical conductivities. Dijk et al. [28] also compared the steering lead (SureStim1) to the conventional 3389 lead, however they quantified the stimulation effect in terms of the maximum amount of subthalamic nucleus (STN) cells activated based on axon models. They observed equivalent results between the standard and the directional lead by activating 12 consecutive contacts on the latter lead. In addition, this group used biphasic current pulses and neuron diameters of 5.7 μm. Due to the differences in the evaluation methodology and the model itself, our results are not directly comparable to the results of other groups.

4.4. Patient-Specific Stimulation Amplitude Setting

For the actual amplitude programmed, 1.6 V, the EF volume within the 0.2 V/mm isosurface was around 46 mm^3, and the extension was approximately 2.5 mm measured from the lead axis in all

directions. The clinical effect was satisfactory according to the patient journal, however, considering the dimensions of the ZI which has an elongated shape of approximately 2 mm (latero-medial) and 4–5 mm (anterio-posterior), a symmetrical stimulation field could possibly be improved by steering the field in the desired direction. The current amplitude required to achieve the same EF was 1.3 mA, which in comparison to the equivalence for the homogeneous model, indicates a larger impedance for the patient-specific model.

4.5. Steering DBS Leads

The steering function of lead 6180 and SureStim1 was evaluated in voltage and current mode. As for the symmetrical configuration, the EF was larger for current control. Setting 3.4 mA to a single contact of lead 6180 (1.8 mm^2) and to 4 contacts in SureStim1 (1.6 mm^2) derived in a large EF which did not show the directionality of the configuration. By reducing the current stimulation amplitude to 1.3 mA, it was possible to see the same steered profile as that for 3 V. The reason for this behavior is also due to the increase of the current density for smaller contact surface areas. In a similar way, the directionality of the configuration is not observable by lower EF isolevels. For instance, an isolevel of 0.1 V/mm did not show the steered field of 3 V. This is particularly interesting due to the uncertainty of the EF intensity required to activate neighboring neurons. The EF volumes achieved by each lead in the steering configuration do not follow the rationale of smaller surface area, larger EF due to higher current density. One of the reasons for this behavior could be that the active contacts do not have the same orientation. While the electrodes for SureStim1 are oriented towards the anterior part of the model, the single active contact for lead 6180 is oriented towards the lateral side. In voltage mode, the larger EF volume obtained with smaller surface areas may respond to the increase of the current density due to the higher number of edges [28]. Further investigations focused on different configurations for the steering leads are necessary to satisfactorily assess the performance of directional leads.

5. Conclusions

In conclusion, the use of brain models based on patient-specific images and the comparison of two operating modes have enhanced the assessment of the influence from the different lead designs on the EF with a fixed isolevel. The results showed that the EF distribution is influenced by the heterogeneity of the tissue for both operating modes. Computer models can visualize the electric field and thus further increase understanding when switching the stimulation settings, lead designs and inter and intra-patient conductivity variability.

Author Contributions: Karin Wårdell and Peter Zsigmond initiated the study and did the overall planning. Fabiola Alonso, Karin Wårdell and Malcolm Latorre conceived and designed the simulations and analysis methodology. Fabiola Alonso performed and analysed the electric field simulations, and did art work. Malcolm Latorre performed and analysed the neuron simulations and did art work. Peter Zsigmond and Nathanael Göransson were responsible for imaging, planned and performed surgery and calculated targets for simulations. Fabiola Alonso and Karin Wårdell were main responsible for the writing. All other authors contributed to the writing with their special competence.

Conflicts of Interest: The authors declare no conflict of interest.
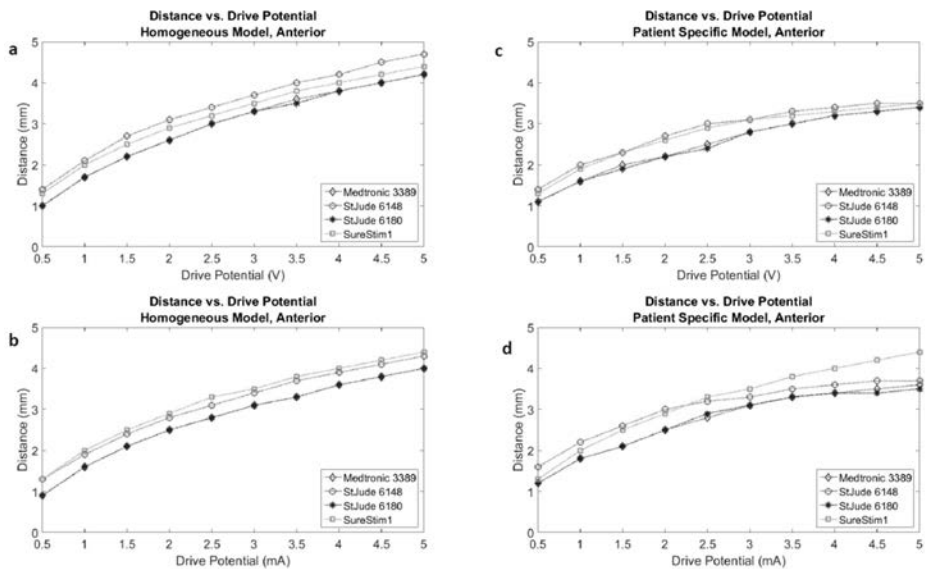
Appendix

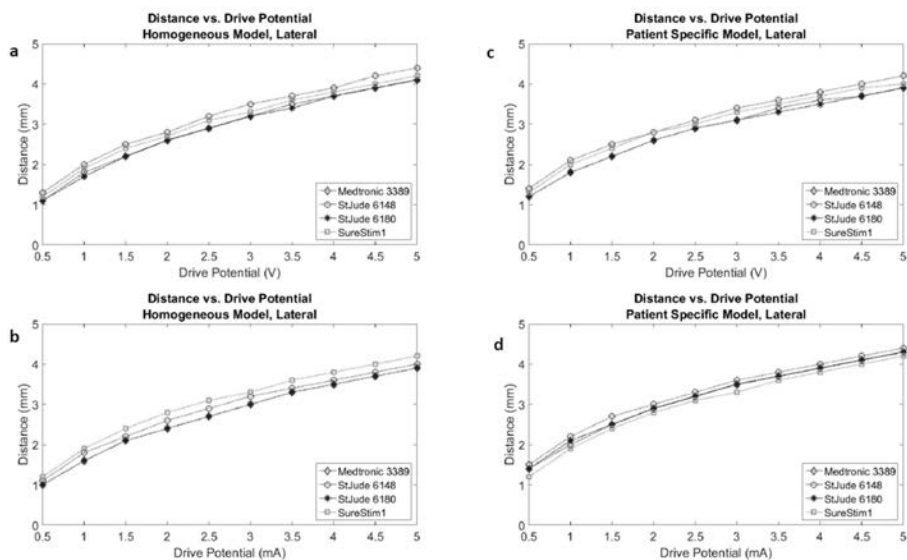**Figure A1.** Neuron modelling: Distance vs. drive potential. Anterior.

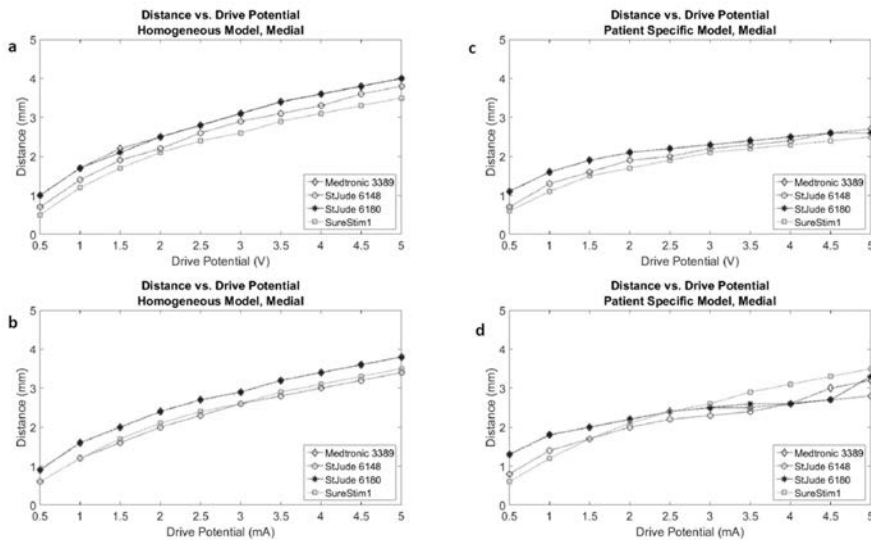**Figure A2.** Neuron modelling: Distance vs. drive potential. Lateral.

Figure A3. Neuron modelling: Distance vs. drive potential. Medial.

References

1. Hariz, M.; Blomstedt, P.; Zrinzo, L. Future of brain stimulation: New targets, new indications, new technology. *Mov. Disord.* **2013**, *28*, 1784–1792. [CrossRef] [PubMed]
2. Martens, H.C.; Toader, E.; Decre, M.M.; Anderson, D.J.; Vetter, R.; Kipke, D.R.; Baker, K.B.; Johnson, M.D.; Vitek, J.L. Spatial steering of deep brain stimulation volumes using a novel lead design. *Clin. Neurophysiol.* **2011**, *122*, 558–566. [CrossRef] [PubMed]
3. Mahlknecht, P.; Limousin, P.; Foltynie, T. Deep brain stimulation for movement disorders: Update on recent discoveries and outlook on future developments. *J. Neurol.* **2015**, *262*, 2583–2595. [CrossRef] [PubMed]
4. Gross, R.E.; McDougal, M.E. Technological advances in the surgical treatment of movement disorders. *Curr. Neurol. Neurosci. Rep.* **2013**, *13*, 371. [CrossRef] [PubMed]
5. Hemm, S.; Mennessier, G.; Vayssiere, N.; Cif, L.; El Fertit, H.; Coubes, P. Deep brain stimulation in movement disorders: Stereotactic coregistration of two-dimensional electrical field modeling and magnetic resonance imaging. *J. Neurosurg.* **2005**, *103*, 949–955. [CrossRef] [PubMed]
6. Åström, M.; Tripoliti, E.; Hariz, M.I.; Zrinzo, L.U.; Martinez-Torres, I.; Limousin, P.; Wårdell, K. Patient-specific model-based investigation of speech intelligibility and movement during deep brain stimulation. *Stereotact. Funct. Neurosurg.* **2010**, *88*, 224–233. [CrossRef] [PubMed]
7. Coenen, V.A.; Allert, N.; Paus, S.; Kronenburger, M.; Urbach, H.; Madler, B. Modulation of the cerebello-thalamo-cortical network in thalamic deep brain stimulation for tremor: A diffusion tensor imaging study. *Neurosurgery* **2014**, *75*, 657–669. [CrossRef] [PubMed]
8. Wårdell, K.; Kefalopoulou, Z.; Diczfalusy, E.; Andersson, M.; Astrom, M.; Limousin, P.; Zrinzo, L.; Hariz, M. Deep brain stimulation of the pallidum internum for gilles de la tourette syndrome: A patient-specific model-based simulation study of the electric field. *Neuromodulation* **2015**, *18*, 90–96. [CrossRef] [PubMed]
9. Butson, C.R.; Cooper, S.E.; Henderson, J.M.; McIntyre, C.C. Patient-specific analysis of the volume of tissue activated during deep brain stimulation. *NeuroImage* **2007**, *34*, 661–670. [CrossRef] [PubMed]
10. Chaturvedi, A.; Butson, C.R.; Lempka, S.F.; Cooper, S.E.; McIntyre, C.C. Patient-specific models of deep brain stimulation: Influence of field model complexity on neural activation predictions. *Brain Stimul.* **2010**, *3*, 65–67. [CrossRef] [PubMed]
11. Alonso, F.; Hemm-Ode, S.; Wårdell, K. Influence on deep brain stimulation from lead design, operating mode and tissue impedance changes—A simulation study. *Brain Disord. Ther.* **2015**, *4*, 3.
12. Åström, M.; Lemaire, J.J.; Wårdell, K. Influence of heterogeneous and anisotropic tissue conductivity on electric field distribution in deep brain stimulation. *Med. Biol. Eng. Comput* **2012**, *50*, 23–32. [CrossRef] [PubMed]

13. Schmidt, C.; van Rienen, U. Modeling the field distribution in deep brain stimulation: The influence of anisotropy of brain tissue. *IEEE Trans. Biomed. Eng.* **2012**, *59*, 1583–1592. [CrossRef] [PubMed]

14. Åström, M.; Diczfalusy, E.; Martens, H.; Wårdell, K. Relationship between neural activation and electric field distribution during deep brain stimulation. *IEEE Trans. Biomed. Eng.* **2015**, *62*, 664–672. [CrossRef] [PubMed]

15. Wårdell, K.; Hemm-Ode, S.; Rejmstad, P.; Zsigmond, P. High-resolution laser doppler measurements of microcirculation in the deep brain structures: A method for potential vessel tracking. *Stereotact. Funct. Neurosurg.* **2016**, *94*, 1–9. [CrossRef] [PubMed]

16. Wårdell, K.; Diczfalusy, E.; Åström, M. Patient-specific modeling and simulation of deep brain stimulation. In *Studies in Mechanobiology, Tissue Engineering and Biomaterials*; Springer Berlin Heidelberg: Heidelberg, Germeny, 2011; Volume 9, pp. 357–375.

17. Åström, M.; Zrinzo, L.U.; Tisch, S.; Tripoliti, E.; Hariz, M.I.; Wårdell, K. Method for patient-specific finite element modeling and simulation of deep brain stimulation. *Med. Biol. Eng. Comput.* **2009**, *47*, 21–28. [CrossRef] [PubMed]

18. Gabriel, S.; Lau, R.W.; Gabriel, C. The dielectric properties of biological tissues: II. Measurements in the frequency range 10 hz to 20 ghz. *Phys. Med. Biol.* **1996**, *41*, 2251–2269. [CrossRef] [PubMed]

19. Audreccetti, D.; Fossi, R.; Petrucci, C. Dielectric Properties of Body Tissue. Italian National Research Council. Available online: http://niremf.ifac.cnr.it/tissprop/htmlclie/htmlclie.htm#atsftag (accessed on 4 April 2016).

20. Wårdell, K.; Zrinzo, L.; Hariz, M.; Andersson, M. Patient-Specific Brain Modelling for Deep Brain Stimulation Simulation. In Proceedings of the 6th International IEEE/EMBS Conference on Neural Engineering proceedings, California, CA, USA, 6–8 November 2013.

21. Yousif, N.; Bayford, R.; Liu, X. The influence of reactivity of the electrode-brain interface on the crossing electric current in therapeutic deep brain stimulation. *Neuroscience* **2008**, *156*, 597–606. [CrossRef] [PubMed]

22. Nielsen, M.S.; Bjarkam, C.R.; Sorensen, J.C.; Bojsen-Moller, M.; Sunde, N.A.; Ostergaard, K. Chronic subthalamic high-frequency deep brain stimulation in Parkinson's disease—A histopathological study. *Eur. J. Neurol.* **2007**, *14*, 132–138. [CrossRef] [PubMed]

23. McIntyre, C.C.; Mori, S.; Sherman, D.L.; Thakor, N.V.; Vitek, J.L. Electric field and stimulating influence generated by deep brain stimulation of the subthalamic nucleus. *Clin. Neurophysiol.* **2004**, *115*, 589–595. [CrossRef] [PubMed]

24. Kuncel, A.M.; Cooper, S.E.; Grill, W.M. A method to estimate the spatial extent of activation in thalamic deep brain stimulation. *Clin. Neurophysiol.* **2008**, *119*, 2148–2158. [CrossRef] [PubMed]

25. Madler, B.; Coenen, V.A. Explaining clinical effects of deep brain stimulation through simplified target-specific modeling of the volume of activated tissue. *AJNR Am. J. Neuroradiol.* **2012**, *33*, 1072–1080. [CrossRef] [PubMed]

26. Bronstein, J.M.; Tagliati, M.; McIntyre, C.; Chen, R.; Cheung, T.; Hargreaves, E.L.; Israel, Z.; Moffitt, M.; Montgomery, E.B.; Stypulkowski, P.; et al. The rationale driving the evolution of deep brain stimulation to constant-current devices. *Neuromodulation* **2015**, *18*, 85–89. [CrossRef] [PubMed]

27. Ning, L.; Setsompop, K.; Michailovich, O.; Makris, N.; Shenton, M.E.; Westin, C.F.; Rathi, Y. A joint compressed-sensing and super-resolution approach for very high-resolution diffusion imaging. *Neuroimage* **2016**, *125*, 386–400. [CrossRef] [PubMed]

28. Wei, X.F.; Grill, W.M. Current density distributions, field distributions and impedance analysis of segmented deep brain stimulation electrodes. *J. Neural. Eng.* **2005**, *2*, 139–147. [CrossRef] [PubMed]

29. Contarino, M.F.; Bour, L.J.; Verhagen, R.; Lourens, M.A.; de Bie, R.M.; van den Munckhof, P.; Schuurman, P.R. Directional steering: A novel approach to deep brain stimulation. *Neurology* **2014**, *83*, 1163–1169. [CrossRef] [PubMed]

30. Cubo, R.; Åström, M.; Medvedev, A. Target coverage and selectivity in field steering brain stimulation. *Conf. Proc. IEEE Eng. Med. Biol Soc.* **2014**. [CrossRef]

31. Van Dijk, K.J.; Verhagen, R.; Chaturvedi, A.; McIntyre, C.C.; Bour, L.J.; Heida, C.; Veltink, P.H. A novel lead design enables selective deep brain stimulation of neural populations in the subthalamic region. *J. Neural. Eng.* **2015**, *12*, 046003. [CrossRef] [PubMed]

PAPER **III**

Electric Field Comparison between Microelectrode Recording and Deep Brain Stimulation Systems—A Simulation Study

Fabiola Alonso [1,*] [iD]**, Dorian Vogel** [1,2] [iD]**, Johannes Johansson** [1]**, Karin Wårdell** [1] **and Simone Hemm** [1,2]

[1]   Department of Biomedical Engineering, Linköping University, 58185 Linköping, Sweden;
     dorian.vogel@fhnw.ch (D.V.); johannes.johansson@liu.se (J.J.); karin.wardell@liu.se (K.W.);
     simone.hemm@fhnw.ch (S.H.)
[2]   Institute for Medical and Analytical Technologies, School of Life Sciences,
     University of Applied Sciences and Arts Northwestern Switzerland FHNW, 4132 Muttenz, Switzerland
[*]   Correspondence: fabiola.alonso@liu.se; Tel.: +46-101-030-000

Abstract: The success of deep brain stimulation (DBS) relies primarily on the localization of the implanted electrode. Its final position can be chosen based on the results of intraoperative microelectrode recording (MER) and stimulation tests. The optimal position often differs from the final one selected for chronic stimulation with the DBS electrode. The aim of the study was to investigate, using finite element method (FEM) modeling and simulations, whether lead design, electrical setup, and operating modes induce differences in electric field (EF) distribution and in consequence, the clinical outcome. Finite element models of a MER system and a chronic DBS lead were developed. Simulations of the EF were performed for homogenous and patient-specific brain models to evaluate the influence of grounding (guide tube vs. stimulator case), parallel MER leads, and non-active DBS contacts. Results showed that the EF is deformed depending on the distance between the guide tube and stimulating contact. Several parallel MER leads and the presence of the non-active DBS contacts influence the EF distribution. The DBS EF volume can cover the intraoperatively produced EF, but can also extend to other anatomical areas. In conclusion, EF deformations between stimulation tests and DBS should be taken into consideration as they can alter the clinical outcome.

Keywords: microelectrode recording (MER); finite element method (FEM); deep brain stimulation (DBS); brain model; Dice coefficient; patient-specific

---

1. Introduction

Deep brain stimulation (DBS) is an established surgical therapy to treat the symptoms from movement disorders such as Parkinson's disease, essential tremor, and dystonia [1–3]. The electrical stimulation affects a population of neuron axons in the vicinity of the active electrode. The extension in space of the stimulation depends on several factors, including the surrounding tissue properties, the electrode design, and the stimulation parameters [4].

The success of the surgery is highly dependent on the correct electrode placement, which requires the utmost accuracy in the targeting stage. Ideally placed electrodes results in symptom removal at low stimulation amplitudes and higher thresholds for stimulation-induced side effects.

Due to difficulties in the visualization of some structures with conventional magnetic resonance imaging (MRI), a common procedure to confirm or refine the localization of the target before the insertion of the permanent DBS lead, is to monitor the deep brain structures along the pre-planned

trajectory through a microelectrode recording (MER) system. The MER lead consists of a microelectrode at the tip used to record the spontaneous electrical activity along a pre-planned trajectory down to the target, and a macroelectrode to perform functional stimulation tests for clinical assessment of the patient's symptoms.

Clinical experience [5–7] shows that the position of the DBS contact finally activated for chronic stimulation to induce the best clinical outcome often differs from the intraoperatively chosen position. Possible reasons may include brain shift or the subjective interpretation of stimulation test results.

Computer models using FEM [8,9] have been widely used to investigate the influence of the stimulation parameters and surrounding tissue properties in DBS. The electric field (EF), i.e., the potential's first derivative, can be used to approximate the volume of tissue activated (VTA) for specific stimulation parameters and axon diameters, and thus the volume within a fixed EF isolevel [10]. The EF isolevel approach has been used by numerous studies [11–18] and allows for presentation of the results in the millimeter scale and thus for relative comparisons between simulations. To our knowledge, a comparison between intraoperative stimulation using the MER macroelectrode and chronic stimulation using a standard DBS lead has not yet been addressed through computer models.

The aim of this study was to compare and evaluate the electric field (EF) distributions of the MER macroelectrode and DBS lead assuming that they are positioned along the same trajectory. Differences in lead design, operating modes, and electrical setup were investigated by means of FEM models and simulations.

2. Materials and Methods

FEM simulations performed in this investigation are based on the surgical protocol from the Department of Neurosurgery at Clermont-Ferrand University Hospital, where intraoperative MER and stimulation tests are performed prior to DBS lead implantation [16].

2.1. Intraoperative Stimulation and DBS Implantation

During surgery, one or up to five MER leads are inserted along trajectories according to the preoperative MRI-based planning. Neural activity of the region of interest is recorded with the MER tip followed by stimulation tests using the MER stimulation contact (Figure 1A). The MER lead (Neuroprobe 366-000024, Alpha Omega Engineering, Nazareth, Israel) is steered to the target region through a rigid guide tube (ACS-7905/200-5, DIXI Microtechniques, Besançon, France). The distal end of the guide tube is inserted as deep as 12 mm before the planned target point, and fixed at that position (Figure 1). When more MER leads are used, guide tubes are placed in parallel, 2 mm from each other (Figure 1B). Before the intraoperative stimulation tests are performed, a first path is made to record the activity with the MER tip along the pre-planned trajectory; afterwards, the MER tip is retracted some millimeters inside the stimulation macroelectrode. The stimulation tests are performed in the range between 10 mm before the planned target and 4 mm beyond it, in 1 mm steps. A cathodic monopolar configuration is used to apply constant current pulses through the MER stimulation contact of one of the inserted leads while the parallel one remains off. The anode or reference electrode is set to the guide tubes. A detailed description of the procedure can be found in [16].

The DBS lead (3389, Medtronic Inc., Minneapolis, MN, USA) is subsequently implanted at the location where the highest therapeutic effect is achieved with minimal stimulation amplitudes and side effects with the MER stimulation tests.
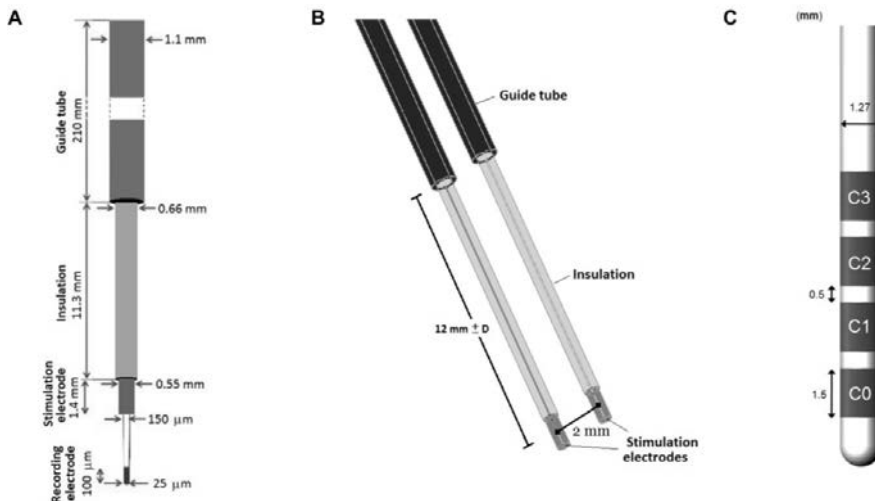
Figure 1. Schematic representation of the microelectrode recording (MER) system and DBS. (**A**) The intraoperative MER lead, including the guide tube and recording electrode. (**B**) 3D model including a parallel lead in the posterior trajectory along the preoperative planned trajectory and (**C**) DBS lead 3389 model.

2.2. Finite Element Method Models

The FEM models were designed in accordance with the clinical configuration for the intraoperative and chronic stimulation. Homogeneous 2D axisymmetric and patient-specific 3D models were developed with COMSOL Multiphysics (Ver. 5.2, COMSOL AB, Stockholm, Sweden) to investigate the differences between the intraoperative and DBS electrodes in terms of the EF distribution.

The electric field magnitude, EF = $|-\nabla V|$, around the electrode was calculated by the equation for steady currents,

$$\nabla \cdot \mathbf{J} = -\nabla \cdot (\sigma \nabla V) = 0 \quad A/m^3 \tag{1}$$

where ∇ is the divergence, $\mathbf{J}$ (A/m^2) is the current density, σ (S/m) is the electrical conductivity, and V (V) is the electric potential.

2.2.1. MER Lead Model

The geometry of the intraoperative lead model corresponds to the Neuroprobe. The recording tip was not considered in the model as it is retracted during stimulation. The guide tube was placed 12 mm apart from the middle point of the stimulation contact and fixed at that position (Figure 1B).

The MER stimulation contact was set to a constant current. The non-active parallel contacts were set to floating potential ($\int -\mathbf{n}\cdot\sigma\nabla V dS = 0$ A; $\mathbf{n} \times (-\nabla V) = 0$ V/m), while the non-conductive shaft was set to insulation ($\mathbf{n}\cdot\nabla V = 0$ V/m), where $\mathbf{n}$ is the surface normal vector. The guide tubes were considered as the anode and were set to ground (V = 0 V).

2.2.2. DBS Lead Model

The geometry of the DBS lead corresponds to the model 3389, surrounded by a 250 μm thick peri-electrode space (PES) in order to mimic the fibrous tissue developed over time after the lead is implanted. The PES was assumed to have the same electrical conductivity as white matter, σ = 0.075 S/m [19,20]. Monopolar configuration was simulated by setting the active contact to a constant voltage and the outer boundaries of the surrounding medium to ground. The non-active contacts were set to floating potential.

2.2.3. Brain Models

Three brain models were created: a 2D axisymmetric homogenous, 3D homogenous, and 3D heterogeneous (patient-specific) model. The surrounding medium of the contact for the 2D axisymmetric (54 × 100 mm^2) and 3D models (100 × 154 × 90 mm^3) was homogeneous and isotropic, with an electrical conductivity of 0.123 S/m corresponding to grey matter.

The 3D heterogeneous model in turn considered a medium corresponding to patient-specific data, obtained from a preoperative stereotactic T1-weighted MRI (1.5 Tesla, Sonata, Siemens GmbH, Munich, Germany) performed with a Leksell$^{®}$ G frame (Elekta Instrument AB, Stockholm, Sweden) mounted to the patient's head [9,14].

An MRI (0.63 × 0.63 × 1.30 mm^3) batch was used from a patient suffering from essential tremor who had been implanted in the ventral intermediate nucleus (Vim) of the thalamus (written consent has been obtained from the patient; ethic approval ref.: 2011-A00774-37/AU905, Comité de Protection des Personnes Sud-Est 6, Clermont-Ferrand, France; approval date: 21st of July 2011) to obtain the brain model, suitable for FEM simulations. The brain model is an interpolation matrix of the corresponding electrical conductivity of the relevant tissue types, i.e., gray matter (0.123 S/m), white matter (0.075 S/m), cerebrospinal fluid (2.0 S/m), and blood (0.7 S/m) [21,22]. The conductivity values considered a pulse width of 60 μs and a pulse frequency of 130 Hz.

The mesh was physics-controlled with a denser distribution around the leads. For the 2D model, the mesh consisted of approximately 17,000 triangular elements. The minimum element size was 0.002 mm with an average element quality of 0.9. For the 3D models, the mesh consisted of approximately 3,000,000 tetrahedral elements with a minimum element size of 0.03 mm and an average element quality of 0.7.

The leads for the 3D models were positioned based on the patient-specific clinical data, i.e., planned trajectory and target coordinates (Figure 1B).

2.3. Simulations

The boundary conditions in the FEM models, stimulation settings, and relative position between the leads were modified in order to investigate the influence of the electrode design, operating mode, and electrical setup. A clinical case was explored to observe differences on the EF obtained between the patient-specific intraoperative vs. postoperative stimulation settings. Simulations were run for clinically relevant stimulation amplitudes (1, 2, 3, or 4 V) for the DBS and 1, 2, 3, or 4 mA for the MER stimulation contact, which achieves the same EF extension using the described 2D homogeneous model.

2.3.1. Grounding the Guide Tube

During the intraoperative stimulation tests, the guide tube is used as the reference electrode (anode) and is set to ground, in contrast to the chronic DBS stimulation, where the ground is set to the neurostimulator case. The 2D axisymmetric model was used to explore how the EF is influenced by the grounded guide tube. Simulations were performed once with the guide tube grounded and once with modified boundary conditions for the intraoperative lead by setting the guide tube to floating potential while the ground was set to the outer boundaries of the medium. The MER stimulation contact was placed at the target (12 mm from the guide tube), and set from 1 to 4 mA in 1 mA steps.

Simulations were also performed displacing the MER stimulation contact up to 10 mm above and 4 mm below the target, i.e., 2 and 16 mm from the guide tube, respectively, in 1 mm steps.

2.3.2. Parallel MER Leads

When more than one lead is inserted during the stimulation tests, the metallic contacts of the parallel leads may affect the EF distribution. The homogenous 3D model was used to compare and evaluate the EF for different scenarios: (a) one single lead (central trajectory); (b) two parallel leads (central and posterior trajectories); and (c) three parallel leads (central, posterior, and medial trajectories). The parallel leads, with identical geometry and material properties, were placed 2 mm posterior, and medially to the central lead. The non-active MER stimulation contacts were set to floating potential and simulations were run setting the active contact to 1 and 3 mA.

2.3.3. Non-Active Contacts for DBS

While the MER lead consists of only one stimulation contact, the presence of non-active contacts on the DBS lead becomes important to assess since they may affect the EF distribution around the lead. The homogeneous 2D model was used to evaluate the EF by activating each of the contacts (C0, C1, C2, C3) (Figure 1C) while setting the non-active ones to floating potential. The DBS lead was displaced along its axis in order to align the active contact to the MER contact, using the middle point of each contact as a reference. The EF was also compared for a fixed position of the DBS lead aligning the first contact, C0, to the target position and activating each of the DBS contacts (C0, C1, C2, C3) separately.

2.3.4. Position of the DBS Active Contact

Simulations were also performed with the patient-specific 3D model in order to consider the heterogeneity of the surrounding medium.

In order to investigate to which extent the EF induced by the MER stimulation can be reproduced by the DBS contacts in different positions, the DBS lead was displaced along the same trajectory as the MER lead so that the middle point and the lower and upper edges of the active DBS contacts were placed consecutively at the target position.

2.3.5. Clinical Case

The patient-specific 3D brain model and the clinical settings were used to compare the EF generated by each contact. The position of the MER lead was based on the preoperative MRI planned trajectory to target the Vim. The stimulation contact of the MER central lead was positioned 2 mm beyond the target and was set to 0.4 mA, corresponding to the stimulation position and amplitude where the best symptom improvement (94%) was achieved [23]. The posterior trajectory contact was set to floating potential. The DBS lead, in turn, was positioned according to the coordinates taken from the postoperative CT scan after image co-registration with preoperative stereotactic MRI. The third contact (C2), set to 2 V, was used for chronic stimulation (80% improvement) programmed six months after surgery. Simulations were also performed for the first (C0) and second (C1) contact at the same stimulation amplitude and 3 V.

2.4. Data Analysis

The EF was visualized and measured using a 0.2 V/mm isolevel for all the cases investigated [10,16]. For the 2D models, the maximum radial extension of the EF isocontour was measured from the lead axis. Differences between the investigated scenarios were visually assessed by superimposing the corresponding EF distribution for each situation. For the 3D patient-specific simulations, the volume within the 0.2 V/mm isosurface was calculated, i.e., the VTA. The volumes for the DBS and the MER lead were compared by calculating the Sørensen-Dice coefficient (DC) [24]. The volume overlap between two structures was rated according to Equation (2),

$$DC = 2 \frac{|V_{MER} \cap V_{DBS}|}{|V_{MER}| + |V_{DBS}|} \tag{2}$$

where V_{MER} corresponds to the volume obtained for the MER system stimulation electrode and V_{DBS} for the implanted DBS lead (vertical bars indicating a summation of the included voxels).

A perfect overlap between two volumes results in a value of 1 for the coefficient, decreasing to DC = 0 when no common volume between the two exists.

V_{MER} and V_{DBS} were calculated by exporting the results of FEM simulations as polygonal meshes and were processed using filters from the VTK toolkit (vtk.org, ver. 7.1, Kitware Inc., Clifton Park, NY, USA), assembled in a Paraview pipeline (paraview.org, ver. 5.4, Kitware Inc., USA). Polygonal (closed) surfaces of electric fields and their respective electrode volume were sampled to binary mask images using a $0.1 \times 0.1 \times 0.1$ mm^3 voxel size. Electrode volume was removed from each corresponding EF using boolean image operations, and both the intersection and union were calculated for each EF permutation. The volume of each resulting mesh volume was then extracted and used to calculate the DC. Together with the DC, the MER EF Coverage Coefficient (CC) was used, expressed as the volume of the intersection of the two volumes normalized to the volume of the MER electric field, according to Equation (3)

$$CC = \frac{|V_{MER} \cap V_{DBS}|}{|V_{MER}|} \tag{3}$$

A summary of all simulations is presented in Table 1.

Table 1. Summary of the settings to investigate the EF due to differences between the MER stimulation and the DBS contacts.

Investigation	Model	Active Contacts and Stimulation Amplitude	Ground
Grounding the guide tube	2D Axisymmetric	MER stim. contact: 1–4 (mA)	Guide tube or Outer boundaries
Parallel MER leads	3D Homogeneous	MER stim. contact: 1, 3 (mA)	Guide tube
Non-active contacts for DBS	2D Axisymmetric	MER stim. contact: 1, 3 (mA)/DBS C0, C1, C2 or C3: 1, 3 (V)	Guide tube/Outer boundaries
Position of the DBS active contact	3D Patient-specific	MER stim. contact: 1, 3 (mA)/DBS C0 or C1: 1, 3 (V)	Guide tube/Outer boundaries
Clinical case	3D Patient-specific	MER stim. contact: 0.4 mA/DBS C0, C1 or C2: 2, 3 (V)	Guide tube/Outer boundaries

3. Results

3.1. Grounding the Guide Tube

The main influence of grounding the guide tube is the presence of an EF around it. The EF around the guide tube increases with the stimulation amplitude when the guide tube is grounded (Figure 2A) in contrast to the negligible EF when the guide tube is set to floating potential (Figure 2B). The EF around the active contact is not visibly modified at any stimulation amplitude. The maximal extension of the 0.2 V/mm isocontour is the same when the guide tube is grounded or in floating potential.

The EF distribution around the active contact is affected at shorter distances to the guide tube (stimulation contact 10 mm above the target) for both cases; grounded and floating potential. The EF loses its spherical shape and is deformed towards the guide tube for all the stimulation amplitudes investigated (Figure 2C). The EF around the active contact does not present any change for distances longer than 6 mm between the stimulation contact and the guide tube (Figure 2C) for the selected amplitudes.
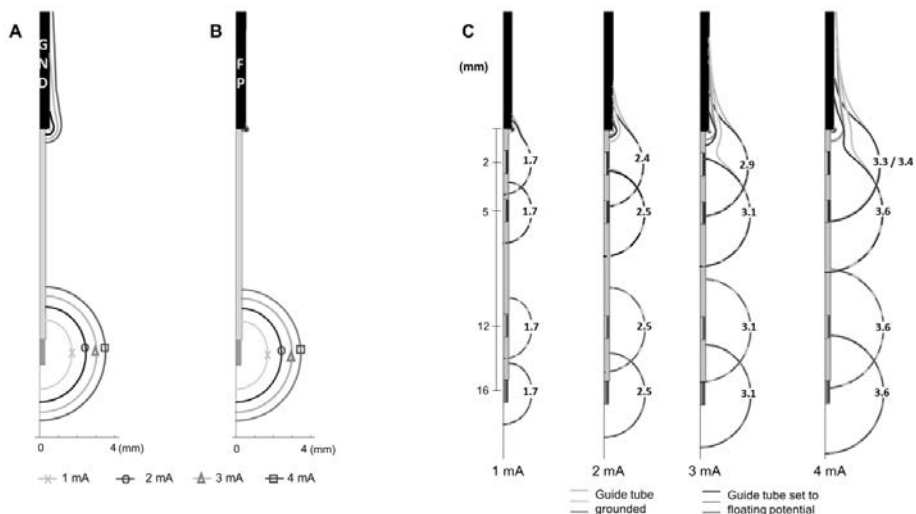
Figure 2. Influence of grounding the guide tube. Electric field (EF) isocontours (0.2 V/mm) simulated in homogeneous grey matter setting the MER stimulation contact to 1 to 4 mA in 1 mA steps. (**A**) Guide tube at target position set to ground (GND), (**B**) guide tube set to floating potential (FP), outer boundaries of the model set to ground. (**C**) EF isocontours overlapped to compare the EF when the guide tube is grounded and set to floating potential. EF simulated placing the MER electrode at different distances from the guide tube (distance to target: +4 mm, 0 mm, −7 mm, −10 mm) exemplified for amplitudes between 1 to 4 mA. Numbers in front of the active contact indicate the maximum distance of the isocontour to the lead axis.

3.2. Parallel MER Leads

The insertion of parallel leads changes the EF around the guide tubes (Figure 3), which is especially visible at high amplitudes (Figure 3B). The EF extension along the central guide tube decreases when adding parallel leads, while the horizontal extension between the different guide tubes increases. Isocontours obtained at the level of the active contact show the presence of an EF around the parallel non-active contacts, which slightly changes the EF extension and shape (Figure 3A–C).
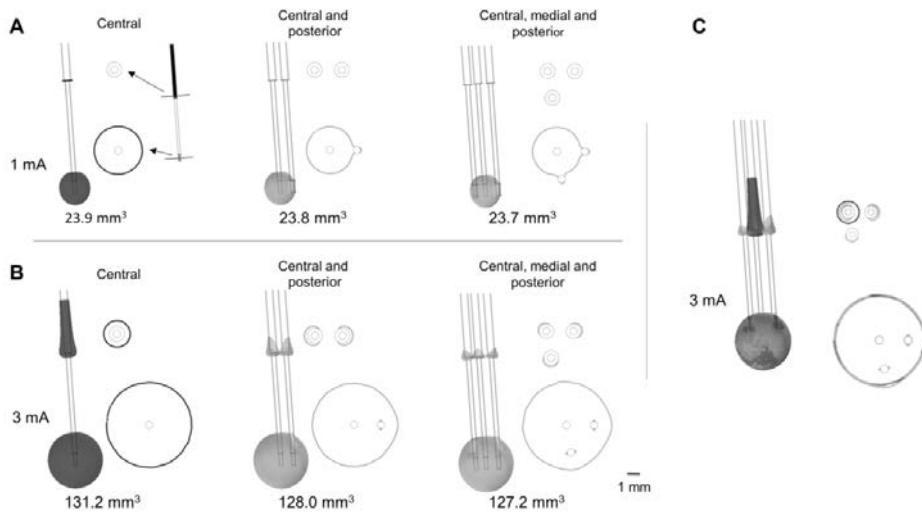
Figure 3. Influence of parallel MER trajectories inserted intraoperatively. EF distribution simulated in a homogeneous medium depicted with isosurfaces and isocontours of 0.2 V/mm. Isocontours obtained at perpendicular planes placed at the target and 12.5 mm above it (red lines shown in A) for stimulation using the central lead at (**A**) 1 mA and (**B**) 3 mA. (**C**) Superposition of the isosurfaces and the isocontours for the three cases at 3 mA. Single lead (dark blue), two leads (cyan), and three leads (yellow). Non active contacts of the posterior and medial leads were set to floating potential. Numbers below the leads indicate the EF volume covered by the 0.2 V/mm isosurface.

3.3. Non-Active Contacts for DBS

The shape of the EF around the DBS lead is modified at all stimulation amplitudes compared to the spherical distribution around the MER contact, due to the adjacent non-active contacts. Despite the deformation, the maximal extension of the EF isocontours (Figure 4A,B) is nearly the same (± 0.03 mm) for each contact at any amplitude: 1.7, 2.5, 3.1, and 3.6 mm for 1, 2, 3, and 4 mA or V, respectively.
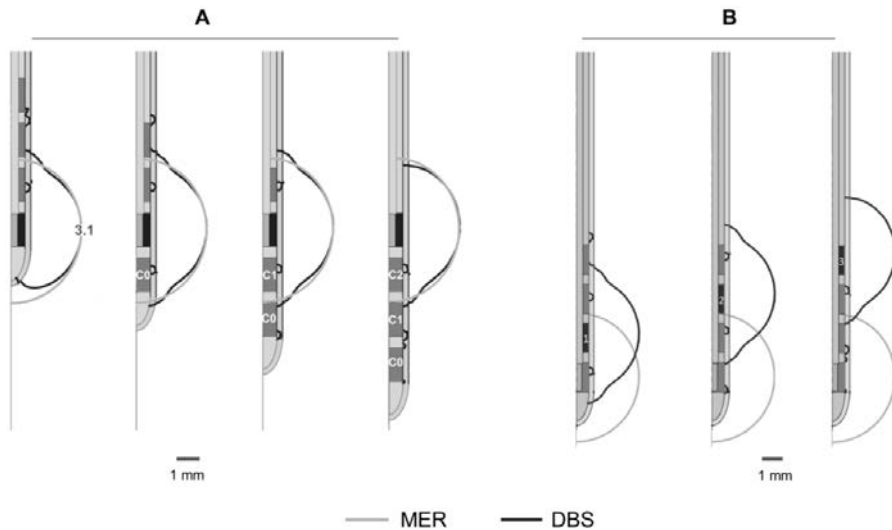
Figure 4. Influence of non-active contacts for DBS. EF simulated in homogeneous grey matter (0.123 S/m) depicted with 0.2 V/mm isocontours. (**A**) Activation of each DBS contact displacing the DBS lead to align the middle point of the active contact (dark blue) to that of the MER stimulation contact (cyan). Numbers in front of the active contact of the first lead indicate the maximal EF extension measured from the lead's axis. (**B**) Activation of each DBS contact while the first contact (C0) is aligned to the middle point of the MER stimulation contact. The DBS contacts were set to 3 V one at the time and the MER stimulation contact was set to 3 mA. Non-active contacts (in dark grey) were set to floating potential. Maximal extension obtained for the MER and DBS contacts: 3.1 mm.

3.4. Position of the DBS Active Contact

The comparison between EF for the MER stimulation and each DBS contact is presented in Figure 5. The highest DC and CC are set to 3 mA/3 V for C0. An EF overlap between the MER stimulation contact and DBS is possible for amplitudes higher than 3 V, even when the position of the contacts differs by 4 or 6 mm (Figure 5B). The highest DC reflects the best match in the case where the DBS contact is aligned to the MER stimulation contact. When comparing differences in EF for alignments of the upper and lower edge and the center of contact C0 in relation to the center of the MER contact, the best match of the EF volumes is also obtained for an alignment of the two middle points at any stimulation amplitude (Figure 6). The DC reveals, however, that it is possible to have a high index of coincidence at high amplitudes when the two contacts are not aligned, as shown for 3 mA/3V in Figure 6C. A higher coverage coefficient is consistently obtained for higher amplitudes (3 mA) in comparison to lower amplitudes (1 mA).

A larger EF volume was obtained for the MER stimulation contact in comparison to the homogeneous case (Figure 3, one lead). The electrical conductivity for the patient-specific model was averaged within a cubic region (10 mm^3) centered at the target resulting in 0.079 S/m, which is a low value compared to the homogeneous model (0.123 S/m). In order to deliver a constant current of 3 mA through the MER stimulation contact, the lower conductivity of this patient-specific model required a voltage of 9.8 V in comparison to the homogeneous grey matter where 6.0 V was applied to obtain the same current.
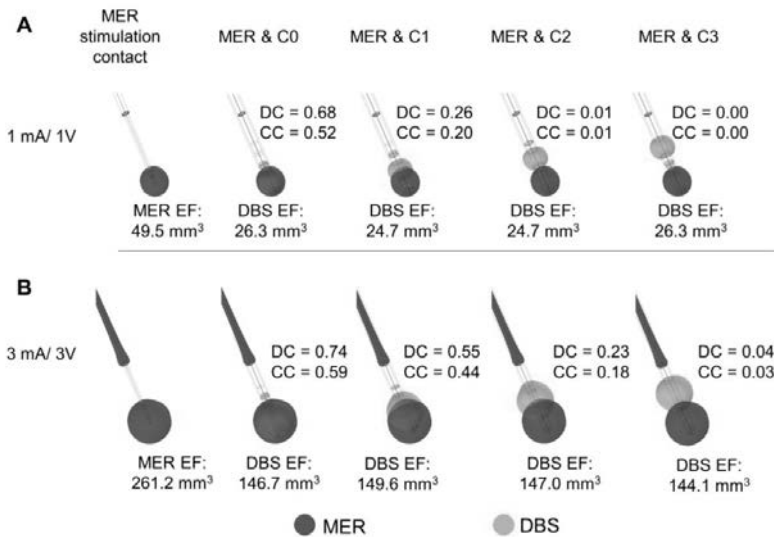
Figure 5. Comparison of the EF between the MER stimulation contact and each DBS contact simulated in a heterogeneous medium (σ ≈ 0.079 S/m). DBS first contact (C0) (cyan) aligned to match the middle point of the MER stimulation contact (dark blue). EF isosurfaces (0.2 V/mm) superimposed for (**A**) MER stimulation contact set to 1 mA and the active DBS contact set to 1 V, and (**B**) for 3 mA and 3 V. EF volume within the selected isosurface shown below the lead and Dice coefficient (DC) and coverage coefficient (CC) shown to the right of each lead.
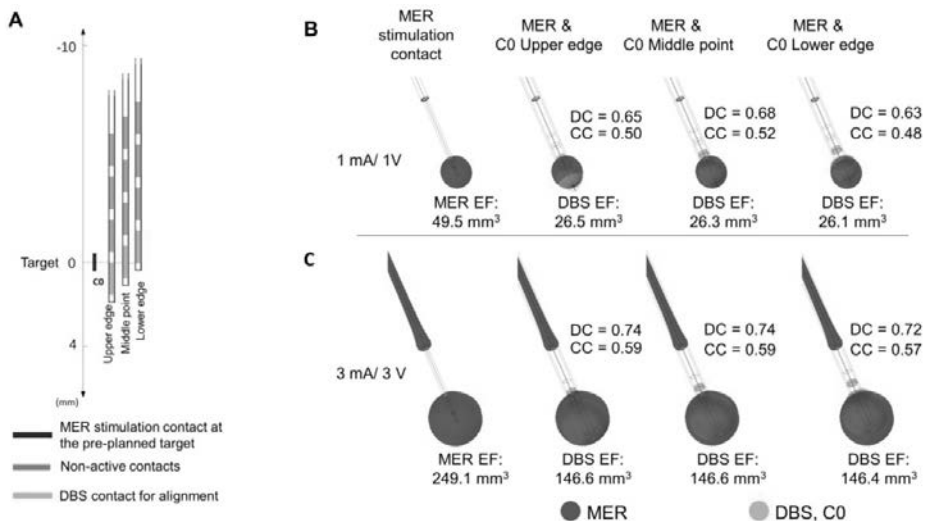
Figure 6. Evaluation of the position of the DBS contact in heterogeneous tissue (σ ≈ 0.079 S/m). (**A**) Displacement of the DBS lead to match the lower edge, the middle point, and the upper edge to the middle point of the MER stimulation contact localized at the target. Overlay of the EF isosurfaces (0.2 V/mm) simulated for the MER stimulation contact (dark blue) and the DBS first contact C0 (cyan) set to (**B**) 1 mA and 1 V and (**C**) 3 mA and 3 V, respectively. EF volume within the selected isosurface shown below the lead. DC and CC shown to the right of each lead.

3.5. Clinical Case

In the presented case, the trajectory and the final position for the implanted DBS lead deviated from the intraoperative MER lead. The EF isosurface using the MER stimulation electrode is smaller compared to the EF obtained setting the DBS electrode to the stimulation amplitude programmed six months after surgery (Figure 7B). The EF isocontours obtained at the perpendicular plane placed at the midpoint of the MER stimulation contact show no overlap at the optimal spot (Figure 7B, lower panel) and a very low DC value. With the same amplitude of 2 V, the activation of DBS contacts closer to the MER stimulation contact increases the coincidence of the EF, and thus the DC (Figure 7C,D). A complete coverage of the intraoperative EF is achieved with a higher amplitude (3 V) using contact C0, the closest DBS contact to the MER (Figure 7E), consequently the large value of the coverage coefficient. The DC, however, is lower than for the other cases investigated.
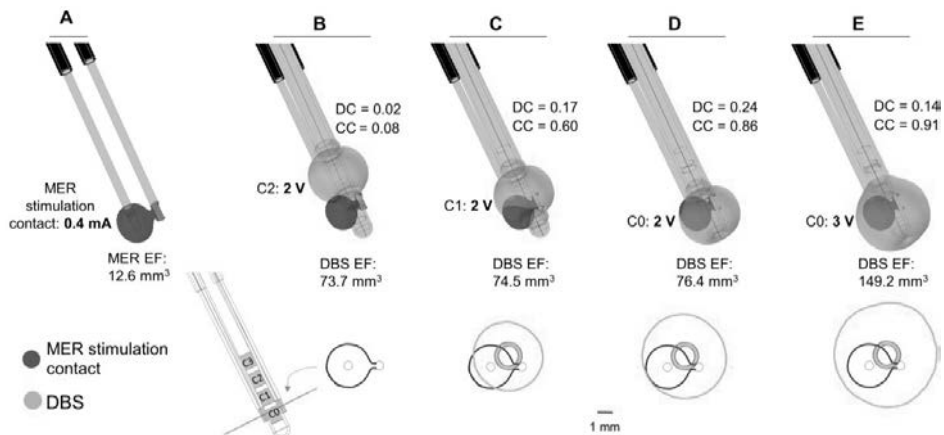
Figure 7. Clinical case. Electric field distribution depicted with 0.2 V/mm isosurfaces (upper panel) and isocontours (lower panel) obtained at the perpendicular plane placed at the middle point of the MER stimulation contact (red line). MER and DBS lead trajectories obtained from the preoperative plan and the postoperative CT scan, respectively. (**A**) Stimulation tests performed with the MER stimulation electrode placed at the optimal position determined intraoperatively: 2 mm beyond the pre-planned target on the central trajectory with a stimulation amplitude of 0.4 mA. (**B**) Overlap of the EF obtained with the MER stimulation electrode (dark blue) and the DBS contact C2 (cyan) set to 2 V, programmed six months after surgery. DBS lead placed 3 mm beyond the target (lower edge of the first contact, C0); (**C,D**) Additional comparisons using DBS contacts C1 and C0 set to 2 V and (**E**) C0 set to 3 V. EF volume within the selected isosurface shown below each lead. DC and CC shown to the right of each case.

4. Discussion

The main objective of the present study was to investigate, by means of FEM models and simulations, differences in the EF distribution between MER stimulation and DBS which could explain variations in clinical outcome. The study was focused on the evaluation and visualization of the EF since it is the electrical entity directly affected by changes in the lead design, operating mode, and electrical setup. Other studies have addressed the influence of the electrode geometry, impedance, and other aspects using evaluation parameters such as the current density or the VTA [25–27]. Those studies, however, examine a single DBS lead or electrode under voltage controlled stimulation. The present investigation, in contrast, compares two electrodes with differences in their operating mode, setup, and dimensions. For this comparison, the specific value of 0.2 V/mm isolevel has been used. The selection of the 0.2 V/mm is based on the results from previous studies [10,14,28] which have investigated the stimulation field combining FEM and neuron models. The 0.2 V/mm isolevel is

the required EF magnitude to stimulate neurons of around 3–4 μm with a pulse width between 60 to 90 μs. Moreover, this isolevel has been used in other FEM-simulation studies [13,18] and represents a useful value for comparative purposes.

4.1. Electrical Setup

The results regarding the influence of the grounded guide tube have shown that the 0.2 V/mm isosurface is present not only around the stimulating contact, but also around the guide tube. This raises the question of whether neuronal activation is possible in those regions, which are not intended to be stimulated. Further studies are necessary to investigate the occurrence of this effect.

Furthermore, the proximity to the grounded guide tube has been shown to influence the form of the EF around the stimulating contact when approaching the guide tube. The importance of this deformation increases with the increase of the stimulation amplitude. Depending on the anatomical position, such deformations might be responsible for some side effects. Even if the optimal stimulation area where the DBS lead is finally implanted is in general somewhere around the chosen anatomical target, i.e., more than 5 mm away from the guide tube, the medical staff should be aware of those differences and consider further retracting the guide tube in those regions.

The presence of the parallel leads during MER also affects the EF distribution. A deformation of the EF in the lateral direction at the level of the stimulating contact and especially of the guide tube exists compared to the use of only one trajectory. Nevertheless, a neuronal activation at the level of the guide tube might still be possible.

4.2. Non-Active Contacts for DBS

The investigation of the influence of the non-activated contacts of the DBS lead, placed in the same position as the MER contact, shows that the EF extension obtained for the MER stimulation contact is quite reproducible with the DBS contact. The highest but still slight difference could be seen for contact C0 with a lower extension down the trajectory. For clinical practice, this means that to limit the influence of this effect and to guarantee the best reproducible form, another contact other than C0 could be put at the position with the best clinical result obtained during intraoperative stimulation.

4.3. Position of the DBS Active Contact

The present study also demonstrated that it is possible to have an overlap of EF between the MER and the DBS, even when the active contacts are not in the same location (Figures 4–6). Nevertheless, to reproduce the same EF extension as with the MER electrode, the center of a DBS contact should be optimally placed at this position as the different DC and CC have shown. At other positions, it is also possible to partially or completely cover the volume generated by the MER lead, but the consequence might be a non-necessary extension in other directions as seen by lower DCs, which could induce side effects and which result in a higher energy consumption.

4.4. Clinical Case

The clinical application shows an example of a patient where the final stimulation position with the DBS lead does not correspond to the intraoperatively identified position, which produced the best clinical effect (Figure 7). The simulations, performed by placing the DBS lead at the coordinates identified on the postoperative CT images, showed no overlap of the EF at the level of the optimal position and a very low Dice coefficient. The DBS contact selected and programmed six months after surgery, however, achieved a satisfactory improvement in the relief of the patient symptoms. Plausible reasons for differences in the MER and DBS trajectories may include imaging uncertainties or brain shift. The hypothetical cases presented in Figure 7D,E suggest a better selection of chronic stimulation according to the EF distribution and a higher coverage coefficient. The application of the presented approach to numerous patients and the correlation with the anatomical positions would be very interesting in terms of further analyzing differences of intraoperative and chronic stimulation.

In order to base the simulations on realistic examples, the chosen electrode types and parameters originate from the clinical DBS protocol at the Department of Neurosurgery, Clermont-Ferrand University Hospital [16]. One has to be aware that there may be differences in protocols depending on the chosen MER system and DBS implantation procedure at the individual clinical center. Some clinics abandon MER and others use the chronic DBS lead for intraoperative tests in a bipolar or monopolar configuration. The monopolar test stimulation uses the addition of a contact, either as a guiding cannula or a scalp needle, to close the current loop substituting the neurostimulator as it is not implanted at this point. The FEM simulations performed in this study do not consider all possible situations, but give an idea of potential influencing factors that the medical staff should keep in mind. As presented in Figure 7, the DBS lead will most likely not be able to exactly reproduce the EF generated by the MER setup. By presenting this general method for modeling and simulation, additional studies for similar clinical protocols and MER-systems can be studied in the future.

4.5. Methodology

The size of the MER and DBS contacts varies, especially in the lateral direction (0.55 mm vs. 1.27 mm). For the 3D models and the DC calculation, the contact volumes have been considered as described in the method section. Nevertheless, the results of the 2D simulations (Figure 4) have to be interpreted with care as the extension has been determined starting from the center line of the electrodes and not from the surface. As the lateral dimension of the MER electrodes is smaller than the one of the DBS lead, the volume of tissue included for the same extension will be higher for MER stimulation than for DBS.

The DC quantifies the similarity between two volumes; however, the ultimate goal for the DBS electrode implantation is to reproduce the improvement observed during MER exploration. To this extent, CC gives a representation of up to how much DBS stimulation can potentially reproduce the effect of the MER stimulation. However, tissue stimulated during DBS, which was not included in the MER stimulation, can be the source of unwanted side-effects, which is why both DC and CC were used in conjunction.

The models of the MER and the DBS system contain several assumptions and simplifications and the results have to be considered as approximations to reality. The MER stimulation contact for instance is assumed to inject current through the entire surface which might not be totally accurate due to the space occupied by the retracted recording microelectrode at the bottom. The influence is assumed to be irrelevant, but it has not been evaluated yet. Another assumption is that there is no electrode-tissue interface for the MER stimulation contact as the PES for the DBS model. This interface is disregarded due to the small dimensions of the MER system and to the short period of time taken to perform the intraoperative stimulation tests.

Furthermore, Figure 4 shows how each system responds differently to conductivity changes in the surrounding media. For the homogeneous electrical conductivity of 0.123 S/m, both systems reached nearly the same EF extension despite differences in the operating mode and contact dimensions. This specific result responds to the conductivity value used and to the inclusion of a PES with a lower conductivity in the DBS model [19]. On the other hand, when using a lower conductivity in the surrounding medium as for the patient-specific models (~0.079 S/m), the EF volume obtained with the MER lead was considerably larger, e.g., from 23.9 mm^3 to 49.5 mm^3 for 1 mA (Figure 3 compared to Figure 5). The magnitude of the EF, dependent on the current density (Equation (1)), increases as the contact surface area decreases [25], and thus the smaller contact of the MER system is capable of generating a similar EF to the larger DBS contacts. For a lower conductivity of the surrounding medium, the system operated under current control has to increase the voltage in order to maintain a constant current through the contact.

The fast technical development and the introduction of new supportive systems for DBS surgery along the improved imaging facilities are making direct targeting more common [29]; however, the selection of the stimulation parameters is still driven by the clinical outcome. In this regard,

computer models represent a valuable aid for the clinical staff due to the possibility to visualize how the stimulation field is influenced by changes in the stimulation parameters and electrical setup.

5. Conclusions

Simulations showed that the EF generated by MER stimulation can be partially reproduced with the DBS electrodes. Nevertheless, the present study demonstrated that differences exist due to different electrical settings, operating modes, and electrode designs, resulting in EF deformations and variations in extension and volume. Those results might explain the differences between the intraoperatively identified optimal position and the one induced during chronic DBS. Clinicians should be aware of this and take these influences and differences into account during MER stimulation.

Author Contributions: F.A., S.H. and K.W. initiated the study and conducted the overall planning. All authors contributed to the design of the study. F.A. ran the simulations and performed the data analysis together with D.V. J.J. supported with expertise regarding the FEM models. F.A. was mainly responsible for writing the paper and the other authors contributed with their special competence.

Conflicts of Interest: The authors declare no conflict of interest.

References

1. Benabid, A.L.; Chabardes, S.; Mitrofanis, J.; Pollak, P. Deep brain stimulation of the subthalamic nucleus for the treatment of parkinson's disease. *Lancet Neurol.* **2009**, *8*, 67–81. [CrossRef]

2. Blond, S.; Siegfried, J. Thalamic stimulation for the treatment of tremor and other movement disorders. *Acta Neurochir. Suppl.* **1991**, *52*, 109–111. [PubMed]

3. Krauss, J.K.; Pohle, T.; Weber, S.; Ozdoba, C.; Burgunder, J.M. Bilateral stimulation of globus pallidus internus for treatment of cervical dystonia. *Lancet* **1999**, *354*, 837–838. [CrossRef]

4. Kuncel, A.M.; Grill, W.M. Selection of stimulus parameters for deep brain stimulation. *Clin. Neurophysiol.* **2004**, *115*, 2431–2441. [CrossRef] [PubMed]

5. Bour, L.J.; Contarino, M.F.; Foncke, E.M.; de Bie, R.M.; van den Munckhof, P.; Speelman, J.D.; Schuurman, P.R. Long-term experience with intraoperative microrecording during DBS neurosurgery in STN and GPi. *Acta Neurochir.* **2010**, *152*, 2069–2077. [CrossRef] [PubMed]

6. Mehanna, R.; Machado, A.G.; Connett, J.E.; Alsaloum, F.; Cooper, S.E. Intraoperative microstimulation predicts outcome of postoperative macrostimulation in subthalamic nucleus deep brain stimulation for parkinson's disease. *Neuromodulation J. Int. Neuromodulation Soc.* **2017**, *20*, 456–463. [CrossRef] [PubMed]

7. Hrabovsky, D.; Balaz, M.; Bockova, M.; Feitova, V.; Novak, Z.; Chrastina, J. Learning curve in anatomo-electrophysiological correlations in subthalamic nucleus stimulation. *Turk. Neurosurg.* **2017**, *1*. [CrossRef] [PubMed]

8. McIntyre, C.C.; Mori, S.; Sherman, D.L.; Thakor, N.V.; Vitek, J.L. Electric field and stimulating influence generated by deep brain stimulation of the subthalamic nucleus. *Clin. Neurophysiol.* **2004**, *115*, 589–595. [CrossRef] [PubMed]

9. Åström, M.; Zrinzo, L.U.; Tisch, S.; Tripoliti, E.; Hariz, M.I.; Wårdell, K. Method for patient-specific finite element modeling and simulation of deep brain stimulation. *Med. Biol. Eng. Comput.* **2009**, *47*, 21–28. [CrossRef] [PubMed]

10. Åström, M.; Diczfalusy, E.; Martens, H.; Wårdell, K. Relationship between neural activation and electric field distribution during deep brain stimulation. *IEEE Trans. Biomed. Eng.* **2015**, *62*, 664–672. [CrossRef] [PubMed]

11. Åström, M.; Lemaire, J.J.; Wårdell, K. Influence of heterogeneous and anisotropic tissue conductivity on electric field distribution in deep brain stimulation. *Med. Biol. Eng. Comput.* **2012**, *50*, 23–32. [CrossRef] [PubMed]

12. Åström, M.; Tripoliti, E.; Hariz, M.I.; Zrinzo, L.U.; Martinez-Torres, I.; Limousin, P.; Wårdell, K. Patient-specific model-based investigation of speech intelligibility and movement during deep brain stimulation. *Stereotact. Funct. Neurosurg.* **2010**, *88*, 224–233. [CrossRef] [PubMed]

13. Hemm, S.; Mennessier, G.; Vayssiere, N.; Cif, L.; El Fertit, H.; Coubes, P. Deep brain stimulation in movement disorders: Stereotactic coregistration of two-dimensional electrical field modeling and magnetic resonance imaging. *J. Neurosurg.* **2005**, *103*, 949–955. [CrossRef] [PubMed]

14. Alonso, F.; Latorre, M.A.; Goransson, N.; Zsigmond, P.; Wårdell, K. Investigation into deep brain stimulation lead designs: A patient-specific simulation study. *Brain Sci.* **2016**, *6*, 39. [CrossRef] [PubMed]

15. Coenen, V.A.; Allert, N.; Paus, S.; Kronenburger, M.; Urbach, H.; Madler, B. Modulation of the cerebello-thalamo-cortical network in thalamic deep brain stimulation for tremor: A diffusion tensor imaging study. *Neurosurgery* **2014**, *75*, 657–669, discussion 669–670. [CrossRef] [PubMed]

16. Hemm, S.; Pison, D.; Alonso, F.; Shah, A.; Coste, J.; Lemaire, J.J.; Wardell, K. Patient-specific electric field simulations and acceleration measurements for objective analysis of intraoperative stimulation tests in the thalamus. *Front. Hum. Neurosci.* **2016**, *10*, 577. [CrossRef] [PubMed]

17. Akbarian-Tefaghi, L.; Akram, H.; Johansson, J.; Zrinzo, L.; Kefalopoulou, Z.; Limousin, P.; Joyce, E.; Hariz, M.; Wardell, K.; Foltynie, T. Refining the deep brain stimulation target within the limbic globus pallidus internus for tourette syndrome. *Stereotact. Funct. Neurosurg.* **2017**, *95*, 251–258. [CrossRef] [PubMed]

18. Horn, A.; Reich, M.; Vorwerk, J.; Li, N.; Wenzel, G.; Fang, Q.; Schmitz-Hübsch, T.; Nickl, R.; Kupsch, A.; Volkmann, J. Connectivity predicts deep brain stimulation outcome in parkinson's disease. *Ann. Neurol.* **2017**, *82*, 67–78. [CrossRef] [PubMed]

19. Alonso, F.; Hemm-Ode, S.; Wårdell, K. Influence on deep brain stimulation from lead design, operating mode and tissue impedance changes—A simulation study. *Brain Disord. Ther.* **2015**, *4*. [CrossRef]

20. Yousif, N.; Bayford, R.; Liu, X. The influence of reactivity of the electrode-brain interface on the crossing electric current in therapeutic deep brain stimulation. *Neuroscience* **2008**, *156*, 597–606. [CrossRef] [PubMed]

21. Gabriel, S.; Lau, R.W.; Gabriel, C. The dielectric properties of biological tissues: III. Parametric models for the dielectric spectrum of tissues. *Phys. Med. Biol.* **1996**, *41*, 2271–2293. [CrossRef] [PubMed]

22. Åström, M.; Johansson, J.D.; Hariz, M.I.; Eriksson, O.; Wårdell, K. The effect of cystic cavities on deep brain stimulation in the basal ganglia: A simulation-based study. *J. Neural Eng.* **2006**, *3*, 132–138. [CrossRef] [PubMed]

23. Shah, A.; Coste, J.; Lemaire, J.J.; Taub, E.; Schupbach, W.M.M.; Pollo, C.; Schkommodau, E.; Guzman, R.; Hemm-Ode, S. Intraoperative acceleration measurements to quantify improvement in tremor during deep brain stimulation surgery. *Med. Biol. Eng. Comput.* **2017**, *55*, 845–858. [CrossRef] [PubMed]

24. Sørensen, T. A method of establishing groups of equal amplitude in plant sociology based on similarity of species and its application to analyses of the vegetation on danish commons. *Biol. Skr.* **1948**, *5*, 1–34.

25. McIntyre, C.C.; Grill, W.M. Finite element analysis of the current-density and electric field generated by metal microelectrodes. *Ann. Biomed. Eng.* **2001**, *29*, 227–235. [CrossRef] [PubMed]

26. Wei, X.F.; Grill, W.M. Current density distributions, field distributions and impedance analysis of segmented deep brain stimulation electrodes. *J. Neural Eng.* **2005**, *2*, 139–147. [CrossRef] [PubMed]

27. Butson, C.R.; McIntyre, C.C. Role of electrode design on the volume of tissue activated during deep brain stimulation. *J. Neural Eng.* **2006**, *3*, 1–8. [CrossRef] [PubMed]

28. Kuncel, A.M.; Cooper, S.E.; Grill, W.M. A method to estimate the spatial extent of activation in thalamic deep brain stimulation. *Clin. Neurophysiol.* **2008**, *119*, 2148–2158. [CrossRef] [PubMed]

29. Hemm, S.; Wårdell, K. Stereotactic implantation of deep brain stimulation electrodes: A review of technical systems, methods and emerging tools. *Med. Biol. Eng. Comput.* **2010**, *48*, 611–624. [CrossRef] [PubMed]

PAPER **IV**

frontiers
in Human Neuroscience

Patient-Specific Electric Field Simulations and Acceleration Measurements for Objective Analysis of Intraoperative Stimulation Tests in the Thalamus

Simone Hemm[1,2]*[†], Daniela Pison[1†], Fabiola Alonso[2], Ashesh Shah[1], Jérôme Coste[3,4], Jean-Jacques Lemaire[3,4] and Karin Wårdell[2]

[1] Institute for Medical and Analytical Technologies, School of Life Sciences, University of Applied Sciences and Arts Northwestern Switzerland FHNW, Muttenz, Switzerland, [2] Department of Biomedical Engineering, Linköping University, Linköping, Sweden, [3] Université Clermont Auvergne, Université d'Auvergne, EA 7282, Image Guided Clinical Neurosciences and Connectomics (IGCNC), Clermont-Ferrand, France, [4] Service de Neurochirurgie, Hôpital Gabriel-Montpied, Centre Hospitalier Universitaire de Clermont-Ferrand, Clermont-Ferrand, France

Despite an increasing use of deep brain stimulation (DBS) the fundamental mechanisms of action remain largely unknown. Simulation of electric entities has previously been proposed for chronic DBS combined with subjective symptom evaluations, but not for intraoperative stimulation tests. The present paper introduces a method for an objective exploitation of intraoperative stimulation test data to identify the optimal implant position of the chronic DBS lead by relating the electric field (EF) simulations to the patient-specific anatomy and the clinical effects quantified by accelerometry. To illustrate the feasibility of this approach, it was applied to five patients with essential tremor bilaterally implanted in the ventral intermediate nucleus (VIM). The VIM and its neighborhood structures were preoperatively outlined in 3D on white matter attenuated inversion recovery MR images. Quantitative intraoperative clinical assessments were performed using accelerometry. EF simulations ($n = 272$) for intraoperative stimulation test data performed along two trajectories per side were set-up using the finite element method for 143 stimulation test positions. The resulting EF isosurface of 0.2 V/mm was superimposed to the outlined anatomical structures. The percentage of volume of each structure's overlap was calculated and related to the corresponding clinical improvement. The proposed concept has been successfully applied to the five patients. For higher clinical improvements, not only the VIM but as well other neighboring structures were covered by the EF isosurfaces. The percentage of the volumes of the VIM, of the nucleus intermediate lateral of the thalamus and the prelemniscal radiations within the prerubral field of Forel increased for clinical improvements higher than 50% compared to improvements lower than 50%. The presented new concept allows a detailed and objective analysis of a high amount of intraoperative data to identify the optimal stimulation target. First results indicate agreement with published data hypothesizing that the stimulation of other structures than the VIM might be responsible for good clinical effects in essential tremor.
(Clinical trial reference number: Ref: 2011-A00774-37/AU905)

INTRODUCTION

Deep brain stimulation (DBS) is a common neurosurgical procedure for relieving movement disorders such as those observed in Parkinson's disease (PD) (Benabid et al., 1993, 2009; Hemm and Wårdell, 2010), essential tremor (ET) (Benabid et al., 1991) and dystonia (Coubes et al., 2000; Cif et al., 2010). Despite an increasing use and an extension of the indications (Hariz et al., 2013), the fundamental mechanisms underlying stimulation-induced effects, either therapeutic or adverse, remain largely unknown. The exact anatomical regions or white matter fibers responsible for these effects are still subject of discussion (Herrington et al., 2015). During a typical surgical planning, the optimal implantation position for a specific target is first approached based on anatomical images. Intraoperatively, the micro contact of an exploration electrode is often used for micro-electrode recordings (MER) (Coste et al., 2009) to evaluate the neuronal activity at previously planned positions of deep brain structures. In a further step, intraoperative stimulation tests are performed through the macro contact of the exploration electrode at different locations with help of the MER-system, and changes in the patient's symptoms are observed by clinical examination. The DBS electrode is finally implanted at the location with the highest therapeutic effect on the symptom with minimal stimulation amplitude and side effects, or with side effects occurring only for high stimulation amplitudes. This procedure is completely based on the physicians experience and will therefore vary depending on the clinical skills (Post et al., 2005).

A way to objectify this evaluation is to use accelerometer recordings of the movements. We have previously presented a method to support the physician's evaluation during surgery by quantifying intraoperatively obtained therapeutic effects on tremor (Shah et al., 2016b) and rigidity (Shah et al., 2016a) with the help of wrist acceleration measurements. These results suggest that mathematical parameters extracted from the acceleration signal are more sensitive to detect changes in tremor during intraoperative stimulation tests than the subjective neurologist's evaluation. An enhancement of this methodology would be to relate the wrist accelerometer measurements for the evaluation of intraoperative stimulation tests with the patient's own brain anatomy and patient-specific simulations of the EF around the stimulation electrode.

The finite element method (FEM) is commonly used to simulate the distribution of the EF around DBS electrodes often taking into account the individual patient's anatomical data (Åström et al., 2009; Chaturvedi et al., 2010; Wårdell et al., 2015). The established models have been applied to relate the results of long term chronic stimulation to anatomical structures surrounding the stimulating contact. However, the use of patient-specific models to simulate data acquired during intraoperative stimulation tests has not yet been proposed.

To support the patient-specific simulations and also the surgical planning, different brain atlases have been suggested over the years (Schaltenbrand and Bailey, 1959; Morel, 2007). This is especially important for brain nuclei generally not visible with current conventional magnetic resonance imaging (MRI).

With specific sequences it is possible to detail most common substructures of the thalamus and of other deep brain regions (Zerroug et al., 2016). Lemaire et al. (2010) introduced a high resolution atlas of the thalamus which makes extraction of such nuclei possible.

The aim of the present study was to introduce a new methodology combining different patient-specific data to identify the optimal implant position of the chronic DBS lead: thalamic patient-specific brain maps, EF simulations for intraoperative stimulation tests based on patient-specific simulation models and the corresponding therapeutic effects quantitatively evaluated by wrist accelerometer recordings. To illustrate the feasibility of this methodology, it was applied to five patients with ET who underwent stimulation tests during targeting of the ventral intermediate nucleus of the thalamus (VIM). An exemplary way of analysis is presented by comparing the extension of stimulation for no/low and intermediate/high improvements.

MATERIALS AND METHODS

An overview of the methodology including imaging, generation of patient-specific maps of the thalamic region, surgical planning, surgical procedure, stimulation tests, accelerometer measurements, patient-specific EF simulations and data analysis is presented in **Figure 1**.

Surgical Protocol

Stereotactic exploration and lead implantation were performed at the Department of Neurosurgery, Clermont-Ferrand University Hospital, France, under local anesthesia in a two-day procedure.

The first day, the stereotactic frame was mounted on the patient's head (Leksell® G frame, Elekta Instrument AB, Sweden) under local anesthesia. T1 MRI (0.63 mm × 0.63 mm ×1.30 mm) and white matter attenuated inversion recovery images (WAIR, 0.53 mm × 0.53 mm × 2.00 mm) (Magnotta et al., 2000; Lemaire et al., 2007) were acquired (Sonata, 1.5T, Siemens, Germany). Using a stereotactic planning software (iPlan 3, Brainlab, Feldkirchen, Germany), the VIM and its anatomic neighbors were carefully identified and manually outlined on the coronal plane of the WAIR sequence (Lemaire et al., 2010; Zerroug et al., 2016). The nuclei identification followed the previously published nomenclature (Lemaire et al., 2010; Vassal et al., 2012) based on their relative positions, intrinsic MRI tissue contrasts on 1.5T WAIR images (see Figure 6 in Zerroug et al., 2016) and an in-house microscopic 4.7T 3D T1 MRI atlas (see Figure 1 in Vassal et al., 2012). Target coordinates and two parallel trajectories were defined according to the stereotactic reference system, without AC-PC referencing. **Figure 2** shows a stereotactic planning including the patient-specific brain map and the planned trajectory.

The second day, after repositioning of the frame and stereotactic computed tomography (CT) acquisition (0.59 mm × 0.59 mm × 1.25 mm), the planned trajectories were checked and adjusted if necessary with the stereotactic reference system of the CT after rigid image fusion of WAIR and CT data sets. The target region was then explored intraoperatively

FIGURE 1 | Overview of the surgical workflow and the different data acquisition methods. WAIR, white matter attenuated inversion recovery.
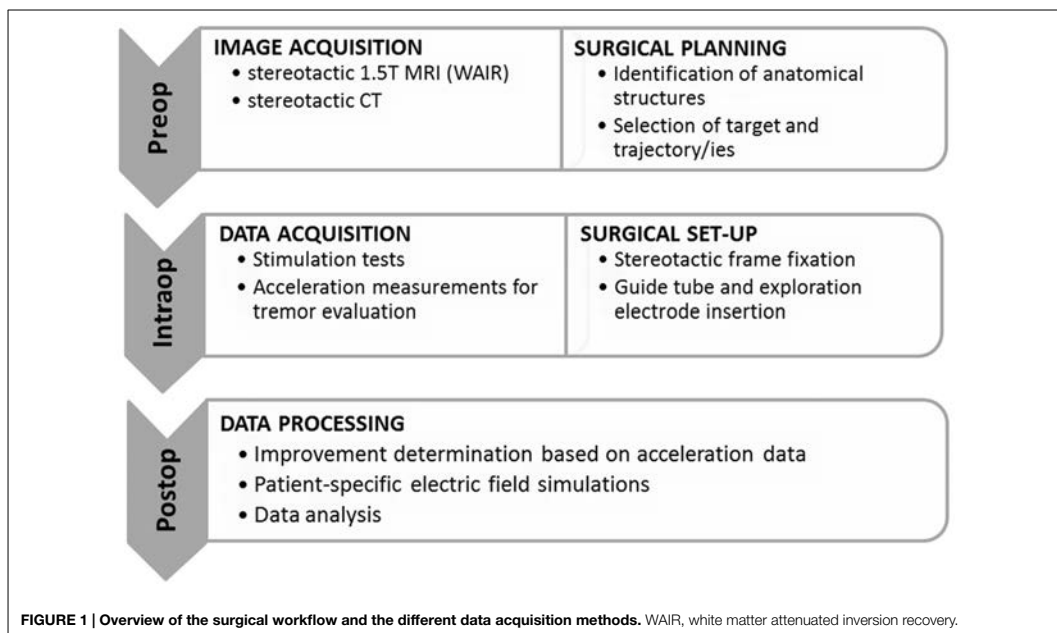
(MicroGuide Pro; Alpha Omega Engineering, Nazareth, Israel) (Slavin and Burchiel, 2002) under local anesthesia using two exploration electrodes (Neuroprobe 366-000024, Alpha Omega Engineering, Nazareth, Israel) that were steered by rigid guide tubes (ACS-7905/200-5, DIXI Microtechniques, Besançon, France): one for the planned track (named the central track) and one placed 2 mm in parallel, usually posterior or posterolateral to the central one. MER was acquired in millimeter steps using the micro contact of the electrode which was retracted before starting stimulation tests in order to avoid tissue damage. Gradual stimulation tests were performed at the same locations through a macro contact to assess clinical benefit and adverse effects and to identify the optimal target. For each stimulation test, the surgical team identified and noted the maximum change in the patient's tremor relative to the initial state of the patient (baseline), and the corresponding stimulation amplitude as well as the occurrence of side effects. MER and stimulation tests were in general performed in a range starting some millimeters in front of the target point and going slightly below depending on the anatomical location. In addition to this routine assessment of tremor, wrist accelerometer measurements and video recordings were performed. Following the stimulation tests, a quadripolar DBS-lead (Lead 3389, Medtronic Inc., USA) was implanted at the optimal stimulation spot for chronic stimulation.

Acceleration Measurements

To perform intraoperative acceleration measurements, a 3-axis accelerometer, placed inside an in-house developed plastic case, was tied to the patient's wrist on the opposite side of the stimulated hemisphere. Via a USB cable, the device was connected to a laptop based data recorder using homemade software LemurDBS (Java 1.6, Oracle, USA) (Shah et al., 2013). Synchronization between acceleration data and test stimulation amplitudes was assured by a pulse sent from the laptop to the stimulating equipment. The sensor was always attached at the same position on the wrist of the patient, and at each position a baseline recording was acquired before initiation of each stimulation sequence.

In order to quantify the clinical improvement for each stimulation amplitude, a previously developed analysis method in Matlab (R2014b) was used (Shah et al., 2016b). As a first step, movements other than tremor were removed offline by using the smoothness priors method (Tarvainen et al., 2002) and thereafter a second order Butterworth low pass-filter was applied at 10 Hz in order to suppress noise. Statistical features (standard deviation, signal energy and the spectral amplitude of the dominant frequency, defined as the frequency of the signal with maximum spectral power) were extracted by moving a 2 second-window over the data. These features were then normalized to the feature set representing the most intense tremor at baseline, i.e., during an initial off-stimulation period at the same position. For each stimulation amplitude the mean of the obtained quantitative clinical improvement was retained as a percentage value. An example is presented in **Figure 3A** where a typical acceleration signal in one position is presented together with the clinical improvement based on the calculated features. In the presented example, it can be seen that an improvement of 98.1% was obtained at a stimulation amplitude of 1.0 mA.
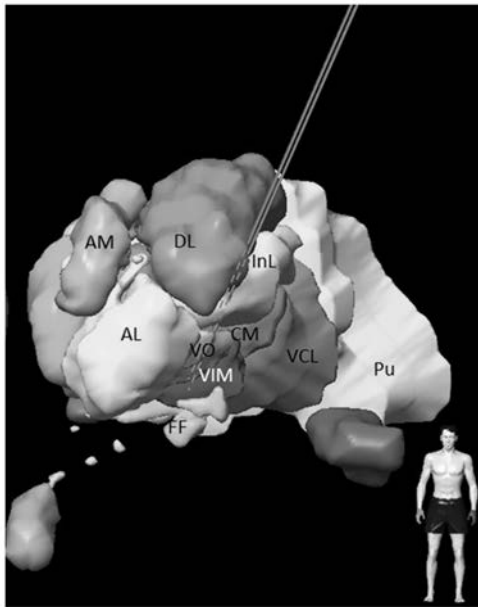
FIGURE 2 | Frontal view of left hemisphere of a 3D stereotactic planning for targeting the VIM, after manual outlining of the thalamic nuclei on 1.5 T WAIR images: VIM; VO; nucleus intermedio lateral (InL); nucleus ventrocaudal lateral (VCL); nucleus dorsolateral (DL); pulvinar (PU); nucleus anterolateral (AL); nucleus ventro-oral (VO); field of Forel (FF); nucleus centromedian (CM); the nucleus ventrocaudal medial (VCM) and the pre-lemniscal radiations (PLR) within the prerubral field of Forel are not visible. Central and posterior left trajectories are visible (brown lines) and marked as dashed lines if inside the nuclei.

Electric Field Simulations

In order to simulate the EF spatial distribution within the brain, a 3D FEM model of the exploration electrode with the surrounding brain tissue was built (Comsol Multiphysics, Version 4.4 Comsol AB, Sweden) for adapting an already established patient-specific modeling technique for DBS leads (Åström et al., 2010; Wårdell et al., 2015).

Brain Tissue Model

The axial preoperative T1 MRI was registered and resampled to the stereotactic preoperative axial CT dataset. In a next step, it was imported into the in-house developed software (Matlab R2013) (Wårdell et al., 2012) modified for the creation of the brain tissue models. A separate filtered axial T1 image batch with enhanced region of interest was used to segment cerebrospinal fluid (CSF), gray matter and white matter (Alonso et al., 2016). The segmented image voxels were assigned with the corresponding electrical conductivities

(σ) (Gabriel et al., 1996)[1]. CSF and blood were set to 2.0 Siemens/meter (S/m) and 0.7 S/m, respectively. Considering the frequency (130 Hz) and pulse length (60 µs) of the stimulation (Wårdell et al., 2013), to gray matter was assigned 0.123 S/m and to white matter 0.075 S/m. Interpolation was done for conductivity values in-between the thresholds used. In order to reduce the simulation time, a region of interest (a cuboid of approximately 100 mm per side) covering the thalamus and its surroundings was selected from the brain tissue model.

Exploration Electrode and Guide Tube Model

A model of the stimulating contact of the exploration electrode and the guide tube was developed. **Figure 4A** presents the outer and inner dimensions of the exploration electrode and the guide tube, **Figure 4B** the corresponding model. The end of the guide tube was fixed 12 mm above the chosen target point, i.e., above the *a priori* optimal anatomic spot. A second exploration electrode and guide tube model was positioned in parallel at a distance of 2 mm. The distance between the guide tube and the center of the stimulating contact decreased or increased when the simulation site was ahead or beyond the target point, respectively. The center of the stimulating contact was placed at the different planned stimulation positions. The micro contact was not considered as it was retracted during the stimulation tests.

Simulations

The EF was calculated by using the equation of continuity for steady current according to:

$$\nabla \cdot \overline{J} = \nabla \cdot (\sigma \nabla V) = 0$$

where J is the current density, σ a matrix containing the electrical conductivity values for the region of interest (thalamus and neighborhood) and V the electric potential. A monopolar configuration was conducted using the guide tube as the reference electrode setting it to ground, and the active electrode set to the same current as used during the stimulation tests. The non-active contact of the parallel lead was set to floating potential (Schmidt et al., 2013). The exterior boundaries of the tissue model were set to electrical insulation. The mesh density (consisting of about 250,000 tetrahedral elements) was defined by the built in physics-controlled mesh generator, where the smallest elements (0.204 mm) were located nearby the stimulating contacts in order to capture the strong EF gradients. The Cartesian coordinates of the points describing the surface of the simulated EF volume (**Figure 3C**) were exported for further analysis. In this study an EF isolevel of 0.2 V/mm was used in order to be able to perform relative comparisons between the simulations and to comply with approximate axon diameters in the thalamus (Kuncel et al., 2008; Åström et al., 2015; Alonso et al., 2016).

---

[1] Andreuccetti, D., R. Fossi and C. Petrucci, Florence, Italy. (2005). "Dielectric properties of the tissue." from http://niremf.ifac.cnr.it/tissprop/.

FIGURE 3 | Workflow for the generation of patient-specific 3D brain maps. (A) Typical data in one stimulation position showing changes in tremor in relation to the increasing stimulation amplitude [mA] (red curve), filtered acceleration data [g] (gray curve), clinical improvement relative to baseline, quantified by acceleration measurements in percentage values from 0 to 100% (mean value for each stimulation amplitude; black dotted line). **(B)** MR-WAIR sequence used for planning including manually outlined structures. **(C)** Patient-specific EF simulation visualized at isolevel 0.2 V/mm at the stimulation position for an amplitude of 1 mA (green circle) corresponding to 98.1% improvement. **(D)** Manually outlined structures: CM (red), VO (light blue), VIM (dark blue) and VCM (pink). **(E)** Brain map with superimposed EF isosurface (green). **(F)** Close up view of **(E)** with the structure volumes inside the EF isosurface indicated in orange.

Thalamic Brain Maps and Electric Field Visualization

The thalamic structures (**Figures 2** and **3B**) initially outlined on the WAIR weighted sequence in the iPlan software were exported in form of slices parallel to the stereotactic CT data set via an interface based on VVLink and VTK (VTK 5.2.0, Kitware Inc., Clifton Park, NY, USA). Target and trajectory coordinates were also exported in CT image coordinates by the same software interface. The CT data set was chosen

as it provides a higher resolution and no distortion of the stereotactic reference system compared to MR sequences. With the exported data a 3D thalamic brain map with trajectories was generated in Matlab (R2014b) (**Figure 3D**). For each stimulation test position and amplitude, the EF isosurface generated through FEM simulations was imported, superimposed to the 3D thalamic brain map and color-coded depending on the induced, quantitatively evaluated improvement (**Figure 3E**).

FIGURE 4 | (A) Schematic representation of the guide tube and the exploration electrode including the micro contact for recording and the macro contact for stimulation, **(B)** FEM model of the exploration electrode (recording tip is excluded as it is retracted during stimulation) and the guide tube. The probe slides within the fixed grounded guide tube placed 12 mm from a target point corresponding to the *a priori* optimal anatomic spot. Explorations were performed moving the stimulation point along the trajectory, D millimeters proximal or distal to the target position.

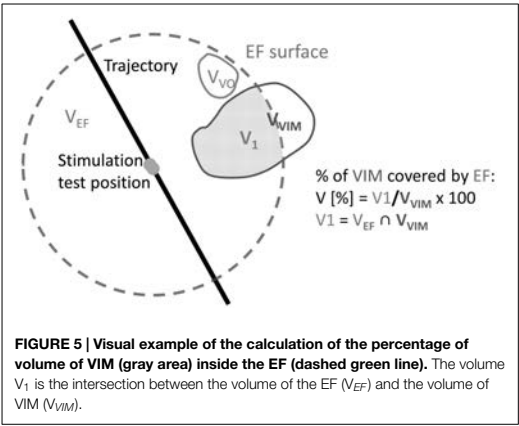## Volumetric Analysis

An in-house algorithm developed by FHNW in Matlab (R2014b) was applied to detect and calculate the volume of the anatomical structures inside each EF isosurface. To reduce the computational time, a list of candidate structures (e.g., VIM, VO, and CM) was identified from the entire structure group by excluding the structures outside the coordinate's ranges of the EF volume. For each candidate structure, the points of the EF isosurface inside the structures' volume were detected by considering them as a concave or convex hull according to their shape. The obtained volume based on the selected point cloud was then calculated and associated with the respective clinical improvement. The algorithms then generated a list of the thalamic structures lying partially or completely inside the 0.2 V/mm EF isosurface, their volumes as well as the volume covered by the EF surface and the associated improvement value (**Figure 3F**).

Clinical Application

The above presented protocol was applied to five ET patients (three male and two female) undergoing bilateral DBS electrode implantation in the VIM region and successively to both hemispheres. They gave their written informed consent to participate in the study (Ref: 2011-A00774-37/AU905, Comité de Protection des Personnes Sud-Est 6, Clermont-Ferrand, France). No alterations were made to the routine surgical procedure. In all patients a central and a posterior trajectory were chosen per hemisphere for MER and stimulation tests (stimulation parameters: amplitude = 0.2 to 3.0 mA in steps of 0.2 mA, pulse width = 60 µs, frequency = 130 Hz). At each stimulation position stimulation lasted 1 to 3 min depending on the response of the patient and on side effect occurrence or not. Between all stimulation tests, a non-stimulation period was maintained to leave time to the symptoms to come back. The duration of this period depended on patient symptoms (minimum 2 min). Acceleration measurements were performed in parallel to the

FIGURE 5 | Visual example of the calculation of the percentage of volume of VIM (gray area) inside the EF (dashed green line). The volume V_1 is the intersection between the volume of the EF (V_{EF}) and the volume of VIM (V_{VIM}).

test stimulation in 31, 22, 30, 28, and 32 positions for Patient 1 to 5, respectively, mostly from 5 mm above the target point down to 4 mm below depending on the individual anatomical locations. The final electrode implantation site was based on clinical subjective evaluations.

Electric field simulations were performed for all stimulation test positions in both hemispheres of the five patients. At each position, up to four tested stimulation amplitudes were chosen for simulations using the following criteria based on the quantitatively evaluated symptom improvements (I_{acc}): (1) The highest amplitude not resulting in any improvement in tremor compared to baseline; (2) the lowest amplitude at which a first improvement in tremor was measured; (3) The lowest amplitude resulting in at least 50% improvement in tremor; (4) The lowest amplitude resulting in at least 75% improvement. When the first improvement in tremor was more than 75%, criteria (2–4) gave the same amplitude. When the first improvement was identified already between 0.2 and 0.6 mA, no simulations were performed for the criterion 1. The extracted patient-specific 3D brain maps of the thalamus were superimposed with the four trajectories of each patient and with the simulated patient-specific EF isosurfaces. To make the data comparable between patients, the volume inside the isosurface was normalized to the size of the structure resulting in the percentage of the structure covered by the EF (**Figure 5**). For example, if the volume of VIM was 10 mm^3 and only 2 mm^3 of it was encompassed by an EF isosurface, the covered volume of VIM for that EF would have been (2/10)*100 = 20%.

In order to identify structures responsible for the reduction in tremor, the results of all patients together were classified following the quantity of improvement detected by accelerometry (I_{acc}). Data were divided into two groups considering no/low improvements ($I_{acc} \leq 50\%$) and intermediate/high improvements ($I_{acc} > 50\%$), respectively. The resulting data are presented in two different ways for comparison of these two improvement groups. Firstly, for each thalamic structure, the relative number of occurrences (the structure is at least partially

covered by the EF) was determined: the absolute number of occurrences of *each structure* in the considered improvement range was normalized to the total number of occurrences of *all structures* in this range. Second, the percentage volume of each structure covered by a specific EF isosurface was analyzed to see for example if the covered volume of some structures increases for higher improvements. These percentage volumes were graphically represented and visually analyzed together with the induced clinical improvement for all simulations. Furthermore, mean values and the standard error of the mean (SEM) were determined for each structure for the two improvement groups. The results for each structure in the two improvement ranges were statistically compared applying the Mann–Whitney U test. Mean stimulation amplitudes for 50% or less improvement and more than 50% improvement were determined.

RESULTS

Simulations
The proposed concept has been successfully applied to the five patients, resulting in 272 simulations at 143 different stimulation test positions. The detailed numbers of simulations for each patient and different improvement ranges are presented in **Table 1**.
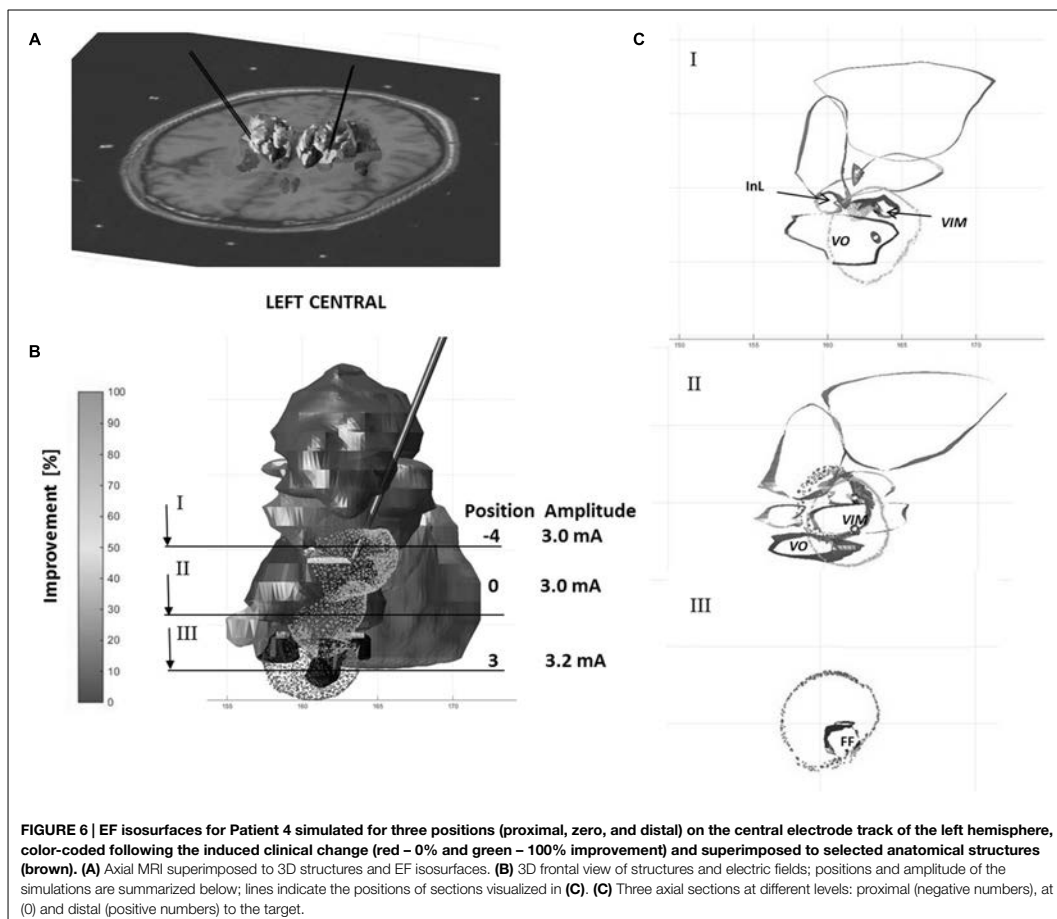
Visualization
Figure 6 shows an example of visualization for Patient 4 with three simulated EF isosurfaces in the left hemisphere along the central tract. Each isolevel is superimposed to the extracted anatomical structures (seen in brown) and the patient-specific MRI (**Figure 6A**). At the target position or the *a priori* optimal anatomic spot for the left central trajectory an improvement of 90% was reached with a stimulation amplitude of 3 mA (**Figure 6B**). 3 mm below the target no improvement in tremor could be observed. The corresponding EF in red overlays the EF of 90% of improvement as can be seen at cross section II through the stimulation electrode as presented in **Figure 6C**.

Involvement of Anatomical Structures
The relative occurrences of the different thalamic structures within the isosurfaces for improvements above and below 50% are presented in **Figure 7**. It shows that the percentage

TABLE 1 | Number of simulations per patient and clinical improvement range as recorded by accelerometry (I_{acc}).

	$0 < I_{acc} \leq 25\%$	$25 < I_{acc} \leq 50\%$	$50 < I_{acc} \leq 75\%$	$75\% < I_{acc} \leq 100\%$	Total
Patient 1	3	13	17	12	45
Patient 2	3	11	20	10	44
Patient 3	1	23	15	22	61
Patient 4	2	9	23	18	52
Patient 5	2	15	23	30	70
Total	11	71	98	92	272

FIGURE 6 | EF isosurfaces for Patient 4 simulated for three positions (proximal, zero, and distal) on the central electrode track of the left hemisphere, color-coded following the induced clinical change (red – 0% and green – 100% improvement) and superimposed to selected anatomical structures (brown). (A) Axial MRI superimposed to 3D structures and EF isosurfaces. **(B)** 3D frontal view of structures and electric fields; positions and amplitude of the simulations are summarized below; lines indicate the positions of sections visualized in **(C)**. **(C)** Three axial sections at different levels: proximal (negative numbers), at (0) and distal (positive numbers) to the target.
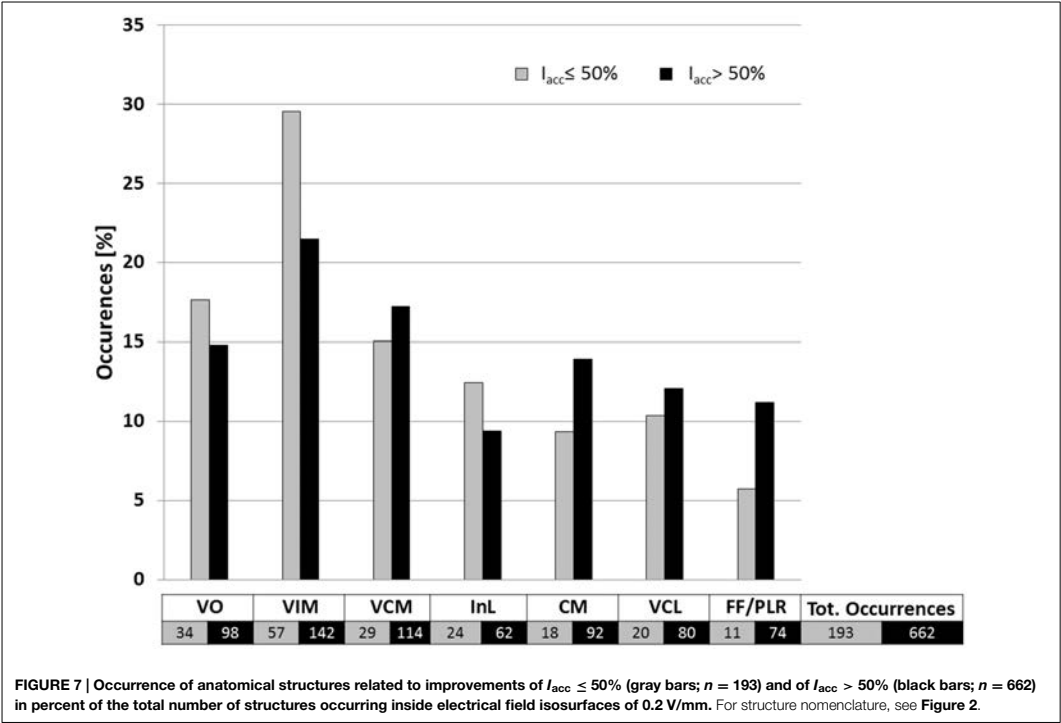
of occurrences of the different structures was always inferior or equal to 30%. The relative occurrence of InL, VO and especially VIM decreases for higher improvements. This means that their appearance does not as much increase as for CM, VCM, VCL and especially for FF/PLR. For all four structures the relative occurrence increases for higher improvements. Mean stimulation amplitudes for improvements $I_{acc} \leq 50\%$ and $I_{acc} > 50\%$ were 0.9 ± 1.1 mA and 1.5 ± 1.2 mA, respectively.

Relation of Structure Occurrences, Clinical Improvement, and Volumes Covered by the Isosurfaces

A comparison between the clinical improvement and the volume of the structures included in the isosurface of the corresponding simulation is presented in **Figure 8**. While

Figure 8A shows all available data of the five patients, **Figures 8B,C** summarize the data in form of mean and SEM for improvements ≤50% and >50%. All SEM values remain below 3% except for the VO and the InL for the range $I_{acc} \leq 50\%$ and the FF/PLR for both improvement ranges. A closer analysis of the volume of the different structures covered by the EF isosurface shows that the percentage volumes of the target structure VIM, of the InL and of the FF/PLR increase with significant clinical improvements. The difference for the VIM was statistically significant ($p < 0001$). Only small volumes of CM and VCL are covered by the isosurface in both improvement ranges. Nevertheless the difference for the CM could be shown to be significant ($p < 0.01$). The neighboring nuclei VIM and VCM appear together for nearly all simulations. FF/PLR and VO occur mostly in combination with VIM and VCM (same horizontal line) (**Figure 8A**).

FIGURE 7 | Occurrence of anatomical structures related to improvements of $I_{acc} \leq 50\%$ (gray bars; $n = 193$) and of $I_{acc} > 50\%$ (black bars; $n = 662$) in percent of the total number of structures occurring inside electrical field isosurfaces of 0.2 V/mm. For structure nomenclature, see **Figure 2**.

DISCUSSION

In the present study, a methodology is described that has the potential to give new insights into the efficacy of different anatomical structures in DBS. It consists in the combined analysis of intraoperatively acquired accelerometry data, patient-specific EF simulations for intraoperative stimulation tests and patient-specific anatomy. The method was successfully applied to five patients with ET and included more than 250 EF simulations. An exemplary way of analysis and preliminary results have been presented for the identification of the therapeutically effective anatomical region.

Quantitative Symptom Evaluation

In order to overcome the limits of existing routinely used clinical rating scales, i.e., the inter- and intra-observer variability (Post et al., 2005; Palmer et al., 2010), the discrete evaluation levels and the high dependence on the experience of the evaluating neurologist (Griffiths et al., 2012), we have used accelerometry-based, quantitative tremor evaluations during intraoperative stimulation tests.

Tremor quantification outside the OR has been proposed since a long time by various authors (Mansur et al., 2007), many of whom have concluded that a quantitative evaluation method is more sensitive than the visually performed clinical evaluation.

Birdno et al. (2008) used an acceleration sensor to study the effects of temporal variations of the stimulation pulse during the replacement of the implantable pulse-generator. Journee et al. (2007) and Papapetropoulos et al. (2008) used quantitative tremor evaluation after the DBS lead was implanted, in order to compare the effects of stimulation through different contacts. But those systems were not designed to be used in different clinical centers or during stimulation tests performed through an exploration electrode. In a previous study, we have demonstrated the use of our system in 15 DBS surgeries in two different clinical centers, the possibility to visualize and revisit recorded data during surgery and the possible influences of quantitative evaluations on the choice of the final implant position of the lead for chronic stimulation (Shah et al., 2016b).

Determination of the Therapeutically Implicated Structures

In the present clinical study, structures individually outlined by the neurosurgeon were available and could be used as anatomical reference. The use of the patient-specific MR-WAIR sequence together with a 4.7 T in-house atlas as reference and stereotactic books make an approximate identification of the structures possible (Zerroug et al., 2016). Other groups have proposed various approaches (Caire et al., 2013) among them projecting the position of the active contact(s) directly onto anatomical
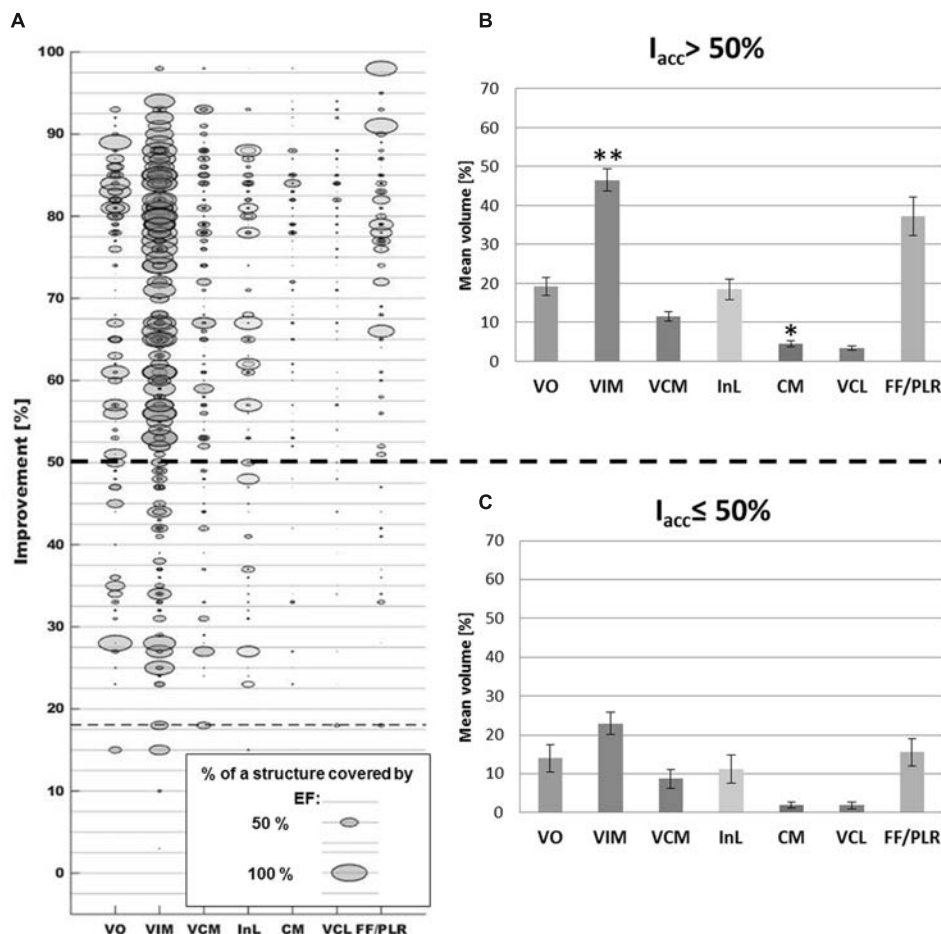
FIGURE 8 | (A) Comparison of the occurrences of the different thalamic brain structures (x-axis; each color represents one structure) with the corresponding clinical improvement evaluated by accelerometry (y-axis) for all simulations (n = 272). Structures appearing in a same simulation have identical clinical improvement and can in consequence be found on the same horizontal level. As an example, the horizontal line at an improvement of approximately 18% indicates that VIM, VCM, VCL, and FF/PLR were present inside a same EF isosurface. **(B)** Summary of the mean percentage volume included in the EF isosurfaces and the standard error of the mean for the different structures in the improvement range >50% and **(C)** in the improvement range ≤50%. **: Statistically significant difference between the results of the two improvement groups for a specific structure with $p < 0.001$. *: Statistically significant difference with $p < 0.01$.

images (Vayssiere et al., 2004), onto anatomical (Saint-Cyr et al., 2002; Sarnthein et al., 2013) or probabilistic functional atlases (Lalys et al., 2013), or linking them to MER results (Zonenshayn et al., 2004) sometimes combined with imaging data (Weise et al., 2013) and white matter tracking (Coenen et al., 2012). To analyze the relationship between the anatomical location of stimulating contacts and the clinical effectiveness of stimulation, we have decided to take into account the extent of stimulation by using EF simulations (Åström et al., 2012) as discussed in detail in the

next paragraph. Other published approaches consider either the anatomical position of the center of the contact (Starr et al., 2002; Voges et al., 2009; Garcia-Garcia et al., 2016) or of the whole contact taking into account its dimensions (Saint-Cyr et al., 2002; Zonenshayn et al., 2004; Herzog et al., 2007; Hemm et al., 2008).

Electric Field Simulations

Finite element method models are commonly used to simulate and visualize the EF distribution around DBS electrodes and the

EF is one of the electrical entities that may be used to represent the stimulation field. In comparison with the electric potential or the second derivative of the electric potential with respect to the distance (activating function), EF has been shown to be the most stable and unchanged entity for different stimulation parameters (amplitude and pulse width) (Åström et al., 2015).

Today, FEM models have progressed from non-specific (McIntyre et al., 2004; Hemm et al., 2005; Åström et al., 2006) to patient-specific taking into account the individual's data (Åström et al., 2009; Chaturvedi et al., 2010; Wårdell et al., 2015). There is no consensus of the degree of complexity of the model to accurately simulate the neural response, however, many groups (Chaturvedi et al., 2010; Schmidt et al., 2013; Alonso et al., 2016; Howell and McIntyre, 2016) have shown that the inclusion of the heterogeneity and anisotropy of the brain tissue increases the model accuracy and prediction capability. For instance, Chaturvedi et al. (2010) and Åström et al. (2012) observed an overestimation of neural activation for homogeneous models. The present study relies on a brain model built upon the segmentation of the gray matter, white matter, CSF and blood from the patients' MRI and in consequence takes into consideration the inhomogeneity of brain tissue. An even more realistic model may be based on DTI which provides more anisotropic information, however, its resolution is lower than the one of MRI and may introduce other errors (Åström et al., 2012). The simulations in this study were performed for constant current while the dispersive components of the brain tissue have been considered by adjusting the conductivity values for gray and white matter to the particular stimulation frequency and pulse width (Wårdell et al., 2013).

According to previous studies where neuron activation distances were calculated using neuronal models (Åström et al., 2015), an isolevel of 0.2 V/mm represents an equivalent activation distance for neurons within 3–4 μm of diameter (Alonso et al., 2016) and thus seems to comply with axon diameters in the thalamus as previously calculated by Åström et al. (Figure 6, 2015) based on Kuncel et al. (2008). The selection of a fixed EF isolevel allows then to compare the volume recruited for different amplitude settings and different positions.

Transferability

The described methodology has been presented for an institution-specific surgical protocol but can be transferred to other clinical centers. The approach can be adapted to any kind of anatomical information. Instead of using manually outlined structures, it is possible to combine the generated data with anatomical atlases – with the limitations inherent to such an approach (Vayssiere et al., 2002; Wodarg et al., 2012; Anthofer et al., 2014) – or with fiber tracking data in order to analyze the implication of different fibers in the mechanism of action of DBS (Coenen et al., 2012). The MR image data (T1, T2) that are needed for the EF simulations are generally acquired in every institution for the surgical planning procedure. A modification of the developed model to the institution-specific stimulation test protocol in awake patients might be necessary: the characteristics of the stimulating electrode as well as the position of the guide tube during

stimulation have to be adapted. The acceleration data recording can relatively easily be added in the intraoperative phase without any changes in the surgical protocol, without lengthening surgery and most importantly, without any discomfort for the patient. Nevertheless, the correlation of the simulation results can be performed as well based on subjective visual evaluations.

Clinical Application

The results of the present paper are described as relative occurrences and percentage volumes of the different anatomical structures covered by the EF isosurface. Even if the number of patients presenting ET in our clinical study was low and thus the confidence concerning the analysis of the mechanism of action of VIM-DBS is limited, we can present preliminary results thanks to the high number of stimulation test positions and EF simulations per patient. First results of these EF simulations in **Figure 7** show that the percentage of occurrence of VCM, CM, and FF/PLR increases for higher improvements while the percentage of VIM occurrences decreases. This can be explained by the fact that in 60 out of 143 measurement sites the center of the stimulation contact was already within the VIM. Furthermore, as shown, there is a tendency that higher improvements are linked to higher stimulation amplitudes leading in general to a larger distribution of EF for a same tissue type. When looking at the percentage of volume of the VIM covered by the isosurface between the two improvement groups (**Figures 8B,C**), a statically significant difference exists. Nevertheless, the size of the individual volumes varies inside each group. This result can be interpreted in two ways: either (I) a specific part of the VIM, for example the efferent fibers, has to be stimulated or (II) other structures than the VIM might at least partially be responsible for the therapeutic effect. Following our preliminary results such structures could be the InL or especially the fiber tracks FF/PLR. This hypothesis would confirm previously published data: parts of the InL have been earlier mentioned for tremor reduction (Hirai and Jones, 1989) and several authors (Spiegelmann et al., 2006; Vassal et al., 2012) have reported that chronic stimulation of PLR works very well. Some authors (Caparros-Lefebvre et al., 1999; Vassal et al., 2012) already suggested that parts of the VO or of the zona incerta (Fytagoridis et al., 2012) could be appropriate targets as well. Recently Groppa et al. (2014) proposed the dentatothalamic tract as key therapeutic DBS target structure.

Following **Figure 7** our data suggest that parts of VCL and CM might be stimulated in some cases. However, **Figure 8** shows that the structure volumes included in the isosurface are below 5% in both improvement ranges. In order to avoid misinterpretation, either patient-specific improvement maps should be used for presentation or thresholds should be introduced to exclude insignificant volumes.

An optimal stimulation position and statistically significant clinical conclusions can only be provided after the analysis of more intraoperative data, the identification of occurring structure combinations and especially the side effect occurrences, which have a major influence on the choice of the final implant position of the chronic DBS lead.

Limitations and Future Work

The suggested methodology allows a detailed interpretation of intraoperatively acquired data but one has to be aware of certain limitations. First of all, the substantial caveats of non-stimulation factors influencing tremor are undeniable and unfortunately inherent in the operating room conditions. Nevertheless, we have employed various signal analysis techniques to minimize the effect of such non-stimulation factors on the evaluation of tremor using accelerometer. Furthermore, the method was defined in a way trying to limit transformation and fusion errors as much as possible (Zrinzo, 2010). Nevertheless due to the available data, WAIR and T1 MRI data sets containing the anatomic information had to be fused to the stereotactic preoperative CT data set providing the reference for the targeting procedure. Concerning the position of the stimulating contact in relation to the structures, we assumed that the microelectrode was positioned exactly as planned. This seems to be a reasonable approach as the microelectrode was the first entering the brain, and it has been observed that brain shifts in the final electrode position and trajectory can appear when the exploration electrode is replaced by the DBS lead (unpublished data).

As the anatomical information is based on the structures manually outlined on the preoperative image data set, the approach does not consider the movement of the tissue due to the electrodes' insertion or brain shift between implantation sides. On the other hand, the use of these preoperative image data sets is common in analysis and simulation methods. The limitations are acceptable as postoperative image data sets present disturbing artifacts around the implanted DBS leads, in the region of interest. To increase the power of the statistic test performed in the present study, more data should be acquired from further patients and included in the analysis. A further limitation, specific to the anatomical information, concerns the availability of only some anatomical structures and the FF/PLR and that always part of the volume of the EF isosurface is outside any manually defined anatomical structure. In consequence, information from white matter fiber tracking would be helpful to define the region anterior to the VIM and the InL and for further investigating possible activation of fiber tracks (Coenen et al., 2012).

The method could in a next step also be complemented with the available MER data at the different positions including the analysis of time patterns describing the network dynamics as proposed by Andres et al. (2015).

The data analysis approach proposed in the present paper considers the percentage of the structure volume covered by the simulated EF isosurface and not which parts of the structure. Further data interpretation could consider the 3D position as well and should generate improvement maps taking into account stimulation positions of amplitudes as well as the occurrence of side effects.

CONCLUSION

A new concept for the analysis of data acquired during DBS surgery has been proposed. A workflow and methodology combining objective intraoperative tremor evaluation with patient-specific EF simulations on manually outlined anatomical structures has been defined and applied to five patients with ET undergoing DBS-implantation. This new approach is combined with an algorithm for detection of the volume of the anatomical structures involved during intraoperative microelectrode stimulation. It can be adapted to further surgical protocols, intraoperative set-ups and to other anatomical data. Its application will allow the analysis of intraoperative data obtained in clinical routine and will support the identification of anatomical structures, parts of them or white matter fibers responsible for the therapeutic effect. The analysis of more data and inclusion of occurrence of side effects are necessary to draw any final conclusions of the most efficient brain targets. The first results, however, indicate agreement with published data hypothesizing that the stimulation of structures other than the VIM might be responsible for good clinical effect in ET.

AUTHOR CONTRIBUTIONS

All authors contributed in writing the manuscript and critically reviewed the last version. SH: Idea and conception of whole approach; design of protocols and clinical study, especially acceleration measurements; set-up of whole method; development of brain map extraction; participation in data analysis and interpretation; main drafting of manuscript. DP: Technical set-up and implementation of the defined workflow; final data analysis of all available multimodal data; participation in data interpretation; main drafting of manuscript. FA: Set-up of the EF simulation with its patient-specific models; performing all the simulations; data analysis. AS: Realization of acceleration measurements and their analysis; choice of parameters for simulation. JC: Set-up of clinical study and intraoperative realization of study; stimulation data acquisition. J-JL: Set-up of clinical study; patient selection and operation; data interpretation. KW: Set-up of initial e-field simulations; conception of work from simulation point of view; support and critical review of whole concept and especially patient-specific simulations.

FUNDING

ACKNOWLEDGMENT

REFERENCES

Alonso, F., Latorre, M., Göransson, N., Zsigmond, P., and Wårdell, K. (2016). Investigation into deep brain stimulation lead designs: a patient-specific simulation study. *Brain Sci.* 6:39. doi: 10.3390/brainsci6030039

Andres, D. S., Cerquetti, D., and Merello, M. (2015). Neural code alterations and abnormal time patterns in Parkinson's disease. *J. Neural. Eng.* 12:026004. doi: 10.1088/1741-2560/12/2/026004

Anthofer, J., Steib, K., Fellner, C., Lange, M., Brawanski, A., and Schlaier, J. (2014). The variability of atlas-based targets in relation to surrounding major fibre tracts in thalamic deep brain stimulation. *Acta Neurochir. (Wien)* 156, 1497–1504. doi: 10.1007/s00701-014-2103-z

Åström, M., Diczfalusy, E., Martens, H., and Wårdell, K. (2015). Relationship between neural activation and electric field distribution during deep brain stimulation. *IEEE Trans. Biomed. Eng.* 62, 664–672. doi: 10.1109/TBME.2014.2363494

Åström, M., Johansson, J. D., Hariz, M. I., Eriksson, O., and Wårdell, K. (2006). The effect of cystic cavities on deep brain stimulation in the basal ganglia: a simulation-based study. *J. Neural. Eng.* 3, 132–138. doi: 10.1088/1741-2560/3/2/007

Åström, M., Lemaire, J. J., and Wårdell, K. (2012). Influence of heterogeneous and anisotropic tissue conductivity on electric field distribution in deep brain stimulation. *Med. Biol. Eng. Comput.* 50, 23–32. doi: 10.1007/s11517-011-0842-z

Åström, M., Tripoliti, E., Hariz, M. I., Zrinzo, L. U., Martinez-Torres, I., Limousin, P., et al. (2010). Patient-specific model-based investigation of speech intelligibility and movement during deep brain stimulation. *Stereotact. Funct. Neurosurg.* 88, 224–233. doi: 10.1159/000314357

Åström, M., Zrinzo, L. U., Tisch, S., Tripoliti, E., Hariz, M. I., and Wårdell, K. (2009). Method for patient-specific finite element modeling and simulation of deep brain stimulation. *Med. Biol. Eng. Comput.* 47, 21–28. doi: 10.1007/s11517-008-0411-2

Benabid, A. L., Chabardes, S., Mitrofanis, J., and Pollak, P. (2009). Deep brain stimulation of the subthalamic nucleus for the treatment of Parkinson's disease. *Lancet Neurol.* 8, 67–81. doi: 10.1016/S1474-4422(08)70291-6

Benabid, A. L., Pollak, P., Gervason, C., Hoffmann, D., Gao, D. M., Hommel, M., et al. (1991). Long-term suppression of tremor by chronic stimulation of the ventral intermediate thalamic nucleus. *Lancet* 337, 403–406. doi: 10.1016/0140-6736(91)91175-T

Benabid, A. L., Pollak, P., Seigneuret, E., Hoffmann, D., Gay, E., and Perret, J. (1993). Chronic VIM thalamic stimulation in Parkinson's disease, essential tremor and extra-pyramidal dyskinesias. *Acta Neurochir. Suppl. (Wien)* 58, 39–44.

Birdno, M. J., Kuncel, A. M., Dorval, A. D., Turner, D. A., and Grill, W. M. (2008). Tremor varies as a function of the temporal regularity of deep brain stimulation. *Neuroreport* 19, 599–602. doi: 10.1097/WNR.0b013e3282f9e45e

Caire, F., Ranoux, D., Guehl, D., Burbaud, P., and Cuny, E. (2013). A systematic review of studies on anatomical position of electrode contacts used for chronic subthalamic stimulation in Parkinson's disease. *Acta Neurochir. (Wien)* 155, 1647–1654. doi: 10.1007/s00701-013-1782-1

Caparros-Lefebvre, D., Blond, S., Feltin, M. P., Pollak, P., and Benabid, A. L. (1999). Improvement of levodopa induced dyskinesias by thalamic deep brain stimulation is related to slight variation in electrode placement: possible involvement of the centre median and parafascicularis complex. *J. Neurol. Neurosurg. Psychiatry* 67, 308–314. doi: 10.1136/jnnp.67.3.308

Chaturvedi, A., Butson, C. R., Lempka, S. F., Cooper, S. E., and McIntyre, C. C. (2010). Patient-specific models of deep brain stimulation: influence of field model complexity on neural activation predictions. *Brain Stimul.* 3, 65–67. doi: 10.1016/j.brs.2010.01.003

Cif, L., Vasques, X., Gonzalez, V., Ravel, P., Biolsi, B., Collod-Beroud, G., et al. (2010). Long-term follow-up of DYT1 dystonia patients treated by deep brain stimulation: an open-label study. *Mov. Disord.* 25, 289–299. doi: 10.1002/mds.22802

Coenen, V. A., Schlaepfer, T. E., Allert, N., and Madler, B. (2012). Diffusion tensor imaging and neuromodulation: DTI as key technology for deep brain stimulation. *Int. Rev. Neurobiol.* 107, 207–234. doi: 10.1016/B978-0-12-404706-8.00011-5

Coste, J., Ouchchane, L., Sarry, L., Derost, P., Durif, F., Gabrillargues, J., et al. (2009). New electrophysiological mapping combined with MRI in parkinsonian's subthalamic region. *Eur. J. Neurosci.* 29, 1627–1633. doi: 10.1111/j.1460-9568.2009.06698.x

Coubes, P., Roubertie, A., Vayssiere, N., Hemm, S., and Echenne, B. (2000). Treatment of DYT1-generalised dystonia by stimulation of the internal globus pallidus. *Lancet* 355, 2220–2221. doi: 10.1016/S0140-6736(00)02410-7

Fytagoridis, A., Sandvik, U., Astrom, M., Bergenheim, T., and Blomstedt, P. (2012). Long term follow-up of deep brain stimulation of the caudal zona incerta for essential tremor. *J. Neurol. Neurosurg. Psychiatry* 83, 258–262. doi: 10.1136/jnnp-2011-300765

Gabriel, C., Gabriel, S., and Corthout, E. (1996). The dielectric properties of biological tissues: I. Literature survey. *Phys. Med. Biol.* 41, 2231–2249. doi: 10.1088/0031-9155/41/11/001

Garcia-Garcia, D., Guridi, J., Toledo, J. B., Alegre, M., Obeso, J. A., and Rodriguez-Oroz, M. C. (2016). Stimulation sites in the subthalamic nucleus and clinical improvement in Parkinson's disease: a new approach for active contact localization. *J. Neurosurg.* 125, 1068–1079. doi: 10.3171/2015.9.JNS15868

Griffiths, R. I., Kotschet, K., Arfon, S., Xu, Z. M., Johnson, W., Drago, J., et al. (2012). Automated assessment of bradykinesia and dyskinesia in Parkinson's disease. *J. Parkinsons Dis.* 2, 47–55. doi: 10.3233/JPD-2012-11071

Groppa, S., Herzog, J., Falk, D., Riedel, C., Deuschl, G., and Volkmann, J. (2014). Physiological and anatomical decomposition of subthalamic neurostimulation effects in essential tremor. *Brain* 137(Pt 1), 109–121. doi: 10.1093/brain/awt304

Hariz, M., Blomstedt, P., and Zrinzo, L. (2013). Future of brain stimulation: new targets, new indications, new technology. *Mov. Disord.* 28, 1784–1792. doi: 10.1002/mds.25665

Hemm, S., Caire, F., Coste, J., Vassal, F., Nuti, C., Derost, P., et al. (2008). Postoperative control in deep brain stimulation of the subthalamic region: the contact membership concept. *Int. J. CARS* 3, 69–77. doi: 10.1007/s11548-008-0152-r6

Hemm, S., Mennessier, G., Vayssiere, N., Cif, L., and Coubes, P. (2005). Co-registration of stereotactic MRI and isofieldlines during deep brain stimulation. *Brain Res. Bull.* 68, 59–61. doi: 10.1016/j.brainresbull.2005.08.024

Hemm, S., and Wårdell, K. (2010). Stereotactic implantation of deep brain stimulation electrodes: a review of technical systems, methods and emerging tools. *Med. Biol. Eng. Comput.* 48, 611–624. doi: 10.1007/s11517-010-0633-y

Herrington, T. M., Cheng, J. J., and Eskandar, E. N. (2015). Mechanisms of deep brain stimulation. *J. Neurophysiol.* 70, 163–171. doi: 10.1152/jn.00281.2015

Herzog, J., Hamel, W., Wenzelburger, R., Potter, M., Pinsker, M. O., Bartussek, J., et al. (2007). Kinematic analysis of thalamic versus subthalamic neurostimulation in postural and intention tremor. *Brain* 130(Pt 6), 1608–1625. doi: 10.1093/brain/awm077

Hirai, T., and Jones, E. G. (1989). A new parcellation of the human thalamus on the basis of histochemical staining. *Brain Res. Brain Res. Rev.* 14, 1–34. doi: 10.1016/0165-0173(89)90007-6

Howell, B., and McIntyre, C. C. (2016). Analyzing the tradeoff between electrical complexity and accuracy in patient-specific computational models of deep brain stimulation. *J. Neural. Eng.* 13:036023. doi: 10.1088/1741-2560/13/3/036023

Journee, H. L., Postma, A. A., and Staal, M. J. (2007). Intraoperative neurophysiological assessment of disabling symptoms in DBS surgery. *Neurophysiol. Clin.* 37, 467–475. doi: 10.1016/j.neucli.2007.10.006

Kuncel, A. M., Cooper, S. E., and Grill, W. M. (2008). A method to estimate the spatial extent of activation in thalamic deep brain stimulation. *Clin. Neurophysiol.* 119, 2148–2158. doi: 10.1016/j.clinph.2008.02.025

Lalys, F., Haegelen, C., Mehri, M., Drapier, S., Verin, M., and Jannin, P. (2013). Anatomo-clinical atlases correlate clinical data and electrode contact coordinates: application to subthalamic deep brain stimulation. *J. Neurosci. Methods* 212, 297–307. doi: 10.1016/j.jneumeth.2012.11.002

Lemaire, J. J., Coste, J., Ouchchane, L., Hemm, S., Derost, P., Ulla, M., et al. (2007). MRI anatomical mapping and direct stereotactic targeting in the subthalamic region: functional and anatomical correspondance in Parkinson's disease. *Int. J. CARS* 2, 75–85. doi: 10.1007/s11548-007-0124-2

Lemaire, J. J., Sakka, L., Ouchchane, L., Caire, F., Gabrillargues, J., and Bonny, J. M. (2010). Anatomy of the human thalamus based on spontaneous contrast and microscopic voxels in high-field magnetic resonance imaging. *Neurosurgery* 66(3 Suppl. Operative), 161–172.

Magnotta, V. A., Gold, S., Andreasen, N. C., Ehrhardt, J. C., and Yuh, W. T. (2000). Visualization of subthalamic nuclei with cortex attenuated inversion recovery MR imaging. *Neuroimage* 11, 341–346. doi: 10.1006/nimg.2000. 0552

Mansur, P. H., Cury, L. K., Andrade, A. O., Pereira, A. A., Miotto, G. A., Soares, A. B., et al. (2007). A review on techniques for tremor recording and quantification. *Crit. Rev. Biomed. Eng.* 35, 343–362. doi: 10.1615/ CritRevBiomedEng.v35.i5.10

McIntyre, C. C., Mori, S., Sherman, D. L., Thakor, N. V., and Vitek, J. L. (2004). Electric field and stimulating influence generated by deep brain stimulation of the subthalamic nucleus. *Clin. Neurophysiol.* 115, 589–595. doi: 10.1016/j. clinph.2003.10.033

Morel, A. (2007). *Stereotactic Atlas of the Human Thalamus and Basal Ganglia.* Boca Raton, FL: CRC Press.

Palmer, J. L., Coats, M. A., Roe, C. M., Hanko, S. M., Xiong, C., and Morris, J. C. (2010). Unified Parkinson's Disease rating scale-motor exam: inter-rater reliability of advanced practice nurse and neurologist assessments. *J. Adv. Nurs.* 66, 1382–1387. doi: 10.1111/j.1365-2648.2010.05313.x

Papapetropoulos, S., Jagid, J. R., Sengun, C., Singer, C., and Gallo, B. V. (2008). Objective monitoring of tremor and bradykinesia during DBS surgery for Parkinson disease. *Neurology* 70, 1244–1249. doi: 10.1212/01.wnl.0000308936. 27780.94

Post, B., Merkus, M. P., de Bie, R. M., de Haan, R. J., and Speelman, J. D. (2005). Unified Parkinson's disease rating scale motor examination: are ratings of nurses, residents in neurology, and movement disorders specialists interchangeable? *Mov. Disord.* 20, 1577–1584. doi: 10.1002/mds.20640

Saint-Cyr, J. A., Hoque, T., Pereira, L. C., Dostrovsky, J. O., Hutchison, W. D., Mikulis, D. J., et al. (2002). Localization of clinically effective stimulating electrodes in the human subthalamic nucleus on magnetic resonance imaging. *J. Neurosurg.* 97, 1152–1166. doi: 10.3171/jns.2002.97.5.1152

Sarnthein, J., Peus, D., Baumann-Vogel, H., Baumann, C. R., and Surucu, O. (2013). Stimulation sites in the subthalamic nucleus projected onto a mean 3-D atlas of the thalamus and basal ganglia. *Acta Neurochir. (Wien)* 155, 1655–1660. doi: 10.1007/s00701-013-1780-3

Schaltenbrand, G., and Bailey, P. (1959). *Introduction to Stereotaxis with an Atlas of the Human Brain.* Stuttgart: Thieme Verlag.

Schmidt, C., Grant, P., Lowery, M., and van Rienen, U. (2013). Influence of uncertainties in the material properties of brain tissue on the probabilistic volume of tissue activated. *IEEE Tran. Biomed. Eng.* 60, 1378–1387. doi: 10. 1109/TBME.2012.2235835

Shah, A., Coste, J., Lemaire, J., Schkommodau, E., Taub, E., Guzman, R., et al. (2016a). A novel assistive method for rigidity evaluation during deep brain stimulation surgery using acceleration sensors. *J. Neurosurg.*

Shah, A., Coste, J., Lemaire, J. J., Schkommodau, E., and Hemm-Ode, S. (2013). "A method to quantitatively evaluate changes in tremor during deep brain stimulation surgery," in *Proceedings of the 6th International IEEE/EMBS Conference: Neural Engineering* (Rome: IEEE), 1202–1205.

Shah, A., Coste, J., Lemaire, J., Taub, E., Schüpbach, M., Pollo, C., et al. (2016b). Intraoperative acceleration measurements to quantify tremor during deep brain stimulation surgery. *Med. Biol. Eng. Comput.* doi: 10.1007/s11517-016-1559-9 [Epub ahead of print].

Slavin, K. V., and Burchiel, K. J. (2002). MicroGuide microelectrode recording system. *Neurosurgery* 51, 275–278. doi: 10.1097/00006123-200207000-00048

Spiegelmann, R., Nissim, O., Daniels, D., Ocherashvili, A., and Mardor, Y. (2006). Stereotactic targeting of the ventrointermediate nucleus of the thalamus by direct visualization with high-field MRI. *Stereotact. Funct. Neurosurg.* 84, 19–23. doi: 10.1159/000092683

Starr, P. A., Christine, C. W., Theodosopoulos, P. V., Lindsey, N., Byrd, D., Mosley, A., et al. (2002). Implantation of deep brain stimulators into the subthalamic nucleus: technical approach and magnetic resonance imaging-verified lead locations. *J. Neurosurg.* 97, 370–387. doi: 10.3171/jns.2002.97.2. 0370

Tarvainen, M. P., Ranta-Aho, P. O., and Karjalainen, P. A. (2002). An advanced detrending method with application to HRV analysis. *IEEE Trans. Biomed. Eng.* 49, 172–175. doi: 10.1109/10.979357

Vassal, F., Coste, J., Derost, P., Mendes, V., Gabrillargues, J., Nuti, C., et al. (2012). Direct stereotactic targeting of the ventrointermediate nucleus of the thalamus based on anatomic 1.5-T MRI mapping with a white matter attenuated inversion recovery (WAIR) sequence. *Brain Stimul.* 5, 625–633. doi: 10.1016/j.brs.2011.10.007

Vayssiere, N., Hemm, S., Cif, L., Picot, M. C., Diakonova, N., El Fertit, H., et al. (2002). Comparison of atlas- and magnetic resonance imaging-based stereotactic targeting of the globus pallidus internus in the performance of deep brain stimulation for treatment of dystonia. *J. Neurosurg.* 96, 673–679. doi: 10.3171/jns.2002.96.4.0673

Vayssiere, N., van der Gaag, N., Cif, L., Hemm, S., Verdier, R., Frerebeau, P., et al. (2004). Deep brain stimulation for dystonia confirming a somatotopic organization in the globus pallidus internus. *J. Neurosurg.* 101, 181–188. doi: 10.3171/jns.2004.101.2.0181

Voges, J., Kiening, K., Krauss, J. K., Nikkhah, G., and Vesper, J. (2009). [Neurosurgical standards in deep brain stimulation : consensus recommendations of the German Deep Brain Stimulation Association]. *Nervenarzt* 80, 666–672. doi: 10.1007/s00115-009-2698-0

Wårdell, K., Diczfalusy, E., and Åström, M. (2012). "Patient-Specific modeling and simulation of deep brain stimulation," in *Patient-Specific Modeling in Tomorrow's Medicine*, ed. A. Gefen (Berlin: Springer), 357–375.

Wårdell, K., Kefalopoulou, Z., Diczfalusy, E., Andersson, M., Astrom, M., Limousin, P., et al. (2015). Deep brain stimulation of the pallidum internum for gilles de la tourette syndrome: a patient-specific model-based simulation study of the electric field. *Neuromodulation* 18, 90–96. doi: 10.1111/ner.12248

Wårdell, K., Zrinzo, L., Hariz, M., and Andersson, M. (2013). "Patient-specific brain modelling for deep brain stimulation simulations," in *Proceedings of the 6th International IEEE/EMBS Conference: Neural Engineering* (Rome: IEEE), 148–151.

Weise, L. M., Seifried, C., Eibach, S., Gasser, T., Roeper, J., Seifert, V., et al. (2013). Correlation of active contact positions with the electrophysiological and anatomical subdivisions of the subthalamic nucleus in deep brain stimulation. *Stereotact. Funct. Neurosurg.* 91, 298–305. doi: 10.1159/000345259

Wodarg, F., Herzog, J., Reese, R., Falk, D., Pinsker, M. O., Steigerwald, F., et al. (2012). Stimulation site within the MRI-defined STN predicts postoperative motor outcome. *Mov. Disord.* 27, 874–879. doi: 10.1002/mds.25006

Zerroug, A., Gabrillargues, J., Coll, G., Vassal, F., Jean, B., Chabert, E., et al. (2016). Personalized mapping of the deep brain with a white matter attenuated inversion recovery (WAIR) sequence at 1.5-tesla: experience based on a series of 156 patients. *Neurochirurgie* 62, 183–189. doi: 10.1016/j.neuchi.2016.01.009

Zonenshayn, M., Sterio, D., Kelly, P. J., Rezai, A. R., and Beric, A. (2004). Location of the active contact within the subthalamic nucleus (STN) in the treatment of idiopathic Parkinson's disease. *Surg. Neurol.* 62, 216–225. doi: 10.1016/j.surneu. 2003.09.039

Zrinzo, L. (2010). The role of imaging in the surgical treatment of movement disorders. *Neuroimaging Clin. North Am.* 20, 125–140. doi: 10.1016/j.nic.2009. 08.002